Micromechanisms of Paperboard Deformation

by

Heather M. Dunn

Submitted to the Department of Mechanical Engineering
in partial fulfillment of the requirements for the degree of

Master of Science in Mechanical Engineering

at the

MASSACHUSETTS INSTITUTE OF TECHNOLOGY

September 2000

Author .....
Department of Mechanical Engineering
August 1, 2000

Certified by .....
Mary C. Boyce
Professor
Thesis Supervisor

Certified by .....
David M. Parks
Professor
Thesis Supervisor

Accepted by .....
Ain A. Sonin
Chairman, Department Committee on Graduate Students

Micromechanisms of Paperboard Deformation

by

Heather M. Dunn

Submitted to the Department of Mechanical Engineering
on August 1, 2000, in partial fulfillment of the
requirements for the degree of
Master of Science in Mechanical Engineering

Abstract

An experimental study of the micromechanisms of paperboard deformation has been conducted. Experiments were performed in a scanning electron microscope, allowing visual observation and coincident acquisition of load vs. deformation data. Deformation mechanisms were determined and correlated with features of the load vs. deformation curves for different loading modes. A macroscopic study was performed concurrently to provide accurate continuum-level load vs. deformation data.

This study contributed to an effort to model the creasing process. In creasing, paperboard is punched to create an internal line of damage and then folded along that line to create a corner. It has been determined experimentally that the creasing process involves through-thickness compression and transverse shear loading, as well as in-plane tension loading. Out-of-plane delamination also plays an important role.

Experiments were conducted to determine the stress-strain behavior and corresponding deformation mechanisms under several well-controlled loading conditions. These include through-thickness compression, shear, and tension, as well as combined tension/shear loading. In-plane tensile behavior was also investigated.

Paperboard loaded in out-of-plane compression behaved linearly at small strains, with an exponential increase in stiffness at larger strains. Deformation mechanisms included void closure and fiber collapse. In out-of-plane shear, paperboard initially behaved linearly, but departed from linearity before a peak in load. The dominant failure mechanism at the microscopic scale was sudden fiber disengagement throughout the entire cross-section, corresponding to the peak in load. Loaded in out-of-plane tension, the paperboard first exhibited many small cracks at the interfaces between layers. As these cracks grew, one became dominant, and all further delamination occurred by extension of that crack. Similar behavior was observed in combined loading experiments with tension as the larger load component. With shear as the larger component, delamination generally occurred suddenly rather than being preceded by small local cracks.

In-plane tensile behavior also included an initial linear region, followed by nonlinearity and a peak in load. The dominant mechanisms were fiber break and fiber disengagement in the different layers of the board; this again corresponded to the

Acknowledgments

I would like to thanks my advisors, Professors Boyce and Parks, for guidance and feedback throughout this project, both during the research and the writing phases. For financial support on project, I thank TetraPak, StoraEnso, and AssiDomain. Thanks also to Steve Xia, Niclas Stenberg, Johan Tryding, and Ingrid Rokahr for providing needed project information and data along the way.

Several people provided important technical help on this project. Afreen Siddiqi and Brian Gearing patiently answer my many questions about Labview. Brygg Ullmer helped me by providing access to and guidance in operating the MIT Media Lab laser cutter. Edmund Golaski did some emergency machining on fixtures that I didn't get quite right in the first design iteration. A huge thank you to Don Galler for endless help, advice, and patience regarding the scanning electron microscope used in this research.

Many thanks to the other graduate students in my group for being my computer help center during the writing process. Particular thanks to Mats Danielsson for providing memory space on his computer for me to store my many images and to Rebecca Brown, Greg Nielson, Tom Arsenlis, and Rami Lokas for answering many questions about Unix-based software.

On the personal side, my thanks to my friends who have patiently listened to me talk nonstop about my thesis for the last several months - Mats, Rebecca, Greg, Theresa Burianek, Laura Kwinn, Allison Clayton, and Greg Pollock. Thanks also to my roommates for understanding my frequent long absences and for gently reminding me to turn my rent checks in on time. A big thank you to Mark for nursing back to health during a mid-thesis bout of illness, for searching out obscure journal articles for me, and for being my proofreader, my crisis manager, my cheering section, and my all-around good companion. Finally, of course, my thanks to my family for all of their encouragment and support through the years.

Contents

List of Figures

List of Tables

Chapter 1

Background

1.1 Project Overview

Material models are a useful tool to the manufacturing engineer, as they can often predict how changes in parameters of the manufacturing process will alter the properties and performance of the final product. Models for homogeneous, isotropic materials are relatively simple, requiring only two elastic material constants and a handful of equations to predict behavior under basic loading conditions. However, even for these simple materials, complicated loadings are difficult or even impossible to model analytically and require the use of numerical techniques.

Anisotropy adds complexity to models and requires additional material constants. Heterogeneity further complicates the matter by requiring consideration of multiple sets of material constants and by creating competing deformation responses within the material. Predicting the behavior of anisotropic, heterogenous materials generally requires numerical modelling techniques like finite element analysis.

Paperboard is such a material, both anisotropic and heterogeneous. It is a layered material composed of fibers with a preferred orientation in the plane. The fiber orientation direction is called the machine direction. The perpendicular direction in the plane is the cross direction, and the out-of-plane direction is called the Z direction. The preferred fiber orientation, which causes anistropy, is due to the deposition rolling and squeezing processes in manufacture of paperboard. Paperboard is generally made

on a continuous feed line, so rolling, squeezing, and other similar operations are always performed in the same direction, the machine directon. These operations cause the fibers that comprise paperboard to be preferentially oriented along the machine direction or at a small angle to it. As a result, stiffness and strength of the material in the machine direction are very different than in other directions. Stiffness and strength properties in the machine direction are typically higher than those in the cross direction by a factor of 2-5 and higher than Z direction properties by a factor of 100.

Heterogeneity in paperboard is due to its complex structure. Paperboard is composed of processed wood fibers, and the presence of fibers of different shapes and sizes, as well as gaps and voids between fibers, creates a basic level of heterogeneity. Paperboard is also a layered material, and the material behavior at the interfaces between layers is far different from behavior within the layers themselves, adding another level of heterogeneity. Finally, the layers of a given type of paperboard may have different properties, depending on the way the component fibers were processed and the amount and type of starch added to promote bonding. This adds another source of heterogeneity.

Due to these complicating factors, many important loading conditions of paperboard cannot be predicted analytically. However, a predictive model of paperboard is desirable to manufacturers that work with the material. One particular process that manufacturers would like to be able to predict is creasing, the process of making corners. Paperboard is a common material in packaging, used in containers like milk cartons, cereal boxes, cigarette packs, juice boxes, and many others. Containers require corners, making creasing an important process to understand.

Creasing is done in two steps. In the first step, the paperboard is punched between a narrow male and female die, as shown in Figure 1-1. The width of the male die is generally similar to the thickness of the paperboard, with the female die about three times as wide. Punching creates a line of damage in the paperboard. When a bending moment is applied to the material, it will fold preferentially along this line, ideally creating a straight, even crease. During folding, the compressive side of the bend,

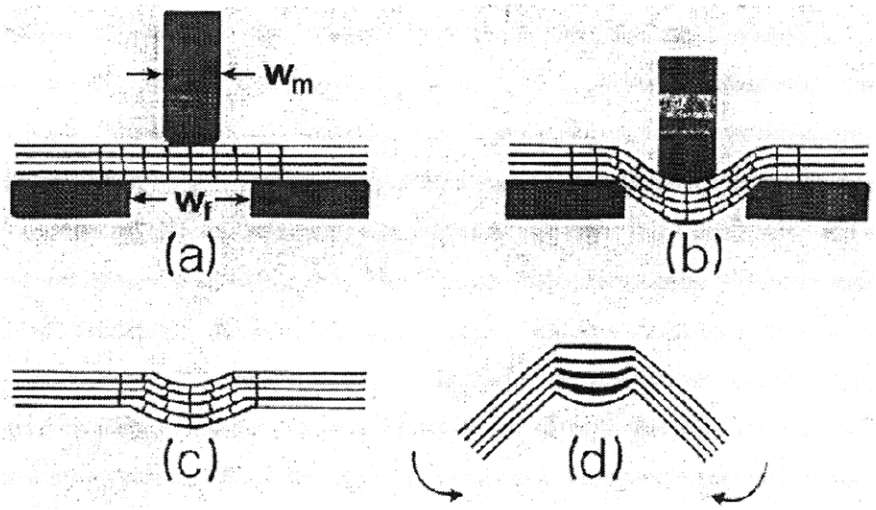

Figure 1-1: Schematic of creasing from Carlsson, et al. [3]. Step (a) shows the paperboard in the punching die. Step (b) shows the punching process. Step (c) shows the damage in the paperboard after punching, and (d) shows the bending process.

together with the damage induced by punching, separates the layers, causing buckling of the interior layers into the package. The extent and location of layer delamination determines the quality of the crease.

If there is insufficient delamination to accomodate the length difference between the outside and inside of the bend, the outside material may tear. This is a bad crease, as it results in an unattractive package. A crease is also considered of poor quality if delamination happens toward one side of the bend rather than in the middle, as this weakens the corner when loaded along its axis and, aesthetically, can result in a wandering outer edge. This second distinction between good and bad creases is illustrated in Figures 1-2 and 1-3.

The seemingly complex loadings of the creasing process can be represented as combinations of simpler loading arrangements like through-thickness compression and tension, interlaminar shear, and in-plane tension. If each of these simple loading conditions can be accurately modeled, the models can be combined to represent the creasing process. This thesis reports on experiments performed on paperboard in each of the simple loading modes listed above. Experiments were performed at both

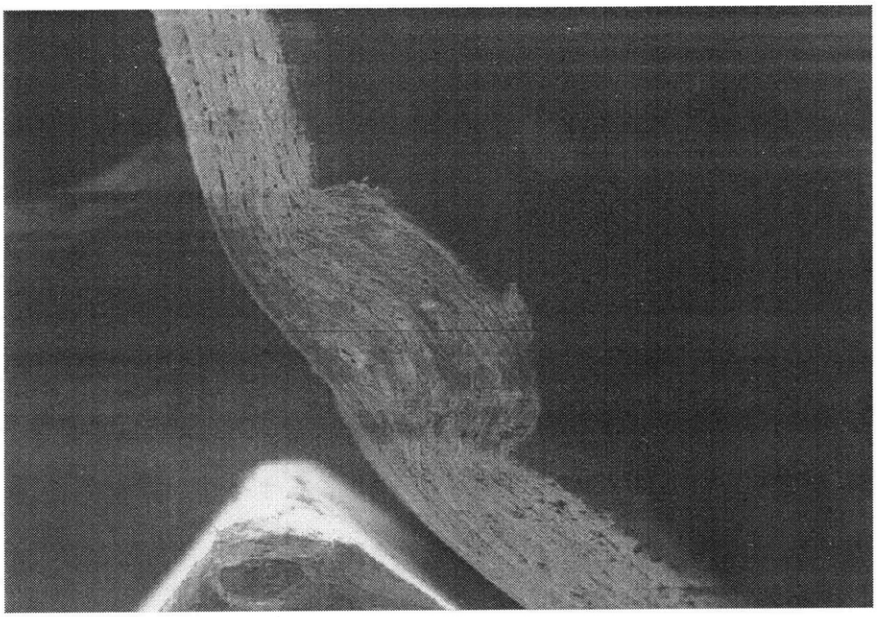

Figure 1-2: An example of a good crease, with delamination in the center of the bend.

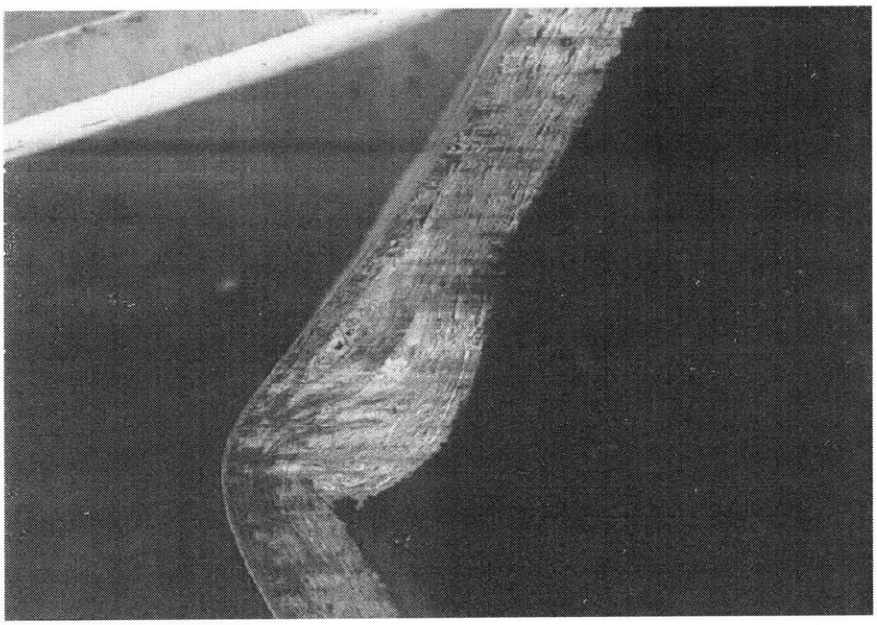

Figure 1-3: An example of a bad crease, with delamination on one side of the bend.

macroscopic and microscopic length scales. Macroscopic experiments were performed at a length scale of several centimeters and were intended to provide quantitative data on which to calibrate empirical constitutive models for paperboard. Microscopic experiments were performed at a scale of a few millimeters, the length of an individual fiber. Microscopic experiments were intended to determine the mechanisms that govern paperboard behavior in each of the basic loading modes and to suggest ways in which those mechanisms could be represented in a numerical model. Macroscopic experiments were performed by Niclas Stenberg of STFI, the Swedish Pulp and Paper Institute. Microscopic experiments were performed by the author at MIT.

This thesis begins with a review of other work on paperboard deformation, particularly under out-of-plane loading. This is followed by a description of the paperboard used in this study and of the experimental equipment and methods. Results of out-of-plane testing – including tension, compression, shear, and combined loadings – are reported next. Results of in-plane tension experiments follow. The thesis concludes with a summary and discussion of the results and suggestions for additional study.

1.2 Literature Review

Treatment of the through-thickness deformation of paperboard in the literature has been very limited. Most of the literature on paper and paperboard behavior focuses on load vs. deformation curves and modelling of in-plane loading. Only a small subset discusses out-of-plane behavior, with an even smaller number focusing on deformation mechanisms out of the plane. However, even the limited about of previous work provides valuable references.

The scarcity of attention to the creasing process in the literature is surprising given the importance of creasing in applications like packaging. Carlsson, et al. [1], studied failure of paperboard in four-point bending. In the plane, paperboard is much stronger in tension than in compression. On this basis, they postulated that failure in bending would be compressive in nature, buckling rather than tearing. Observations confirmed this; failure occurred by compressive buckling and interlaminar crack prop-

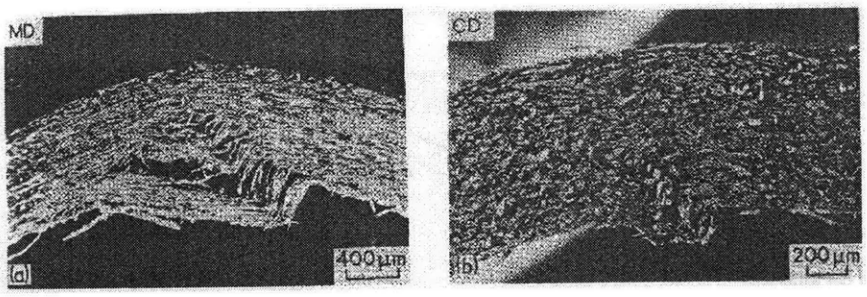

Figure 1-4: Image (a), a machine-direction crease, shows significantly more delamination than image (b), a cross-direction crease. Carlsson, et al. [1].

agation. However, the compressive failure strain was higher than under pure in-plane compression. They found that this was due to the stabilizing effect of the tensile side of the bend, as well as local deformation accomodated by fiber buckling prior to global failure. Additionally, they observed that delamination was more pronounced in the direction of principal fiber orientation (called the machine direction due to the orientation effects of rolling and other processing steps) than in the perpendicular direction, called the cross direction. This is shown in Figure 1-4.

Donner, et al. [2], observed similar failure by compressive buckling. They further found that delamination in the bending process was driven by large shear stresses and occurred preferentially along weak zones in the sheet, parallel to the sheet surface. The layers of the board were still largely intact after bending, indicating that damage evolved primarily at the interfaces between layers of the material.

A second study by Carlsson, et al. [3], supports the idea of delamination at weak zones. In a series of creasing experiments, they implanted defects between layers to create weak zones. Micrographs of the bent specimens, Figures 1-5 through 1-7, show that delamination is concentrated at the defects and is more widely distributed in specimens with more defects implanted. Increasing the number of implanted defects was also found to decrease the bending strength and crease stiffness of the specimens.

Discussion of through-thickness tension in the literature is extremely rare, as it does not have any direct applications in paper and paperboard processing. In a survey of methods for determining the internal bond strength of paper, Koubaa, et

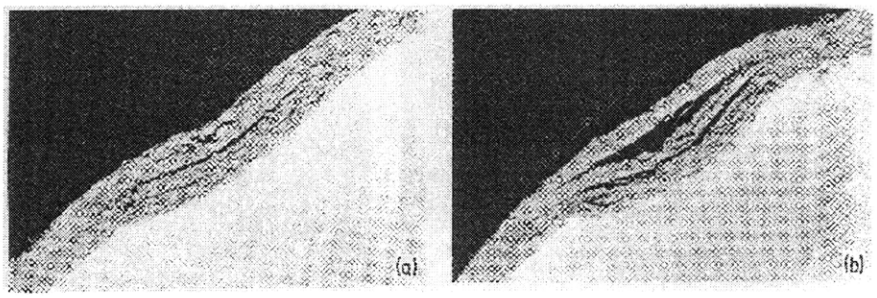

Figure 1-5: Creased board with no implanted defects bent through both a small (a) and large (b) angle. Carlsson, et al. [3].

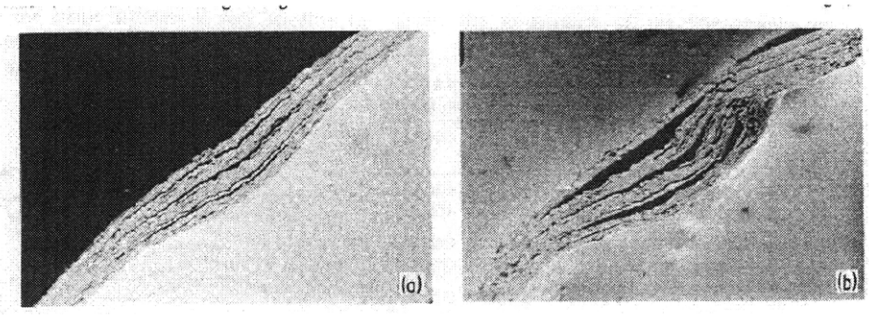

Figure 1-6: Creased board with three implanted defects bent through both a small (a) and large (b) angle. Carlsson, et al. [3].

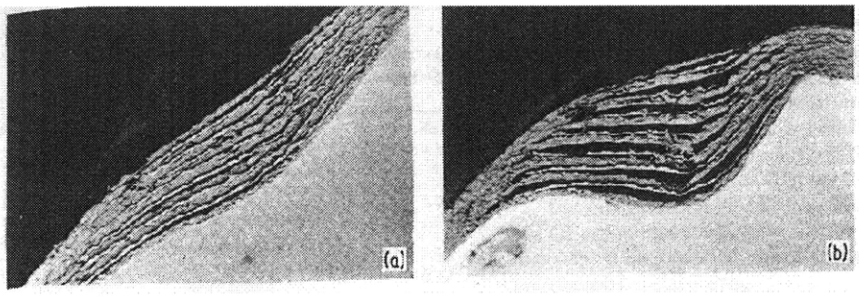

Figure 1-7: Creased board with several implanted defects bent through both a small (a) and large (b) angle. Carlsson, et al. [3].

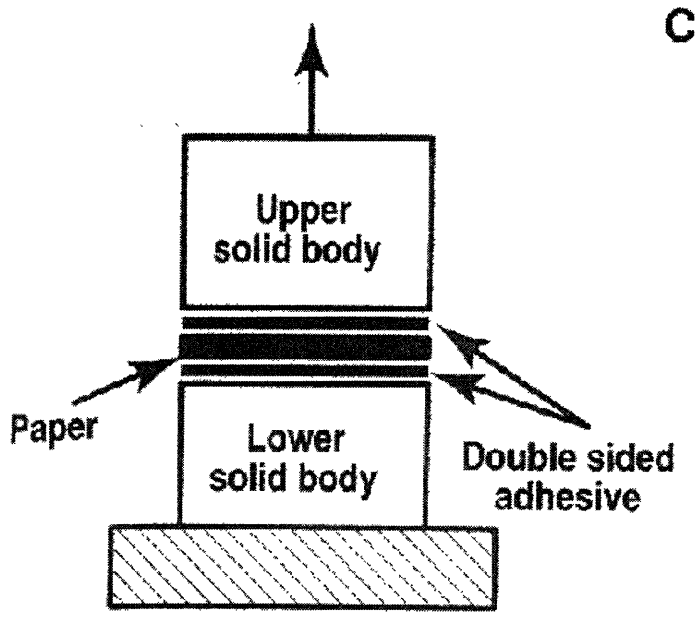

Figure 1-8: Schematic of the ZD tension test. Koubaa, et al. [4].

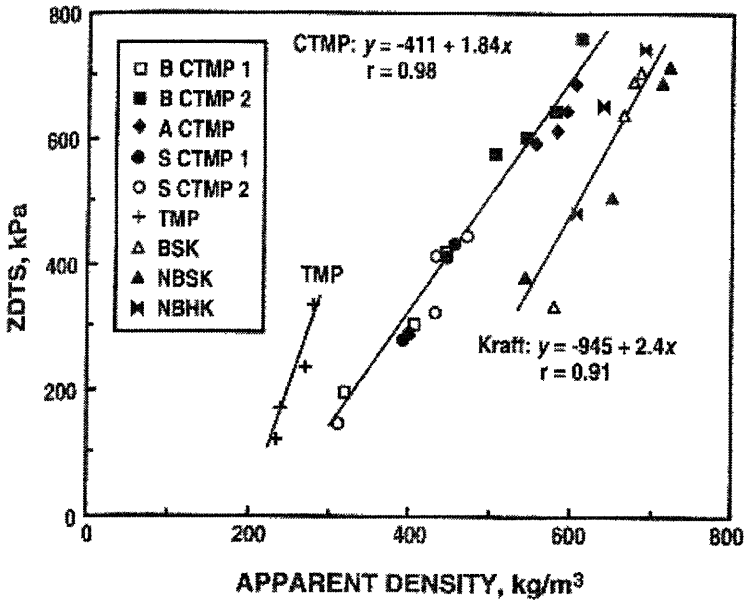

Figure 1-9: ZD tensile strengths for paperboards of various densities and chemical treatments. Koubaa, et al. [4].

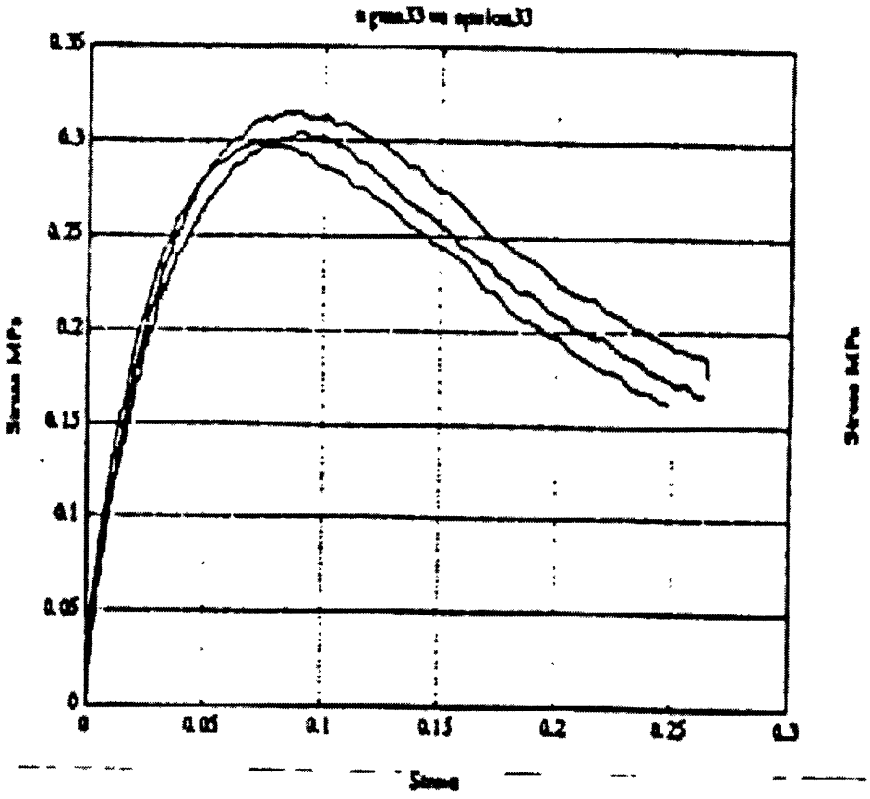

Figure 1-10: Stress-stress data for paperboard loaded in ZD tension. Persson [5].

al. [4], describe a ZD tension test, illustrated in Figure 1-8. They find that this method is the most effective for measuring the internal bond strength of paperboard and other multi-ply materials. Z-direction tensile strengths were measured using this method for paperboard with different chemical treatments and densities. The results, shown in Figure 1-9, indicate that through-thickness tensile strength has significant dependence on both chemical processing and sheet density.

Persson [5] presents stress-strain data for paperboard loaded in ZD tension, shown in Figure 1-10. The data indicates linear behavior up to a strain of 0.3%. Stress increases nonlinearly before peaking at 8% strain, beyond which the material softens.

There has been more work done on through-thickness compression of paper and board because of its role in processes like calendering. Johnston, et. al [6], found that the stress-strain curve of paper in through-thickness compression is nonlinear. As compressive load is applied, voids in the material collapse, causing the stiffness to

increase. Plastic strain under compression was found to be the result of irreversible deformation in the network rather than plastic deformation of the fibers. Fibers which had collapsed during loading typically sprung back when the load was removed, but material voids which had collapsed did not reappear.

Ratto, et al. [7], present similar stress-strain behavior data, but proceed a step further with mechanism analysis. They find that ZD compression occurs in three stages. The first stage is a decrease in void volume, as Johnston, et al., observed. This is followed by the second stage, fiber wall buckling, and in the final stage by fiber crushing. An exponential relationship between stress and strain is demonstrated. Data from pulse loading experiments, presented in Figure 1-11, indicates that a significant amount of plastic strain occurs. A series of pulse experiments were performed with increasing maximum loads. The data from these experiments is included as Figure 1-12 and shows that both maximum strain and plastic strain have an exponential relationship to maximum stress.

Schaffrath, et al. [8], make similar observations of exponential behavior under ZD compression. Figure 1-13 shows load-deformation behavior. Load (druck) is on the vertical axis. Strain, here called relative deformation (verformung) is on the horizontal axis. The plastic and elastic components of deformation are illustrated in Figure 1-14. In agreement with Ratto, et al., this data shows an exponential plastic deformation evolution. This study further concentrated on the effects of surface roughness during through-thickness compression. Surface roughness allows more relative deformation to be accomodated near/at the surface than through the core of the material. The result is a nonlinear relationship between compressive modulus E and material thickness t. Models of paper stacks under compression must account for this effect, as it prevents a stack from being modeled as simply a series of individual sheets.

Persson [5] also presents stress-strain data for through-thickness compression, as shown in Figure 1-15. Persson's data generally agrees with other observations of exponential behavior. However, a careful examination does reveal a region of linear behavior at very small strains. Plotting tension and compression together, as in

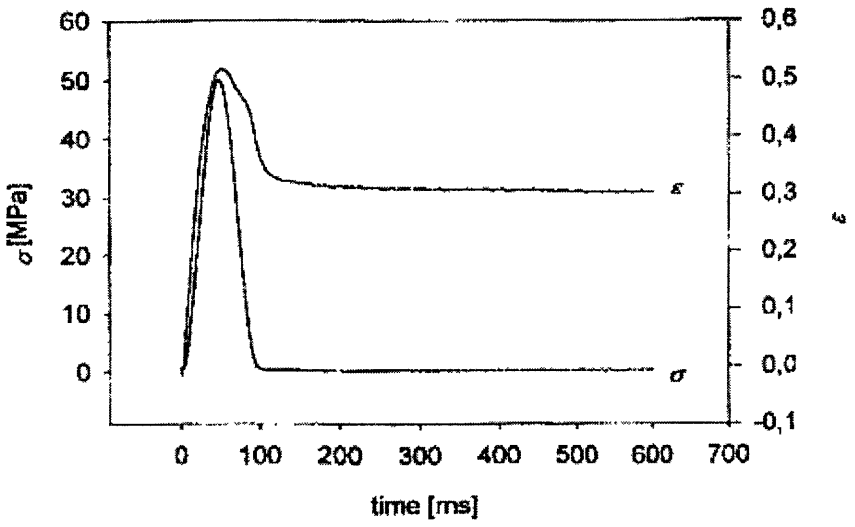

Figure 1-11: Stress and strain versus time for a ZD compression pulse loading experiment. Ratto, et al. [7].

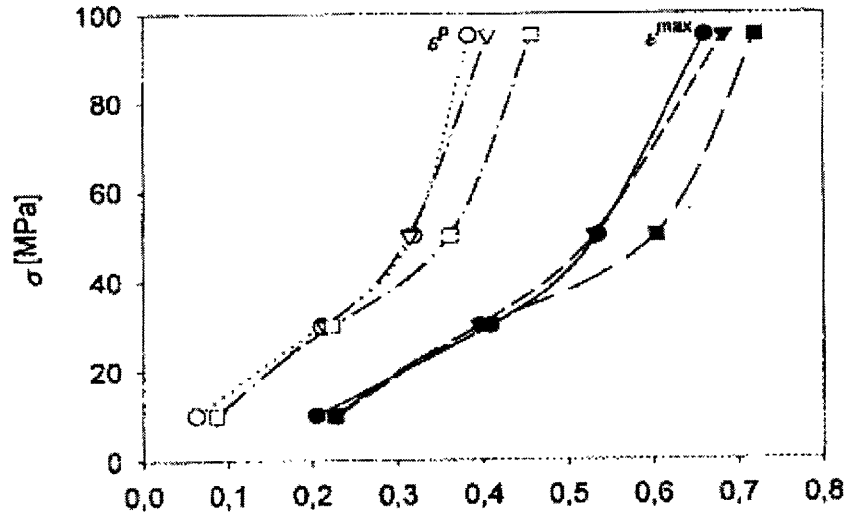

Figure 1-12: Maximum and plastic strain versus maximum stress for a series of ZD compression pulse experiments. Ratto, et al. [7].

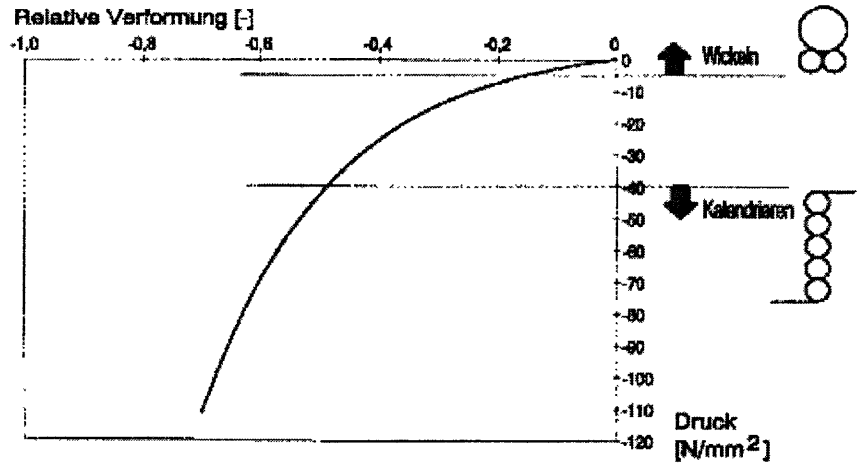

Figure 1-13: Load-deformation curve for ZD compression of paper. Schaffrath, et al. [8].

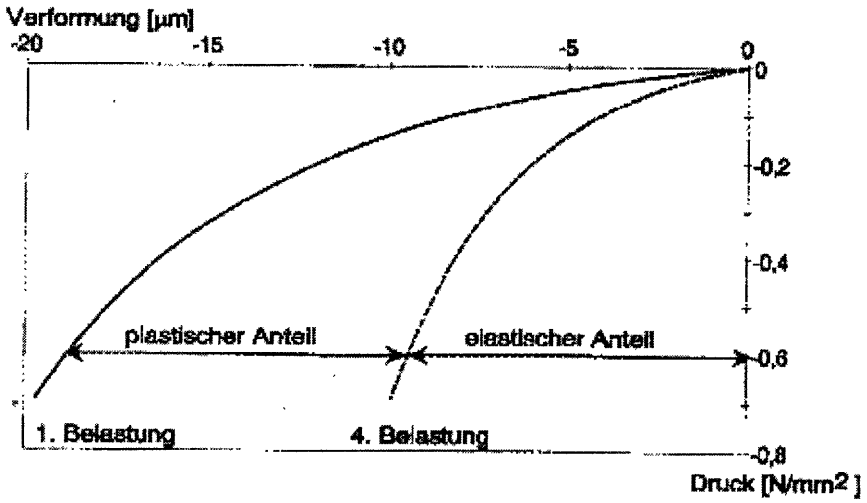

Figure 1-14: Elastic and plastic components of strain in paper loaded in ZD compression. Schaffrath, et al. [8].

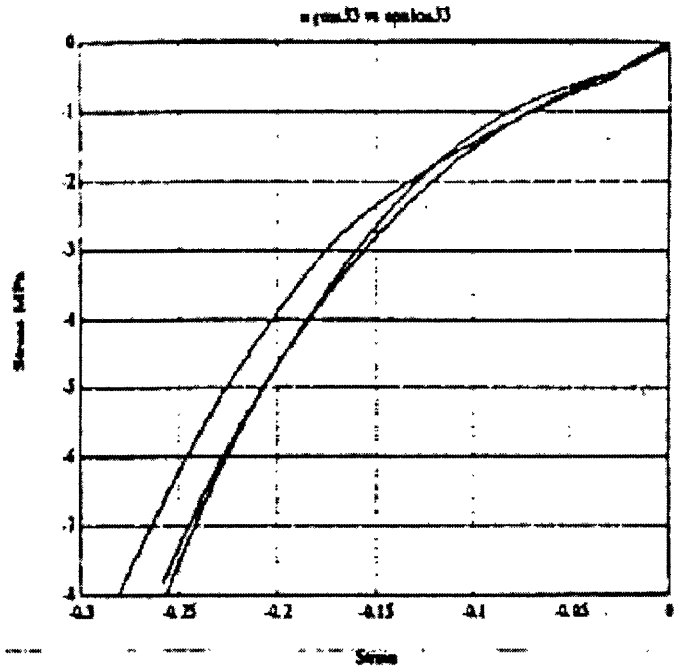

Figure 1-15: Stress-strain data for ZD compression of paperboard. Persson [5].

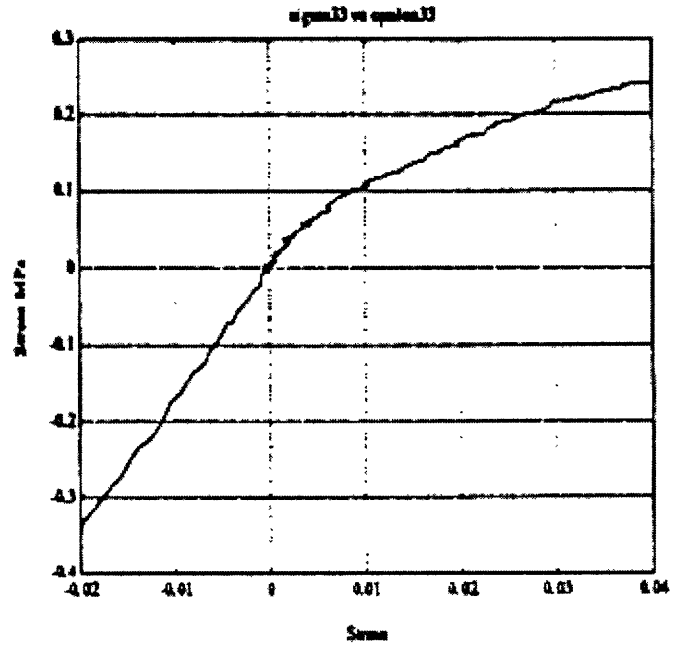

Figure 1-16: ZD tension and compression of paperboard. Persson [5].

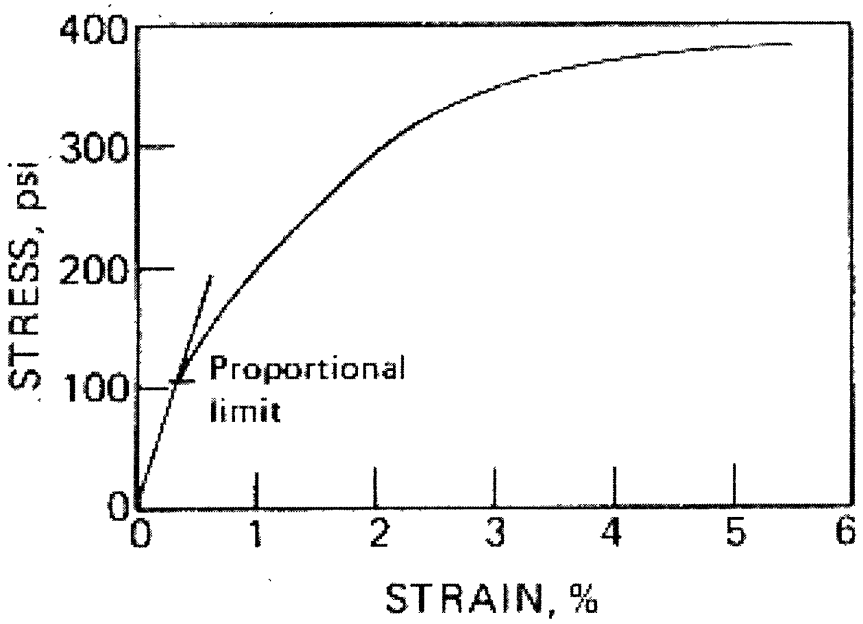

Figure 1-17: Stress-strain curve for paper loaded in interlaminar shear. Byrd, et al. [9].

Figure 1-16, shows that the modulus is symmetric about the origin.

Information on interlaminar shear behavior is also scare in the literature. Accurate shear stress-strain data is difficult to obtain for paper because of problems with adhesive. Significant adhesive penetration can alter the effective thickness of the material, and if the adhesive is not very stiff compared to the material, shear deformation within the adhesive can distort measured strain values.

Byrd, et al. [9], working with a suitably stiff adhesive, collected the data shown in Figure 1-17. The curve has an initial steep linear region, but deviates from linearity at 2% strain. At 5% strain, the slope has decreased almost to zero, but the experiment was not continued to a peak in stress. This measurement method was found to work only with specimens of minimum thickness 0.005 inches. With thinner specimens, an individual fiber could be caught in the adhesive on both faces, causing an overestimate in stiffness. This suggests that shear failure of the material tested was primarily by bond breaking and fibers pulling out of the network, as stiffness increased when some fibers could not be pulled out due to double gluing.

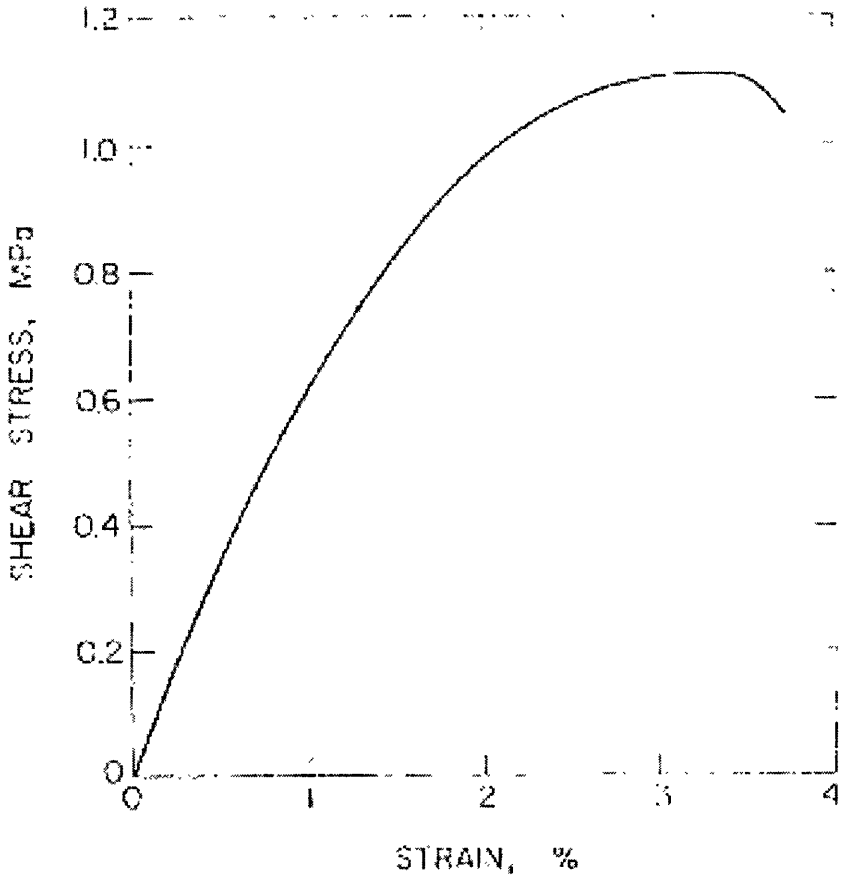

Figure 1-18: Stress-strain curve for paper loaded in interlaminar shear. Fellers [10].

In a study on methods of shear testing, Fellers [10] collected the stress-strain data in Figure 1-18. This curve is similar in shape to that presented by Byrd et al. A peak in stress occurs at about 3.5% strain, but the post-peak behavior is not presented.

Persson obtained interlaminar shear behavior information by loading paper at 45^o between the plane and the Z direction, as illustrated in Figure 1-19. His curves, Figures 1-20 and 1-21, are similar in shape to the others. However, he measures shear moduli of about 8.8 MPa in the MD and 8.0 in the CD, compared to values of 67.8 MPa and 59.2 MPa, respectively, measured by Fellers for the same material. This difference shows significant method sensitivity. The Fellers data is more likely to be accurate, as the component of through-thickness tension in Persson's experiments may have had an effect on shear behavior.

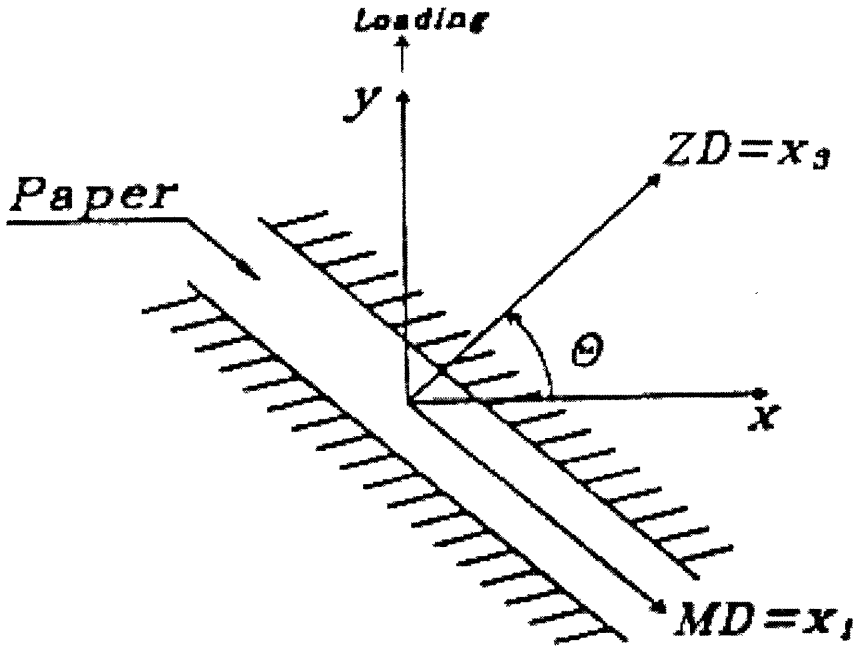

Figure 1-19: Schematic of combined load experiment for determining shear behavior. Persson [5].

In a study on the effects of orientation, Waterhouse [11], established that shear stiffness and strength in the machine direction increase as the degree of anistropy increases. This agrees with the effects of anisotropy seen in the measurements above.

The in-plane behavior of paper has been discussed more extensively in the literature. Only a sample of the available literature is presented here. El Maachi, et al. [12], discussed the in-plane tensile and compressive behavior of paper as part of a study on bending. Figure 1-22 shows data for in-plane tension and compression of paper. In both cases, there is an initial linear region followed by deviation from linearity, a peak in load, and softening. However, the peak is much higher in tension. This has implications in the bending process. In most models of bending, the neutral surface is assumed to remain stationary because of symmetry in tensile and compressive behavior. However, in the case of paper, symmetry does not hold, and bending models must account for the resultant motion of the neutral surface as bending progresses.

Persson presents data only for in-plane tension, shown in Figures 1-23 and 1-24.

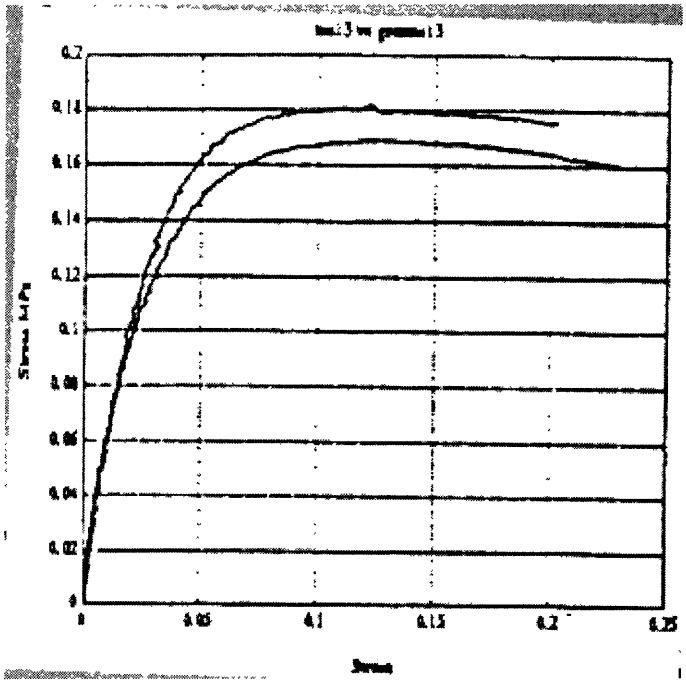

Figure 1-20: Stress-strain curve for paperboard loaded in interlaminar shear in the machine direction. Persson [5].

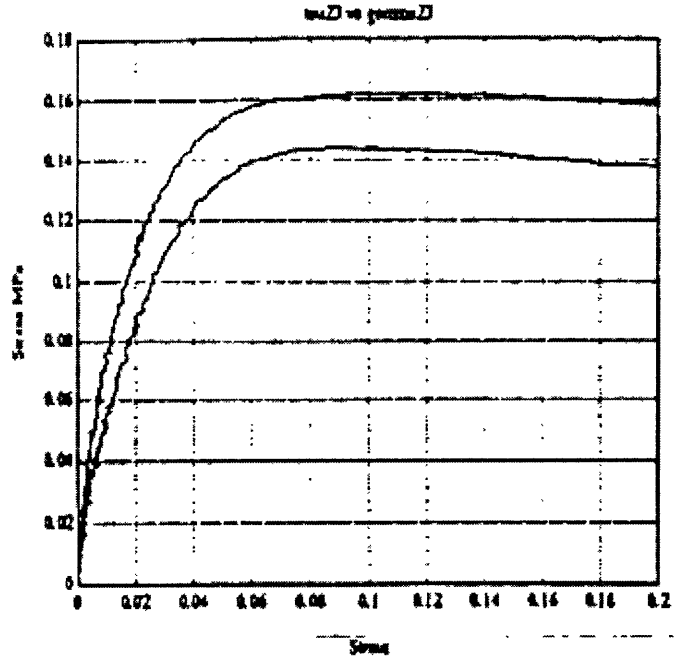

Figure 1-21: Stress-strain curve for paperboard loaded in interlaminar shear in the cross direction. Persson [5].

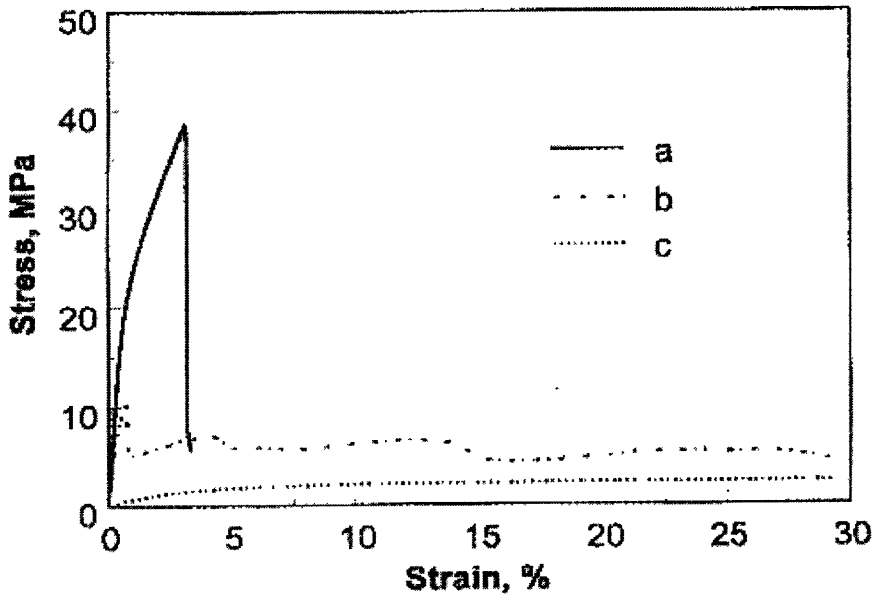

Figure 1-22: In-plane tension and compression of paper. Curve (a) was collected during a pure tension experiment. Curve (b) represents pure compressive behavior. Curve (c) shows tension of a previously compressed specimen. El Maachi, et al. [12].

In both the machine and cross directions, there is a linear region followed by nonlinear behavior. Stiffness is much larger in the machine direction, 5420 MPa compared to only 1900 MPa for cross direction stiffness. However, the change in slope in the nonlinear region is much more pronounced in the cross direction than in the machine direction.

Tryding [13] presents in-plane tension data extending into the post-peak region, which is shown in Figure 1-25. Similar to other authors, he observed initial linear behavior followed by a decrease in slope. Beyond the peak there is a dramatic decrease in load, beginning to flatten out only after dropping to less than a third of the peak value. Tryding found that for all specimen lengths greater than a certiain critical length, this sort of sudden rupture was typical.

The data in Figure 1-25 was collected in MD tension and constrasts with Figure 1-26, collected in CD tension. As Persson observed, the paperboard is stiffer in the machine direction than in the cross direction. However, the decrease in slope in the nonlinear region is much greater in the cross direction. Similarly, the board is stronger

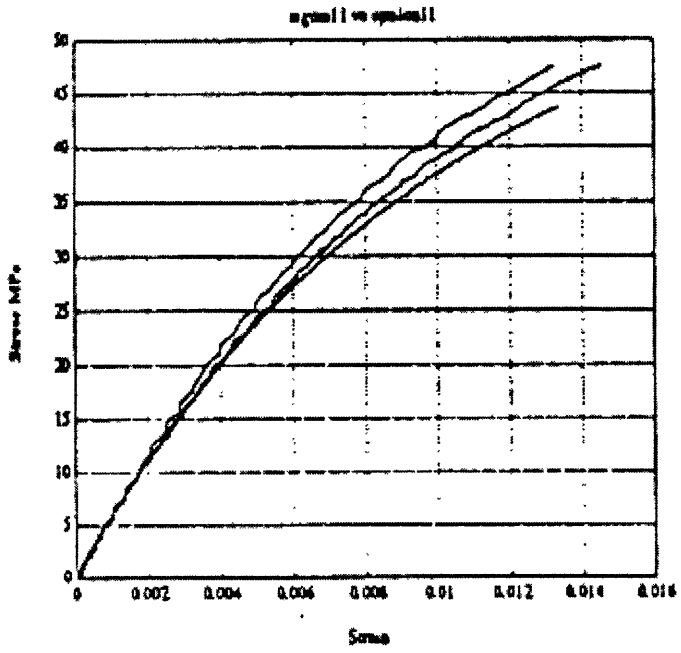

Figure 1-23: Stress-strain data for paperboard loaded in MD tension. Persson [5].

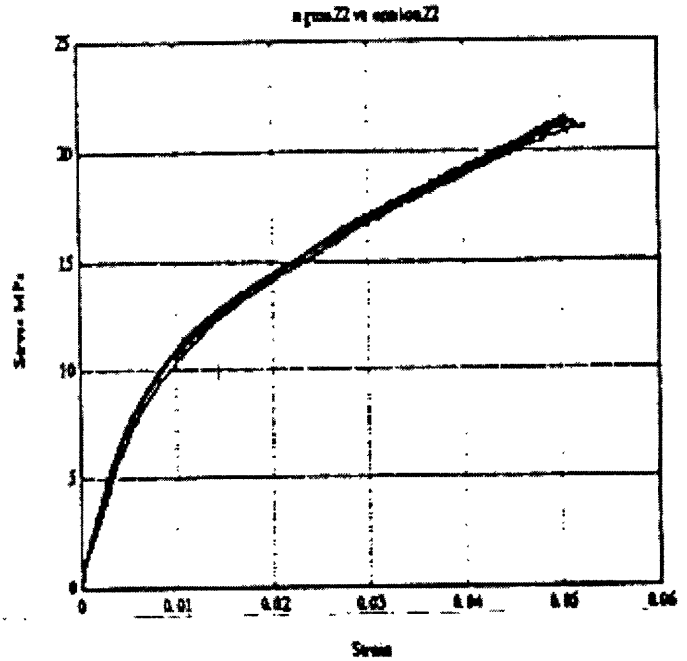

Figure 1-24: Stress-strain data for paperboard loaded in CD tension. Persson [5].

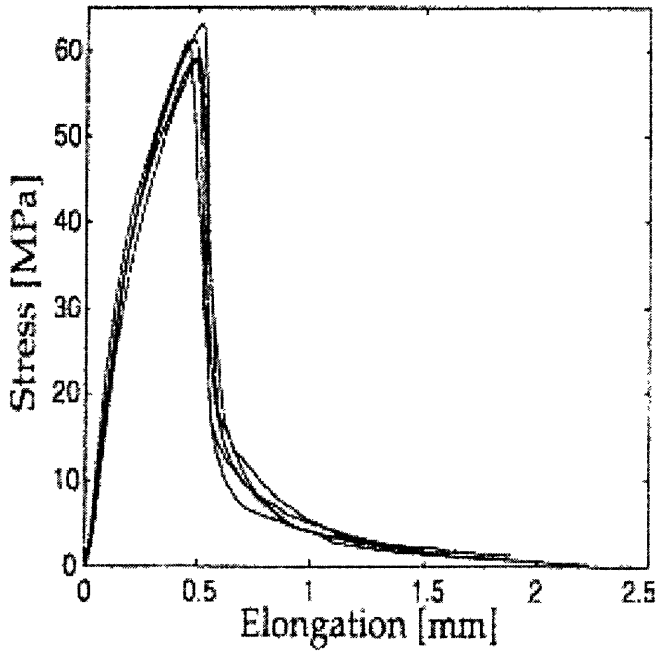

Figure 1-25: Stress-strain curve for paper loaded in MD tension. Tryding [13].

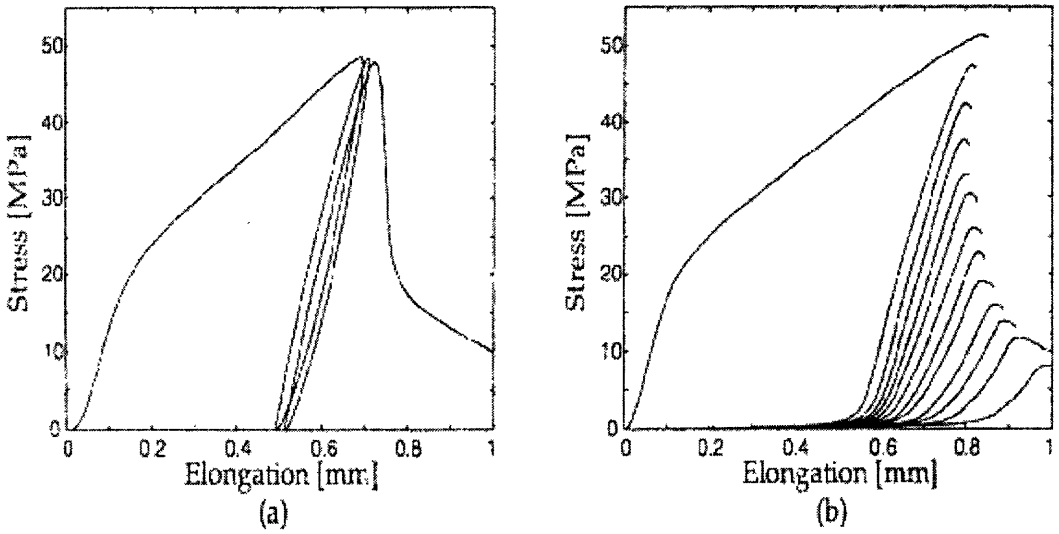

Figure 1-26: Stress-strain curve for paper loaded in MD tension. Specific loadings show plastic strain (a) and damage softening (b). Tryding [13].

in the MD but fails at a larger strain in the CD. The CD data illustrates two other phenomena. Data set (a) shows the plastic strain accumulated just before the peak in load. Data set (b) shows the effects of damage and softening in the post-peak region. The softening is due to bond failure. Beyond this region, only single fibers are observed bridging the rupture zone.

The available literature on mechanical behavior of paper and board focuses largely on in-plane behavior. Very little is available on response to out-of-plane loading. This study contributes to knowledge of out-of-plane paperboard behavior, with a focus on micromechanisms of deformation, a subject particularly neglected in the literature.

Chapter 2

Experimental Procedures

The experimental component of this project was carried out on two different scales. Microscopic experiments allowed observation of deformation mechanisms at the layer and fiber level. Macroscopic experiments were performed to determine material properties of the paperboard. Specimen sizes in the microscopic experiments were on the order of the fiber length, so individual fibers could affect data values gathered on the microscopic level. Macroscopic specimens were large enough to average out the effects of individual fibers, generating more accurate material behavior information. Data collected at the microscopic level serves to check macroscopic data and highlights material parameters affected by the length scale of the material dimensions. More importantly, data collected at the microscopic level can be compared with corresponding images to establish relationships between material behavior curve features and deformation mechanisms.

Microscopic experiments were performed at MIT by the author. Macroscopic experiments were performed at STFI by Niclas Stenberg.

2.1 Description of Material

The primary material used in this study is Triplex, a commercial paperboard produced and provided by StoraEnso. Paperboard is a multi-layered material; Triplex in particular is composed of five layers, three core "mechanical" layers and two outer

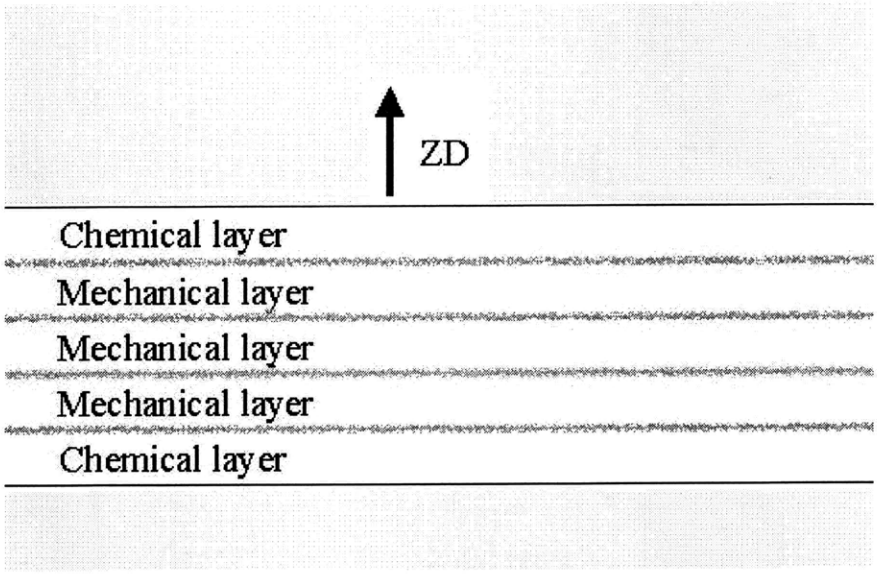

Figure 2-1: Schematic of Triplex in cross section showing layer compositions and interfaces.

"chemical" layers as shown in a schematic of the cross section (Figure 2-1). (Micrographs of the cross-section will be presented later in the chapter.) The core layers are made of mechanically processed softwood pulp, a loosely packed, compliant material. The outer layers surrounding the core are a denser, stiffer, chemically processed, bleached kraft pulp. One surface of the board is triple-coated and the other single-coated.

The basic component of paperboard is wood, ground into a fine pulp. Desired properties are achieved through chemical or mechanical processing. The pulp is suspended in a dilute aqueous solution and sprayed onto a moving wire mesh, creating one layer of the paperboard structure. Starch is sprayed onto the layer to improve fiber bonding within the layer and to allow bonding to subsequent layers. The cycle of spraying on pulp and starch is repeated until the desired structure is achieved. Creating one layer on top of another rather than creating the layers individually and then compiling them into one structure prevents the layers from being entirely distinct. Some fibers of one layer bond to fibers in the next layer. Bond density is lower between layers than within them, but remains significant. The layers of a paperboard

structure are coupled together in this manner.

The completed laminate is fed off the wire mesh and pressed through cylindrical rollers to densify and squeeze moisture out of the material. The laminate is further dried by pressing it through rollers while subjecting it to elevated temperatures. Densification resulting from the rolling operation improves intra-layer and interlayer bonding. In the case of Triplex, the completed structure is 0.45 mm thick and has a grammage [grams/area] of 280 g/m^2.

The rolling operation creates a preferred orientation for the component fibers of paperboard. A majority of fibers will be oriented in the rolling direction or at some small angle from the rolling direction. The rolling direction is usually called the machine direction, abbreviated as MD. Perpendicular to the machine direction in the plane of the board is the cross direction, or CD. The third principal direction of paperboard is the Z direction, perpendicular to the plane of the board.

The structure of Triplex is depicted in micrographs, Figures 2-2 through 2-13. Figures 2-2 through 2-7 are planar views of a coated chemical layer and a mechanical layer of Triplex at varying magnifications. Images of the mechanical layer were obtained by peeling off the chemical layer of a sample of Triplex. The machine direction and the cross direction have been labeled in the low magnification pictures. At first glance, it appears that the fibers are oriented randomly, making it difficult to tell the difference between the two directions. However, a closer examination shows that only a few fibers are oriented along or near the cross direction. The majority are along or are within a small angle of the machine direction. This effect is slightly more pronounced in the chemical layer than in the mechanical layer. This is to be expected, as the chemical layer experiences the directional effects of rolling more directly than does the mechanical layer.

The planar views show additional differences between the chemical and mechanical layers. The fiber density of the chemical layer is notably higher than that of the mechanical layer. The chemical layer also shows less depth variation than the mechanical layer. This is due partially to the manufacturing process; the chemical layer interacts directly with the roller during processing, minimizing depth variation. How-

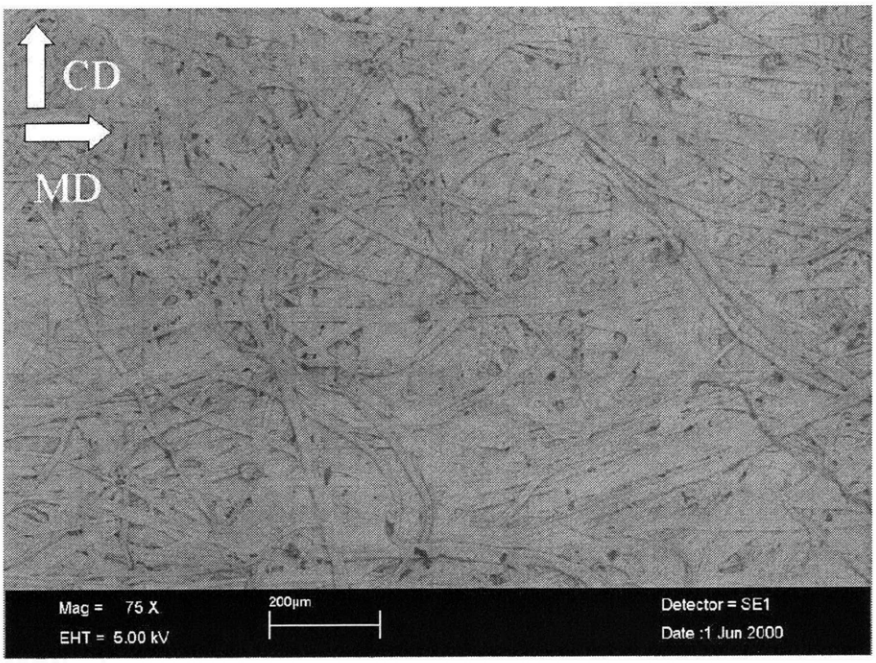

Figure 2-2: Coated Triplex chemical layer at low magnification.

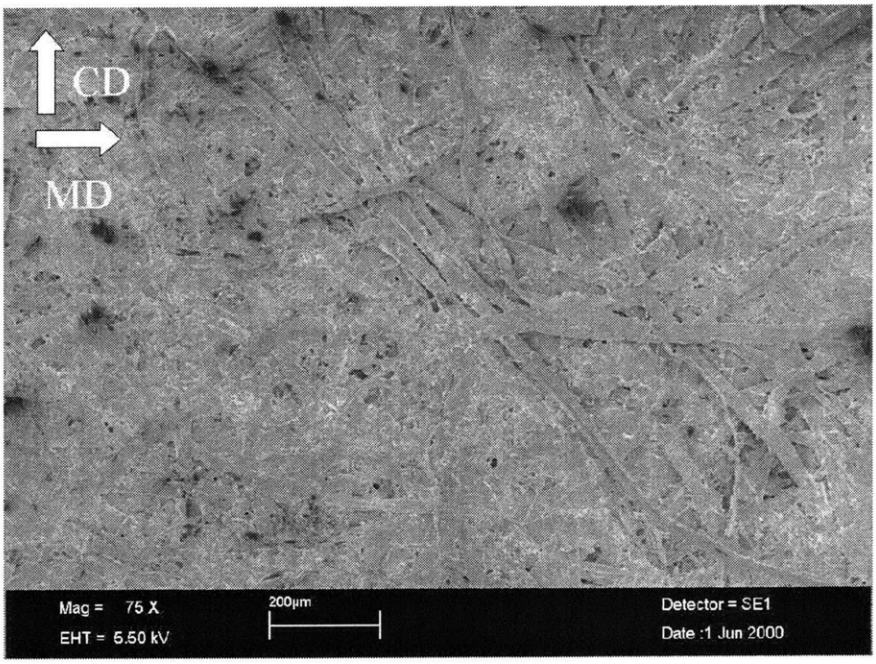

Figure 2-3: Triplex mechanical layer at low magnification.

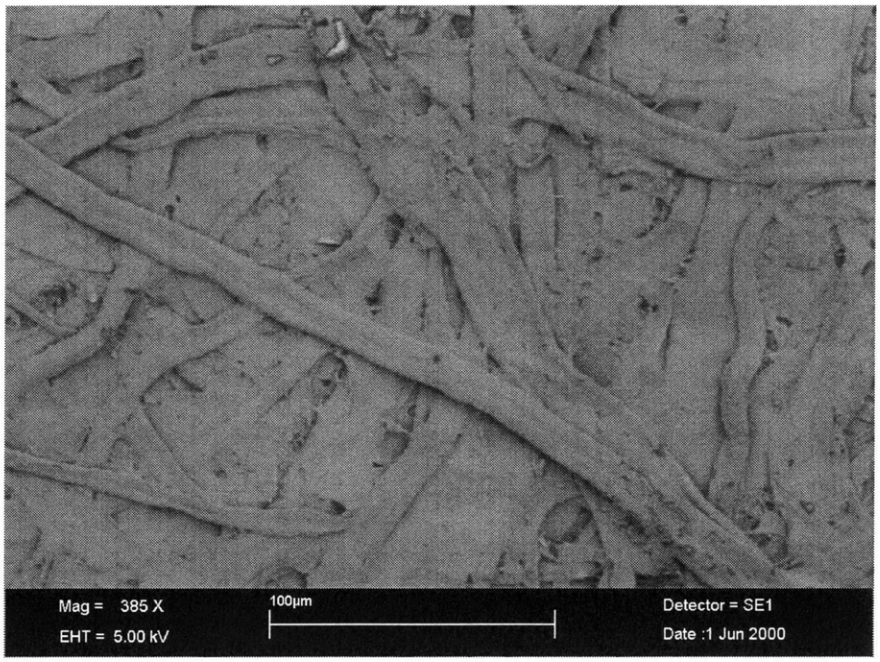

Figure 2-4: Coated Triplex chemical layer at intermediate magnification.

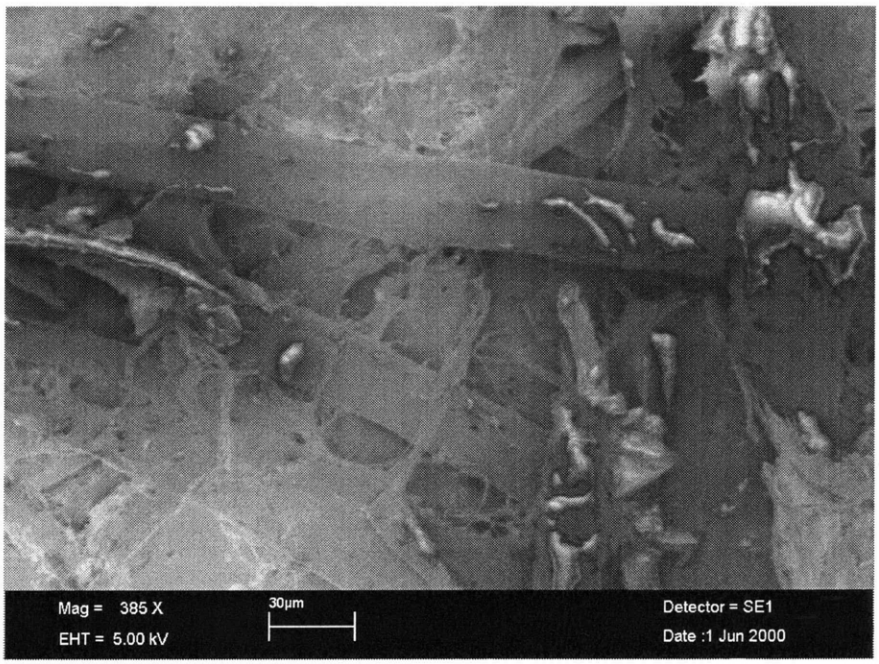

Figure 2-5: Triplex mechanical layer at intermediate magnification.

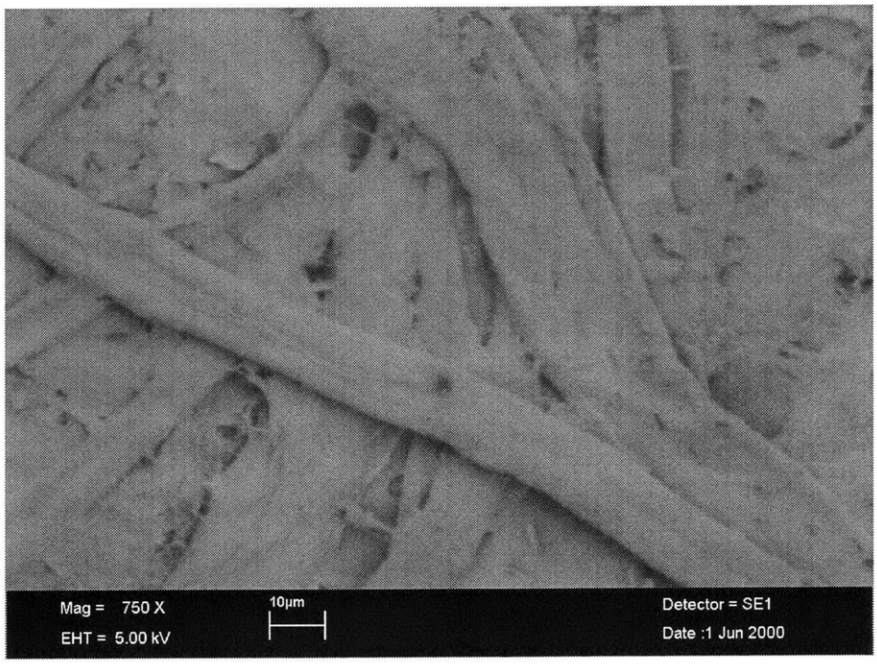

Figure 2-6: Coated Triplex chemical layer at high magnification.

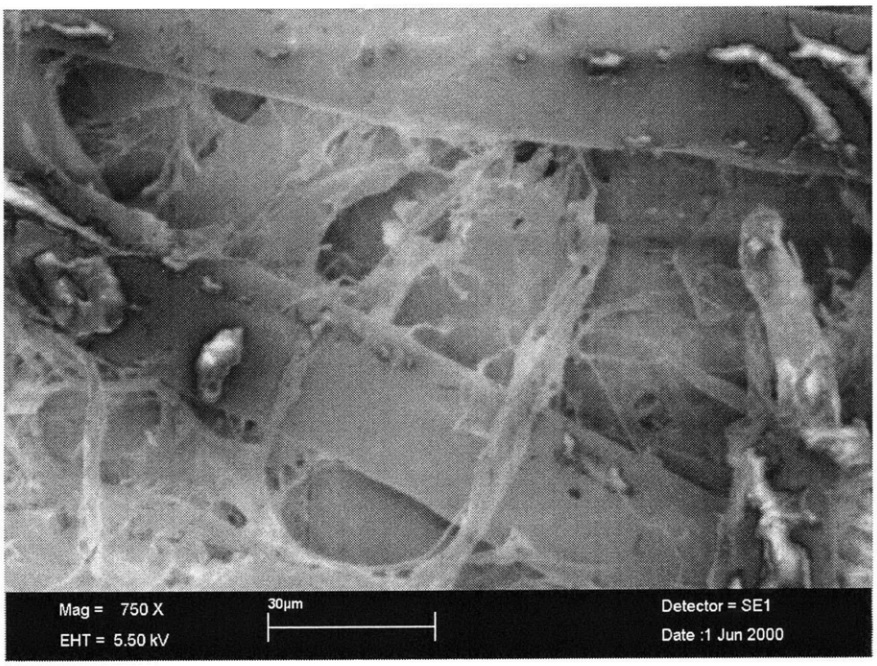

Figure 2-7: Triplex mechanical layer at high magnification.

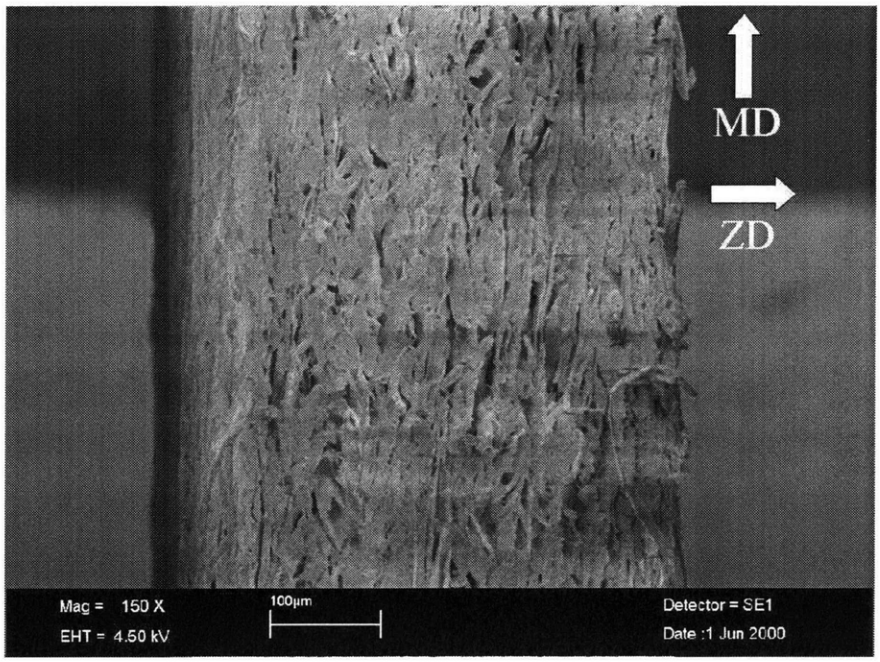

Figure 2-8: Triplex MD cross section at low magnification.

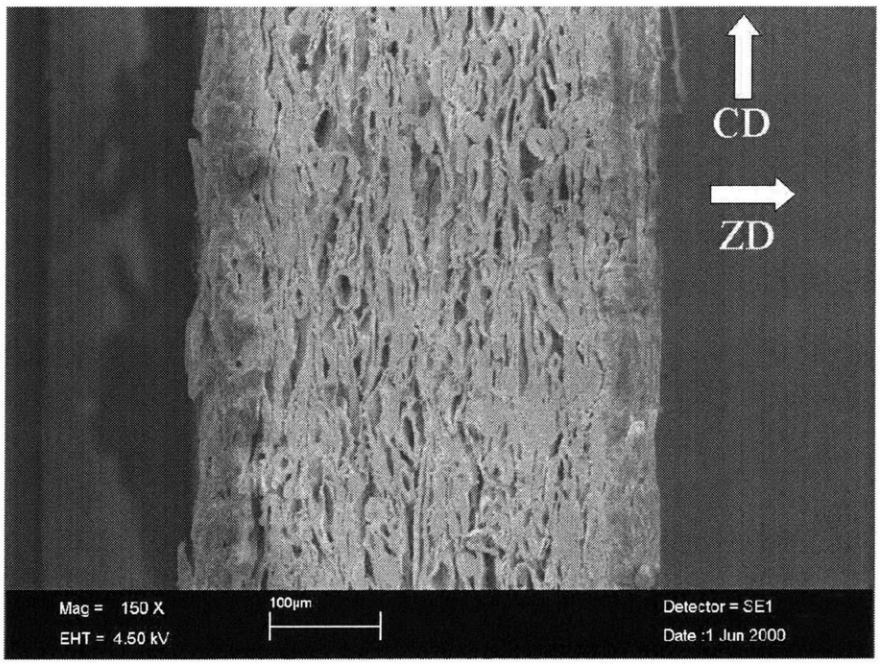

Figure 2-9: Triplex CD cross section at low magnification.

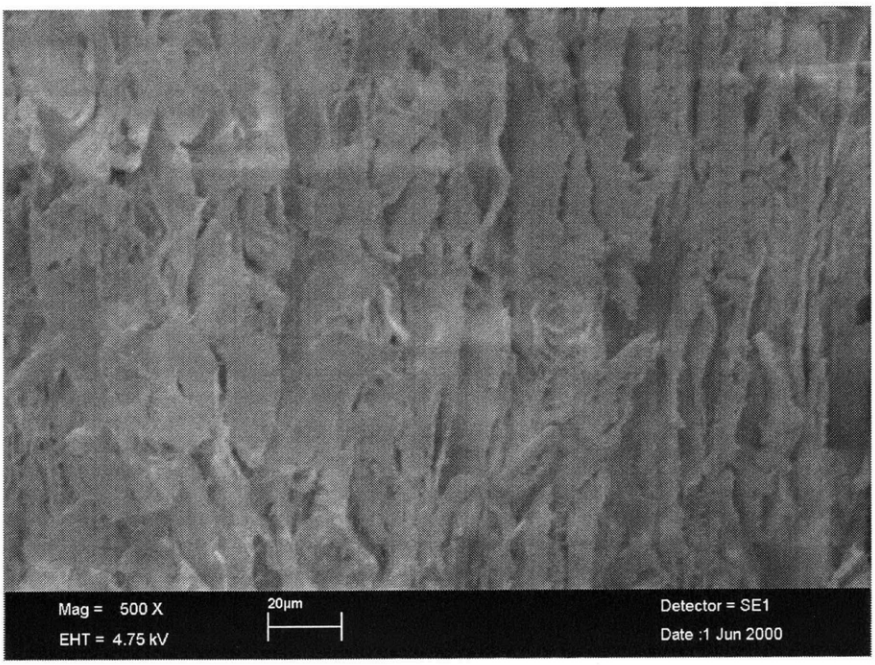

Figure 2-10: Triplex MD cross section at intermediate magnification.

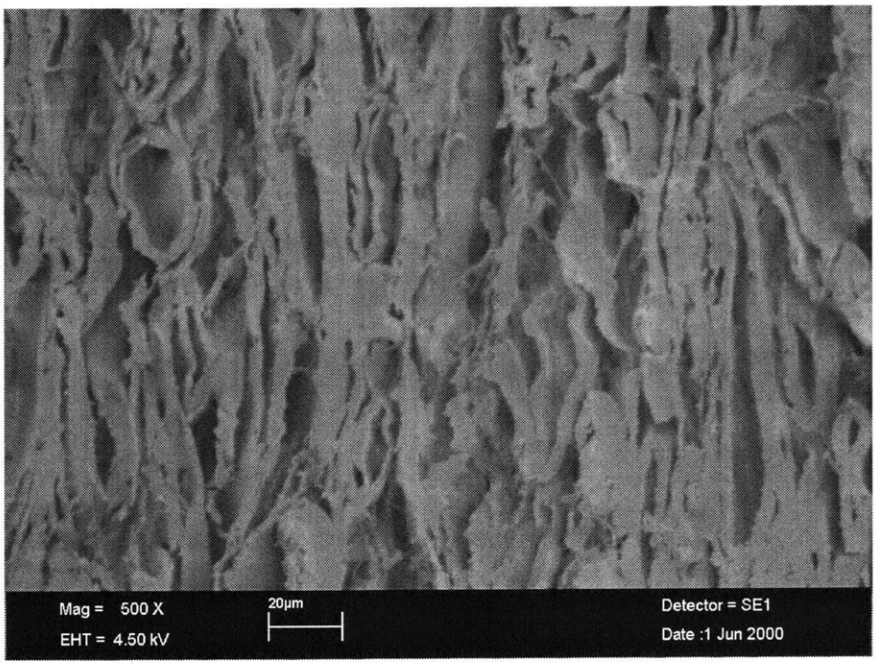

Figure 2-11: Triplex CD cross section at intermediate magnification.

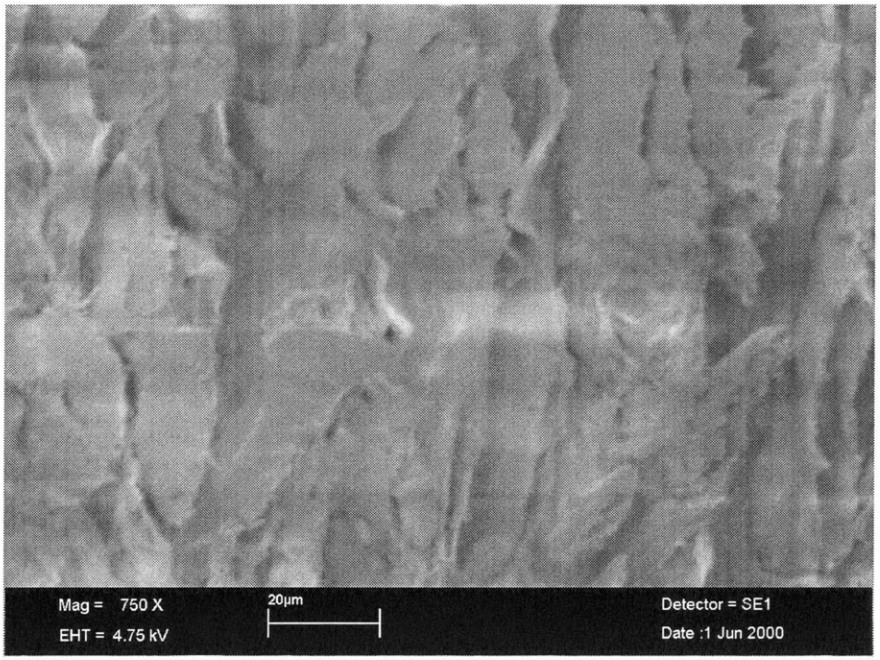

Figure 2-12: Triplex MD cross section at high magnification.

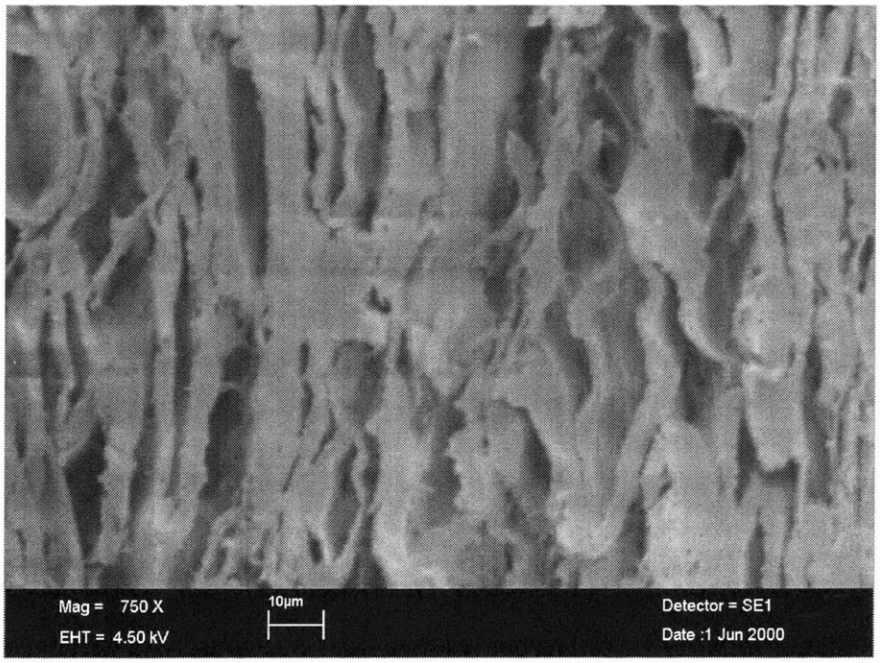

Figure 2-13: Triplex CD cross section at high magnification.

ever, the larger depth variation in the mechanical layer images may be exaggerated due to bonds loosened when the layers were separated for imaging purposes.

Cross-sections of Triplex are shown in Figures 2-8 through 2-13. These images show the differences between the machine and cross directions from a different perspective than the planar images. Paper fibers are tubular in shape, and the tubes become flattened during processing. As the majority of the tubes are lined up along or near the machine direction, we see primarily fibers that have been cut longitudinally in the machine-direction images. In the cross-direction images, we see more fibers that pierce the cross section, clearly displaying the oval shapes of partially flattened tubes. (Special cutting techniques were used to cut the fibers cleanly without any shearing. These techniques are discussed later in the chapter.) The caption notation Triplex MD indicates an image of the MD-ZD plane. Triplex CD analogously refers to the CD-ZD plane.

The low magnification cross-sectional images also show how heavily interconnected by intra-layer bonding the five layers of Triplex are. Although it is usually possible to distinguish between the denser chemical layers and the more loosely packed mechanical layers, the interfaces between individual mechanical layers can be very difficult to identify by observation alone.

2.2 Equipment and Methods

2.2.1 Microscopic Level

Many different types of tests were performed at the microscopic level. Tests representing the punching and bending steps of the creasing process were done to understand the basic mechanisms and loading modes of creasing. Through-thickness tension and shear tests were performed along with a series of tests combining tension and shear. In-plane tension tests were also conducted.

Testing was performed in a scanning electron microscope (SEM), allowing real time observation of material behavior during loading. Tests were fixtured such that

the material cross section was visible, with the exception of some in-plane tension tests. In these tests, the plane of the board was visible.

Deformation Stages

Two deformation stages were used in this project. They will be referred to here as the "old" and the "new" stages. The old stage, pictured in Figure 2-14, has one stationary and one movable platen. The stationary platen was connected to a load cell with capacity 25 kgf, equivalent to 245 N. The moving platen is mounted on a lead screw connected through a set of gears and a shaft to a stepper motor. At a stepper motor speed of 100 steps/second, the platen advanced at 0.00394 mm/s. Tests during which load-deformation data was collected were run at approximately this speed; occassional stuttering in the motor caused small fluctuations around this value. Tests run only for imaging purposes were often run at higher speeds. The lower speed was selected for data collection as it minimized motor stuttering. The stage has a cylindrical base that fits into the standard SEM specimen holder. This stage was used for through-thickness tension tests, certain tests combining through-thickness tension and shear, and in-plane tension tests.

The new deformation stage, pictured in Figures 2-15 and 2-16, also has one stationary and one movable platen. The moving platen is connected to a stepper motor in a similar manner to that of the old stage. However, the gear ratio is different. At a motor speed of 100 steps/second, the stage advances only 0.00294 mm/s. This speed was used for data collection. Faster speeds were used when only imaging was required. This stage does not have an integral load cell, although added fixturing allowed connection of a 10 lbf (44.5 N) capacity load cell. The new stage is attached to the base that supports the SEM specimen holder, making it more stable than the old stage. The new stage was used for punching and bending tests, through-thickness shear tests, and combined loading tests that could not be fixtured for the old stage.

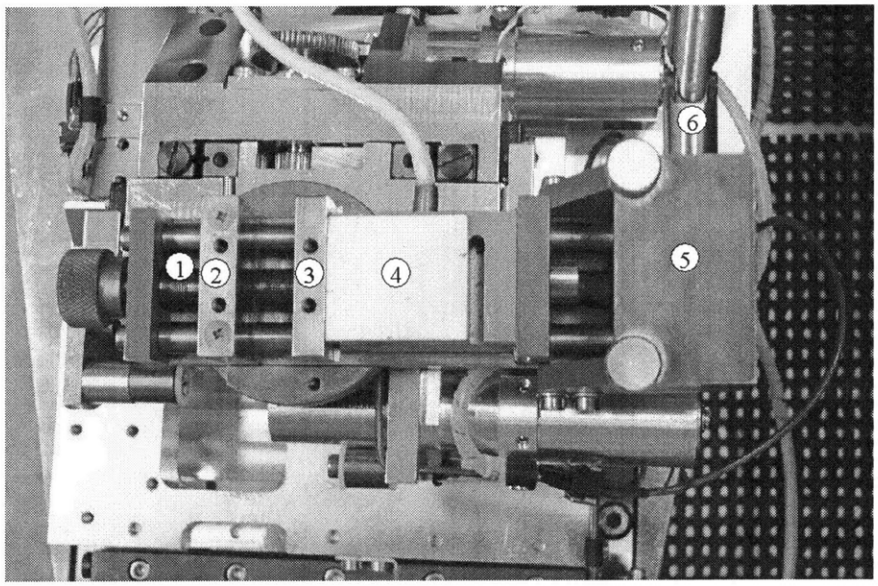

Figure 2-14: Old deformation stage. The numbered components are 1: lead screw, 2: moving platen, 3: stationary platen, 4: load cell, 5: gear box, and 6: stepper motor input.

Creasing Tests

Creasing is a two-step process. In the first step, a paperboard sheet under a small amount of in-plane tension is punched between male and female dies, creating damage in the internal structure of the board. In the second step, bending, the board folds preferentially along the punched line. Fixtures for punching and bending experiments were designed to simulate the creasing process in production and to provide an edge view of the specimen. With an edge view of the specimen, the behavior of individual fibers and layers could be observed through the cross section.

A useful view of the paperboard cross section requires careful specimen preparation to minimize fiber shearing. Before cutting the viewing surface, the board was frozen in liquid nitrogen to make the fibers brittle and more likely to fracture cleanly. The frozen board was removed from the liquid nitrogen and placed on a flat metallic surface. A razor blade was aligned with the desired edge and tapped hard with a hammer or other tool, forcing it through the brittle paperboard. The razor blade was also cooled in liquid nitrogen before cutting so as not to warm the board. After

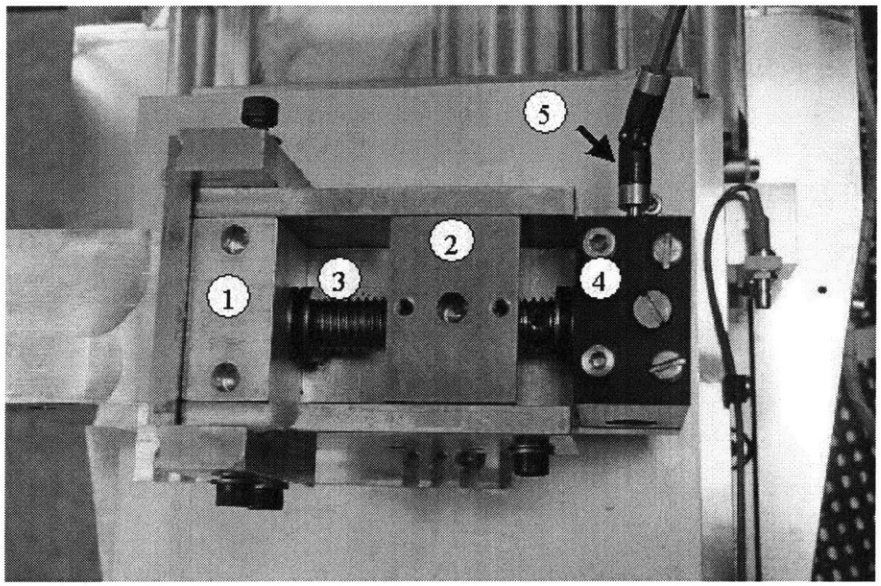

Figure 2-15: New deformation stage. The numbered components are 1: stationary platen, 2: moving platen, 3: lead screw, 4: gear box, and 5: stepper motor input.

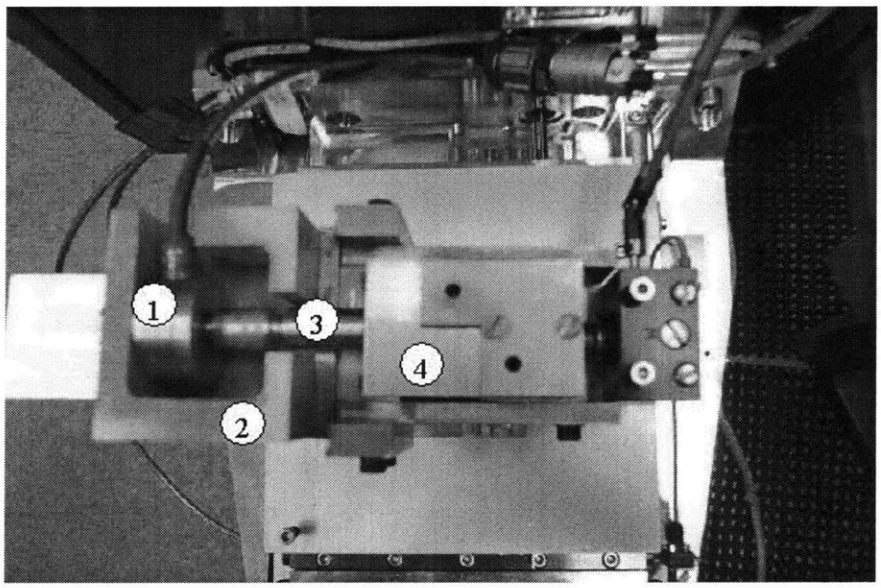

Figure 2-16: New deformation stage with load cell connected. The numbered components are 1: load cell, 2: load cell holding fixture, 3: adapter connecting load cell to test fixtures, and 4: shear fixtures, one example of fixtures connected to the load cell.

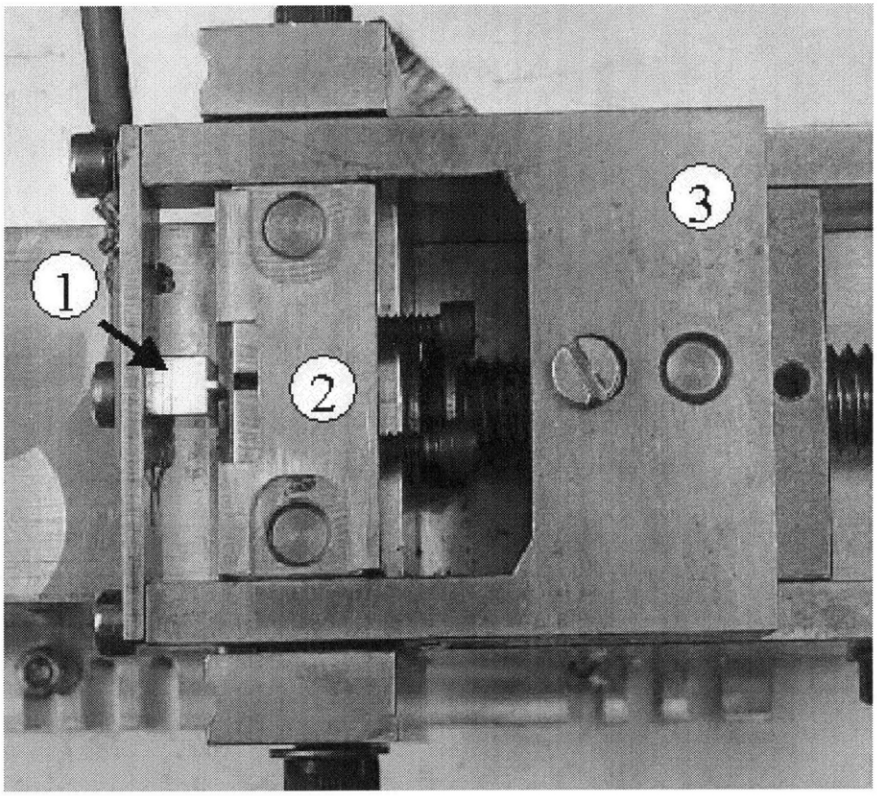

Figure 2-17: Fixtures for punching step of creasing. Numbered components are 1: male die, 2: female die and sleeve, and 3: fixture connecting male die to moving platen.

cutting, the viewing edges were evaporation coated in gold with a layer thickness of less than 500 Å. Following coating, specimens were cut to size as appropriate. For creasing tests, the paperboard was cut into 36 mm by 6 mm strips.

The female die used in punching is a slotted rectangular block; slot widths in this study were between 1.5 mm and 2.03 mm. The male die is a smaller rectangular block with a tab that protrudes from the block by a height equal to approximately twice the paperboard thickness. Tab widths in this study were between 0.5 mm and 0.84 mm. Although the male die is frequently depicted as having sharp corners, the corners on actual dies are gently rounded by wear. One the dies used in this study, the rounded corners had radii estimated at 0.05 mm. Sample dies and associated fixturing are shown in Figure 2-17.

The female die is attached to the stationary platen. The paperboard is placed

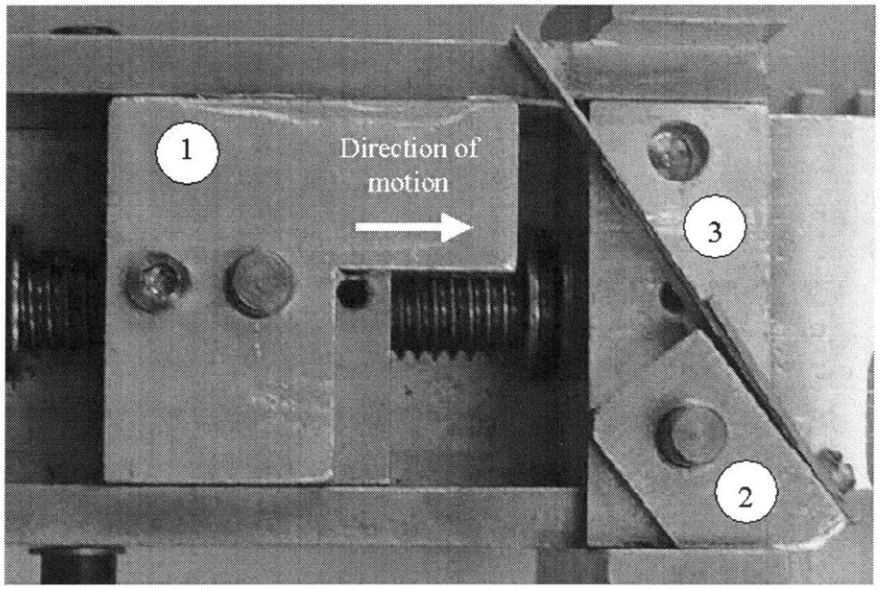

Figure 2-18: Fixtures for bending step of creasing. Numbered components are 1: moving block with attached force application bar, 2: clamping block, and 3: stationary platen.

against the female die, covering the slot. The die and the board aer slipped into a metal sleeve, as shown in the figure. The sleeve is equipped with screws. When the screws are advanced, the female die is pushed against the far wall of the sleeve, with the paperboard sandwiched between. Before a punching test, the screws were engaged just far enough to create a small amount of normal force between the paperboard and the faces of the female die and the sleeve. During a test, the paperboard was pushed into the slot on the female die. This caused board outside the slot to slide along the face of the die. The normal force created by the sleeve resulted in sliding friction, mimicking the web tension present in industrial punching applications. The male die is attached to the moving platen, as shown.

The bending fixtures are shown in Figure 2-18. The paperboard is clamped cantilever-style by a block attached to the stationary platen of the stage. The clamping prevents translation and rotation of the fixed end of the specimen. The angle of the clamping block was chosen to allow the specimen to be bent through more than 90 degrees. Bending force is provided by a narrow beam fixtured to the moving platen of

the stage. This beam contacts the specimen at one point, defining the moment arm for the bending operation. The contact point changes as the paperboard deforms, and the moment arm lengthens throughout the operation.

Through-thickness Tests

In all through-thickness tests, specimens were glued between fixtures that allowed an edge view of the paperboard. Specimens were attached to fixtures with industrial adhesive 4213-NF, produced by 3M. This glue cures in under one hour and requires no pressure applied to the parts to set.

A set of L-shaped fixtures, shown in Figure 2-19, were used for the tension experiments. These fixtures were attached to the old deformation stage by screws, as seen in Figure 2-20. Shear experiments were conducted on the new deformation stage, using the fixtures pictured in Figure 2-21. An additional set of shear fixtures was designed to allow shear specimens to expand freely in the Z direction. These fixtures are shown in Figure 2-22. The holes in the standard shear fixture have been converted to slots in the free expansion fixture, allowing fixture travel in the Z direction. Nonporous Teflon coating was glued to the slot surfaces to prevent friction from interfering with travel.

Combined-loading fixtures were designed to test specimens at 20, 40, 60, and 80 degrees, where 0 degrees corresponds to through-thickness tension and 90 degrees to shear. The 20 and 40 degree fixtures were similar to the through-thickness tension fixtures; the three fixtures are shown together in Figure 2-23. As with the tension tests, 20 and 40 degree tests were performed on the old stage. The 60 and 80 degree fixtures were designed for the new stage, as the allowable travel on the old stage was not sufficient for such large angles. The 60 and 80 degree fixtures are shown with the shear fixture in Figure 2-24.

For all fixtures used on the old stage, the specimen size was 6 mm by 6 mm. On the new stage, 6 mm by 6 mm specimens were used when only images were being taken. Smaller specimens were used during data collection. The shear strength of paperboard is on the order of 1 MPa, and the loads necessary to shear a 6 mm by

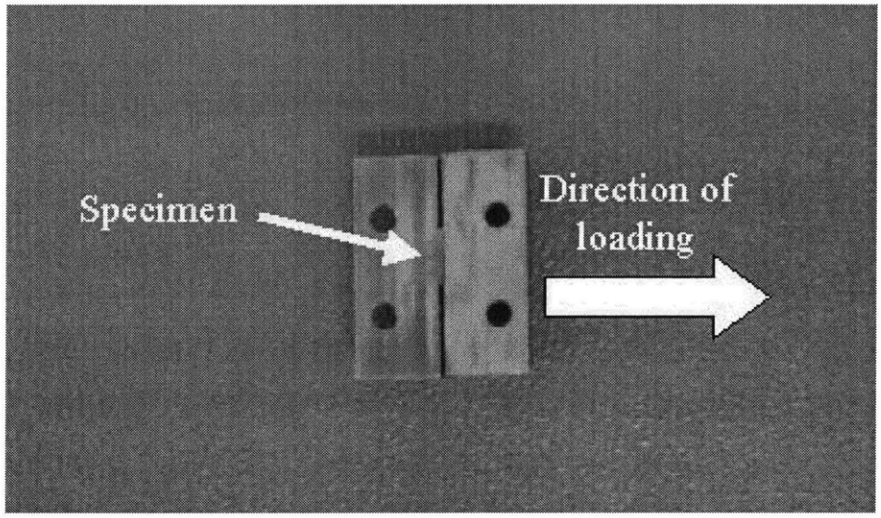

Figure 2-19: Through-thickness tension fixtures with specimen glued in place.

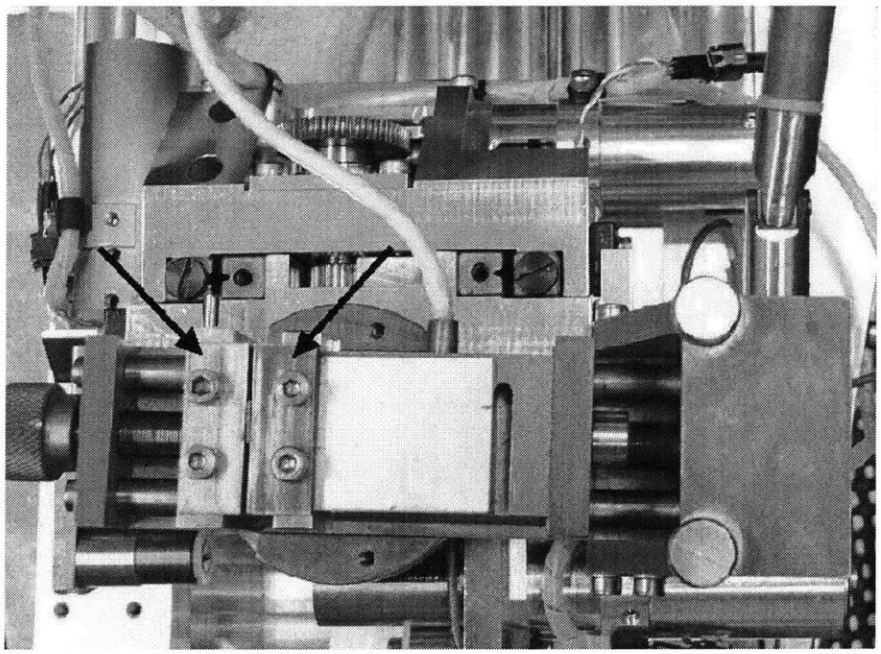

Figure 2-20: Through-thickness tension fixtures mounted on old deformation stage.

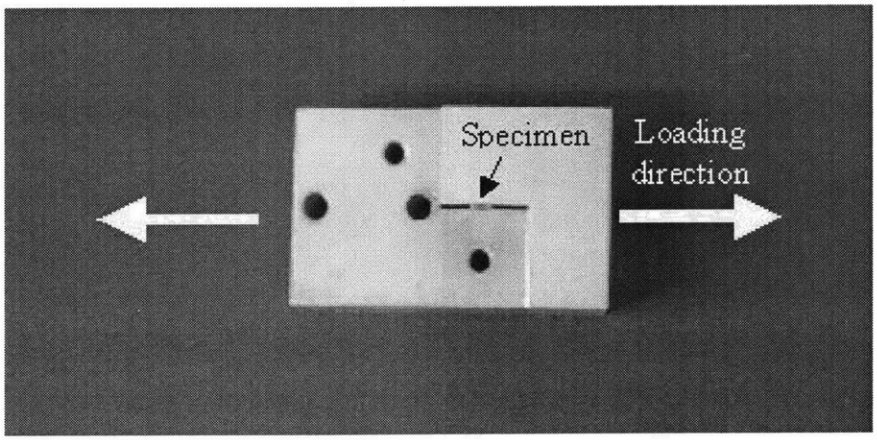

Figure 2-21: Shear fixtures.

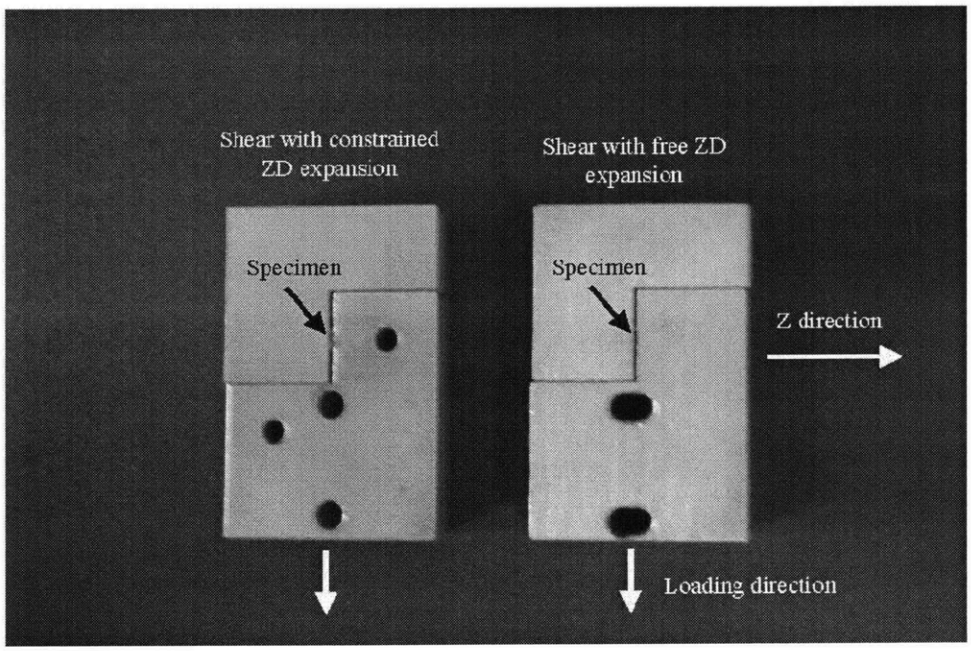

Figure 2-22: Free expansion shear fixtures compared to contrained expansion fixtures. The free expansion fixtures are attached to the platen with slots that allow travel in the Z direction rather than simple holes.

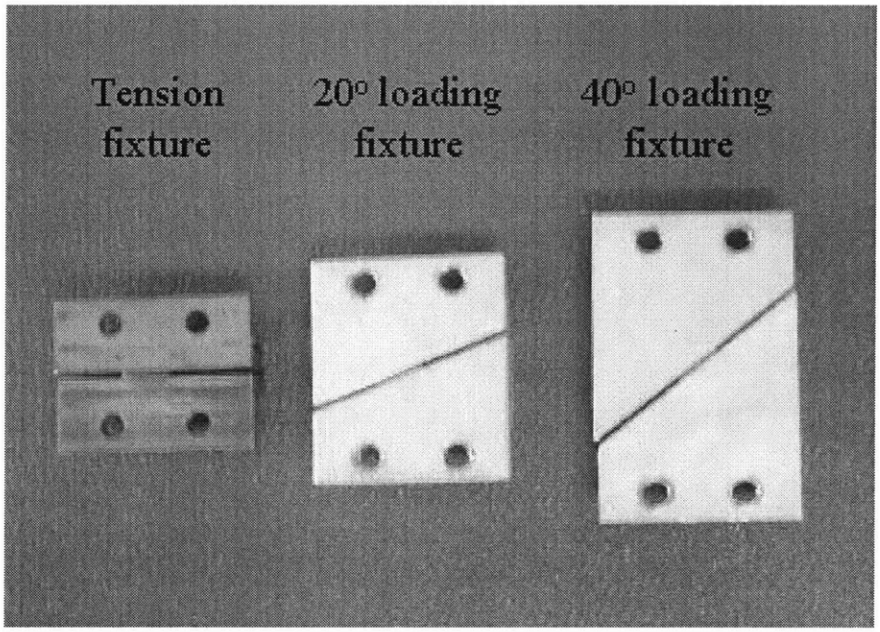

Figure 2-23: Combined-loading fixtures based on tension fixture design.

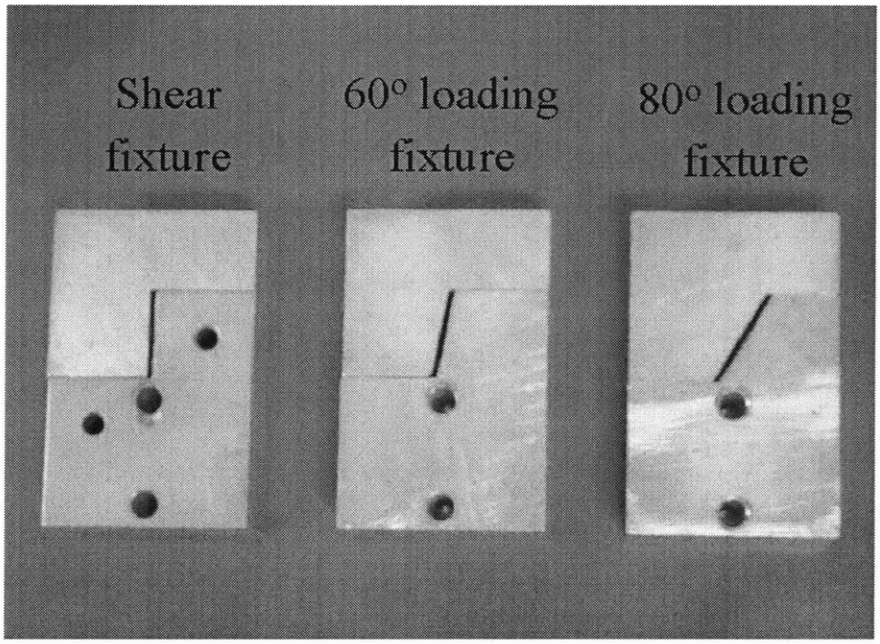

Figure 2-24: Combined-loading fixtures based on shear fixture design.

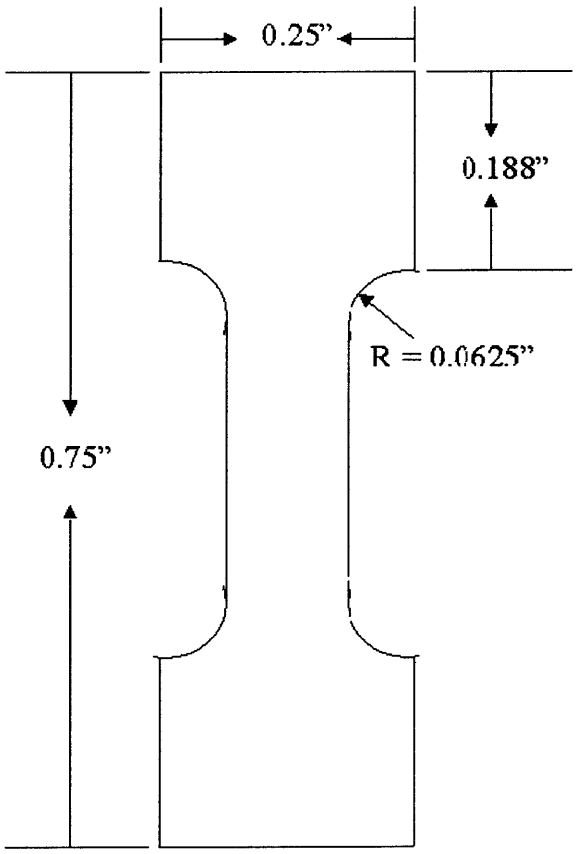

Figure 2-25: In-plane tension test specimen specifications.

6 mm square of board would be too high for the load cell on this stage to measure. Thus, data collection on the new stage used 3 mm by 3 mm specimens. Specimens were prepared as described in the creasing section.

In-plane Tests

In-plane tension tests were performed on the old stage. Paperboard was cut into a dogbone shape with dimensions given in Figure 2-25. This shape is used because failure will happen in a predictable location, the narrower center section of the specimen. Two paperboard tabs were glued onto each end of the specimen to provide further reinforcement. The reinforced ends of the sample were placed onto the platens of the stage. A flat bar was placed over each end and tightened down with screws to clamp the specimen to the platens, as shown in Figure 2-26

As the quality of the edges for a plane view specimen did not matter, the dogbone specimens were cut by hand with a razor blade. After cutting and attachment of the reinforcement tabs, the specimens were coated in a thin layer of gold. For some of the in-plane tests, the outer chemical layer of the paperboard was removed so that behavior of the more compliant fibers in the mechanical layer could be observed. The layer was peeled off of the board by hand before the dogbone shapes were cut.

A set of edge-view, in-plane tension tests was also conducted. The specimen design was identical to that of the plane view tests, but the necessary edge quality would not permit hand cutting. As the shape was too complex to use the liquid nitrogen cutting method described in the creasing section, these specimens were cut using a laser at the MIT Media Lab. The cutter, a Universal Laser Systems model X100, was run at 40% power and 30% speed to make the cuts. The fixturing method for the edge view test was similar to that used for the in-plane tests, although rotated through 90 degrees, as seen in Figure 2-27.

Scanning Electron Microscope and Supporting Equipment

Images and data were collected during testing in a Leo Electron Microscopy Limited model 438 VP scanning electron microscope. Deformation stages in the microscope were driven by a Hurst Manufacturing model EPC-015 stepper motor. Load cell information was acquired through an Omega strain gauge indicator. Images were collected using the Leo software that controls the microscope. Load-displacement data was collected using Labview [TM] software on an associated computer. A virtual instrument written for Labview received load data from the strain gauge indicator. The virtual instrument was able to activate the motor and control its direction, ensuring that the motor and data collection started and ended simultaneously. Motor speed data was input to the software, which used the speed data and time measurements during data collection to generate displacement values. The SEM chamber and control computer, stepper motor controller, and strain gauge indicator are shown in Figure 2-28.

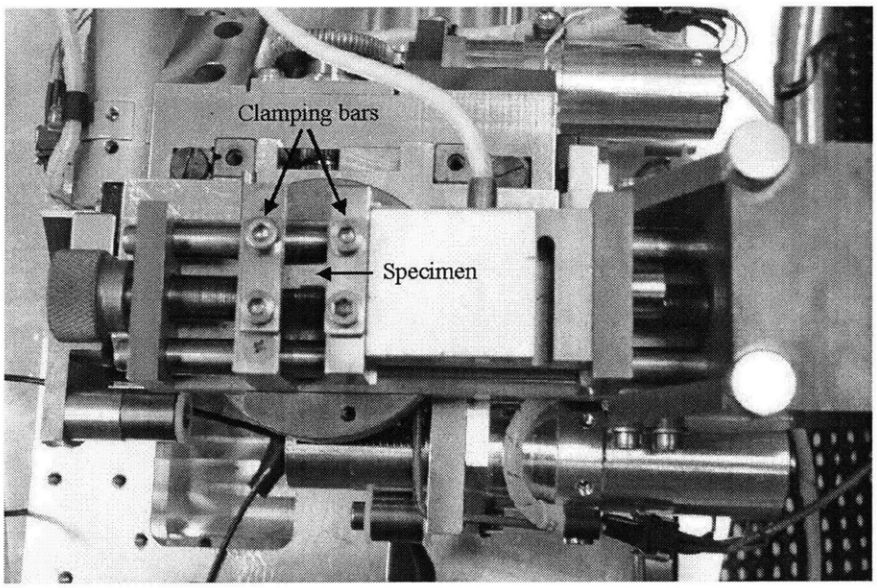

Figure 2-26: In-plane tension test fixtures for the old stage.

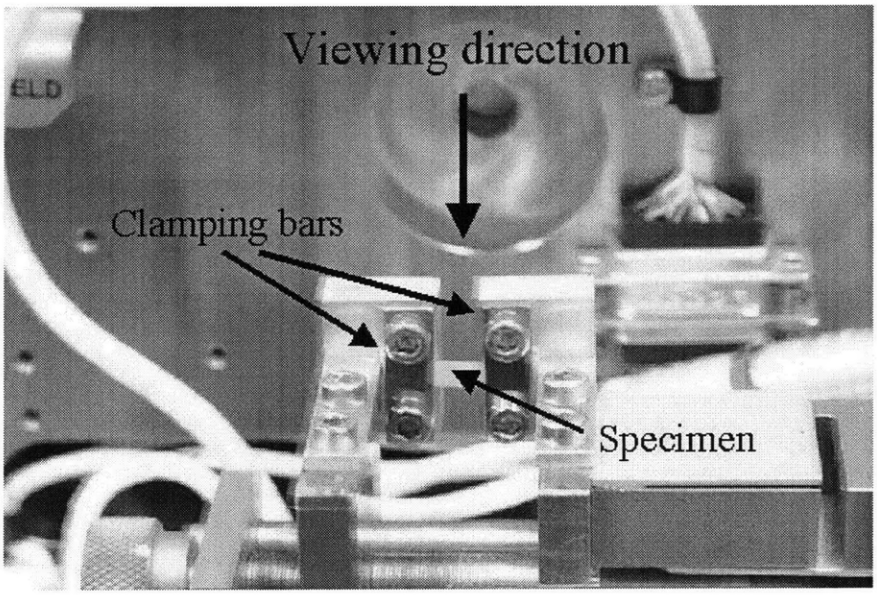

Figure 2-27: Edge-view, in-plane tension test fixtures.

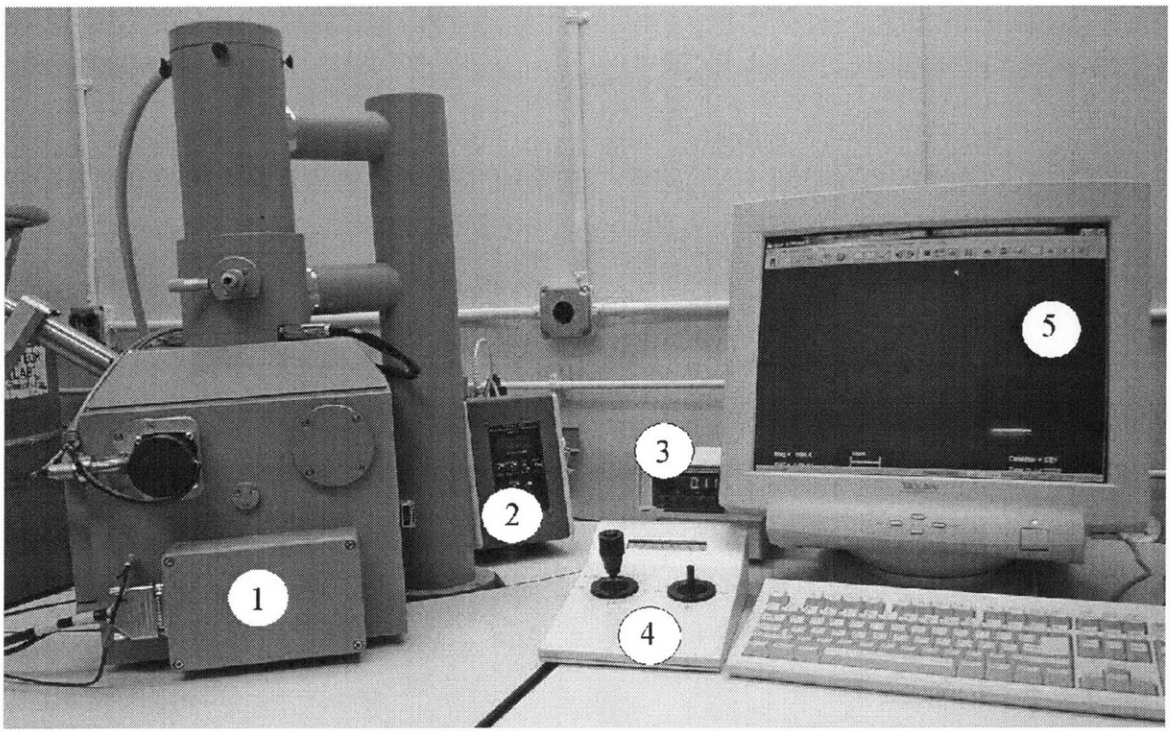

Figure 2-28: Scanning electron microscope and associated equipment. Number components are 1: SEM chamber, 2: stepper motor controller, 3: strain gage indicator, 4: SEM stage position controls, and 5: SEM control computer.

2.2.2 Macroscopic Level

Out-of-plane Testing

Out-of-plane macroscopic tests were conducted using a modified Arcan fixture mounted on a servo-hydraulic test machine. Arcan et al. [14] designed the original Arcan fixture to produce uniform plane stress in a specimen, as shown in Figure 2-29. The modified Arcan fixture is shown in Figure 2-30. It consists of two stiff cantilever beams with a short connecting strip at one end. At the other end, each cantilever is connected to a flat plate similar in shape to a quarter circle. At the interface of the plates is an inset for specimen mounting platens. This design allows for quick specimen changes, as many specimens may be prepared and mounted on individual sets of platens before a testing session begins. However, it was found that this design has insufficient stiffness, and the modified fixture was redesigned to eliminate the platens. In the new design,

specimens are fixed directly to the quarter-circle plates. Although this creates a more laborious testing procedure, the resulting load-deformation information is much more accurate.

The flat plates have regularly spaced mounting holes along their perimeters. Thus, they can be mounted at any angle between 0 and 90 degrees, inclusive, at 15 degree increments. This allows specimens to be loaded in through-thickness tension, inter-laminar shear, or a combination of those loading modes. Deformation is measured by two LVDTs mounted on the fixture, one oriented to measure normal displacement and one to measure shear displacement. The entire fixture is mounted in an MTS servo-hydraulic test machine, and data is recorded using a personal computer.

All specimens for out-of-plane testing are prepared the same way. Paperboard is cut into pieces approximately 20 mm by 45 mm. Each piece is glued in place. In the early version of the fixture, the paperboard was glued to the small platens. In the newer version, it is glued directly to the quarter-circle plates. The interface where the paperboard is mounted has dimensions 15 mm by 40 mm; after the glue has cured, excess paperboard is cut away with a sharp knife. Gluing oversize pieces and later cutting away the excess prevents accidently gluing parts of the platens together around an undersized specimen.

Early tests used an epoxy from Akzo Nobel. The epoxy is a 3:1 or 4:1 mixture by weight of Cacosinol 1761 and hardener 2612. It requires two hours to cure and eight hours to dry. Production of this type of epoxy was halted partway through the project, so a new adhesion method had to be found. In the new method, Cascosinol 1711 is mixed with ethanol to create a very thick paste. This was combined in a 4:1 weight ratio with paraformaldehyde, the active chemical in the hardener previously used. Initial problems with adhesion to the aluminum fixtures were corrected by impregnating the aluminum with a small amount of sodium hydroxide. The type of adhesive used in macroscopic testing was particularly important. To avoid affecting the load-deformation data, the adhesive had to be very stiff and could not penetrate far into the paper thickness. The adhesives were chosen with these constraints in mind.

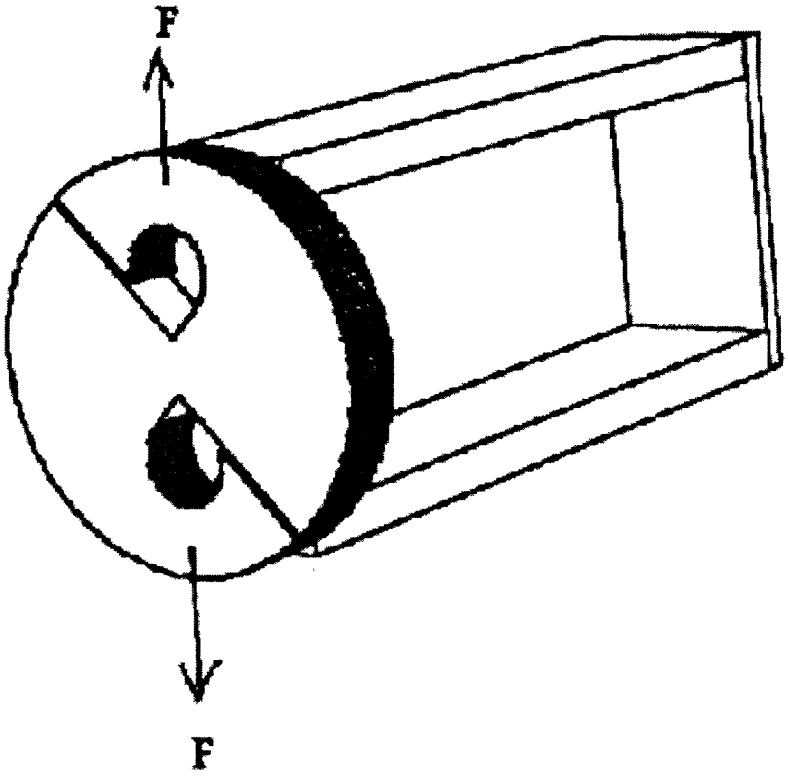

Figure 2-29: The original arcan device. (Courtesy of N. Stenberg.)

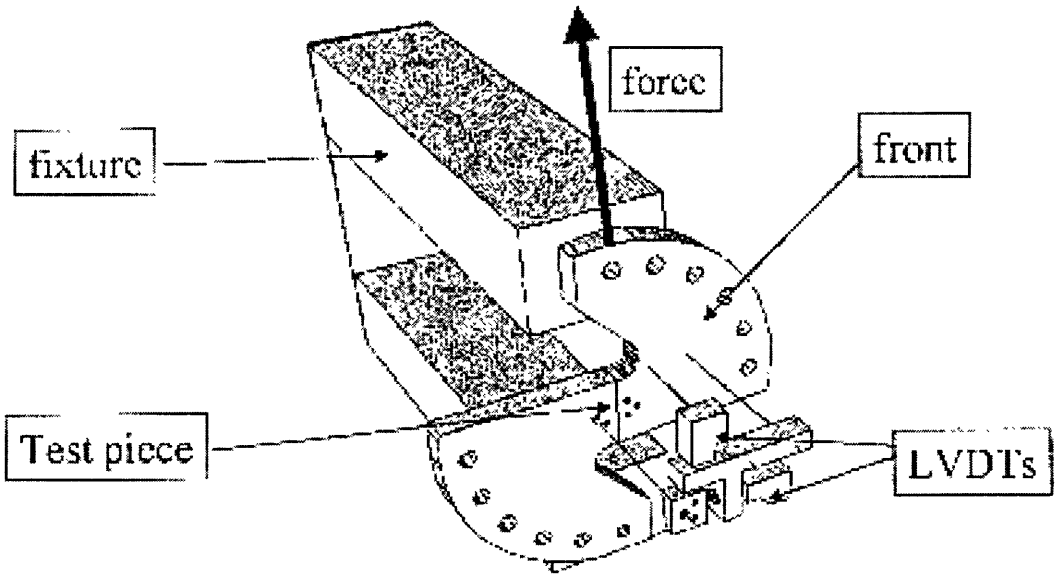

Figure 2-30: The modified arcan device. (Courtesy of N. Stenberg.)

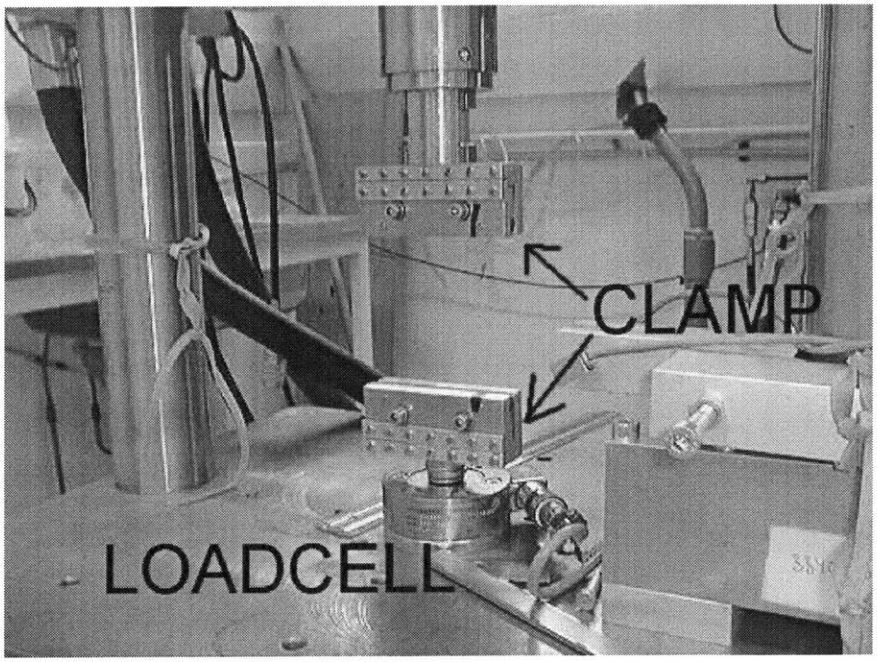

Figure 2-31: Apparatus for macroscale in-plane tension tests. (Photograph courtesy of N. Stenberg.)

All tests were conducted under conditions of 23° C and 50% relative humidity. Stress values are all nominal stress, calculated by dividing measured load by inital cross-sectional area of the specimen. In out-of-plane tension tests, strain is expressed as logarithmic strain, the logarithm of the instantaneous thickness divided by the initial effective thickness. Interlaminar shear strain values are found by dividing shear displacement by effective thickness. (Effective thickness is the thickness of the speciment not penetrated by glue.) In all tests, the deformation rate was 0.02 mm/sec.

In-plane Testing

In-plane tension tests were conducted on the same servo-hydraulic test machine used in the out-of-plane tests. Clamps were attached to the table-mounted load cell and to the piston, as shown in Figure 2-31. The test piece was fixed rigidly in the clamps. Deformation was determined from displacement of the piston. The specimens used had a rectangular shape, as opposed to the dogbone shape used in the microscale tests. The specimens were 100 mm long and 15 mm wide.

Environmental conditions were identical to those cited for out-of-plane testing. As with out-of-plane testing, stress values were expressed as nominal stres. Strain was expressed as logarithmic strain. The deformation rate was 0.3% per second, equivalent to 0.3 mm/s for a 100 mm long specimen.

Chapter 3

Creasing Experimental Results

This chapter presents the results of creasing experiments performed by the author and by previous project contributor Alexis Smith [16]. These experiments have provided information on the loading modes and mechanisms important in the creasing process. The punching step of the creasing process is not rate-dependent, so creases made using the slow SEM mechanism are comparable to creases made on faster industry processing lines. Observation of the paperboard cross-section during low-speed creasing in the SEM revealed the relevant modes of deformation experienced the paperboard. During punching, the paperboard experiences through-thickness compression and shear as well as in-plane tension. In bending, in-plane compression at the inside of the crease causes damage in the form of delamination, the same mechanism observed in through-thickness tension failures.

3.1 Previous Work

A series of creasing experiments were peformed to determine if crease quality was dependent upon speed of the punching step. Punching in the SEM takes several minutes, while punching on an industry production machine takes less than a second. Punching performed in the SEM could thus only be considered representative of industry punching if no rate-dependence existed.

For these experiments, Triplex was punched at various speeds on a production

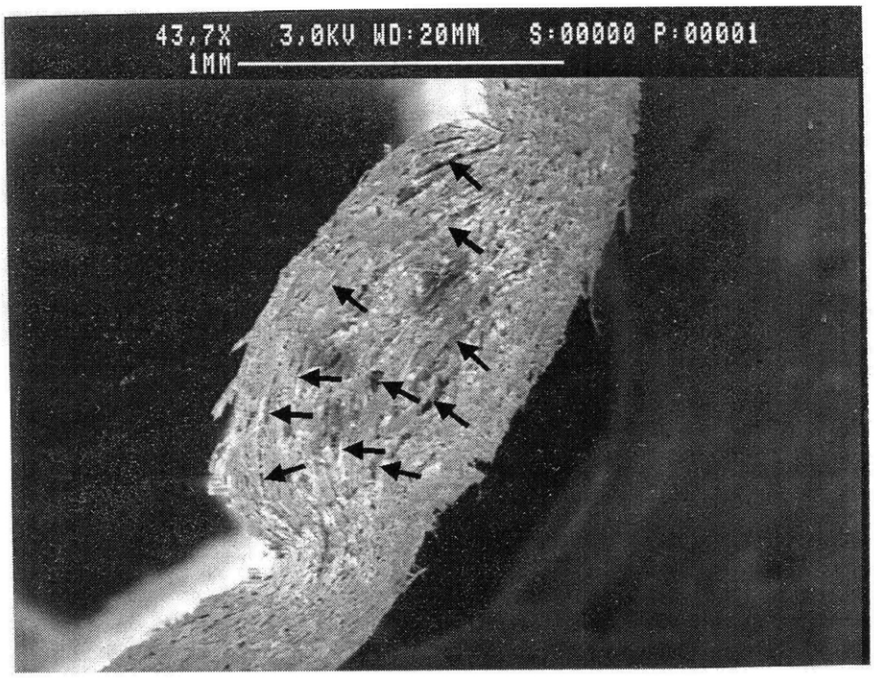

Figure 3-1: Triplex MD punched at low speed (50 m/min). Arrows indicate damage locations.

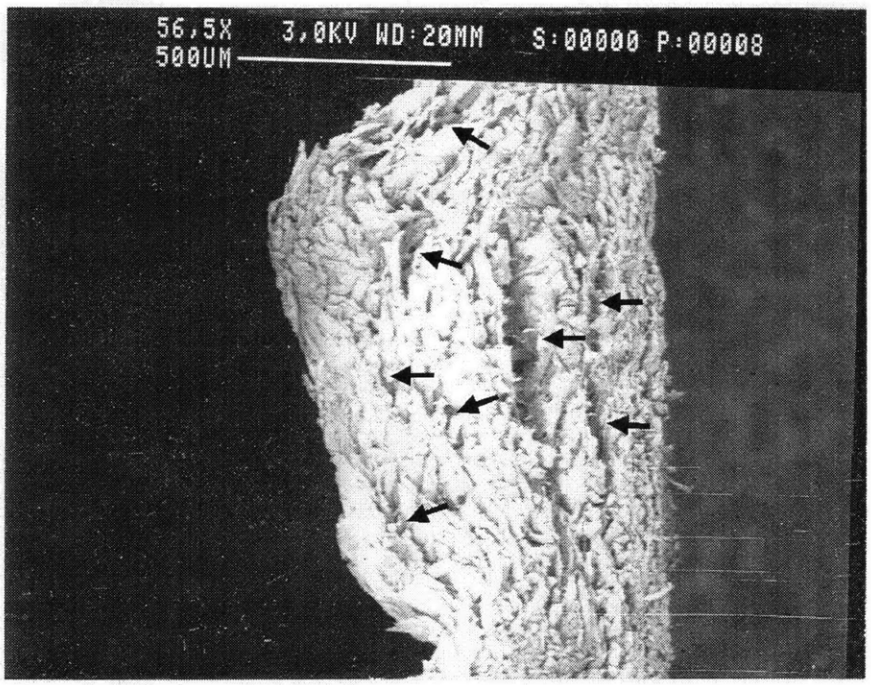

Figure 3-2: Triplex MD punched at high speed (200 m/min). Arrows indicate damage locations.

machine at Tetra in Sweden. The punched board was bent manually and examined in the SEM. Figures 3-1 and 3-2 provide a sample of the SEM images taken. The images clearly showed that punch speed has little or no bearing on crease quality.

Following the punching rate experiments, punching and bending tests were conducted in the SEM to allow observation of loading modes and deformation mechanisms during each process. Sample images taken during one of these tests are included as Figures 3-3 through 3-8; "step" numbers indicated in the figure captions establish chronology. These images show male and female dies used for punching. Recall from Chapter 2 that during the punching step, the paperboard is held against the female die by a metal sleeve that surrounds both the die and the board. The sleeve is equipped with screws that can be tightened to provide a small amount of resistance to slip of the board against the die in the plane; this mimics the web tension of an industrial punching procedure.

These tests showed that the punching process created through-thickness compressive, interlaminar shear, and in-plane tensile loads. The through-thickness compression occurred directly under the punch. Interlaminar shear occured in the paperboard immediately surrounding the punch. In these regions, the layers of the board slipped past each other in shear to maintain integrity of board in the curves formed at fixture corners. If there had been no slip between layers, the outer layers at the curves might have failed in in-plane tension or the inner layers might have buckled in in-plane compression. In-plane tension was also present in the board; in the punching operation, a small amount of web tension is standard.

In the bending test images, layers of material are seen to separate at damage locations created in the punching step. This separation occurs because of the loads created. Bending produces in-plane tensile loads at the outside of the bend and in-plane compressive loads at the inside. Triplex in the plane is weaker in compression than in tension and thus would fail under the compressive loading first. However, the damage created during the punching step dictates how that failure will occur. Rather than sudden failure by buckling, the layers of the paperboard separate in an orderly, predictable manner. This separation is illustrated in Figures 3-5 through 3-8.

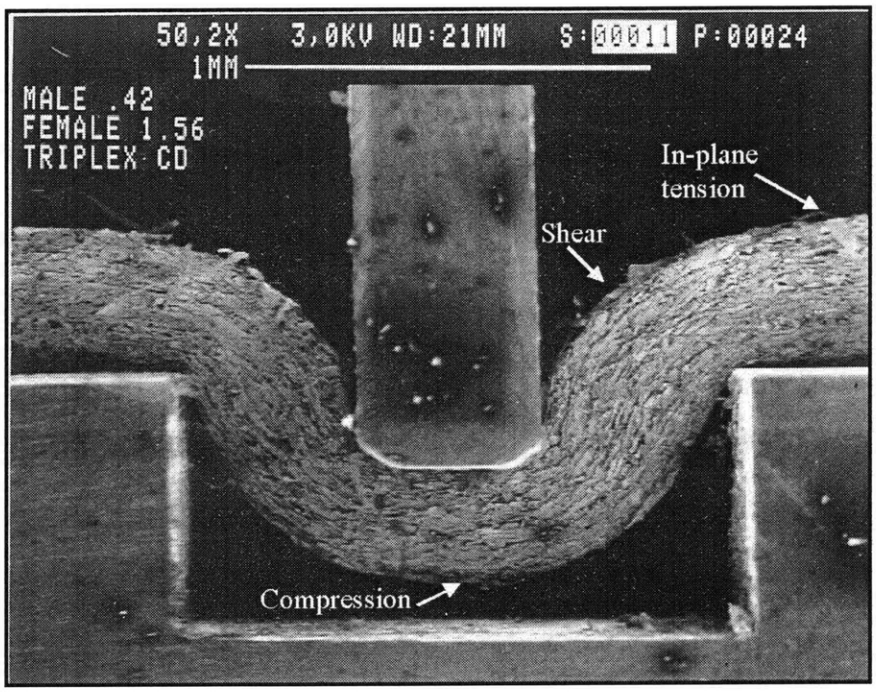

Figure 3-3: Triplex CD punching process. Male die is at its maximum displacement.

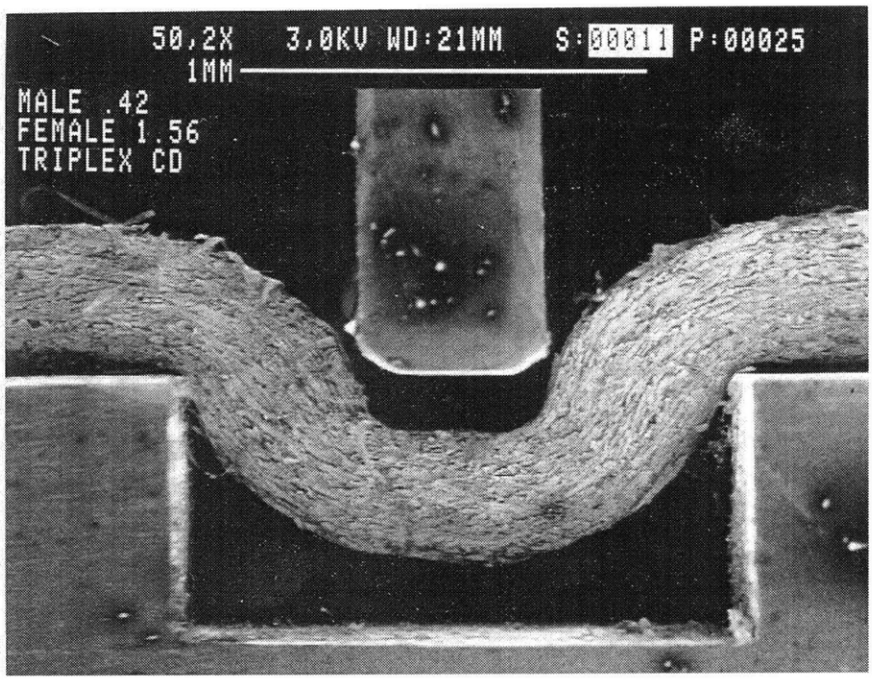

Figure 3-4: Triplex CD punching process. Unloading step.

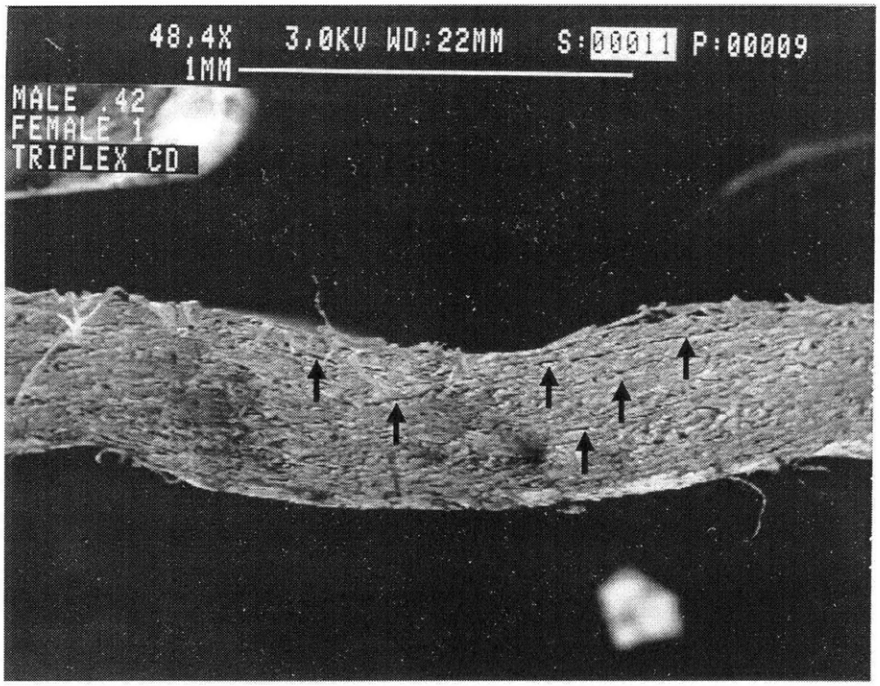

Figure 3-5: Triplex CD bending process at no load (Step 1). Arrows designate damage created by punching process.

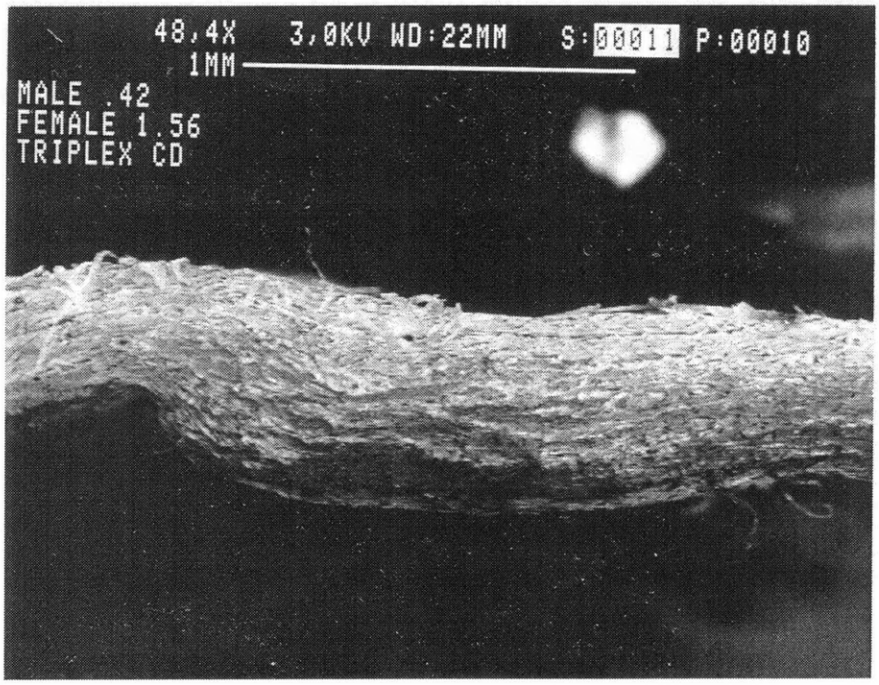

Figure 3-6: Triplex CD bending process (Step 2).

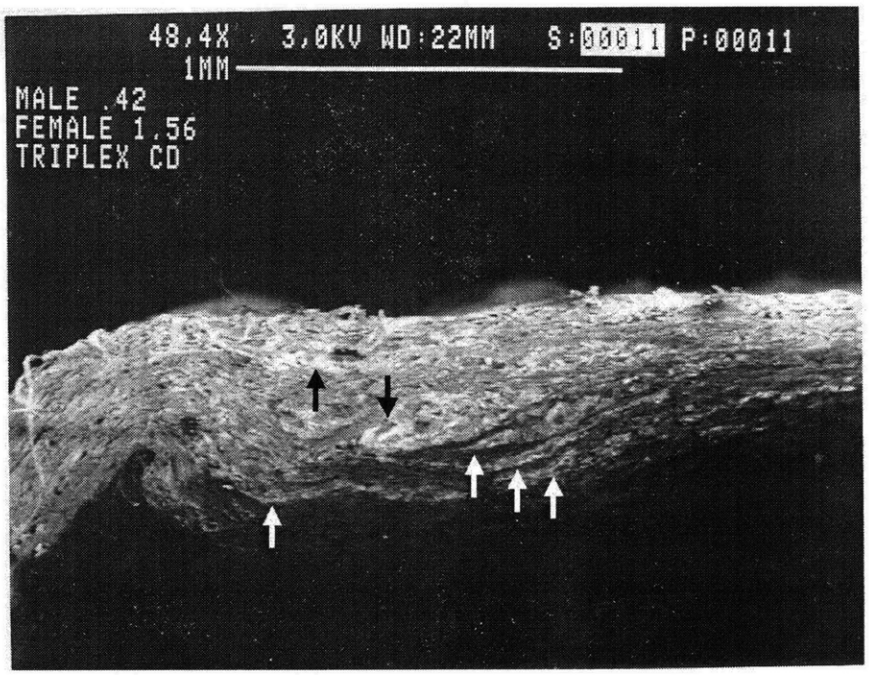

Figure 3-7: Triplex CD bending process (Step 3). Arrows indicate locations where material is delaminating.

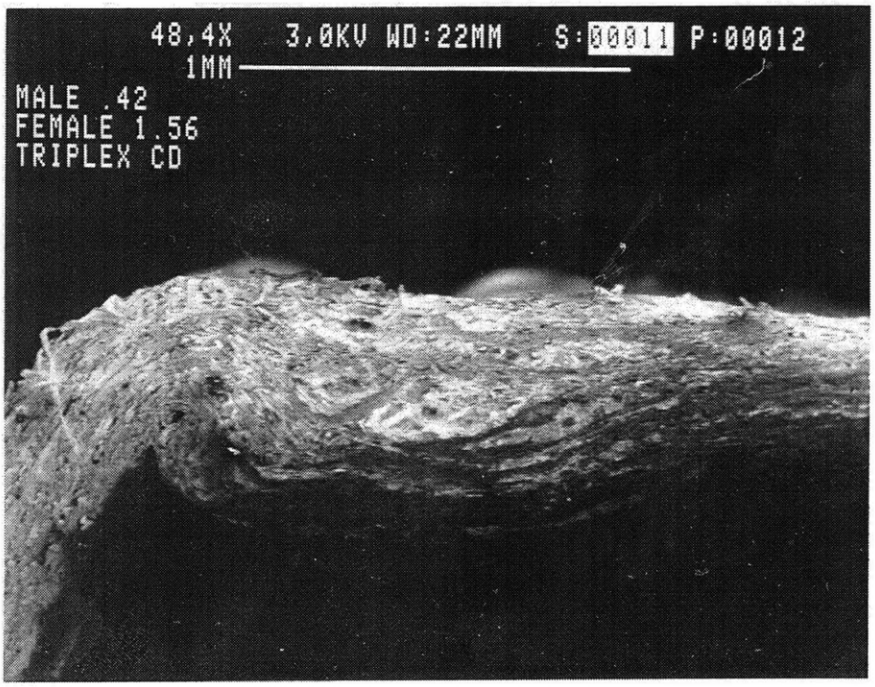

Figure 3-8: Triplex CD bending process (Step 4).

Further experiments were performed on alternate materials to determine the role of the laminate structure and the properties of the individual layers. However, as the project has since progressed to focus solely on Triplex, those results will not be presented here.

3.2 Experimental Procedure Evalutation

The crease shown in Figure 3-8 is not a "good" crease by the industry standard. The crease is unsymmetric, and delamination has happened outside the center of the bend. An unsymmetric crease is weaker under axial load than a symmetric crease and creates a less attractive package. The unsymmetric nature of this crease is due to the geometry of the bending fixture used. Figure 3-9 shows the geometry of bending tests conducted in the SEM. The moment arm is short relative to the in-plane length of the punched area. This results in the moment created being significantly larger at one side of the punched area than the other. Bending deformation occurs preferentially at the side experiencing the larger moment.

The bending fixture was redesigned based on the dimensions of a bending test machine used at StoraEnso. The moment arm, measured as the distance between the force application point and the nearest edge of the punched area, was increased from 10 mm or significantly less to over 25 mm. This required an increase in the bending specimen length, making the bending specimen too long to fit into the punch fixtures. The solution to this was to punch standard specimens, and after punching to glue second paper strip to the end of the punched specimen, creating a specimen of sufficient length. Figure 3-10 shows the new geometry of SEM bending tests.

3.3 Current Work

As extensive creasing studies were performed by Alexis Smith earlier in this project, current work was limited to verifying the new fixture design and confirming earlier observations. To verify the new bending fixture, several creasing experiments were

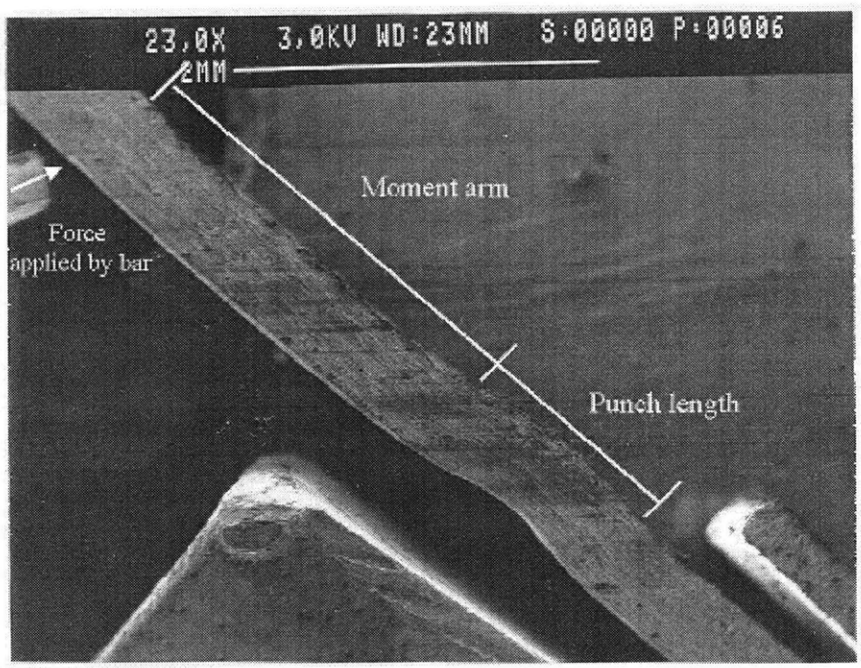

Figure 3-9: Original bending process geometry.

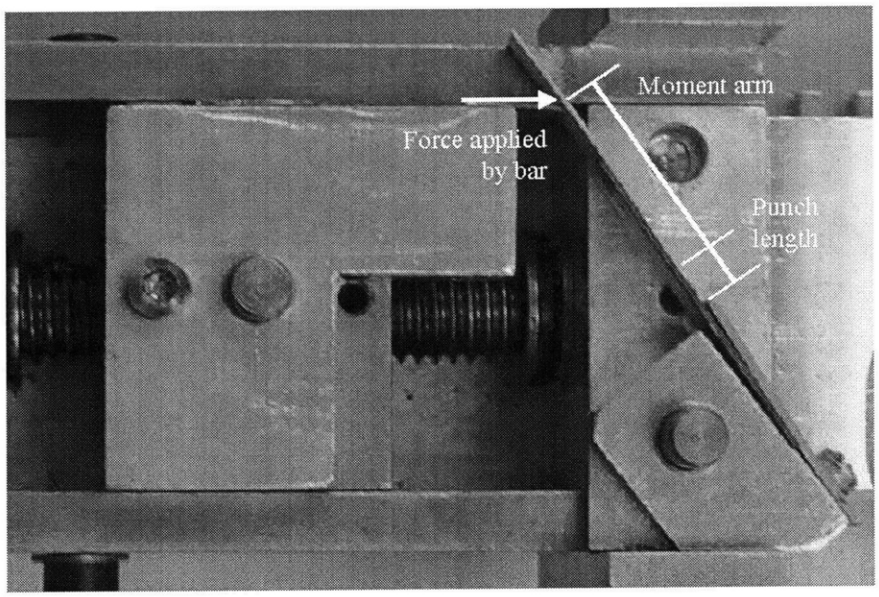

Figure 3-10: New bending process geometry.

performed. Some of the experiments used punching dies chosen to create a high quality crease. The remaining experiments used punching dies chosen to create a crease of poor quality. Punching die choices were made according to the Nystroem report on creasing of Triplex [15].

Images of a punching experiment performed in the current study are presented as Figures 3-11 through 3-18. In this experiment, the male die width was 0.50 mm, and the female die width was 1.56 mm. These widths, indicated by Nystroem to be ideal for machine direction Triplex, were chosen to create a high-quality crease.

Figure 3-11 shows the male die just coming into contact with the paperboard. In the following four images, Figures 3-12 through 3-16, the male die is pushed into the paperboard, creating damage. As discussed previously, damage due to through-thickness compression occurs under the punch. Shear damage occurs around the sides of the punch. This is clearly indicated by shear dilation around the male die, particularly between Figure 3-13 and Figure 3-14. (Shear dilation, which will be discussed further in sections on interlaminar shear, is the tendency for paperboard to dilate in the Z direction when subjected to through-thickness shear.) The paperboard is also subject to an in-plane tensile load.

The male die is at its maximum displacement, about 1.5 times the paperboard thickness, in Figure 3-16. The remaining images show the male die being retracted. At first as the die retracts, the paperboard follows, as in Figure 3-17. This is reversal of elastic deformation. In Figure 3-18, however, the male die pulls away from the board, showing plastic deformation of the material. Arrows in this image indicate damage locations. The paperboard still shows distinct regions of compression and shear; the compressed region at the center of the damaged material is much denser than the dilated shear regions surrounding.

The bending stage of this creasing experiment is presented in Figures 3-20 through 3-26. Figure 3-20 shows the specimen in the bending fixture with no moment load applied. The clamping bar is just visible in the lower right hand corner. Damage caused by punching is indicated by arrows. Many small cracks are visible along interfaces in the punched region, in addition to several substantial cracks in the material outside

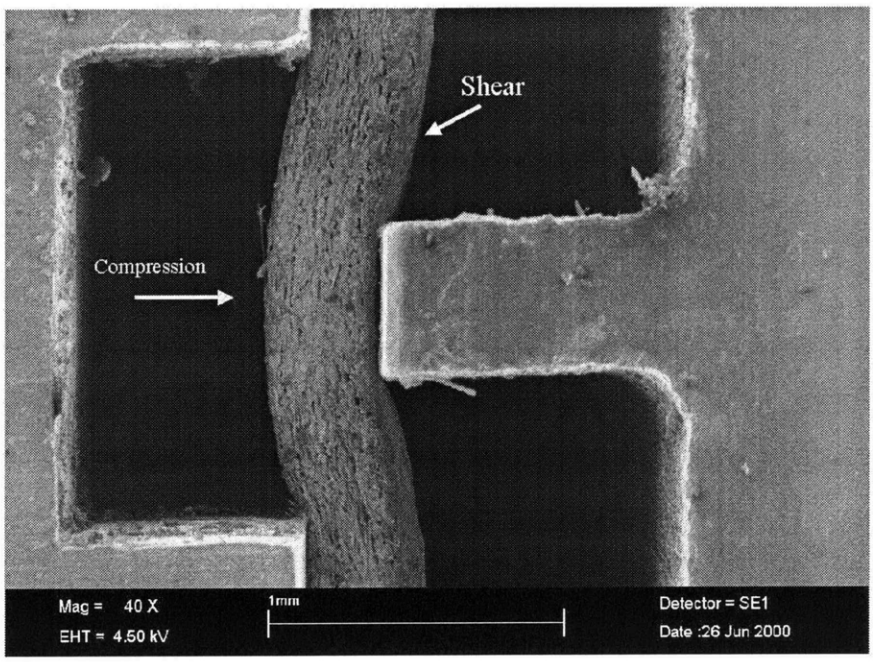

Figure 3-11: Triplex MD punching process (Step 1). Male die width is 0.50 mm. Female die width is 1.56 mm.

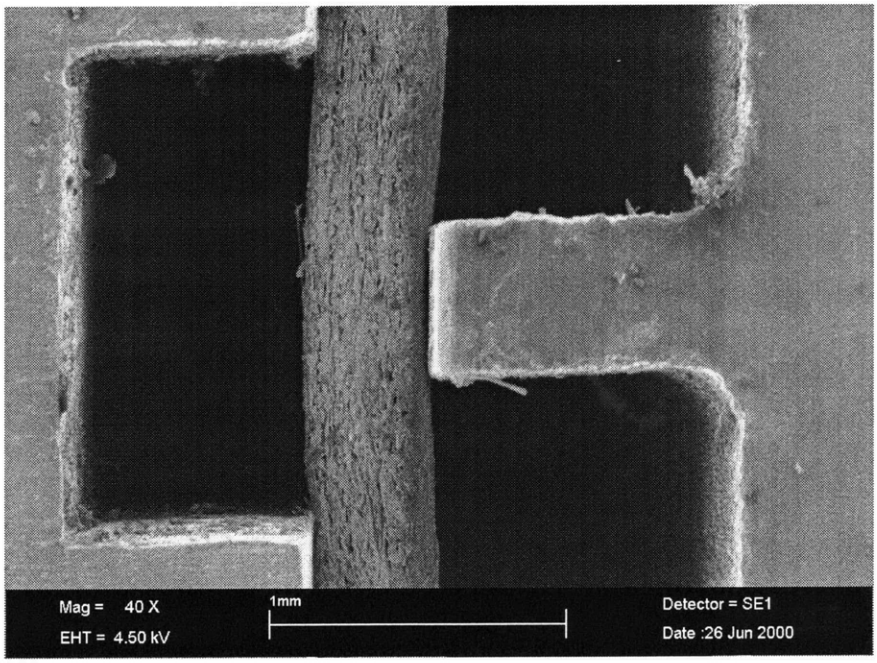

Figure 3-12: Triplex MD punching process (Step 2). Male die width is 0.50 mm. Female die width is 1.56 mm.

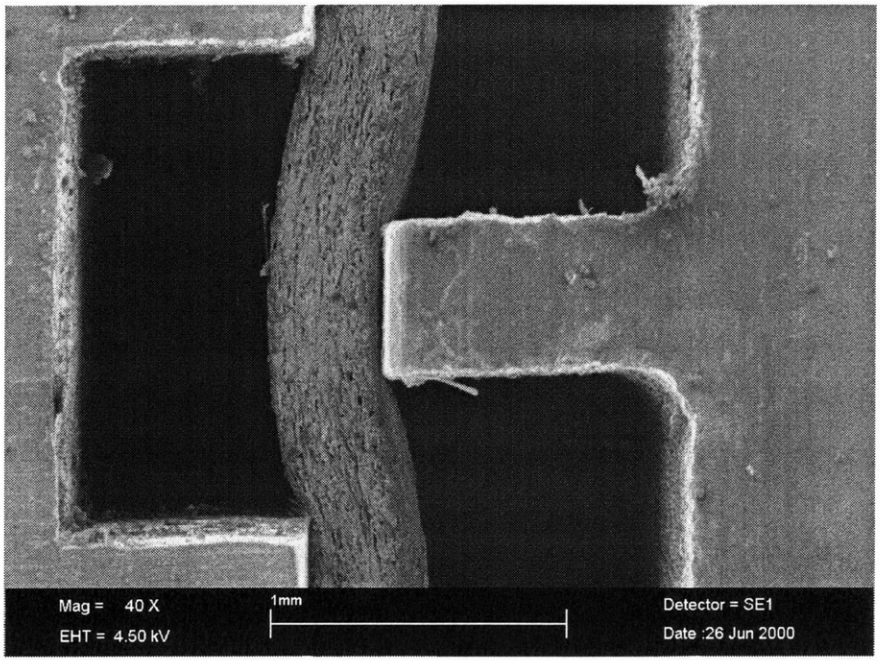

Figure 3-13: Triplex MD punching process (Step 3). Male die width is 0.50 mm. Female die width is 1.56 mm.

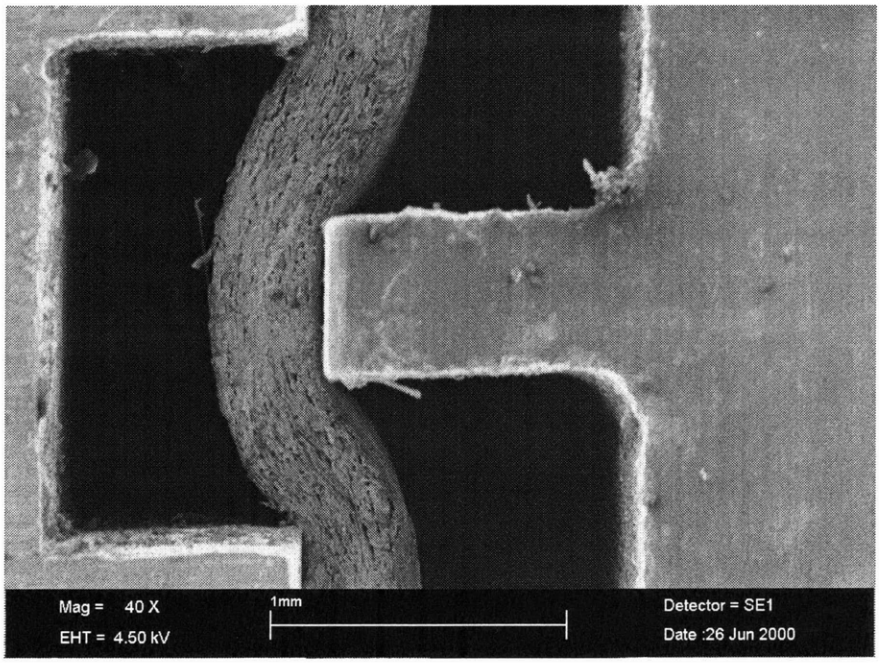

Figure 3-14: Triplex MD punching process (Step 4). Male die width is 0.50 mm. Female die width is 1.56 mm.

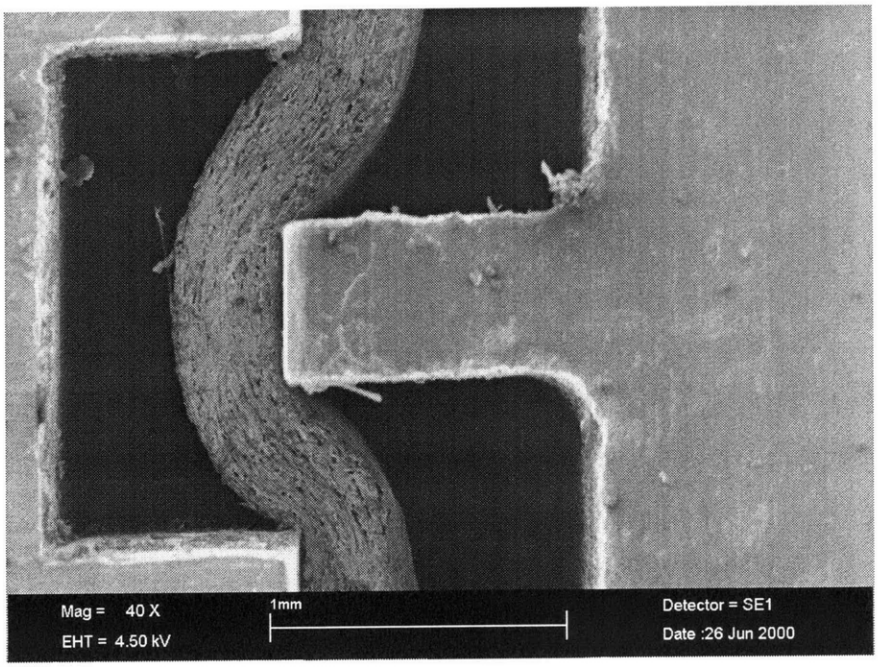

Figure 3-15: Triplex MD punching process (Step 5). Male die width is 0.50 mm. Female die width is 1.56 mm.

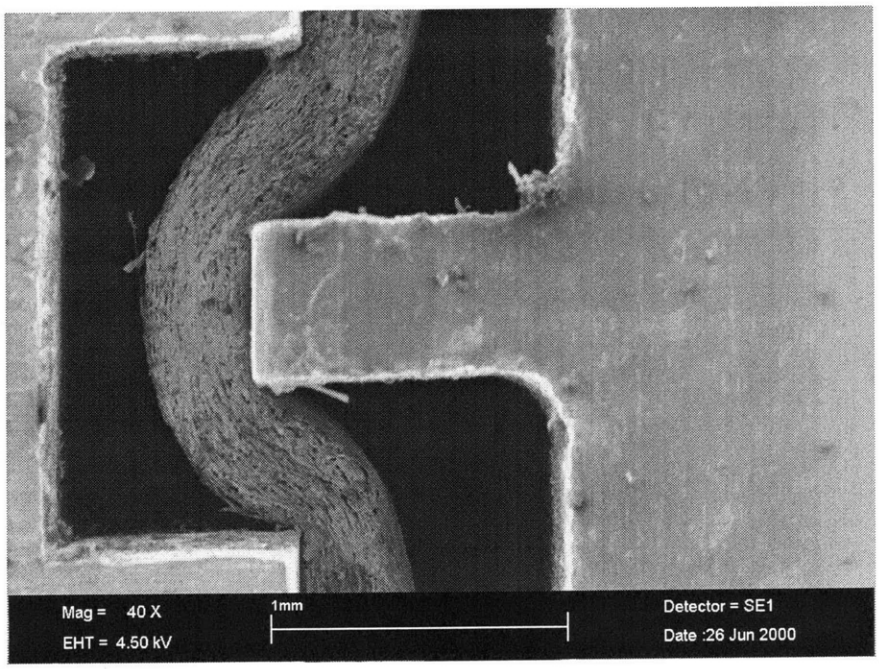

Figure 3-16: Triplex MD punching process (Step 6). Male die width is 0.50 mm. Female die width is 1.56 mm.

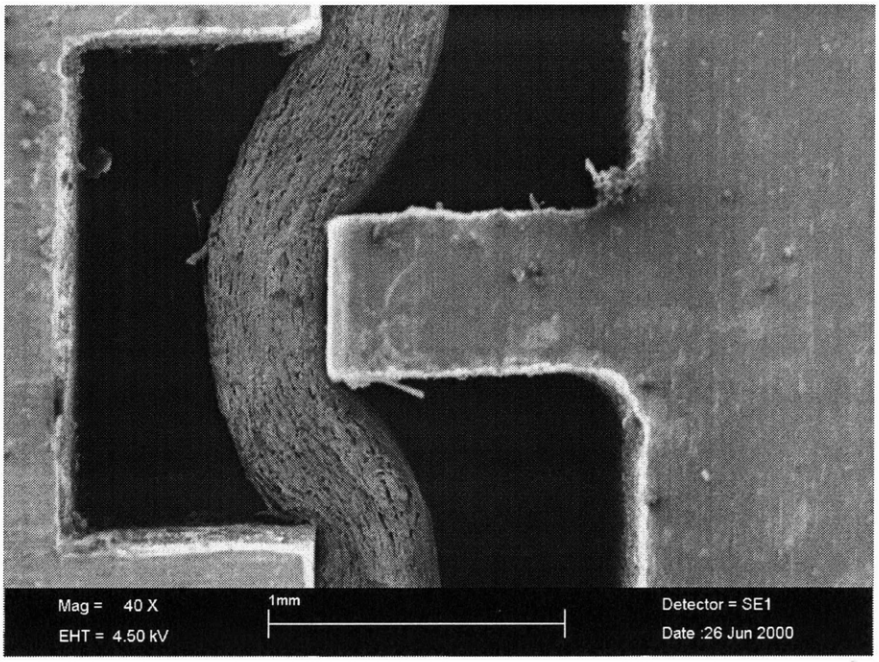

Figure 3-17: Triplex MD punching process (Step 7). Male die width is 0.50 mm. Female die width is 1.56 mm.

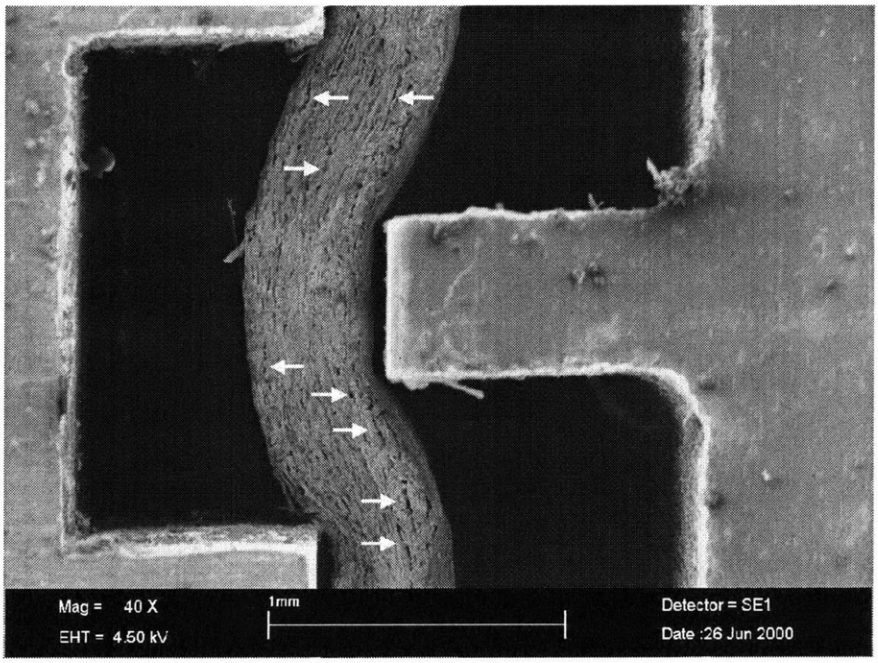

Figure 3-18: Triplex MD punching process (Step 8). Male die width is 0.50 mm. Female die width is 1.56 mm.

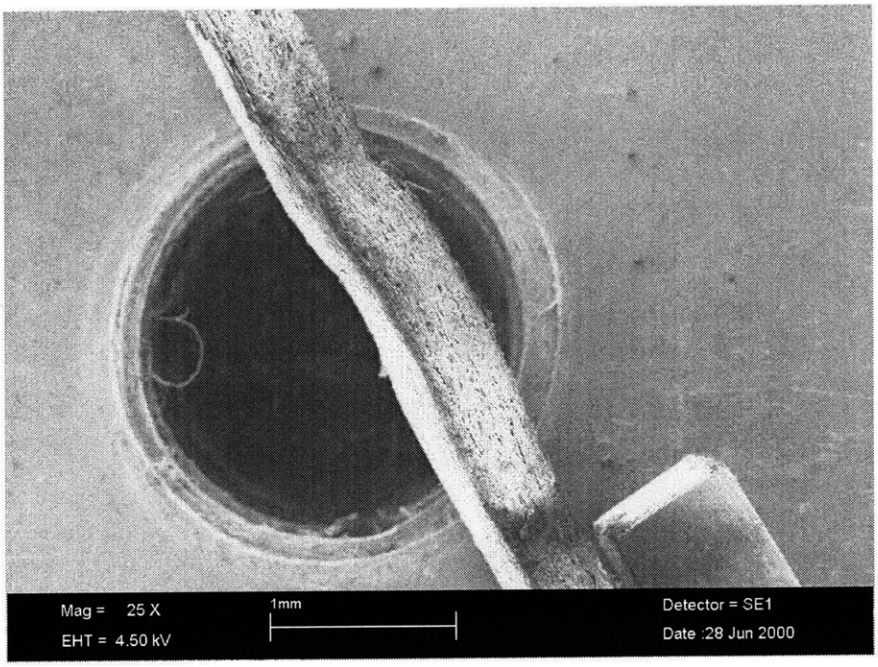

Figure 3-19: Triplex MD bending process (Step 1). Male die width was 0.50 mm. Female die width was 1.56 mm.

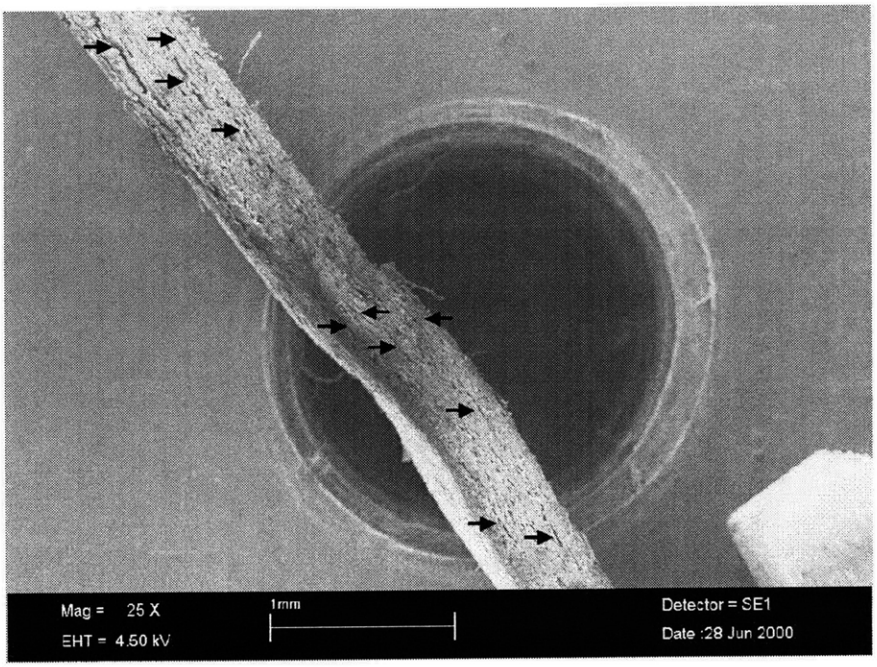

Figure 3-20: Triplex MD bending process (Step 2). Male die width was 0.50 mm. Female die width was 1.56 mm.

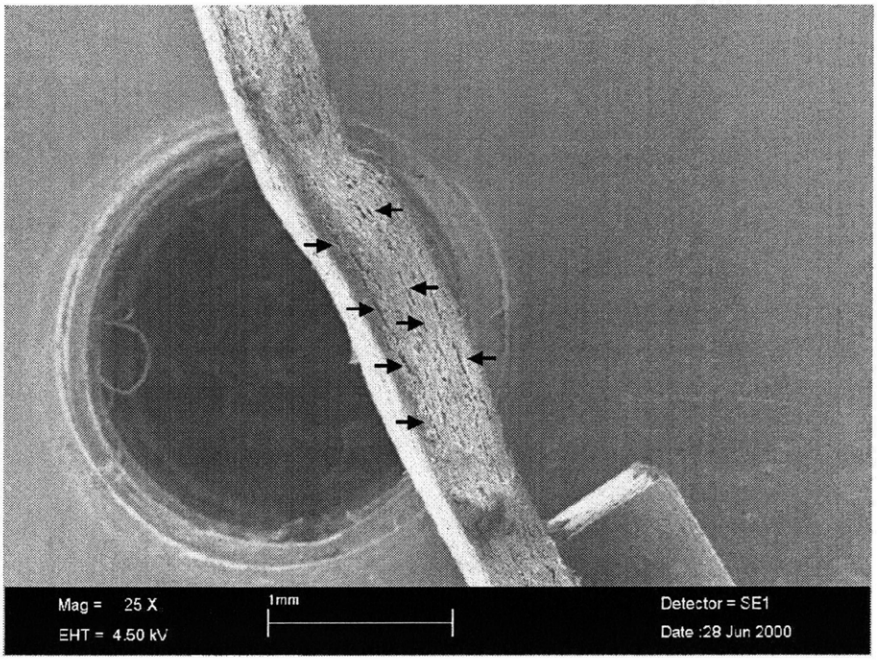

Figure 3-21: Triplex MD bending process (Step 3). Male die width was 0.50 mm. Female die width was 1.56 mm.

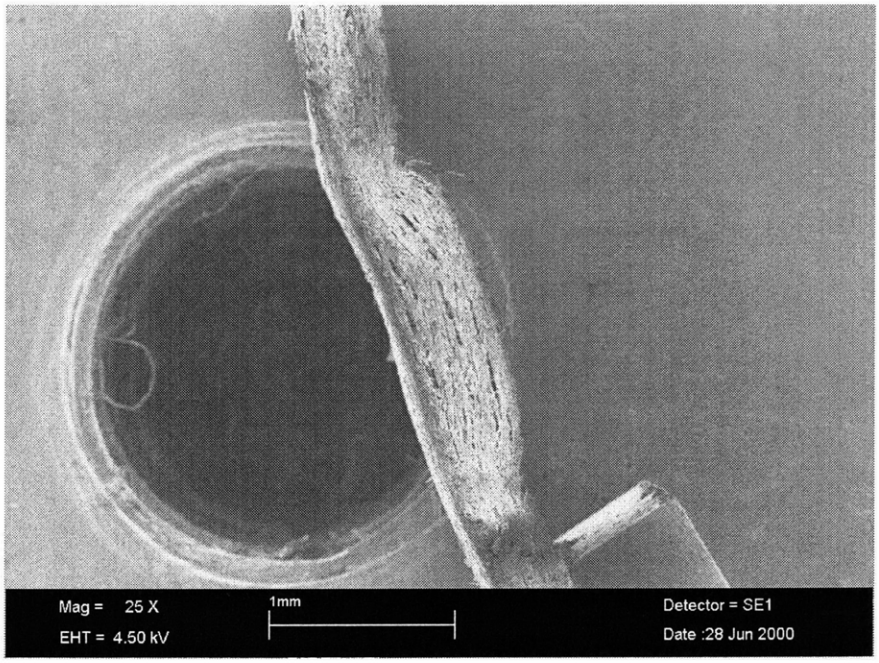

Figure 3-22: Triplex MD bending process (Step 4). Male die width was 0.50 mm. Female die width was 1.56 mm.

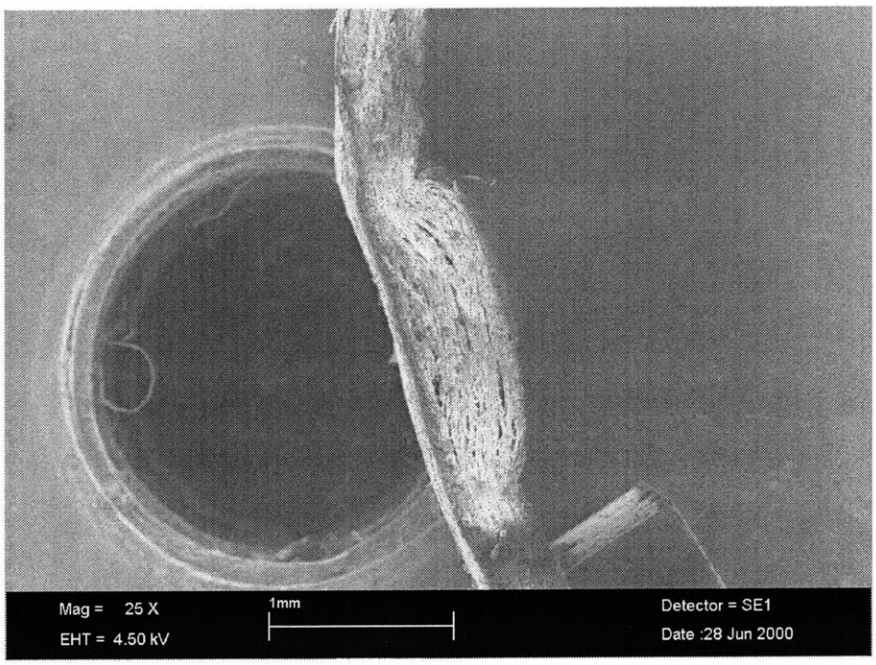

Figure 3-23: Triplex MD bending process (Step 5). Male die width was 0.50 mm. Female die width was 1.56 mm.

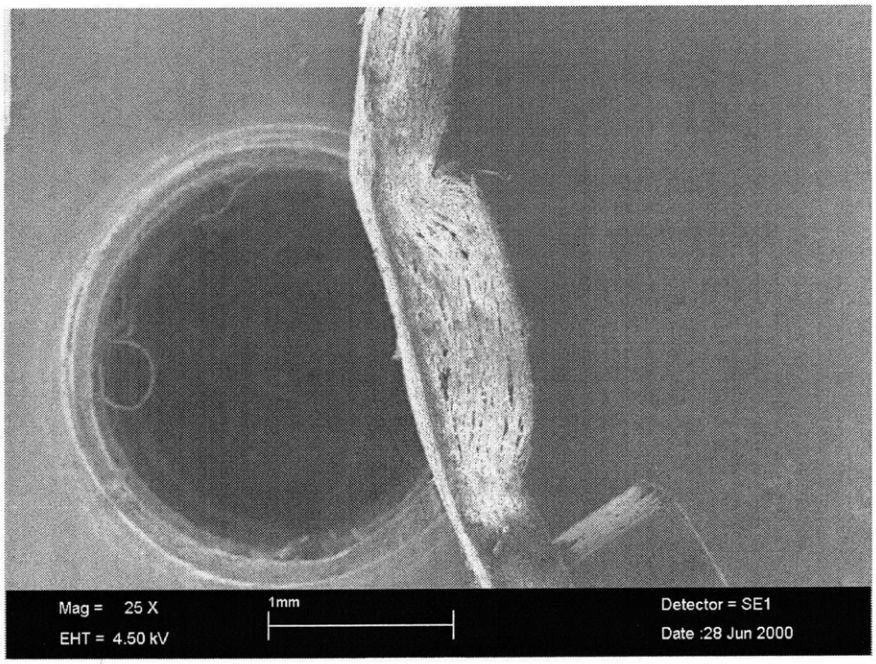

Figure 3-24: Triplex MD bending process (Step 6). Male die width was 0.50 mm. Female die width was 1.56 mm.

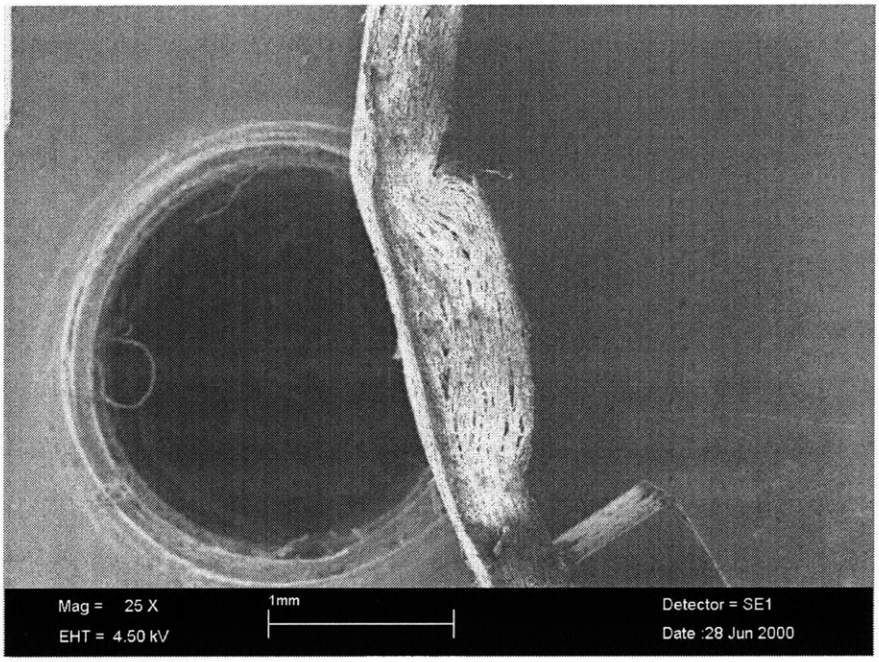

Figure 3-25: Triplex MD bending process (Step 7). Male die width was 0.50 mm. Female die width was 1.56 mm.

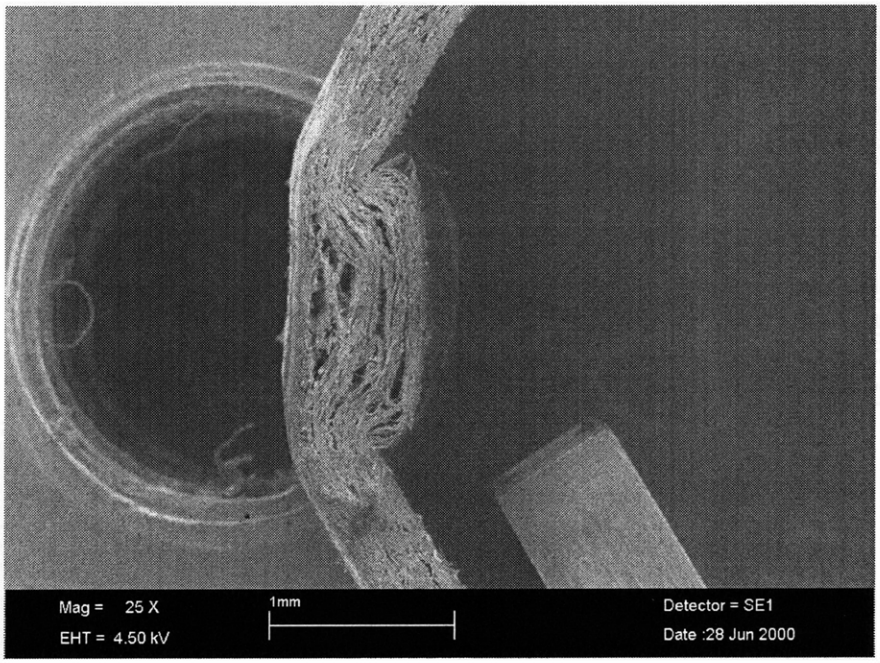

Figure 3-26: Triplex MD bending process (Step 8). Male die width was 0.50 mm. Female die width was 1.56 mm.

the punched region. Buckling will happen preferentially at the punch line rather than at points of surrounding damage because of the bowed shape of the punched region.

In Figure 3-19, sufficient moment load has been applied to push the specimen up against the clamping block. Additional moment load in Figure 3-21 has caused the cracks in the punch region to begin to open, as indicated by arrows. These cracks continue to open further in Figures 3-22 through 3-25. In the last of these images, bending appears to be happening preferentially at the upper end of the punched region instead of being centered around the punched material. However, the final image, Figure 3-26 shows a high quality, centered crease. Delamination is distributed evenly throughout the punched region and is at the center of the bend. These experimental results show that the new bending fixture lengthens the moment arm sufficiently to create a good crease.

To produce a crease of poor quality, larger punching dies were chosen. Larger dies create a wider punched region, increasing the difference in moment arm length between the ends of the punched region and generally resulting in a lopsided crease. The results of a large-die punching experiment are shown in Figures 3-27 through 3-32. The male die used in this experiment was 0.86 mm wide, with a female die 2.03 mm wide.

The first image, Figure 3-27, shows the male die just touching the paperboard. In Figures 3-28 through 3-30, the male die is pushing into the board. A maximum displacement of about 1.5 times the material thickness occurs in Figure 3-30. Figure 3-31 was taken during unloading, and Figure 3-32 shows the permanent damage created. Compressive damage is very clear in these images, although the effects of shear dilation are not as pronounced as in the previous set of punching images.

Bending of this same specimen is shown in Figures 3-33 through 3-38. The first of these images shows the specimen placed in the fixture with no moment load applied. In the second image, Figure 3-34, the specimen has been pushed against the clamping bar. In Figure 3-35, delamination is beginning in the punched region. Notice that at the bottom of the punched region, near the clamping bar, delamination occurs primarily at the inside of the bend. Further away from the clamping bar, delamination is

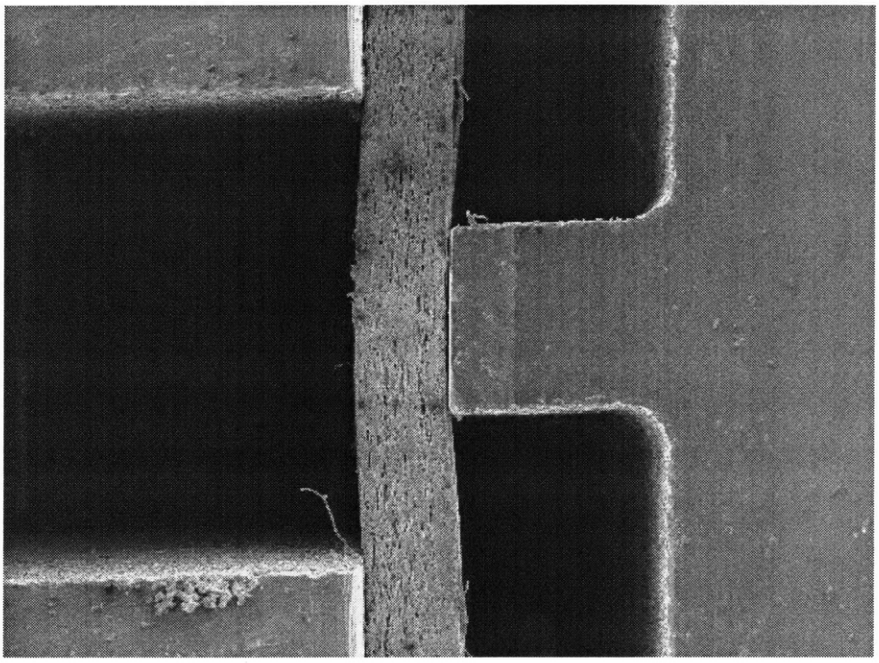

Figure 3-27: Triplex MD punching process (Step 1). Male die width is 0.84 mm. Female die width is 2.03 mm.

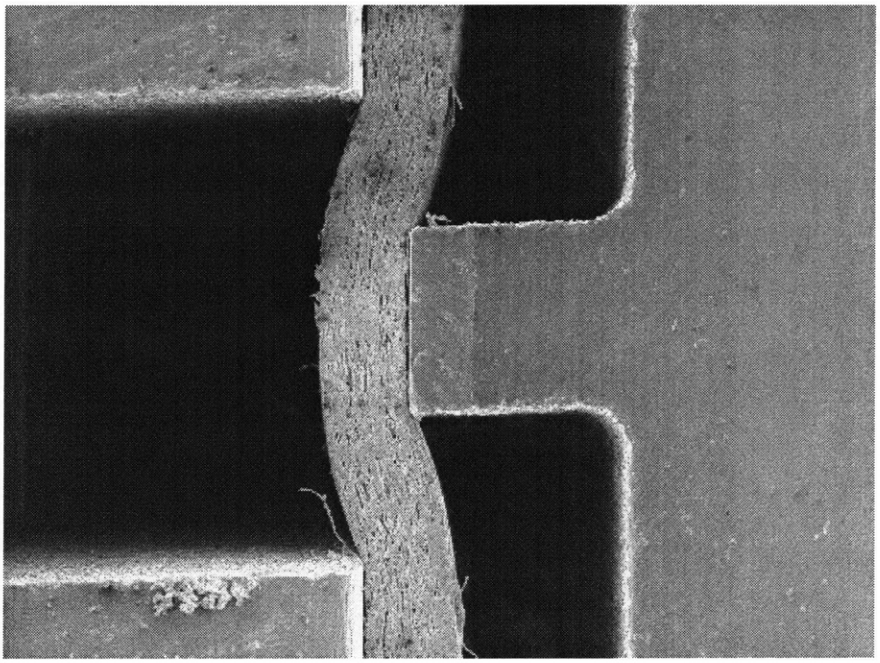

Figure 3-28: Triplex MD punching process (Step 2). Male die width is 0.84 mm. Female die width is 2.03 mm.

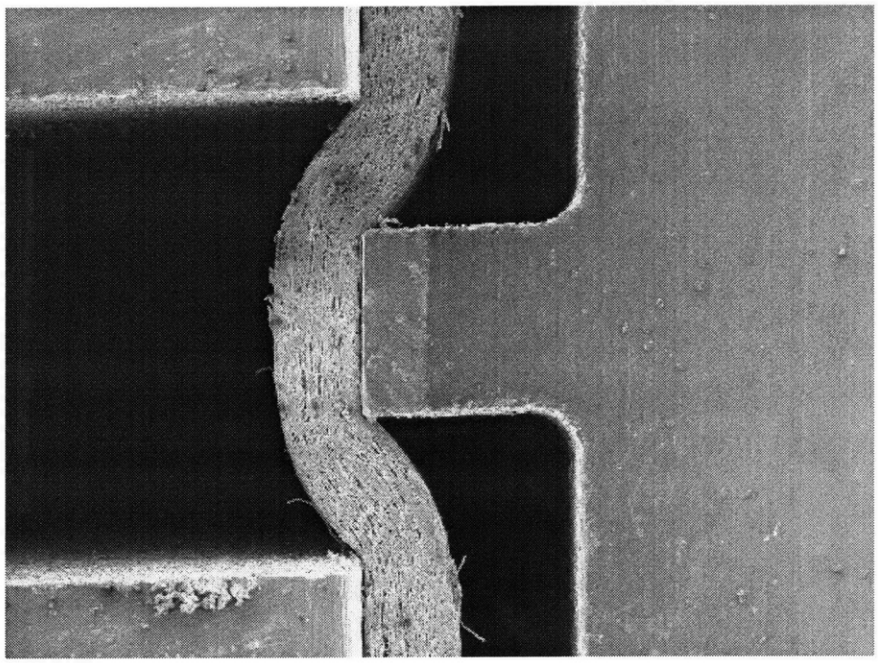

Figure 3-29: Triplex MD punching process (Step 3). Male die width is 0.84 mm. Female die width is 2.03 mm.

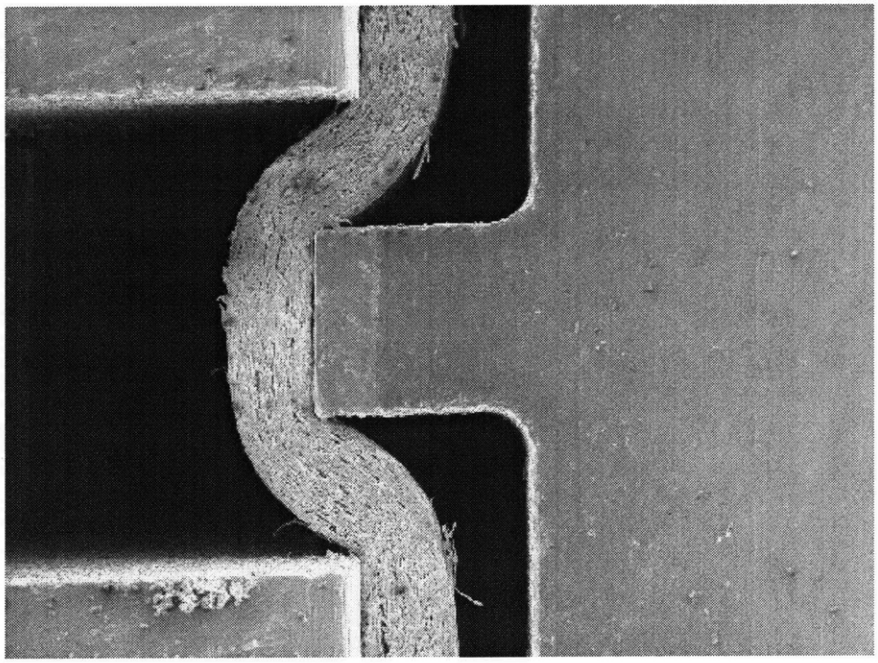

Figure 3-30: Triplex MD punching process (Step 4). Male die width is 0.84 mm. Female die width is 2.03 mm.

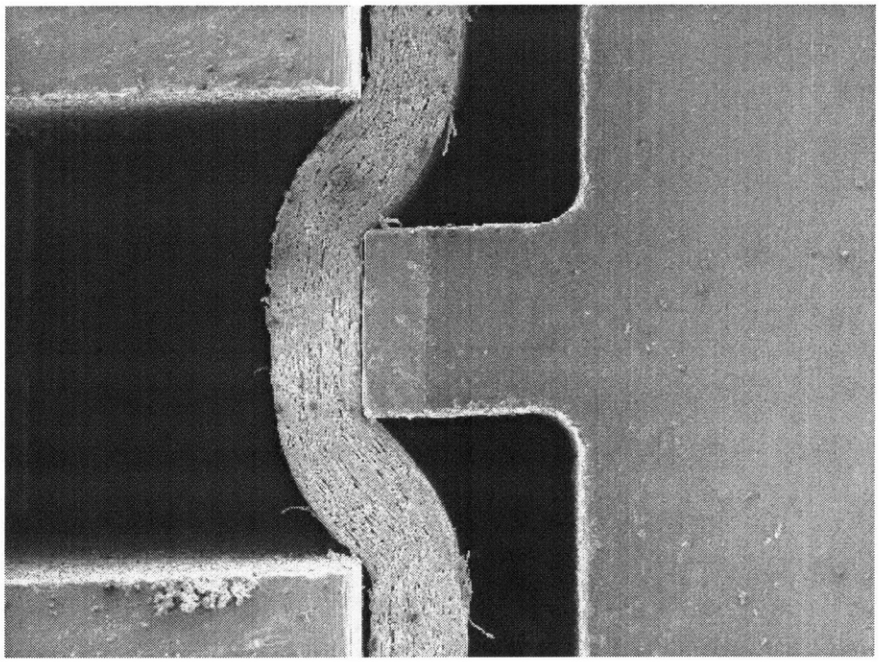

Figure 3-31: Triplex MD punching process (Step 5). Male die width is 0.84 mm. Female die width is 2.03 mm.

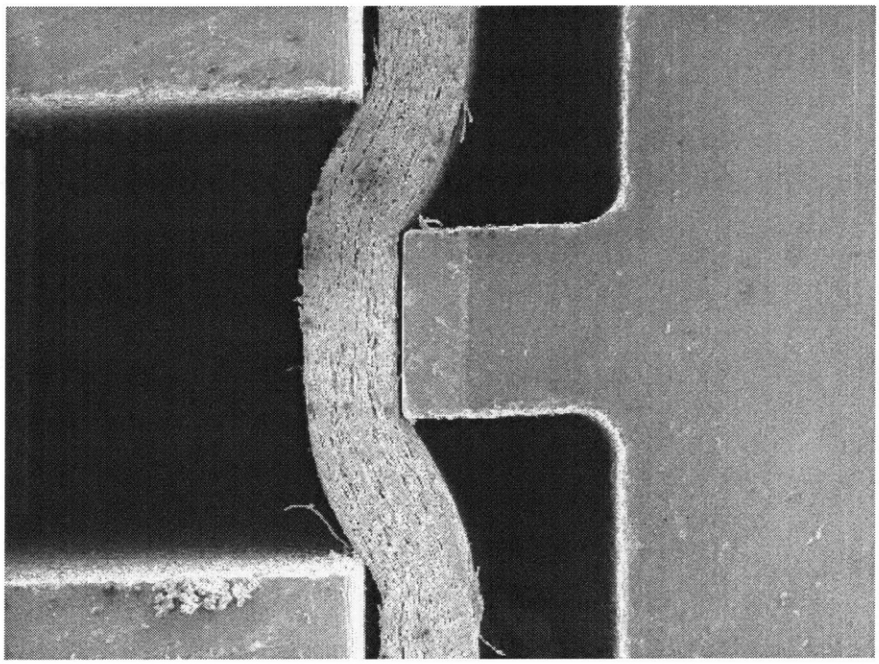

Figure 3-32: Triplex MD punching process (Step 6). Male die width is 0.84 mm. Female die width is 2.03 mm.

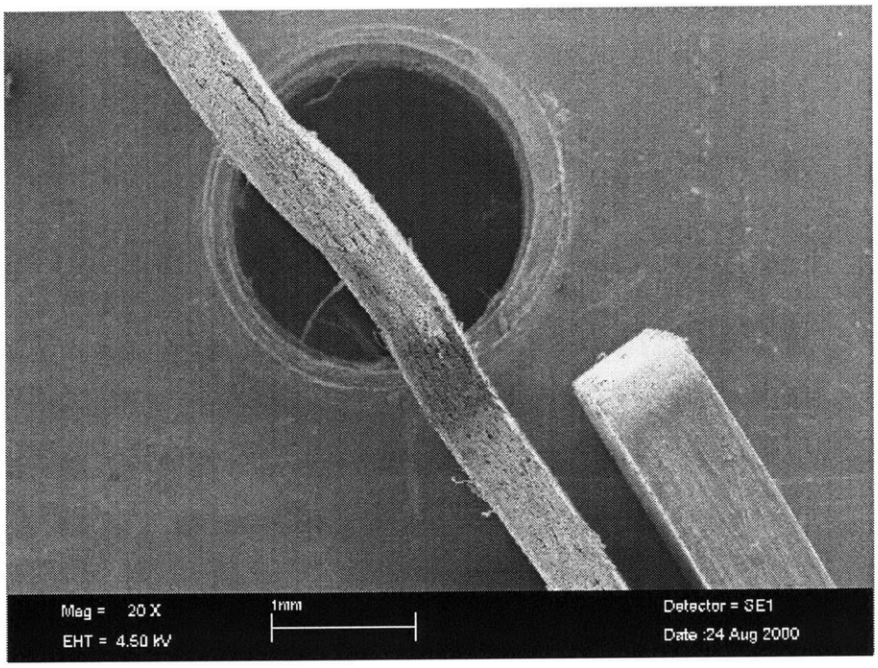

Figure 3-33: Triplex MD bending process (Step 1). Male die width was 0.84 mm. Female die width was 2.03 mm.

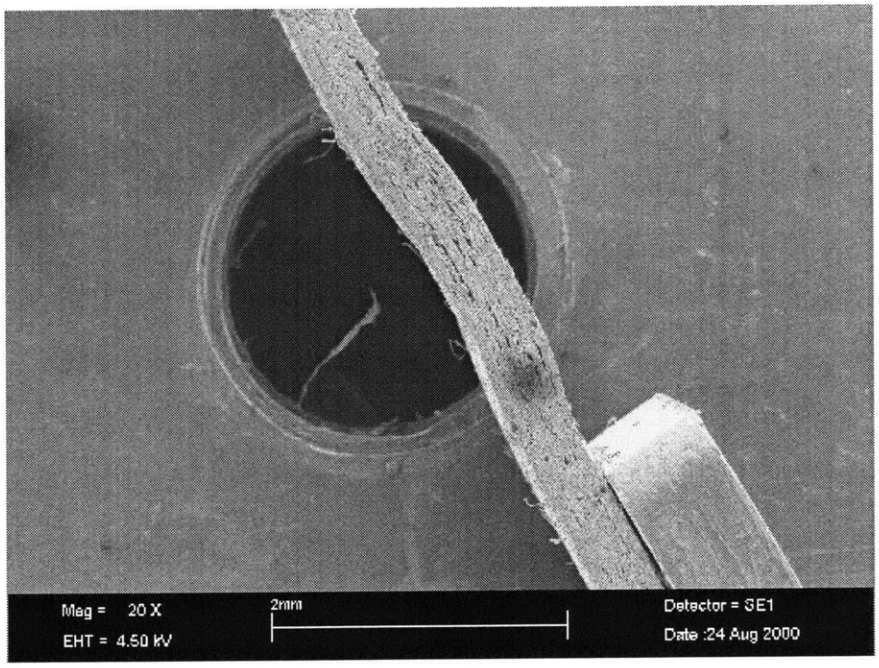

Figure 3-34: Triplex MD bending process (Step 2). Male die width was 0.84 mm. Female die width was 2.03 mm.

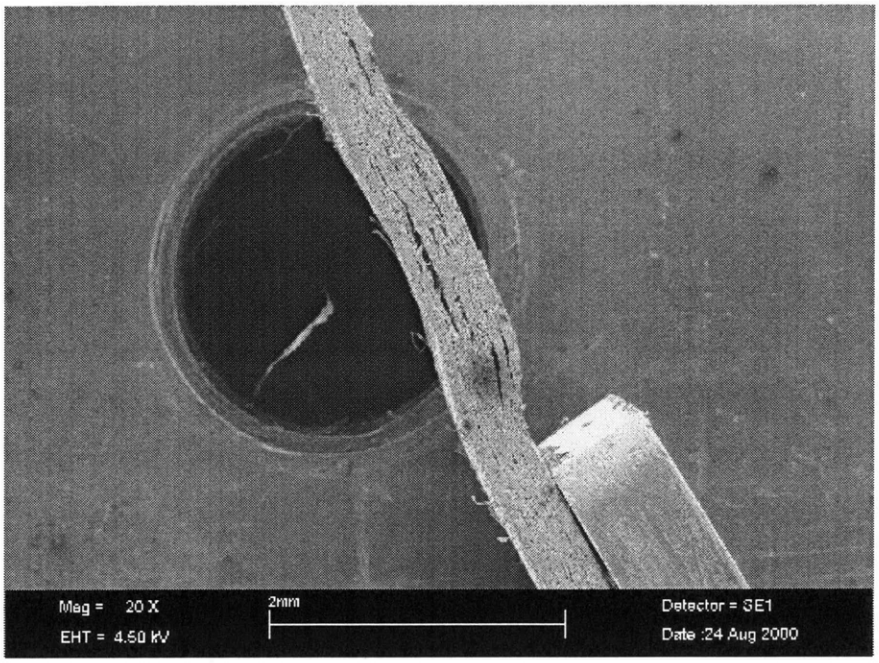

Figure 3-35: Triplex MD bending process (Step 3). Male die width was 0.84 mm. Female die width was 2.03 mm.

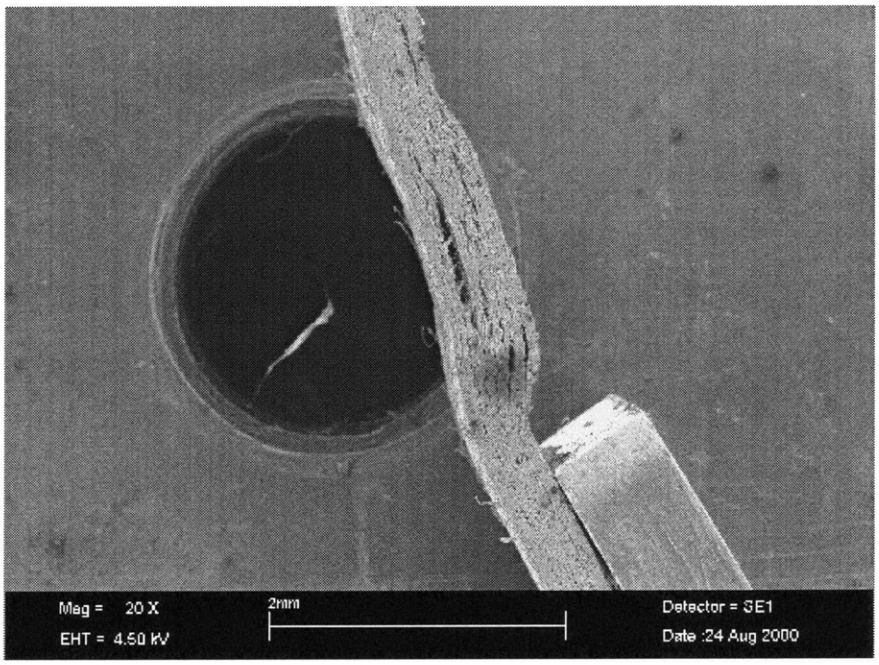

Figure 3-36: Triplex MD bending process (Step 4). Male die width was 0.84 mm. Female die width was 2.03 mm.

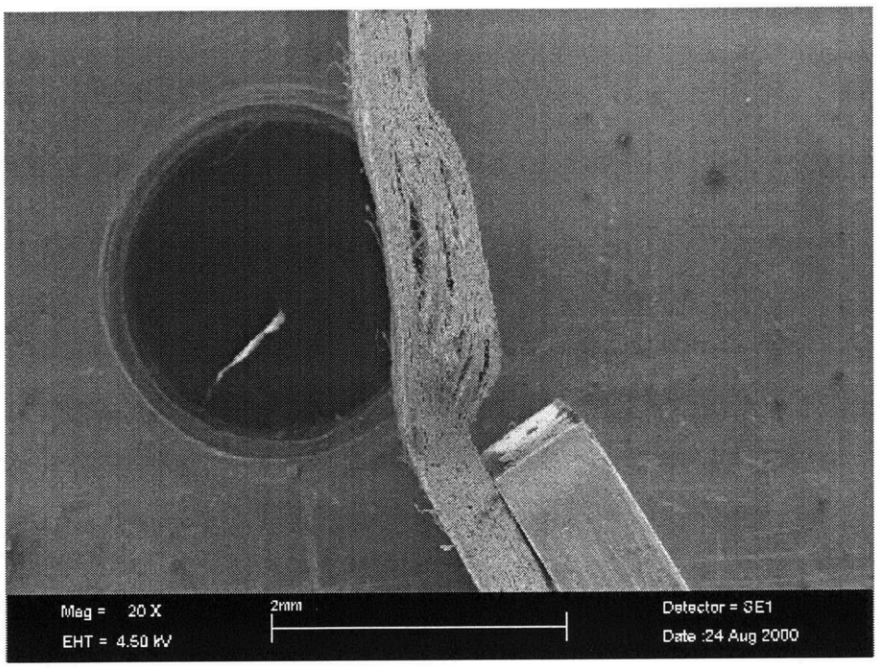

Figure 3-37: Triplex MD bending process (Step 5). Male die width was 0.84 mm. Female die width was 2.03 mm.

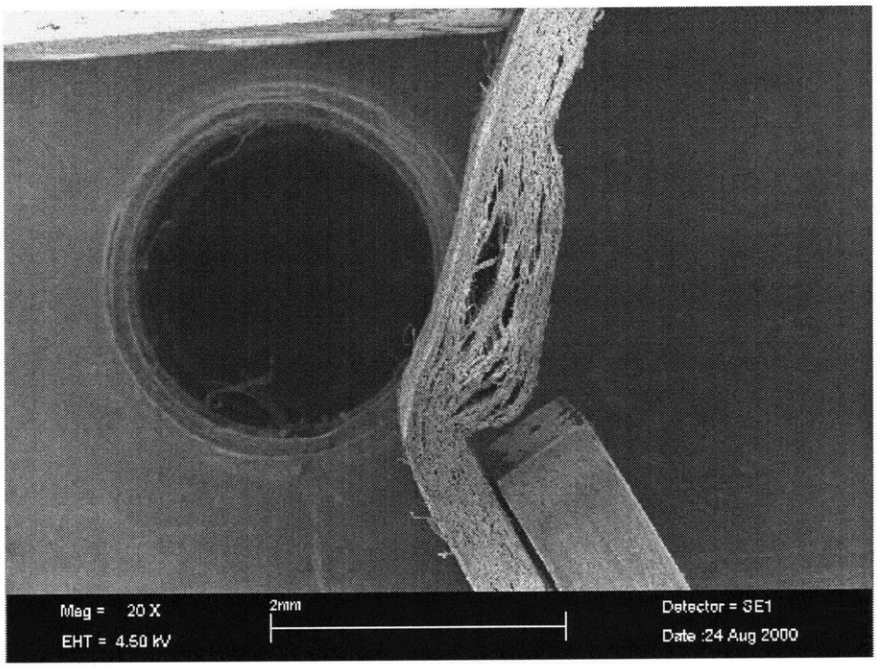

Figure 3-38: Triplex MD bending process (Step 6). Male die width was 0.84 mm. Female die width was 2.03 mm.

happening nearer the outside of the bend. This trend continues through the remaining images. Figure 3-37 shows that bending is occurring preferentially at the clamped end of the punched region, where the moment arm and corresponding moment load are largest. The final image, Figure 3-38, shows a lopsided crease. Delamination is concentrated near the inner suurface at the end of the damaged region closest to the bend. Further from the bend, delamination has happened closer to the outside. A similar delamination pattern was observed in other poor quality crease experiments.

These experimental results confirm that the moment arm of the redesigned bending fixture is sufficiently long to create a good crease. A high-quality, symmetrical crease was produced with properly sized dies. Larger punching dies, which lengthened the in-plane dimension of the punched area, produced a poor quality crease. The width of the punched region created a significant difference in moment arm at each end of the region, and bending occured preferentially at the end with larger moment load.

These results also confirm earlier observations by Alexis Smith. During punching, a specimen is subject to through-thickness compression under the punch and shear deformation around the punch. During bending, delamination occurs at locations damanged during the punching step. The delamination mechanism is similar to that observed in through-thickness tension.

Chapter 4

Out-of-Plane Tension Experimental Results

This chapter details the results of through-thickness tension tests at both the macroscopic and microscopic levels. Macroscopic stress-strain curves show an initial elastic region followed by nonlinearity, a peak in stress, and finally material softening. Stress-strain curves and images taken at the microscopic level reveal the mechanisms responsible for this behavior.

4.1 Macroscopic Results

A stress-strain curve for macroscopic uniaxial through-thickness tension of Triplex is shown in Figure 4-1. The strain measure used here and in all stress-strain information presented in this chapter is true strain. True strain is defined by the following expression.

$$\epsilon = ln(\frac{t}{t_o}) \tag{4.1}$$

In this equation, t represents the deformed thickness of the specimen and t_o the original thickness, 0.45 mm in this case. The stress is nominal stress, as defined in Appendix B.

The curve has an initial linear elastic region; analysis of several similar curves has

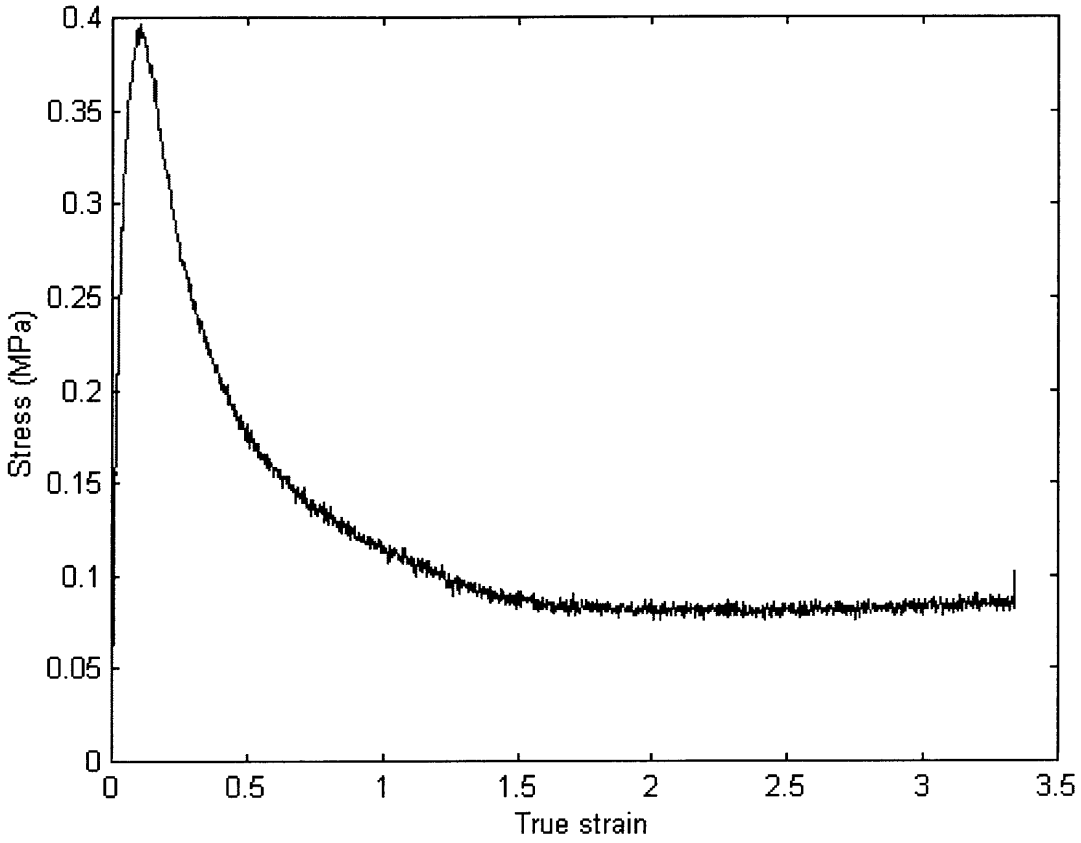

Figure 4-1: Macroscopic stress-strain data for uniaxial through-thickness tension. (Courtesy of N. Stenberg.)

indicated an elastic modulus in the Z direction of 8.15 MPa. As stress increases, the material behavior deviates from linearity, and the slope of the curve decreases. The nonlinearity could be the result of material yield and hardening, but this cannot be determined without additional data, particularly loading and unloading data in the nonlinear region.

The stress peaks and begins to fall as small cracks form and grow in the material. After an initial steep fall, the curve begins to level off. As will be shown, this happens when one of the small, growing cracks becomes dominant. Although it is not shown on this curve, the stress will continue to decrease very slowly with increasing strain. The stress will become zero when all fibers have been disengaged; this happens at

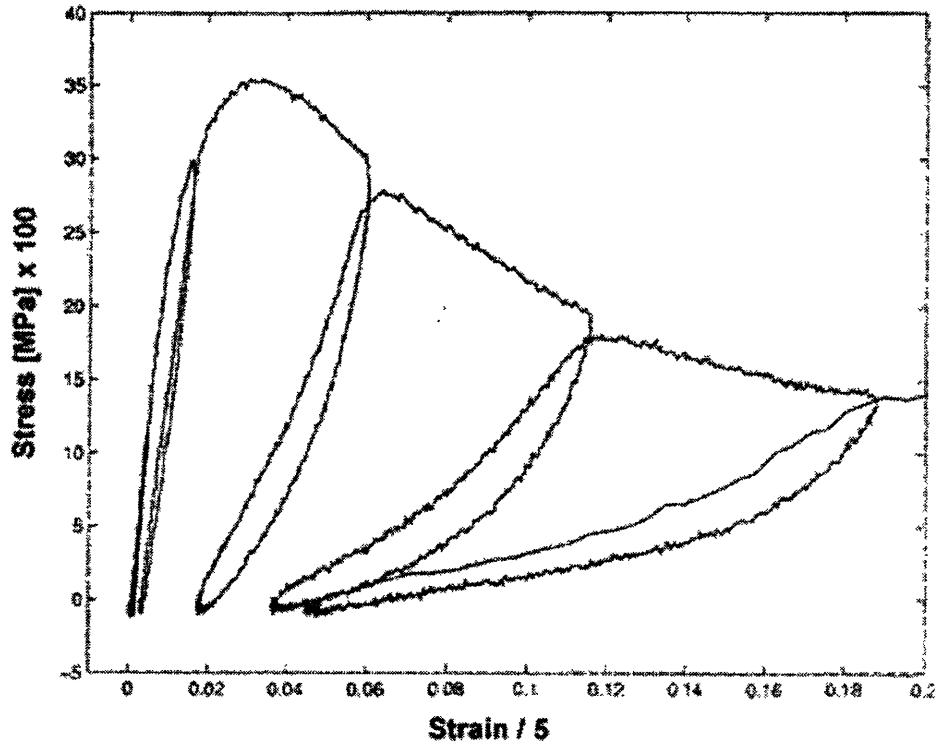

Figure 4-2: Macroscale alternate loading through-thickness tension data.

displacements on the order of the fiber length, about 3 mm.

Alternate loading experiments were also conducted at the macroscopic level. These tests were intended to impart information on elastic and plastic regions of the stress-strain curve, material stiffness evolution, and plastic strain accumulation. Results are shown in Figure 4-2.

Figure 4-2 demonstrates alternate loading behavior over a large strain range. The first unloading occurred when the stress had reached about 0.12 MPa. This is still well within the elastic region, and both the unloading and reloading curves follow the original loading curve almost exactly. Loading further to 0.30 MPa and unloading reveals plastic behavior. The material retains a small plastic strain when completely unloaded. The reloading curve has a slightly shallower slope than the original loading curve, indicating a small decrease in stiffness. As stated previously, this is possibly due to material yield and hardening, but this cannot be determined for certain without

significantly more data.

In the post-peak region, much more dramatic behavior is observed. Each successive unloading indicates larger plastic strains and smaller material stiffness. This is caused by crack growth and fiber reorientation. As the cracks grow, the bonds between fibers are broken. There are not as many bonds to "pull" the material on both sides of a crack back together; cracks do not close completely, creating a residual strain. Growing cracks also decrease the available load-bearing area, decreasing the stiffness of the material. Fibers that originally lay in the plane or at a small angle to it are pulled out of the plane as the material delaminates. Pulling fibers out of the plane and reorienting them in the loading direction requires a large amount of load. If the specimen is unloaded after some fibers have been reoriented and then reloaded, the stiffness will be lower during reloading because those fibers do not have to be pulled out of the plane again.

The correlation between stress-strain curve features and mechanisms discussed here will be explored more fully later in the chapter.

4.2 Microscale Stress-Strain Results

A stress-strain curve for microscopic uniaxial through-thickness tension of Triplex is shown in Figure 4-3. This curve has the same general shape as the macroscopic curve discussed above. It displays a sharp rise followed by a region of material yield and hardening. (In contrast to the macroscopic curve, the rise here is not quite linear. However, this is likely due to limitations of the equipment and does not represent a significant change in behavior between the macroscale and microscale.) Beyond peak stress, the curve falls quickly at first and then begins to level off. However, beyond these general observations the two curves have some significant differences.

At the beginning of the microscopic curve, there is a very short region of relatively constant low stress. This is due to slack in the fixtures used for testing. A small amount of slack is intentionally left in the fixtures while mounting them. All tests conducted in the scanning electron microscope are conducted in a vacuum, and

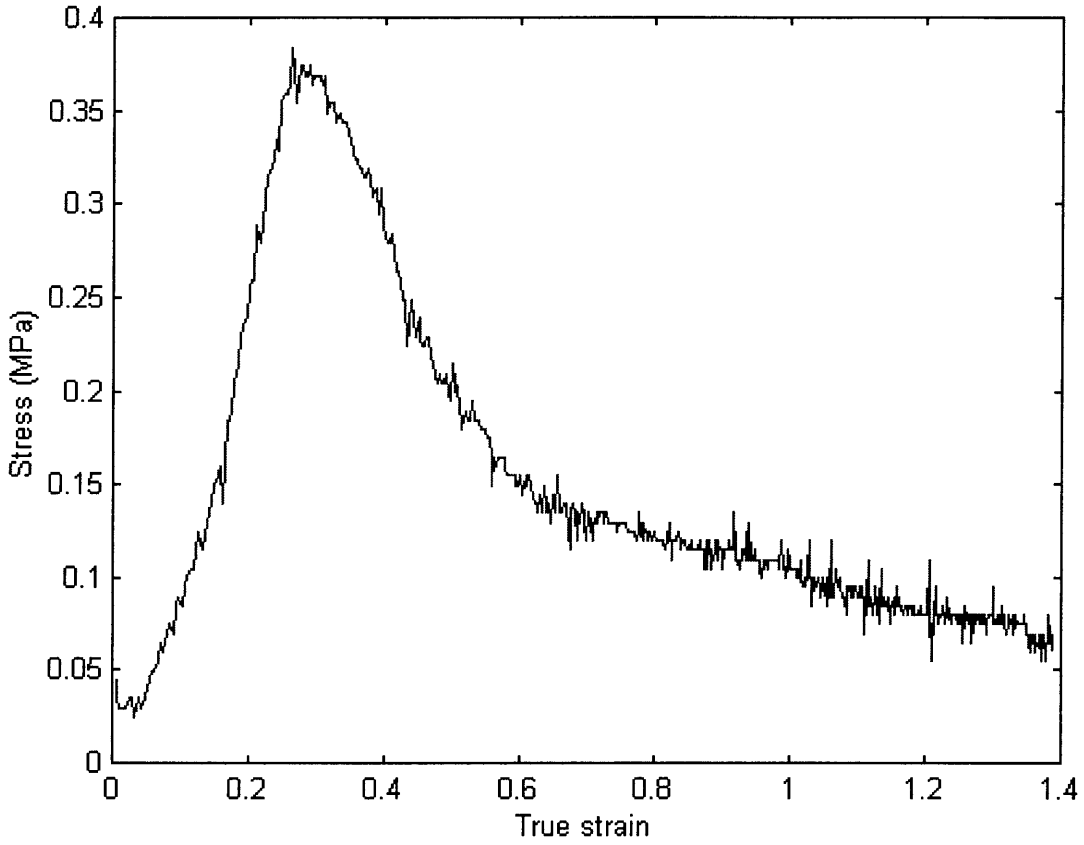

Figure 4-3: Microscale through-thickness tension test data.

pumping the testing chamber down from atmospheric pressure to vacuum often results in a significant tensile stress in the specimen if the fixtures are completely tightened. This can create damage in the specimen, weakening it and changing the observed stress-strain behavior. Thus, a slight amount of slack is left in the fixtures to prevent a vacuum-induced tensile stress.

In the region of increasing stress, there is a slight increase in slope at a strain of about 0.15. There are two possible causes for this slope change. The first is a small amount of remaining fixture slackness. A more likely cause, however, is variation in motor speed. The stepper motor used in these experiments fluctuates slightly about its set value. However, the Labview Virtual Instrument (VI) that collects the stress-strain data cannot detect these fluctuations. The VI receives the motor speed as a

Table 4.1: Microscopic data scatter.

Test number	Peak stress (MPa)	Logarithmic strain at peak stress
1	0.32	0.37
2	0.38	0.26
3	0.39	0.44
4	0.36	0.40
5	0.34	0.27

fixed input and calculates "strain" based on this value and the time elapsed since the beginning of the test. If the motor experienced a small increase in speed, the rate of accumulation of both load and real strain would increase. The strain values calculated by the VI would be too small. The slope is proportional to the actual load divided by the calculated strain. If calculated strain is too small, the slope will be artificially large.

The amount of motor stutter can be estimated for experiments where both stress-strain data and images were collected by comparing the final calculated strain value to the final deformation in the images. As an example, consider the data presented in Figure 4-22 later in this chapter. Images corresponding to this data are also included. Comparing an image of the first step of the experiment, Figure 4-23, to an image of the final step, Figure 4-32, it is clear that total displacement was close to two times the orginal thickness. Thus, final thickness was nearly three times initial, resulting in a logarithmic strain of about 1.1. The calculated strain given is slightly less than 1. In this case, the difference is small, but it does demonstrate the potential of this technique.

Although peak stress values are similar for the macroscale and microscale data, strain at peak stress is very different. In the macroscopic data, peak stress occurs around a strain of 0.1. In the microscopic data, peak stress occurs closer to a strain of 0.25. This is due to a combination of fixture slackness and motor speed variation.

In general, data on the macroscopic level is repeatable, but there is significant data scatter on the microscopic level. Table 4.1, which displays peak stress and the associated strain values for several microscopic through-thickness tension tests, clearly

shows this scatter.

Data scatter in the microscopic tests has a variety of causes. The various causes and estimated magnitude of error resulting from each is discussed in Appendix A.

4.3 Microscale Images

Figures 4-4 through 4-21 are images of Triplex loaded in through-thickness tension. The first set of images, Figures 4-4 through 4-13, show loading in the MD-ZD plane, referred to here simply as MD. The second set, Figures 4-14 through 4-21, were taken of the CD-ZD plane, referred to here as CD.

Figure 4-4 shows Triplex MD at no load. In Figure 4-5, the paperboard is subject to 0.35 MPa of stress, but no noticeable deformation has occurred. A few small cracks, indicated by arrows, have started to form in Figure 4-6. These small cracks are called microcracks and form primarily along the interfaces between the five layers of Triplex paperboard. In Figures 4-7 through 4-8, the cracks are growing. In Figure 4-9, we can see several cracks along an interface near the center of the board. These small cracks combine to form a large crack, called a macrocrack, as seen in Figure 4-10. Through the remaining images, this crack grows while others relax and close up slightly. Relaxation is most noticeable in the large crack at the lower left of the images.

Figure 4-13 shows the entire specimen at the end of the test. The macrocrack has propagated through the entire specimen. As macrocracks typically form along interfaces between layers, a growing crack causes delamination, or separation of layers. Recall from Chapter 2 that there are four layer interfaces in Triplex. Two are between a chemical pulp layer and a mechanical pulp layer, and two are between two mechanical pulp layers. Interfaces between two mechanical pulp layers are usually weaker than those between a chemical pulp and a mechanical pulp layer. Thus, failure by delamination usually occurs at an interface between mechanical pulp layers. These are the two innermost interfaces, which is why the failure of this specimen appears to occur near its center.

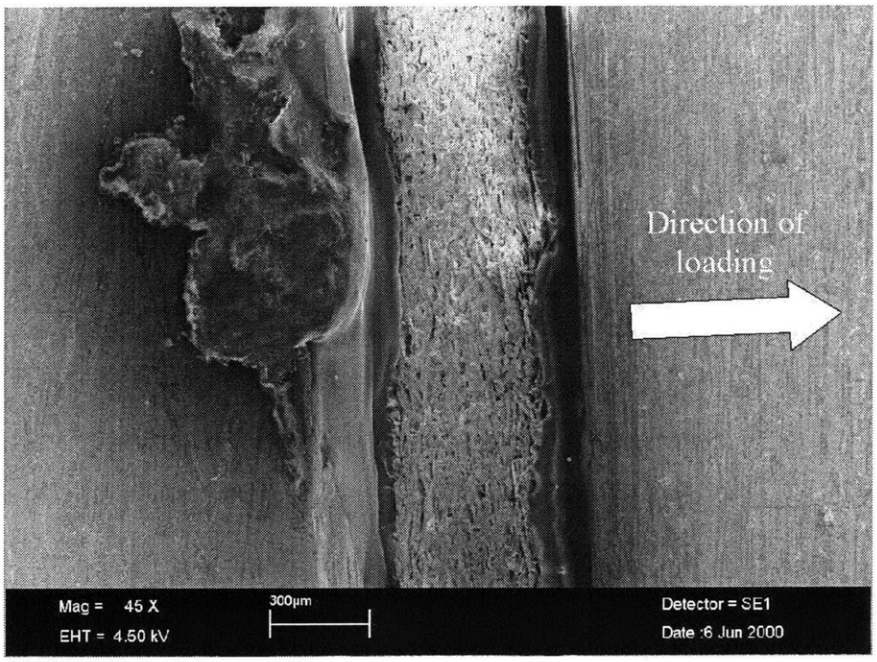

Figure 4-4: Triplex MD through-thickness tension test at no load (Step 1).

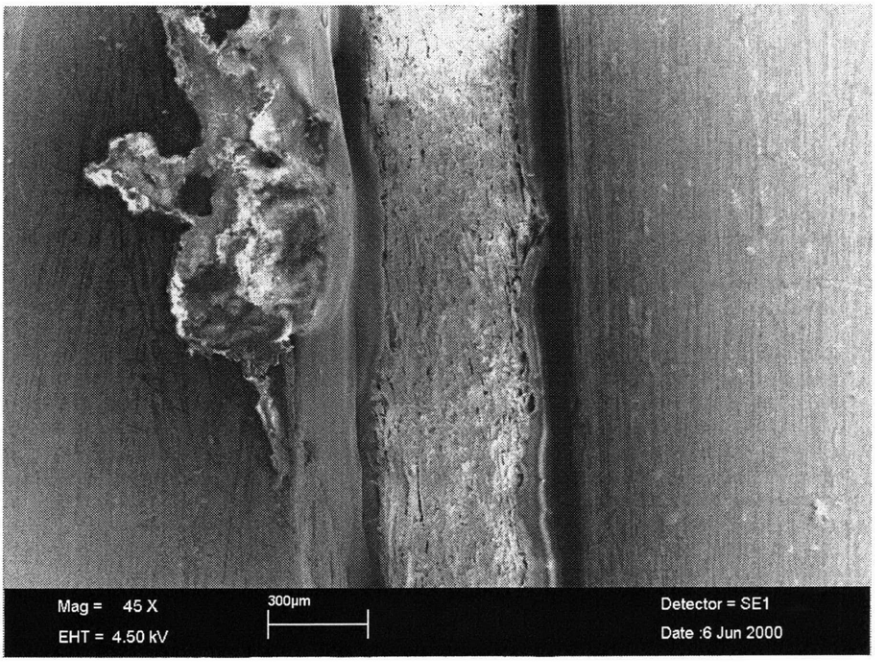

Figure 4-5: Triplex MD through-thickness tension test at 0.36 MPa (Step 2).

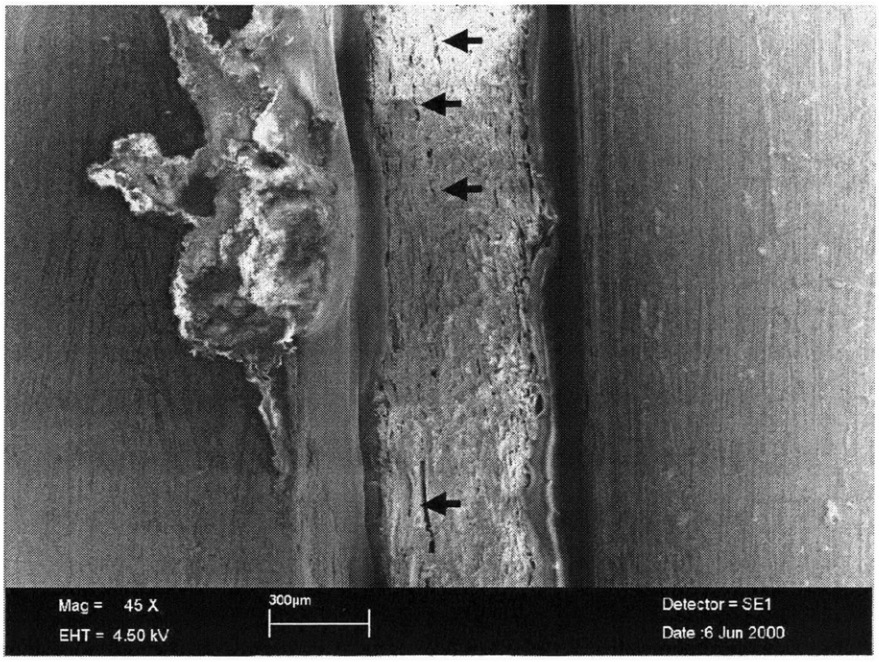

Figure 4-6: Triplex MD through-thickness tension test at 0.39 MPa (Step 3). Arrows indicate microcrack formation.

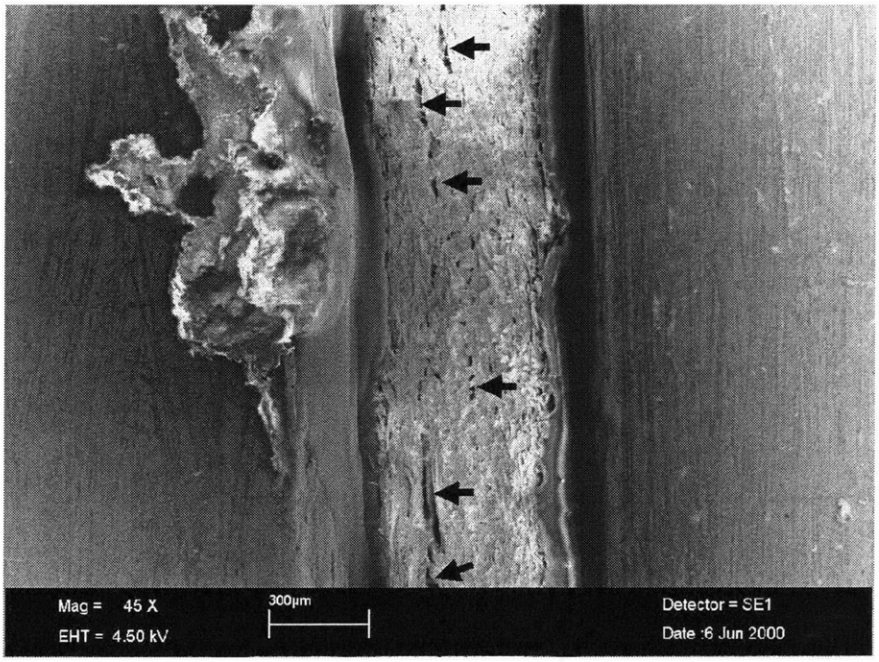

Figure 4-7: Triplex MD through-thickness tension test at 0.35 MPa (Step 4). Arrows indicate growing microcracks.

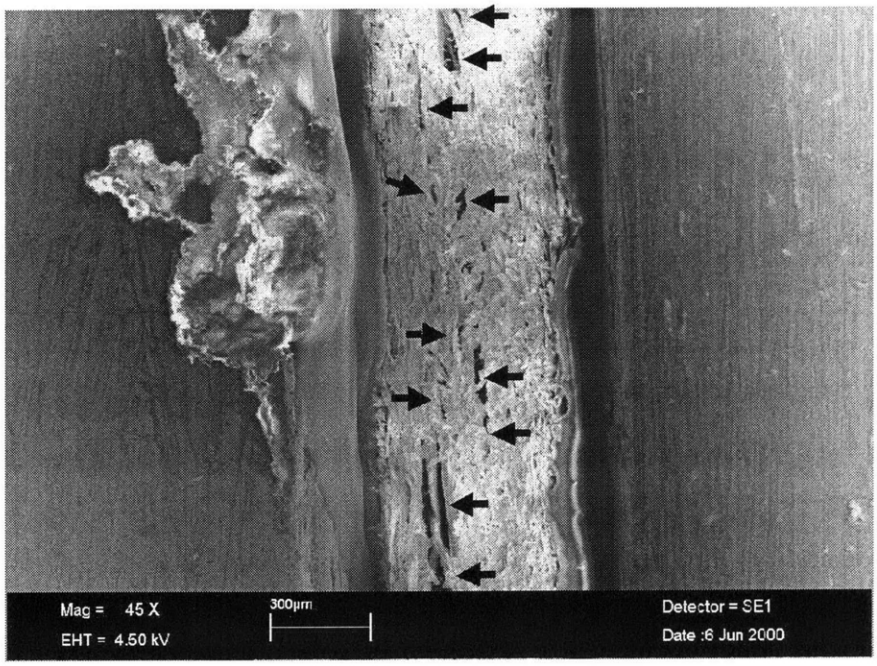

Figure 4-8: Triplex MD through-thickness tension test at 0.24 MPa (Step 5). Arrows indicate growing microcracks.

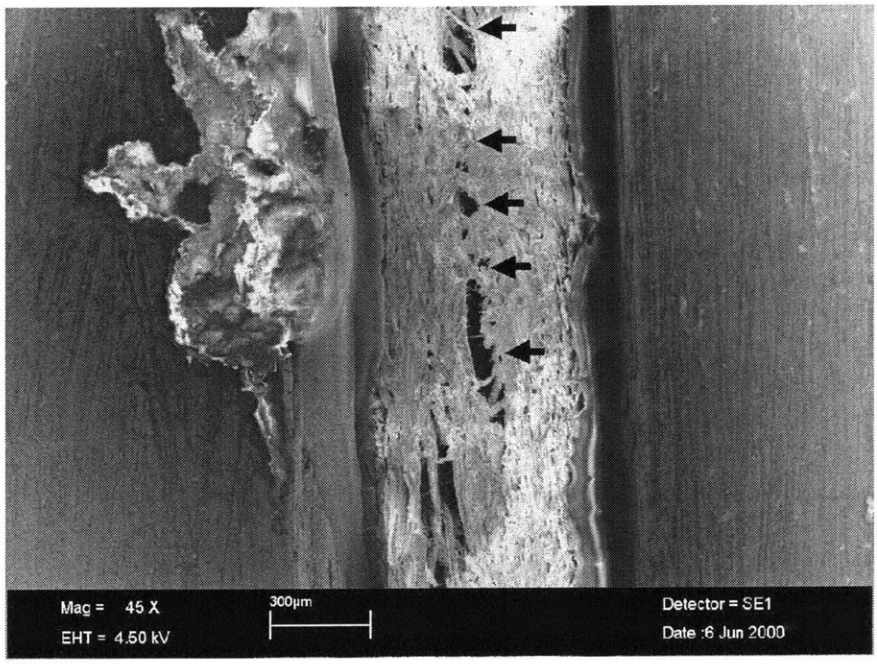

Figure 4-9: Triplex MD through-thickness tension test at 0.21 MPa (Step 6). Arrows indicate cracks beginning to coalesce along one interface.

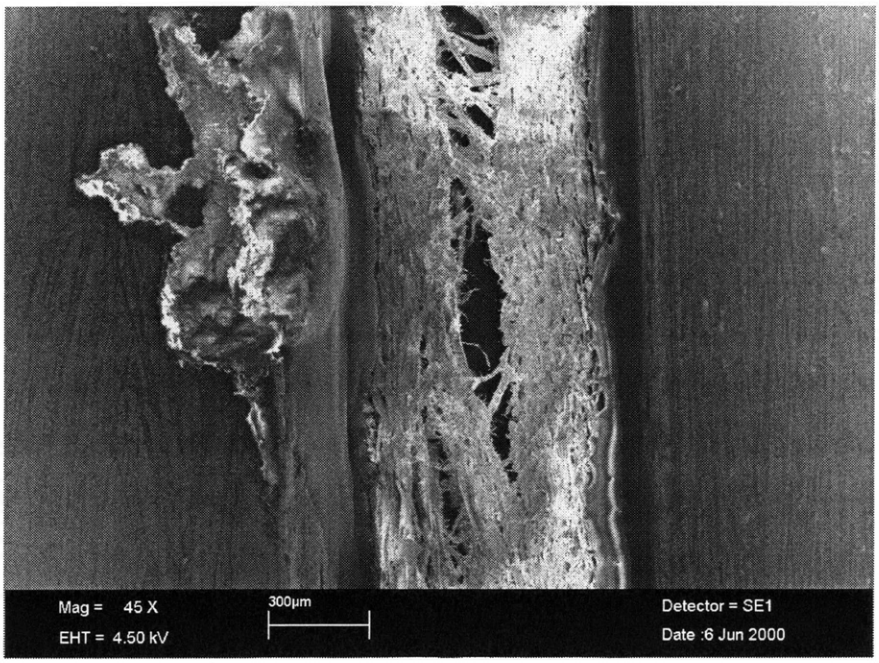

Figure 4-10: Triplex MD through-thickness tension test at 0.18 MPa (Step 7).

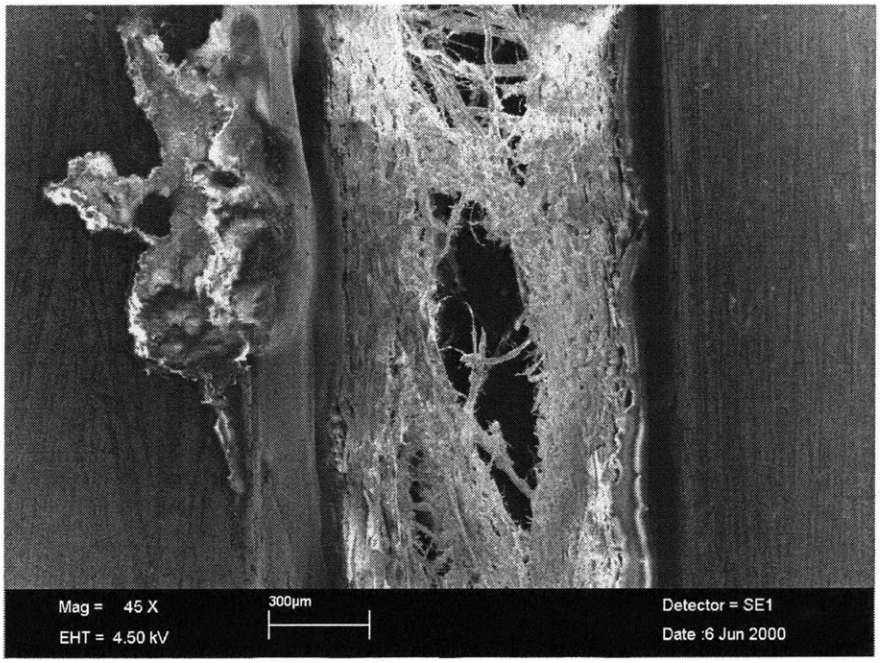

Figure 4-11: Triplex MD through-thickness tension test at 0.17 MPa (Step 8).

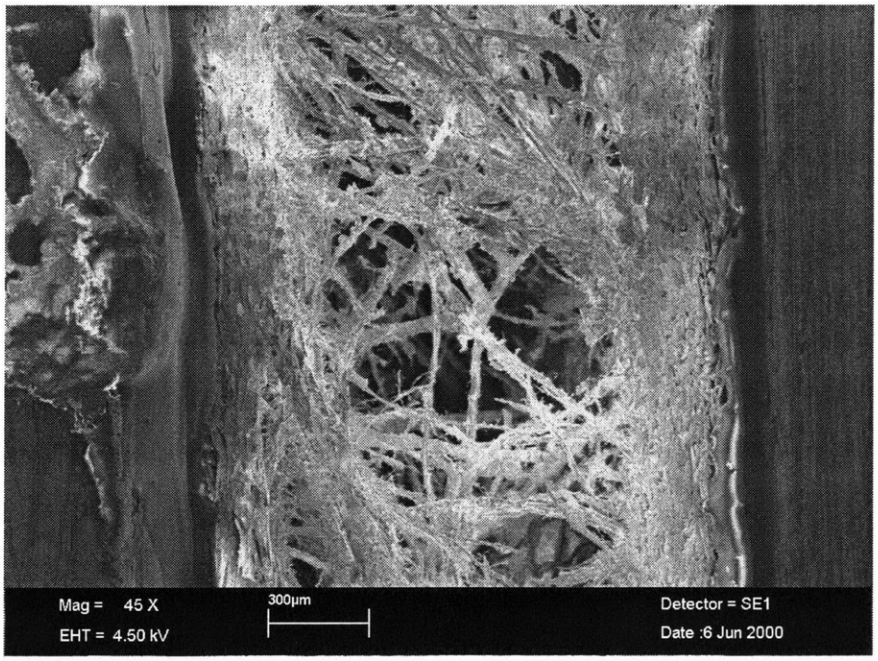

Figure 4-12: Triplex MD through-thickness tension test at 0.05 MPa (Step 9).

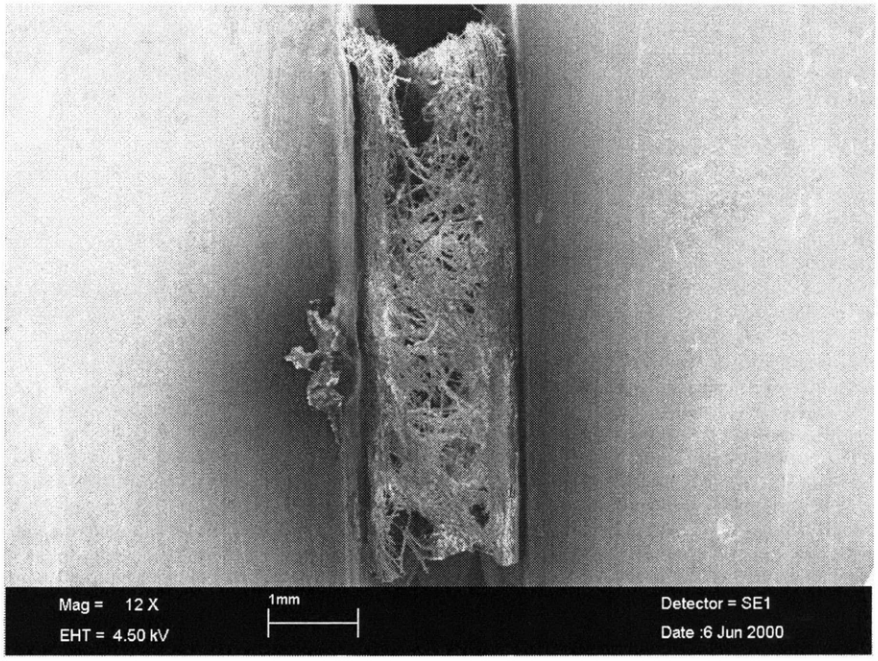

Figure 4-13: Full view of Triplex MD through-thickness tension test at 0.05 MPa (Step 9).

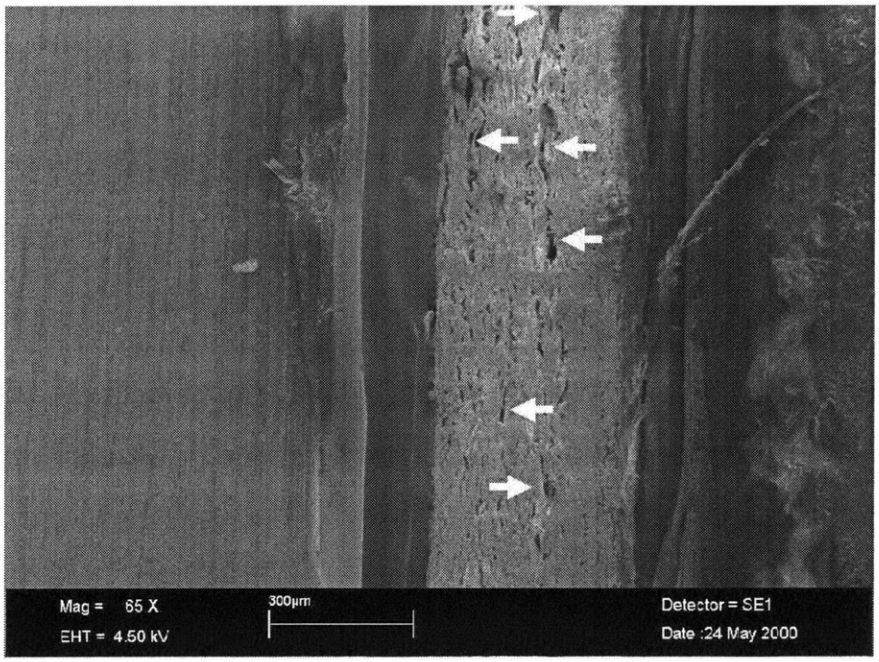

Figure 4-14: Triplex CD through-thickness tension test at no load (Step 1). Arrows indicate preexisting flaws in the material.

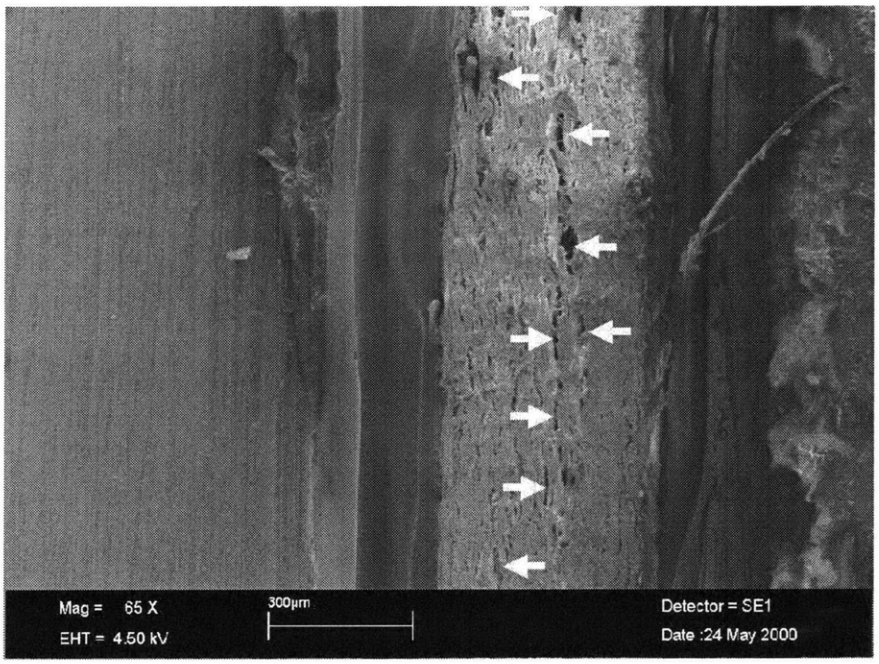

Figure 4-15: Triplex CD through-thickness tension test (Step 2). Arrows indicate microcracks forming at flaws in the material.

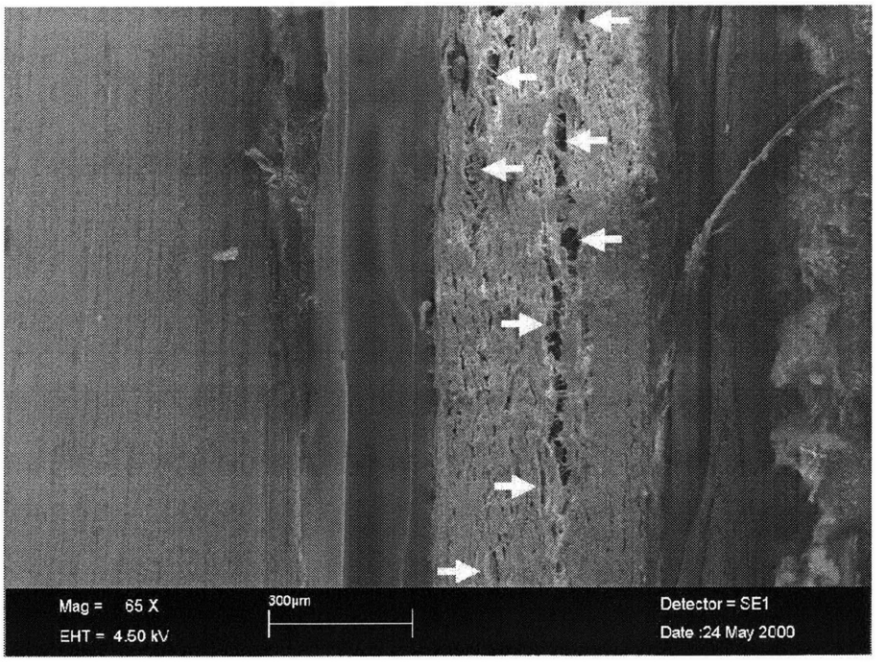

Figure 4-16: Triplex CD through-thickness tension test (Step 3). Arrows indicate growing microcracks.

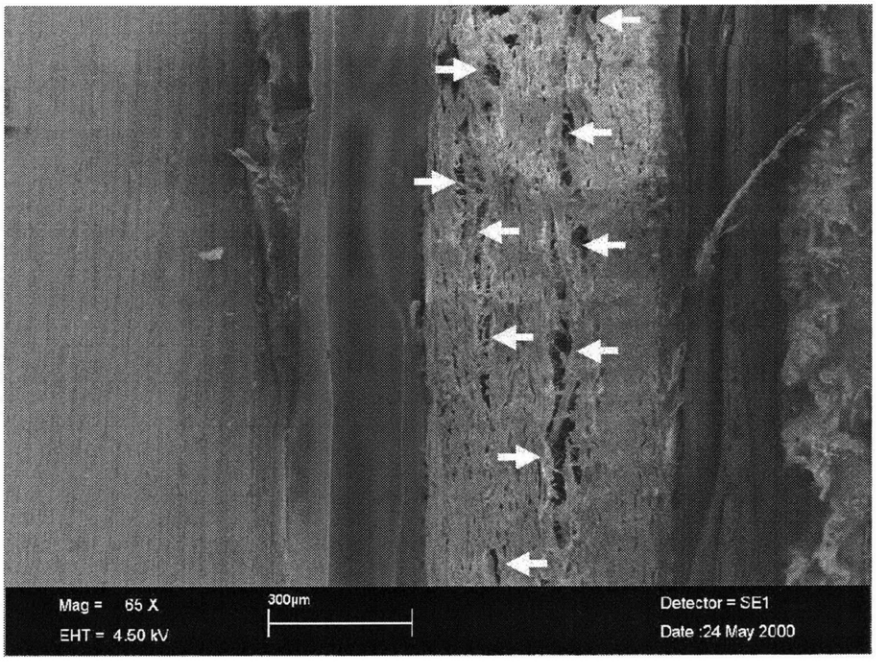

Figure 4-17: Triplex CD through-thickness tension test (Step 4). Arrows indicate growing microcracks.

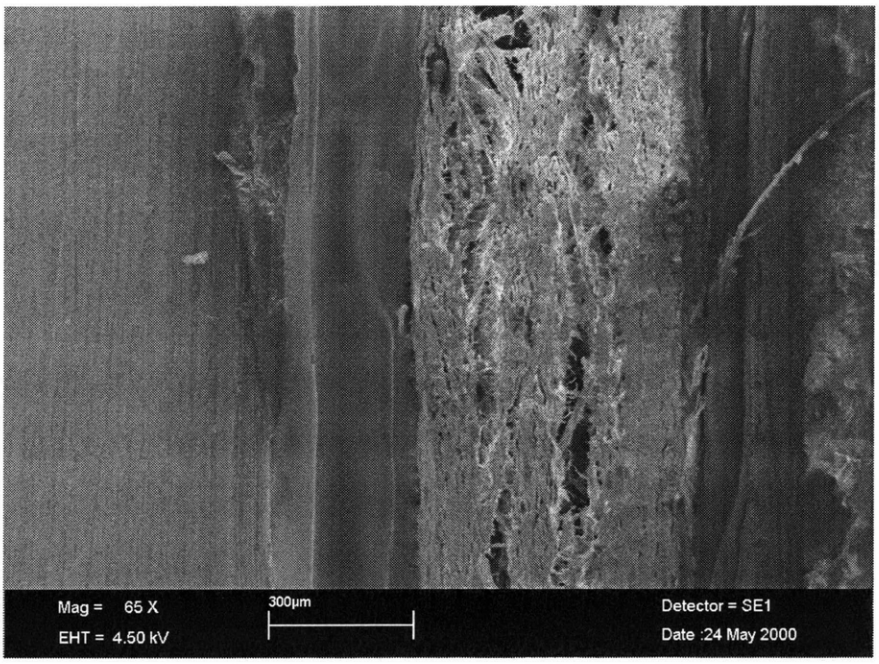

Figure 4-18: Triplex CD through-thickness tension test (Step 5).

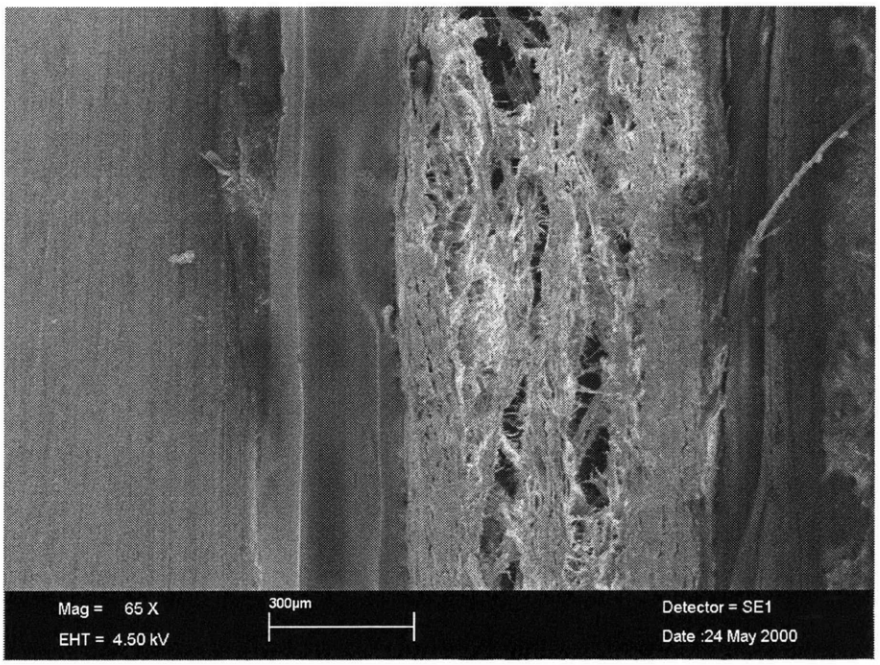

Figure 4-19: Triplex CD through-thickness tension test (Step 6).

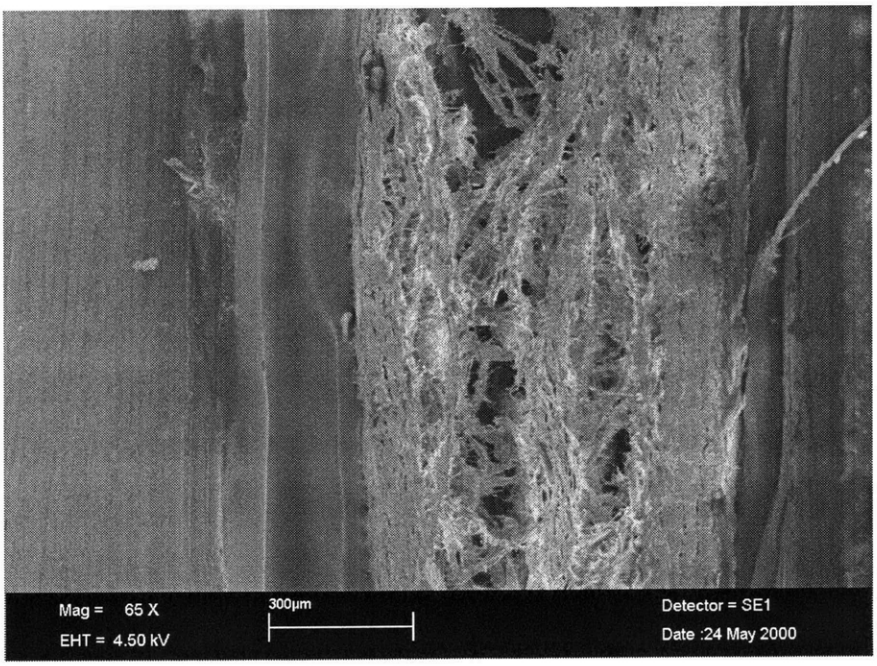

Figure 4-20: Triplex CD through-thickness tension test (Step 7).

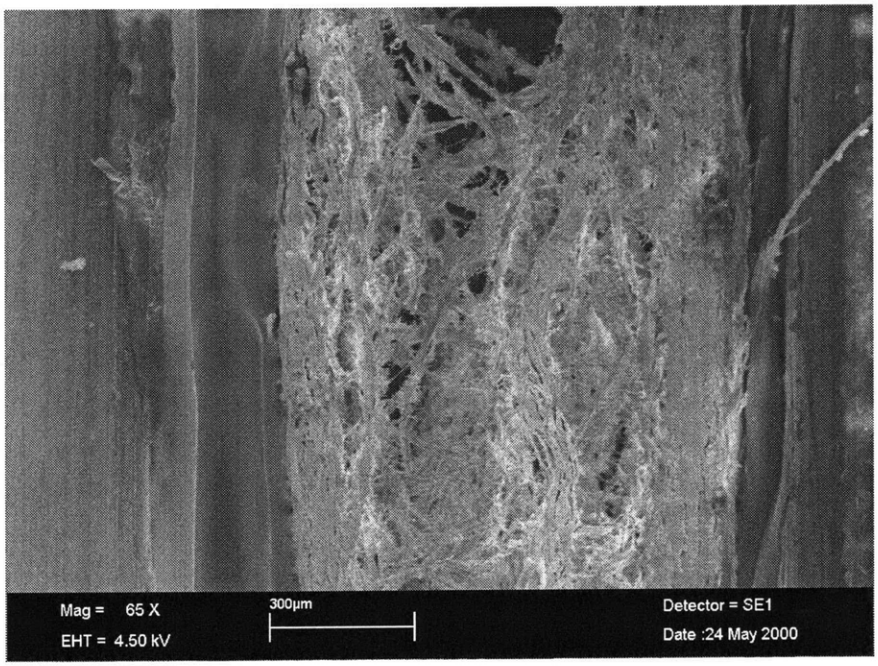

Figure 4-21: Triplex CD through-thickness tension test (Step 8).

Individual fibers can be seen bridging the gap between layers in Figure 4-13; these fibers were woven into both layers as the layers were formed and compacted during rolling. The area near the center of the specimen seems slightly brighter than the surrounding material; this is the area shown in the higher magnification images. Long exposure to the electron beam caused some charging in this area, creating the brightness.

Comparing MD and CD images, the difference in surface appearance between MD and CD is immediately apparent. In the CD plane, pre-existing flaws are easier to see. In Figure 4-14, Triplex CD at no load, pre-existing flaws are indicated with white arrows. In the next image, Figure 4-15, load has been applied and small cracks have started to form at those flaws. Microcracks form preferentially at weak points in the material. As mentioned previously, these points are typically along the interfaces between layers.

Growing cracks in Figures 4-16 and 4-17 are indicated by white arrows. Further growth is seen in Figures 4-18 and 4-19. In the latter of these images, it appears that cracks to the left of center of the specimen are beginning to coalesce. In the last two images, Figures 4-20 and 4-21, the macrocrack near the left side is very clear. As this specimen was not deformed far beyond macrocrack formation, very minimal amounts of relaxation in other cracks are seen.

4.4 Microscale Data and Image Comparison

To facilitate understanding of what mechanisms the different regions of the stress-strain curve represent, sets of data and images were taken concurrently. Figure 4-22 is an example of a stress-strain curve correlated with microscope images. The position on the curve where each image was taken is indicated by its step number. Near each of the image points, the curve drops sharply and recovers. This is due to relaxation. To take an image, separation of the grips is paused for about a minute. During this time the material will relax through load transfer at the bonds or through the growth of small cracks. Relaxation is most pronounced when due to crack growth.

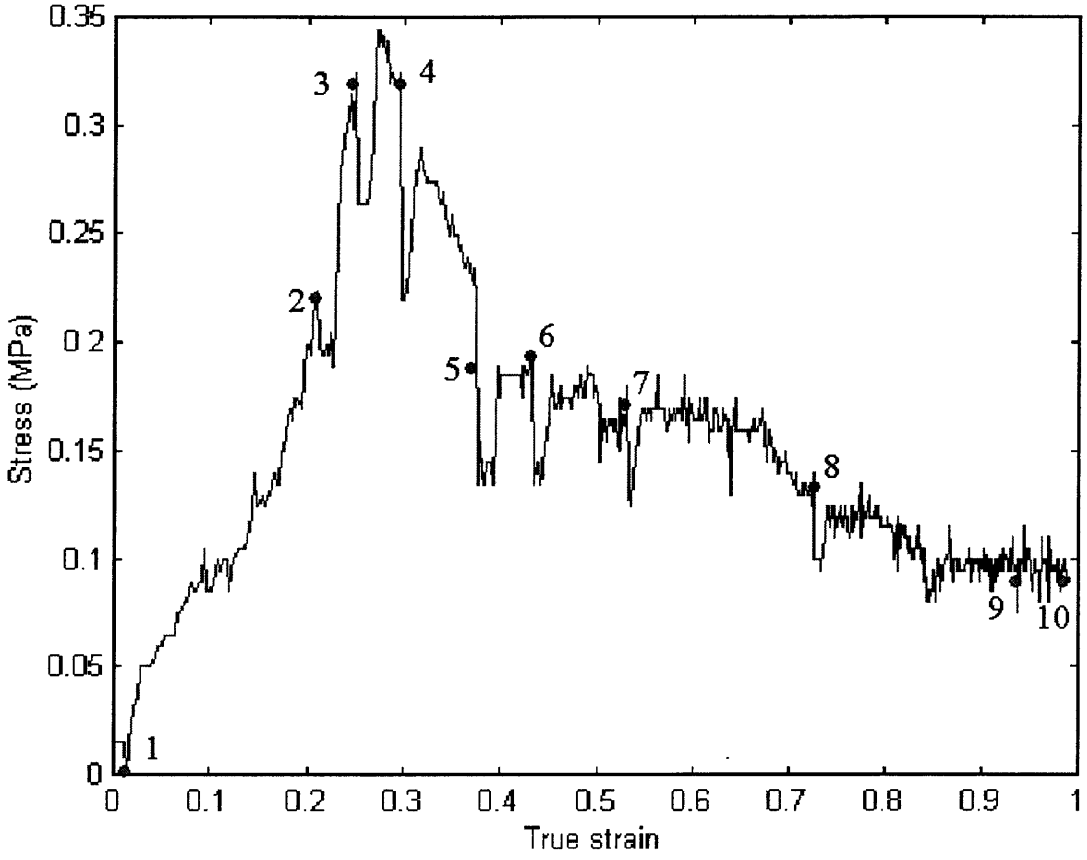

Figure 4-22: Microscopic through-thickness tension data correlated with micrographs.

Figure 4-23 shows the paperboard, viewed in the MD plane, at no load. This corresponds to point 1 on the curve. Step 2, shown in Figure 4-24, is in the region of linearly increasing stress. Very little difference is observed in the micrographs between steps 1 and 2. Although it is possible that there are some damage mechanisms active in this pre-peak region, their physical effects are too small to be seen in any of the images presented here. Steps 3 and 4 are both near the peak in stress, with step 3 being immediately before the peak and step 4 being immediately following it. Figure 4-25, the corresponding image for step 3, does not noticeably differ from the images taken at steps 1 and 2. However, in step 4, we see microcrack formation. Other tests have displayed similar behavior, indicating that the peak in stress correlates with the beginning of microcrack formation at pre-existing weak points in the material.

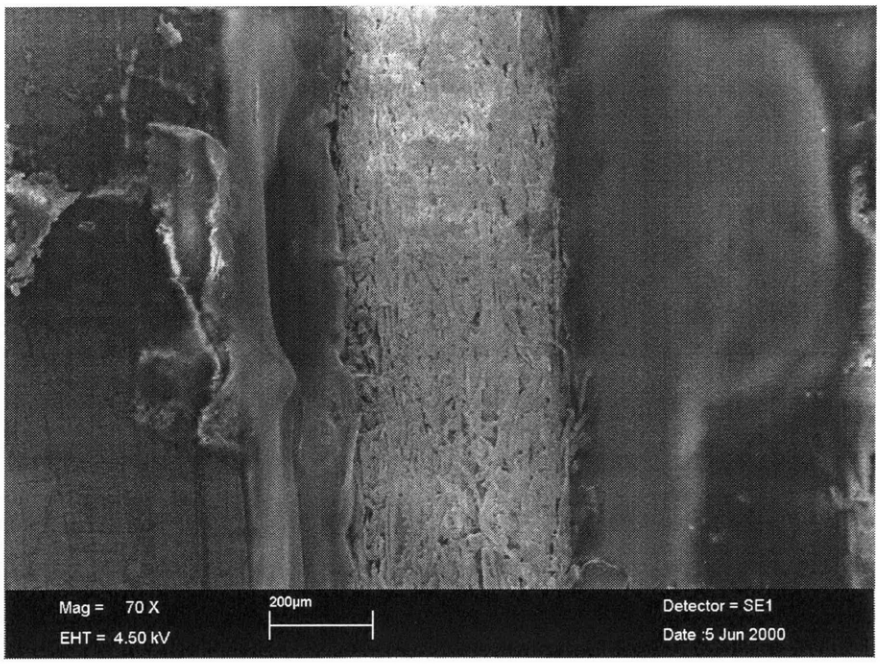

Figure 4-23: Triplex MD through-thickness tension image correlated with stress-strain data (Step 1).

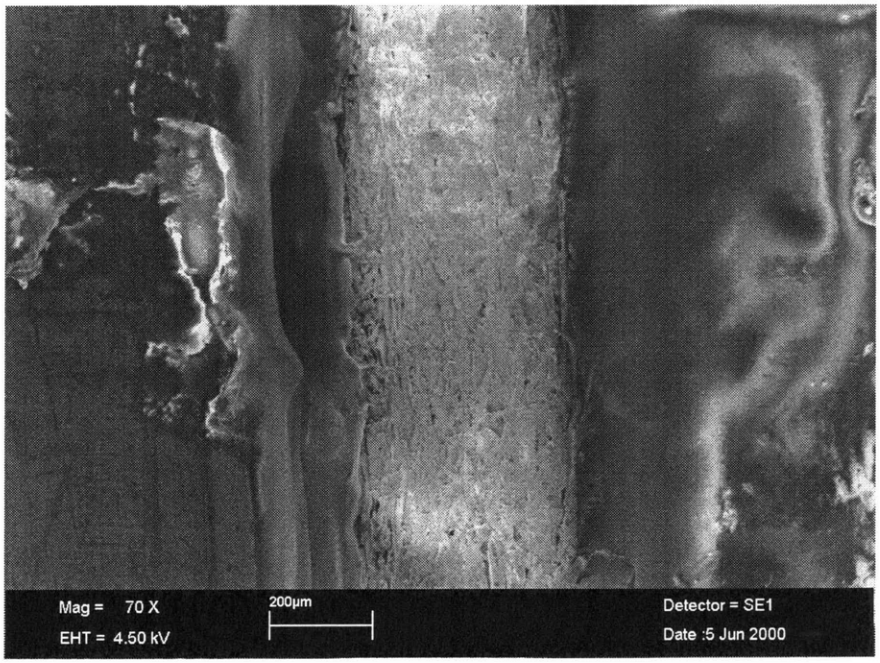

Figure 4-24: Triplex MD through-thickness tension image correlated with stress-strain data (Step 2).

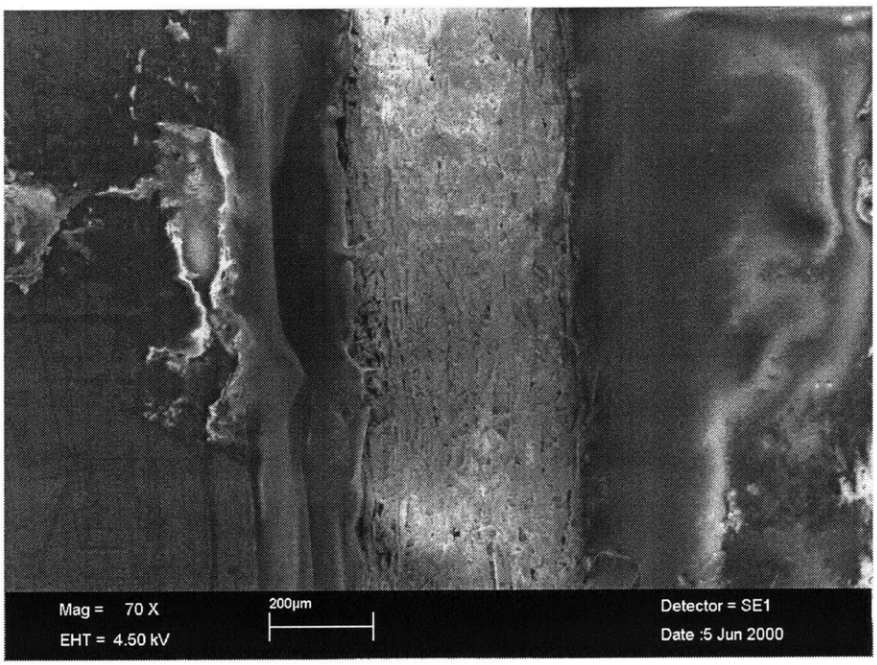

Figure 4-25: Triplex MD through-thickness tension image correlated with stress-strain data (Step 3).

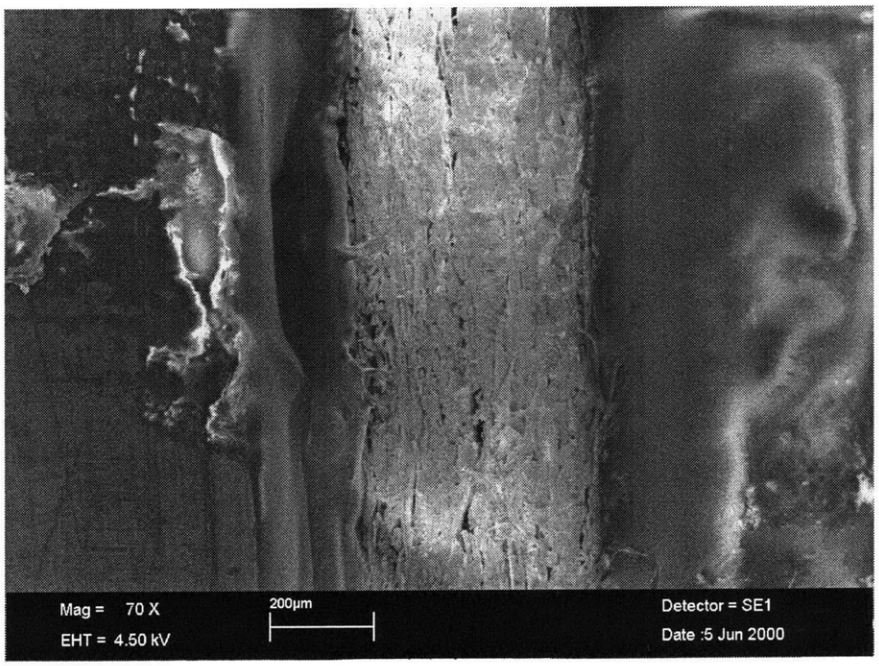

Figure 4-26: Triplex MD through-thickness tension image correlated with stress-strain data (Step 4).

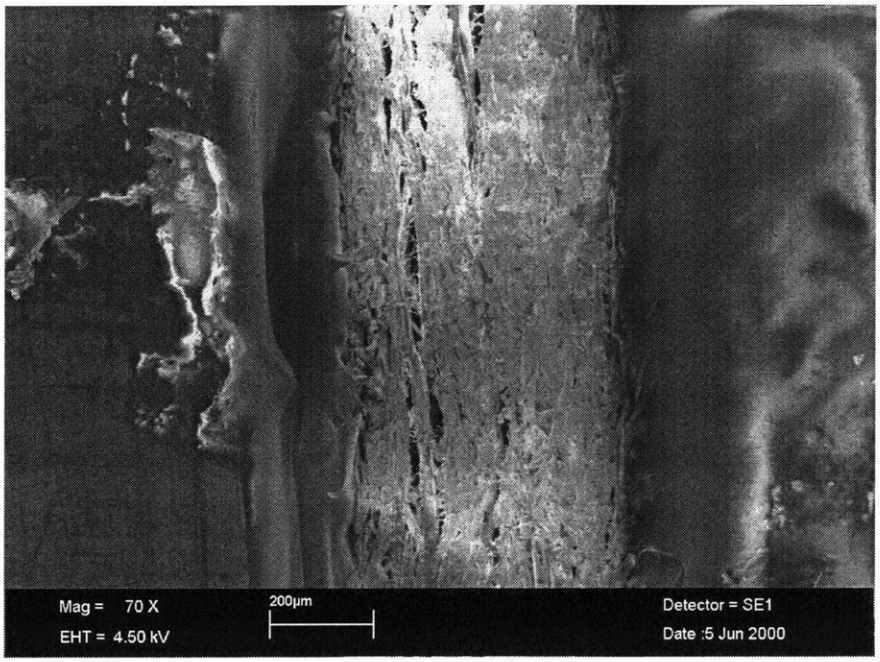

Figure 4-27: Triplex MD through-thickness tension image correlated with stress-strain data (Step 5).

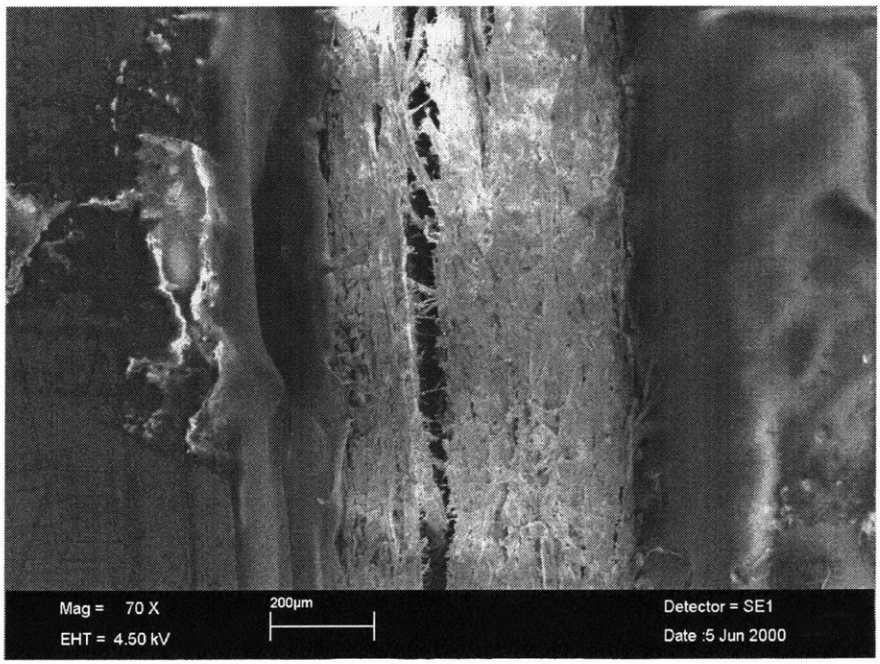

Figure 4-28: Triplex MD through-thickness tension image correlated with stress-strain data (Step 6).

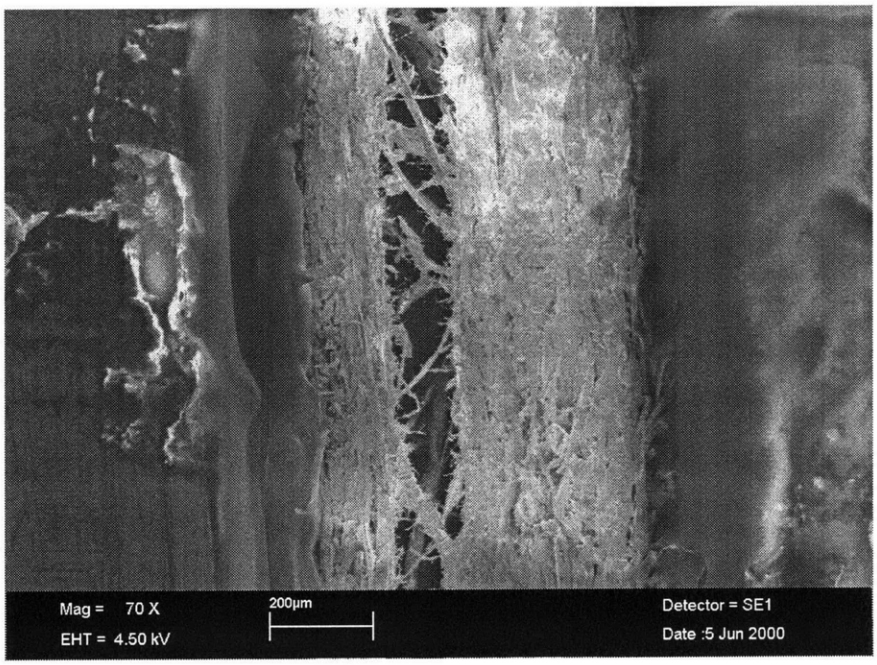

Figure 4-29: Triplex MD through-thickness tension image correlated with stress-strain data (Step 7).

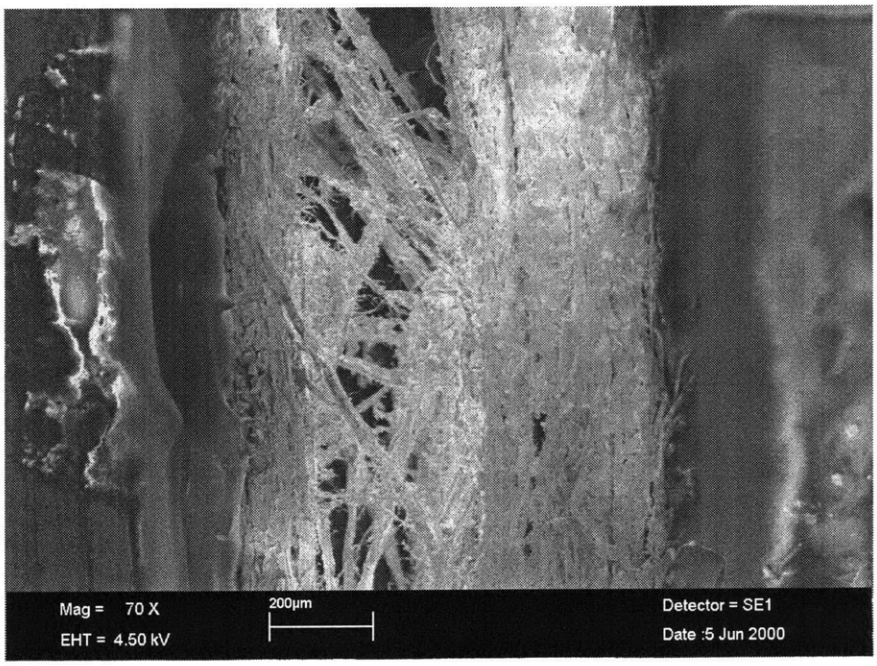

Figure 4-30: Triplex MD through-thickness tension image correlated with stress-strain data (Step 8).

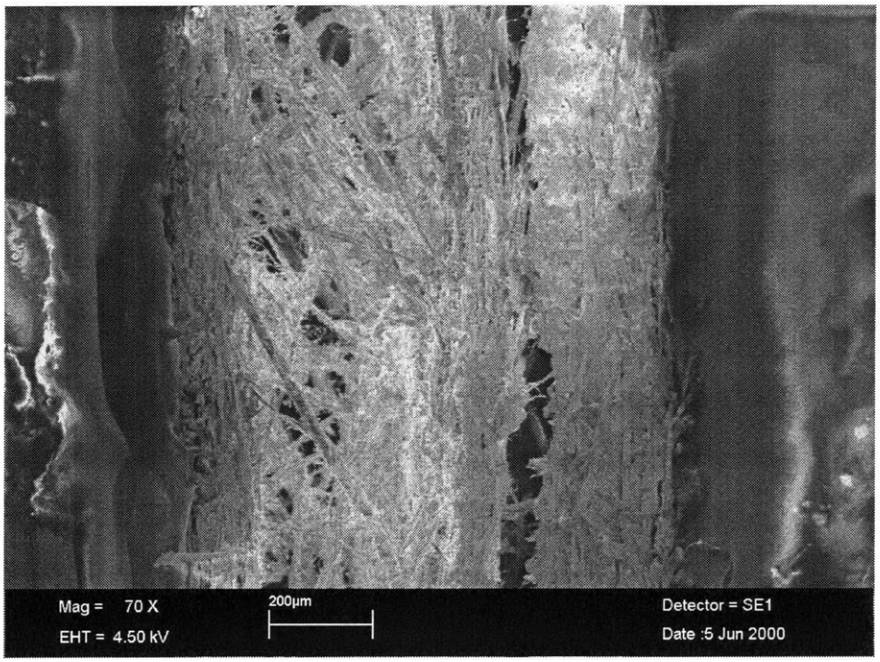

Figure 4-31: Triplex MD through-thickness tension image correlated with stress-strain data (Step 9).

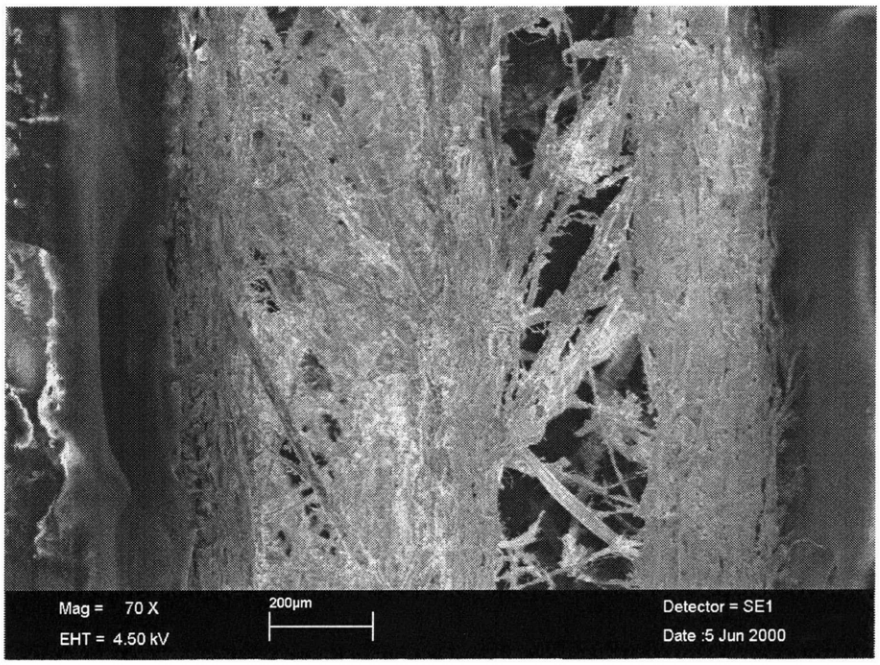

Figure 4-32: Triplex MD through-thickness tension image correlated with stress-strain data (Step 10).

Beyond step 4, the stress falls as microcracks grow. The stress plotted here is nominal stress, load applied divided by initial load-bearing area. A growing crack decreases the load bearing area of the material and consequently the load necessary to continue deformation. The global stress calculation incorporates the decrease in load but not the decrease in effective area. Thus, the global stress measure falls with load.

This particular stress-strain curve is somewhat unusual in the post-peak region. The stress decreases and then levels off around step 6. However, just before step 8, the stress begins to drop significantly again, leveling off to a plateau between steps 8 and 9. Most curves feature only one plateau region. The deformation images show that in this case, two plateaus are to be expected. The same mechanism is active at each plateau and has also been observed in the plateau regions of tests that exhibited only a single plateau. As the stress drops after step 4, the microcracks grow. The growing cracks are shown in Figure 4-27, and correspond to step 5. In steps 6 and 7, the crack to left of center has clearly become the dominant macrocrack. Stress levels off as one crack becomes dominant. The crack has propagated through most or all of the material, so there is no further change in load-bearing area. The residual strength is due to the load necessary to disengage the fibers stretching out across the macrocrack.

This process repeats, beginning between steps 7 and 8. A small crack begins growing, observable to the right of the dominant crack in Figure 4-30, an image of step 8. Again, stress levels out between steps 8 and 9; in the image of step 9, the crack on the right has grown to be a macrocrack. This crack grows further by step 10, and the bridging fibers that cause residual strength are observable. This specimen experienced two essentially complete delaminations, one on each mechanical-mechanical interface. Although only one delamination is commonly observed, the mechanisms involved are the same.

In summary, no significant change in material structure occurs before the peak in stress. At the peak, microcracks begin to form. This decreases the effective load-carrying area of the material. However, the stress measure is nominal stress and

is based on the original load-carrying area. Thus, the drop in effective area causes a drop in stress. Stress continues to decrease as the microcracks grow. As one crack becomes dominant, stress values level off. The dominant crack has caused delamination through most or all of the specimen's cross section, so no further gross reduction in load-carrying area occurs. Beyond this point, stress decreases very slowly as the fibers bridging the delaminated gap are disengaged. At very large strains, all of the fibers would disengage and the stress would fall to zero. As fibers measure roughly 3 mm in length, total displacement would be on the order of millimeters for complete disengagement to occur.

Chapter 5

Out-of-Plane Compression Experimental Results

The results of through-thickness compression experiments are presented in this chapter. Macroscopic level observations of stress-strain behavior show an initial linear response followed by stiffening and plasticity. Images taken at the microscopic level indicate deformation mechanisms corresponding to the behaviors observed at the macroscopic level.

5.1 Macroscopic Results

Stress-strain data for Triplex loaded in uniaxial through-thickness compression at the macroscopic level is presented in Figure 5-1. The stress values shown here and throughout this chapter are nominal stress value, as used in Chapter 4. Strain values are true strain, also as in Chapter 4.

At small strains, below about 2.5%, the material behaves linearly. At small strains, Triplex has a similar stiffness in compression as in tension. The modulus here is about 9 MPa, only slightly larger than that meausured in tension. Beyond 2.5% strain, the stiffness increases and material behavior becomes nonlinear. In this region, stress increases exponentially with strain.

Figure 5-2 shows Triplex through-thickness compressive behavior at larger strains,

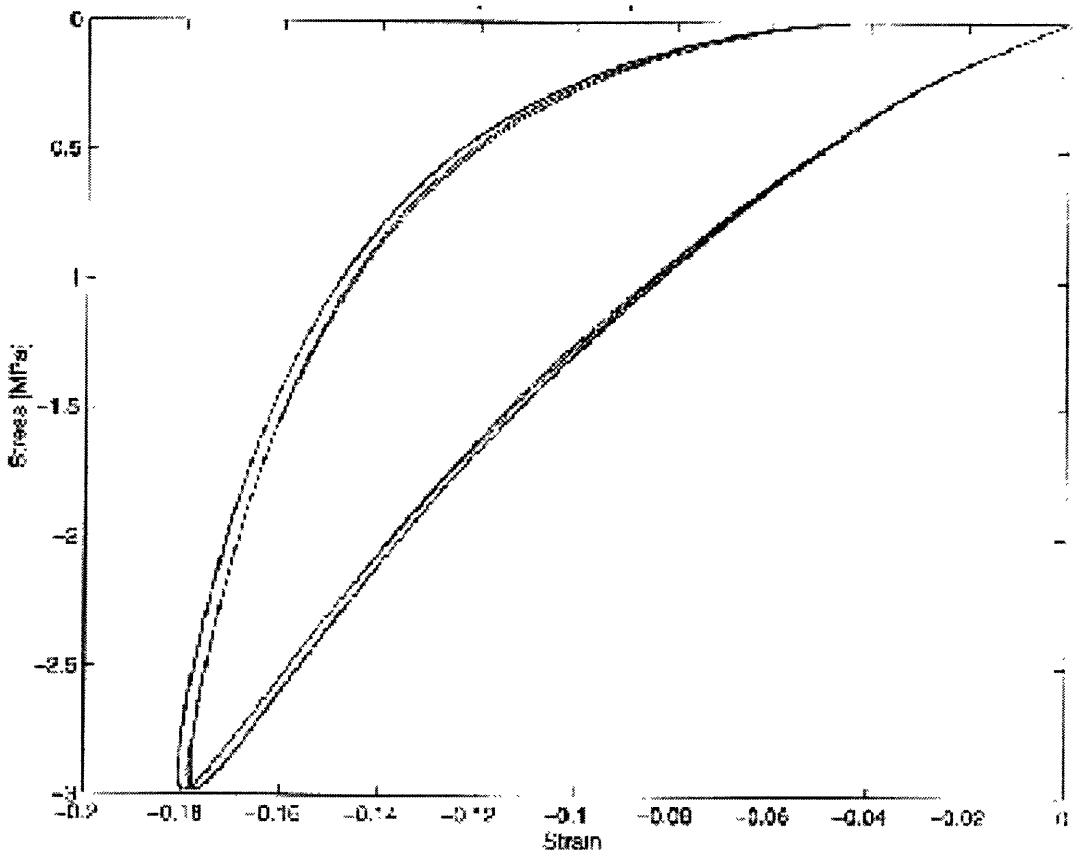

Figure 5-1: Macroscopic stress-strain data for loading in uniaxial through-thickness compression (Courtesy of N. Stenberg).

up to 50%. This curve more clearly shows the exponential relationship between stress and strain in the nonlinear region. It also provides information about the rate of plastic strain accumulation, as it presents data for three subsequent loadings and unloadings, each one to a greater total strain. The increment in total strain was about 10% each time the material was reloaded. The increment in plastic strain at the first reloading was only about 6%. At the second reloading, the plastic strain increases by closer to 16%. Accumulation of plastic strain has a nonlinear relationship with total strain.

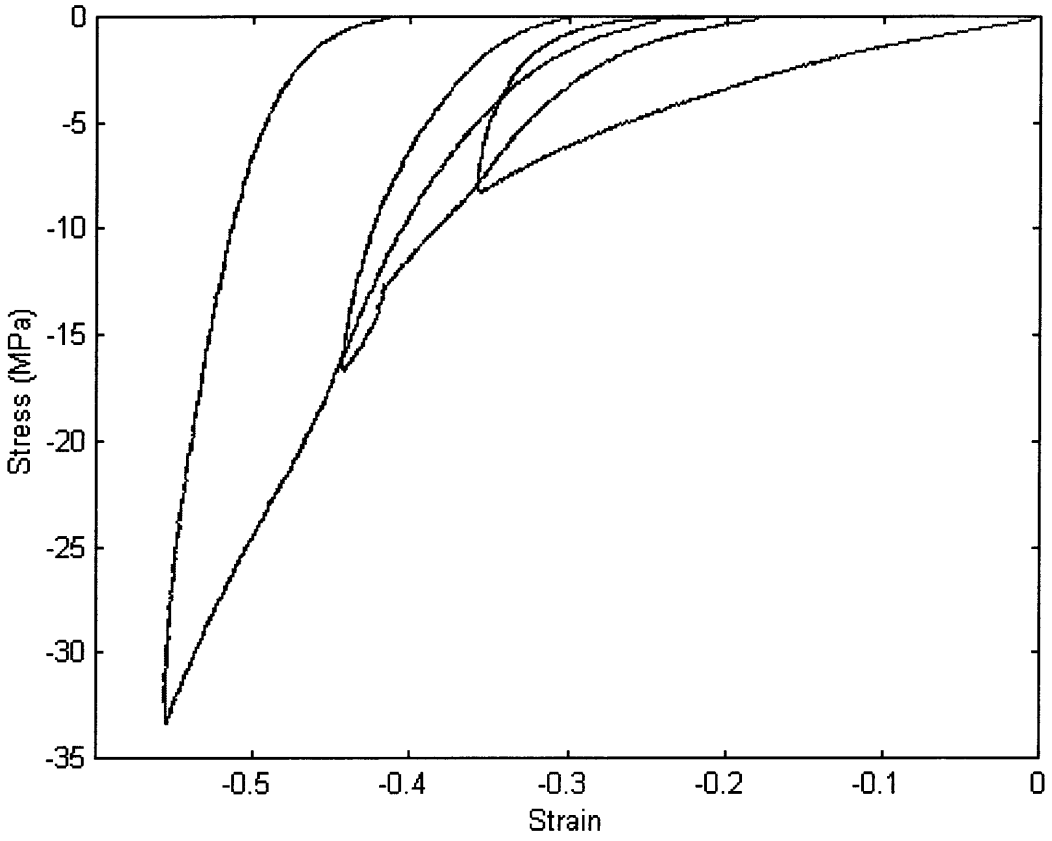

Figure 5-2: Macroscopic stress-strain data for alternate loading in uniaxial through-thickness compression (Courtesy of N. Stenberg).

5.2 Microscopic Results

Microscopic data for through-thickness compression is not presented. As Triplex is very stiff in compression, the loads created during microscale compression testing were out of range for the load cell except at very small strains. The images presented here span an estimated compressive strain range of only 0 to -10%. However, these images are sufficient for the current study, as this strain range is comparable to that experienced by the board during the punching step of creasing. Beyond this point, the stepper motor had difficulty producing sufficient force to continue displacement. The exact stress values that the material in the images was loaded to are not available due to the limitations of the load cell.

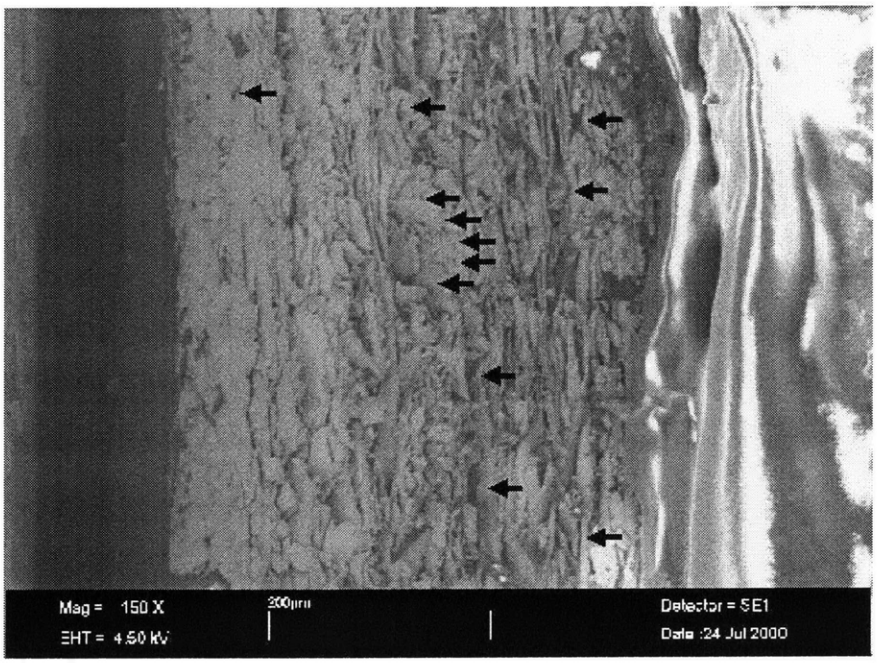

Figure 5-3: Triplex MD through-thickness compression test at no load (Step 1).

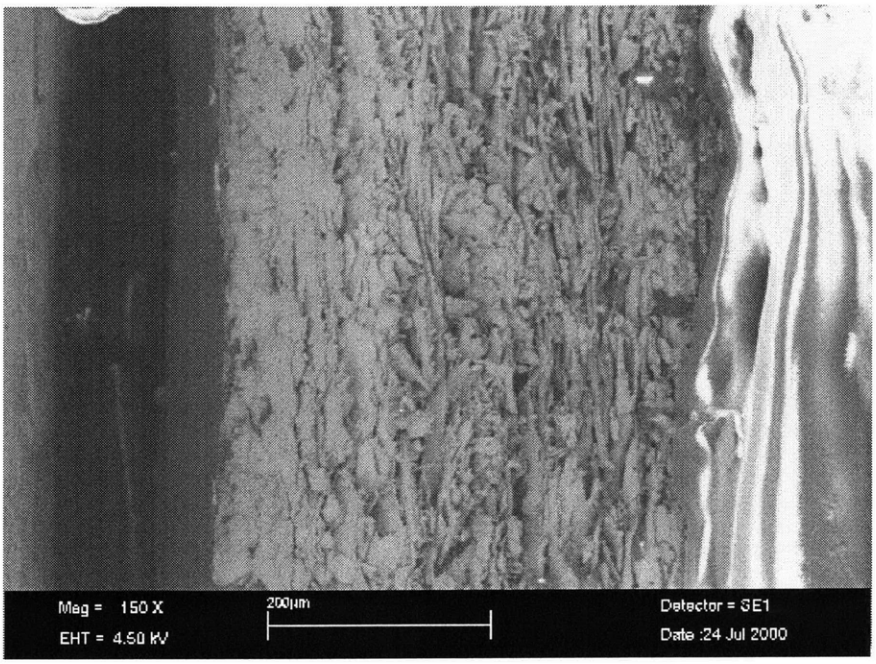

Figure 5-4: Triplex MD through-thickness compression test (Step 2).

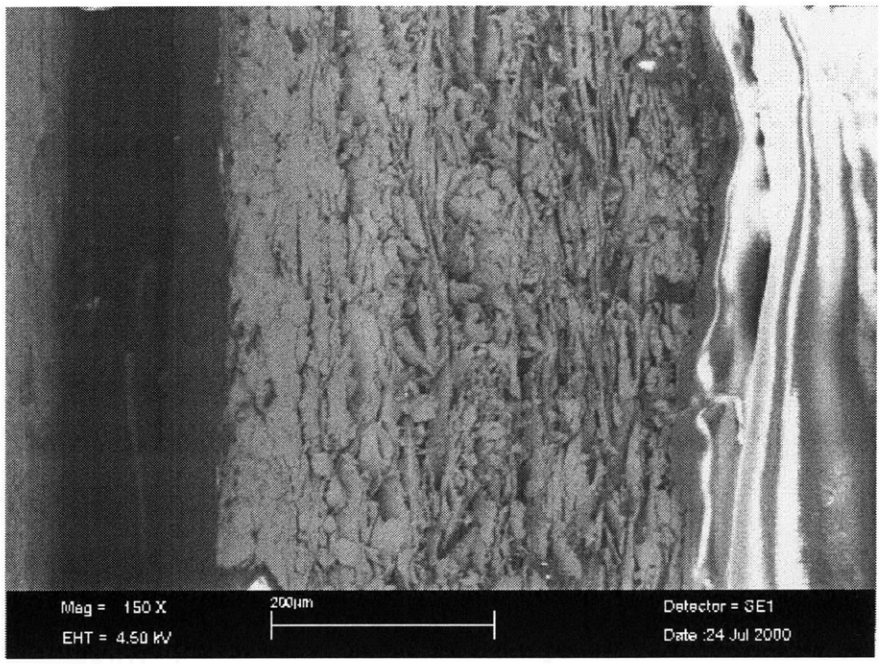

Figure 5-5: Triplex MD through-thickness compression test (Step 3).

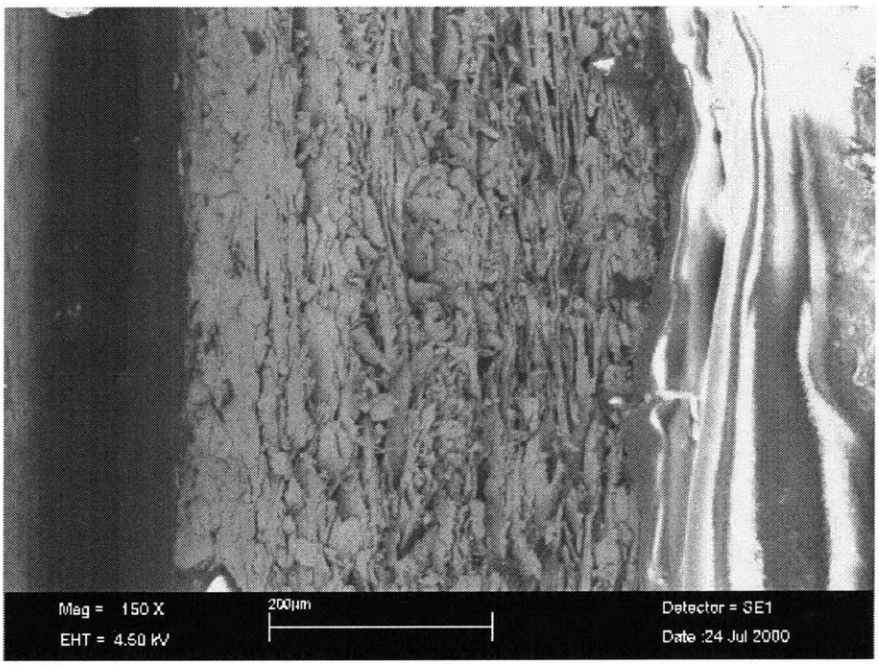

Figure 5-6: Triplex MD through-thickness compression test (Step 4).

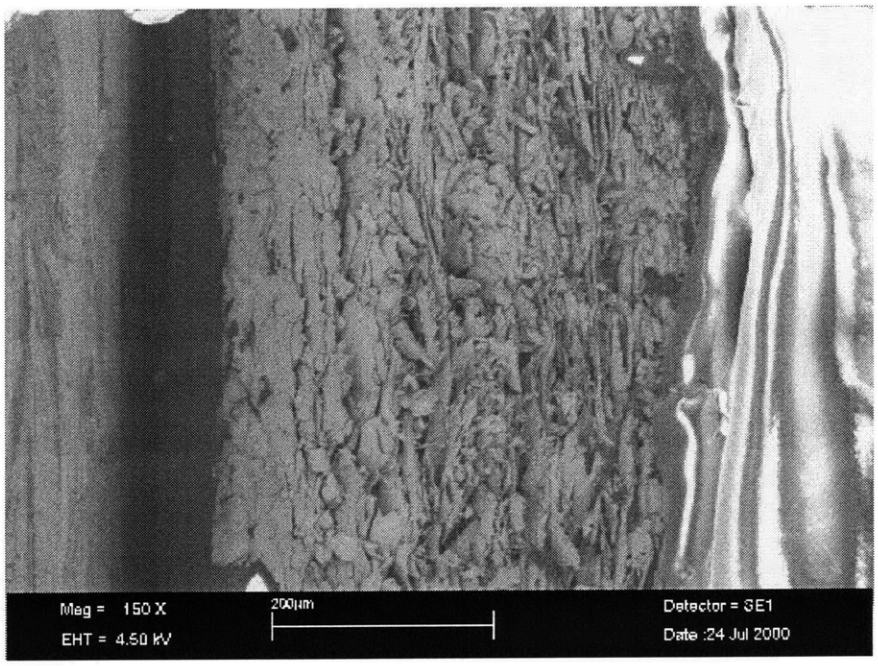

Figure 5-7: Triplex MD through-thickness compression test (Step 5).

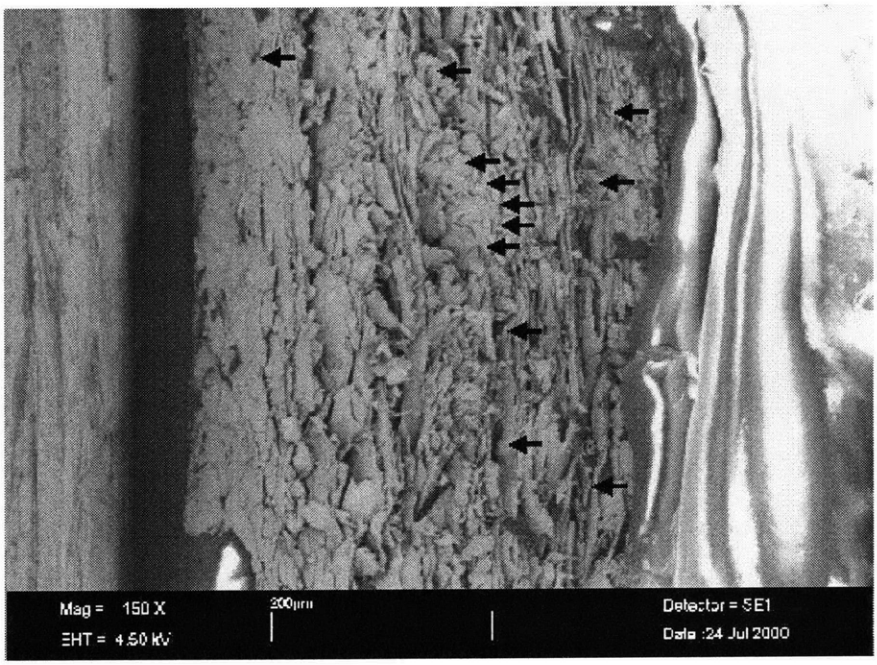

Figure 5-8: Triplex MD through-thickness compression test (Step 6).

Out-of-plane compression in the machine direction is pictured in Figures 5-3 through 5-8. The arrows in the first image indicate features that are easily identified in the subsequent images. These features are pointed out again with arrows in the last image. Observation of these features reveals that compressive deformation in paperboard is very heterogeneous. Some of the indicated features are compressed in the Z direction during the test. One such example is the small gap in material indicated near the upper right corner of the frame in Figure 5-3. Others actually widen slightly, like the fiber cross section indicated near the top center of the frame. Some features show no significant change. This is the case for the gap in material pointed out near the top left of the frame. Although it is not shown in these small strain images, the local material areas that sustain compressive deformation can change as a test progresses.

Through-thickness compression in the cross direction is shown in Figures 5-9 through 5-14. Arrows in the first image again indicate features that are easily identified in each of the images. These images show a second mechanism of compressive deformation in Triplex. In the first four steps of the experiment, gaps in material close up under the compressive load. This is particularly observable at fiber cross-sections. In the remaining steps of the experiment, the deformation is sustained both by gaps closing but also by the material between the gaps being compacted. Thus, compression in paperboard happens in two phases, the first being densitification by void elimination and the second being densification plus material compaction.

These images show that compressive deformation in paperboard is extremely heterogeneous in nature. At small displacements, the deformation occurs at gaps in the material which begin to close. As displacements increase, the matrix material begins to compress. However, even at these larger displacements, deformation continues to be heterogenous, with some material being compacted and some actually expanding slightly. Although it was not possible to correlate images and data for through-thickness compression, it is possible to hypothesize based on the information collected. The linear region of the stress-strain curve likely corresponds to the stage of gap closure, before any significant deformation of the matrix material. The transition

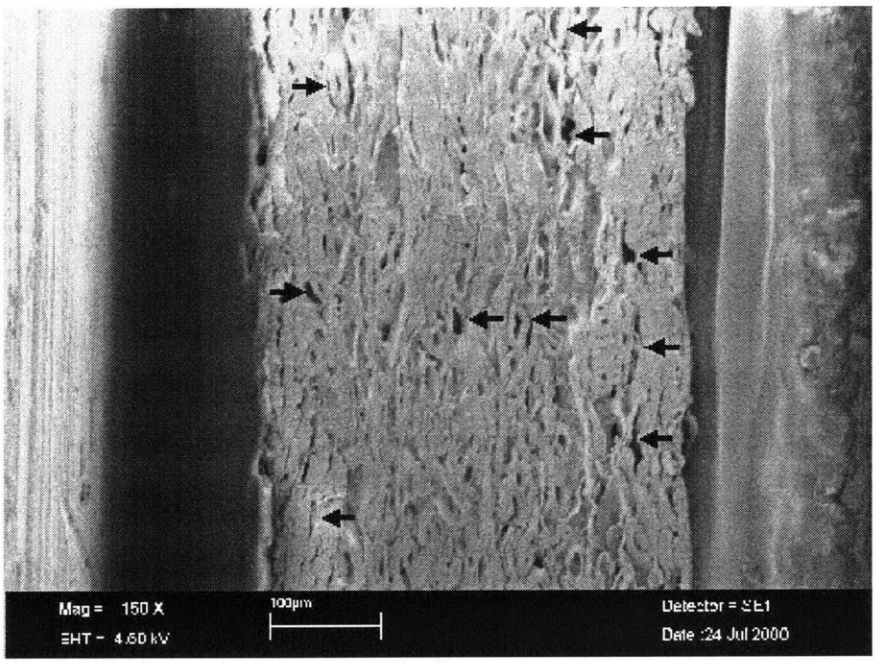

Figure 5-9: Triplex CD through-thickness compression test at no load (Step 1).

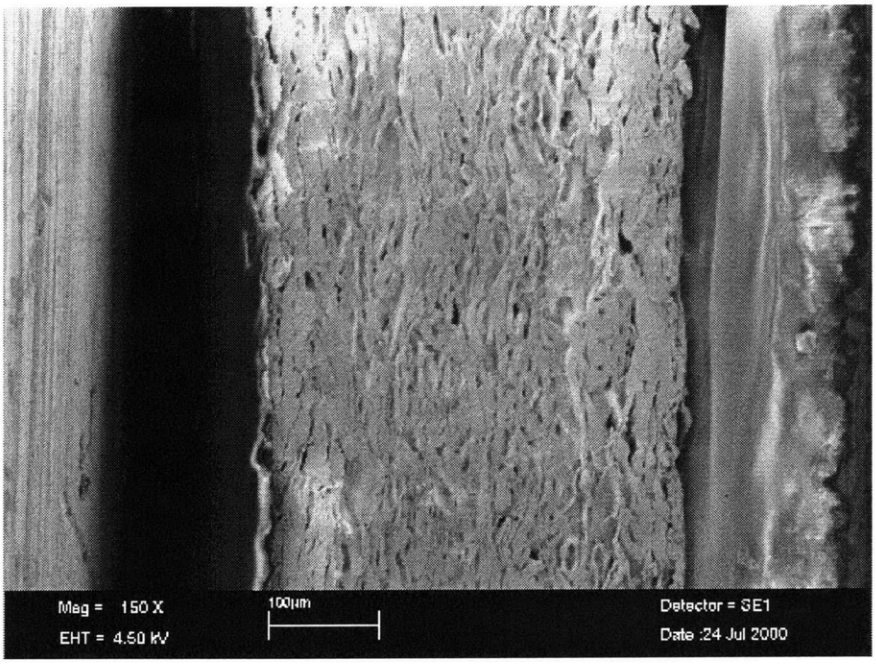

Figure 5-10: Triplex CD through-thickness compression test (Step 2).

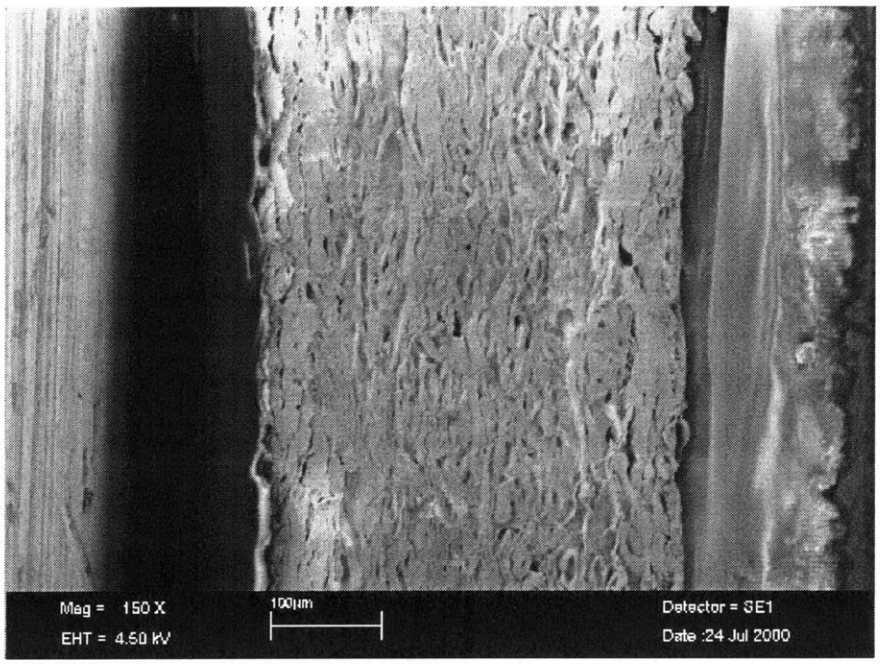

Figure 5-11: Triplex CD through-thickness compression test (Step 3).

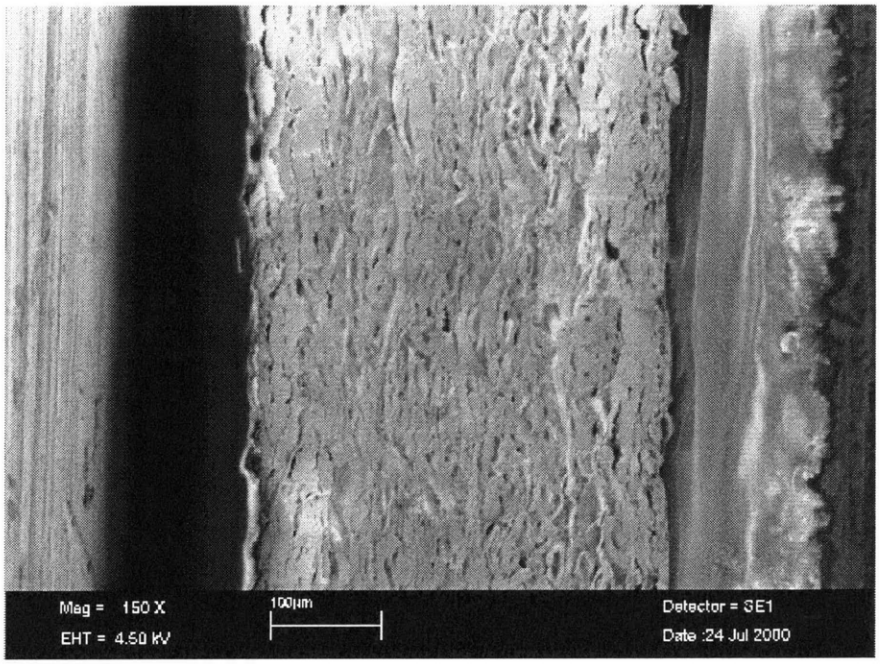

Figure 5-12: Triplex CD through-thickness compression test (Step 4).

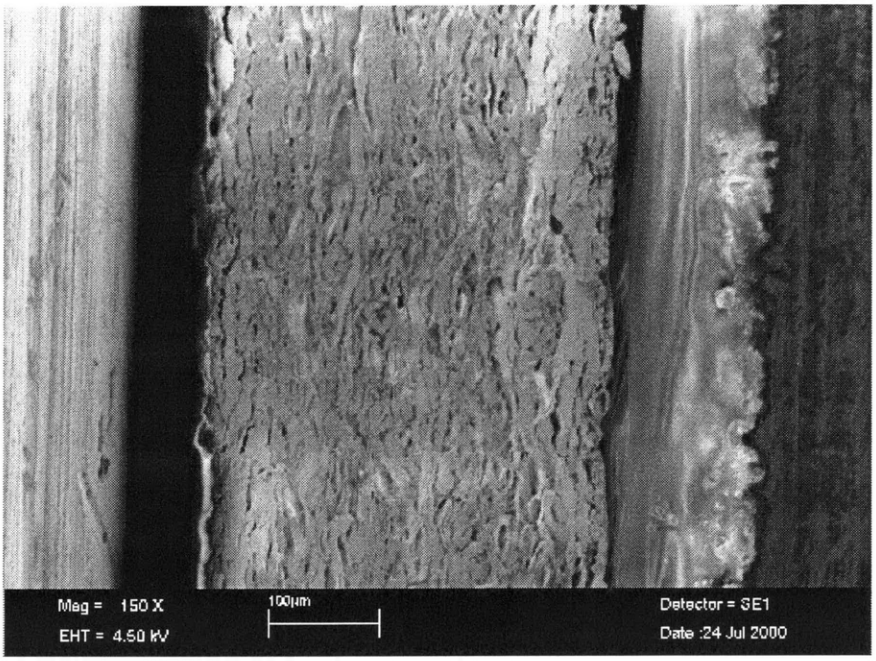

Figure 5-13: Triplex CD through-thickness compression test (Step 5).

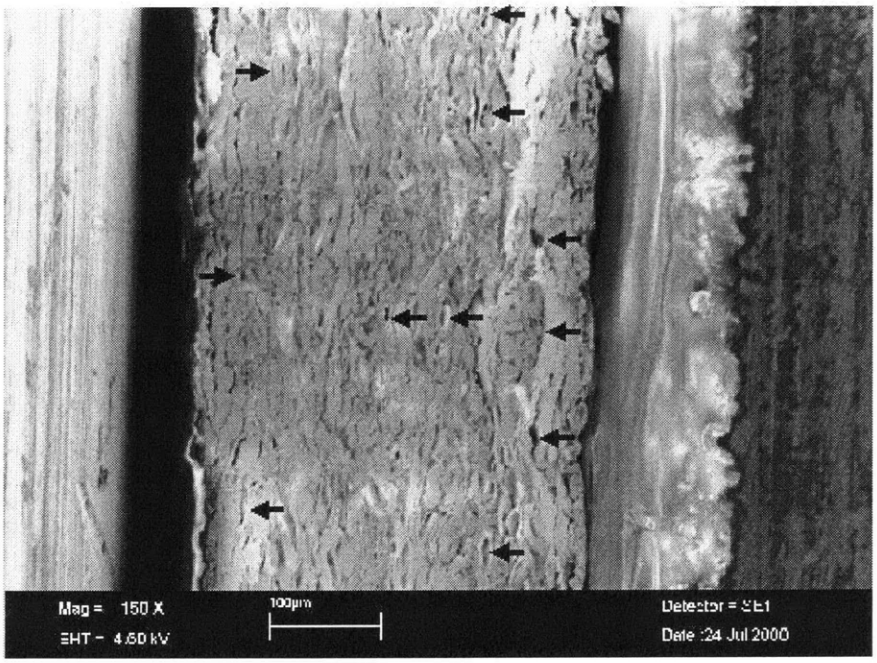

Figure 5-14: Triplex CD through-thickness compression test (Step 6).

to matrix compaction occurs at the transition to nonlinearity. The stiffness of the matrix material would naturally increase as it is compacted, leading to a nonlinear stress-strain relationship.

Chapter 6

Simple Shear Experimental Results

This chapter presents the results of interlaminar shear experiments. Macroscale stress-strain data for constrained shear shows an initial linear region followed by a brief region of material non-linearity, a peak in stress, and material softening. Stress-strain data and images of both constrained and free-expansion at the microscopic level explain the mechanisms corresponding to features of the material behavior curves.

6.1 Constrained Expansion Results

Macroscale stress-strain data for constrained interlaminar shear in the machine direction is presented in Figure 6-1. This curve displays an initial steep linear region. Through analysis of this and several similar curves, the shear modulus of Triplex in the machine direction was found to be 34 MPa. The linear region is followed by a very short region of nonlinear behavior before the peak. In this test, stress peaked at a 1.08 MPa. The corresponding strain was 6%.

Stress values throughout this chapter are nominal stress, as defined in the folowing expression. P represents the shear loading, and A_0 is the initial load-bearing area.

$$\tau = P/A_0 \tag{6.1}$$

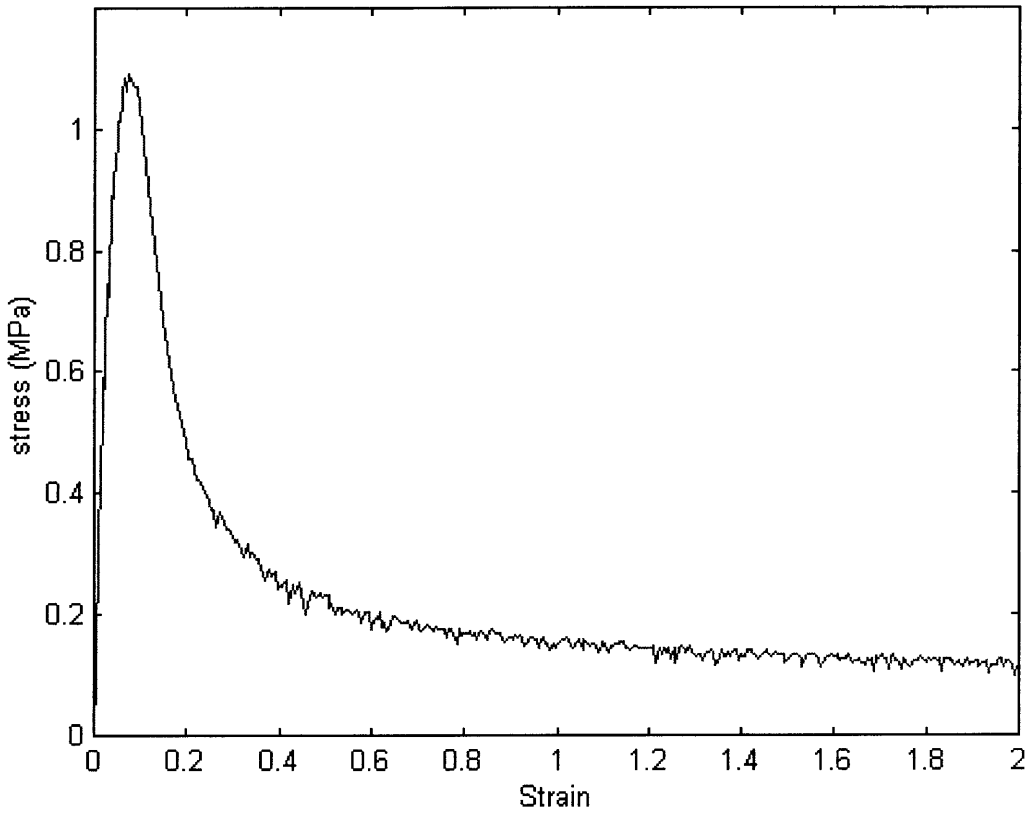

Figure 6-1: Macroscale Triplex MD shear stress-strain curve

Equation 6.2 is a rigorously correct expression for shear strain.

$$\gamma = arctan(d/t) \tag{6.2}$$

In this expression, d represents the displacement in the shear direction, and t is the specimen thickness. For small angles, the tangent of an angle is approximately equal to the angle itself. Applying this fact, the above expression can be simplified for small strains.

$$\gamma = d/t \tag{6.3}$$

The macroscopic data presented here uses this second, simplied definition of strain. However, the microscopic data presented later in the chapter uses the more exact definition of Equation 6.2.

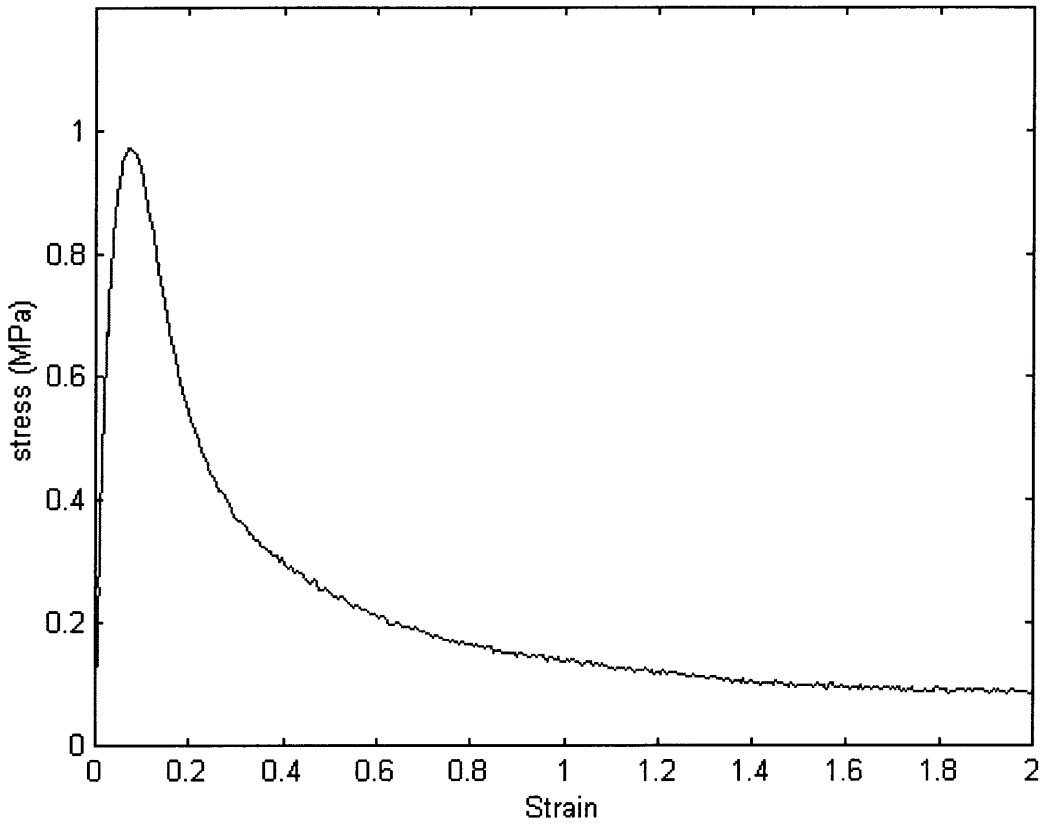

Figure 6-2: Macroscale Triplex CD shear stress-strain curve

Returning to the stress-strain curve, stress falls steeply beyond the peak. At about a third of the peak value, the fall begins to slow, suggesting a logarithmic relationship. Beyond 50%, the stress falls very slowly. At a strain of 50%, the stress is about 0.19 MPa. By 200%, the stress has fallen to 0.12 MPa, a difference of only 0.7 MPa. The deformation mechanisms corresponding to these curve features will be discussed later.

The macroscale stress-strain curve for constrained interlaminar shear in the cross direction, shown in Figure 6-2, is similar in shape to the machine direction curve. However, there are a few differences. Triplex is stiffer in the machine direction than in the cross direction when loaded in interlaminar shear. In the cross direction, the shear modulus is only 26 MPa. The material is also weaker in the cross direction. Failure stress in this test was only 0.99 MPa, although the corresponding strain was similar to that in the machine-direction test.

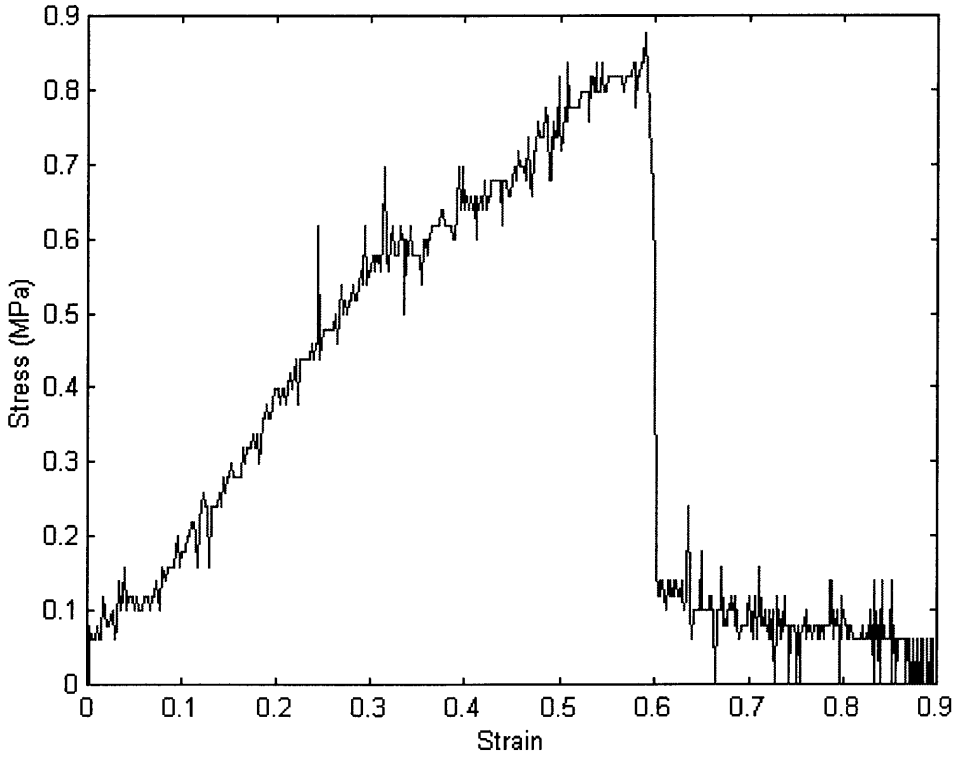

Figure 6-3: Microscale Triplex MD shear stress-strain curve

Beyond the peak, the curve falls off quickly as in the machine-direction case. However, the fall is somewhat more gentle immediately after the peak, and the steepness of the fall is not reduced as significantly at larger strains. In the cross-direction test, the stress was 0.24 MPa at 50% strain. At 200% strain, stress had fallen to 0.09 MPa, a difference of 0.15 MPa. The differences between the two curves are due to the different ways in which deformation mechanisms are manifested in the machine and cross directions.

Microscale stress-strain data for constrained interlaminar shear is given in Figure 6-3. The shape of this curve is somewhat different than the macroscale curves. The microscale data displays the same initial linear region, followed by a very short region of material non-linearity before the peak. In this experiment, the onset of non-linear behavior occurred at 52% strain. The stress peaked shortly afterwards at 0.87 MPa and 59% strain. Following the peak, the stress fell almost instantaneously to a

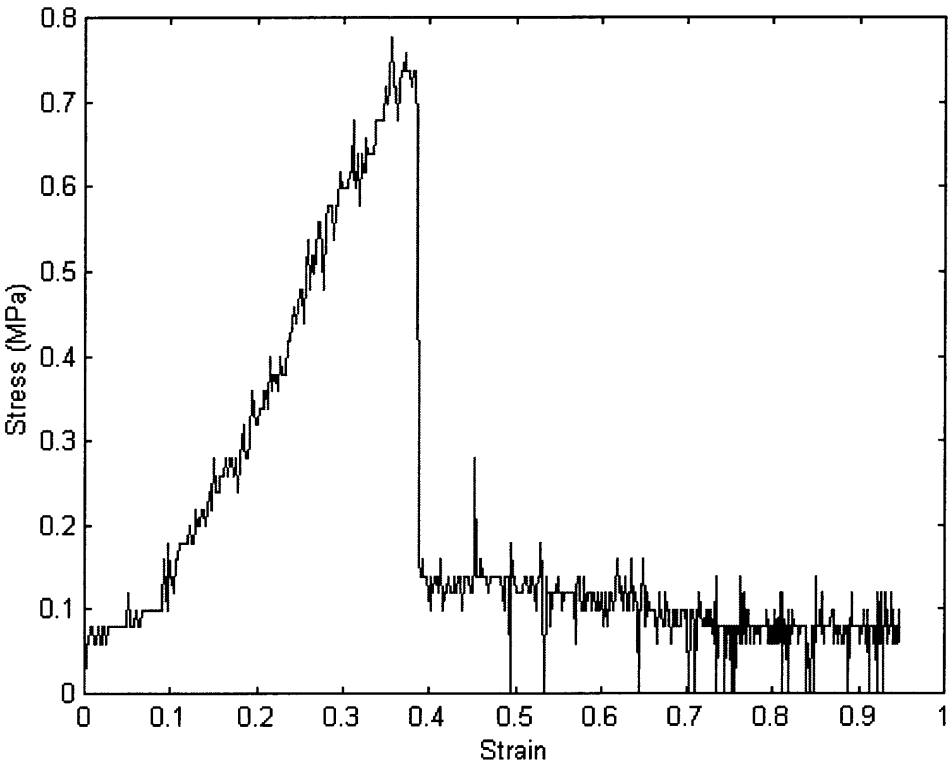

Figure 6-4: Microscale Triplex CD shear stress-strain curve

value of 0.12 MPa, from which it decreased slowly but continuously with increasing strain. This dramatic fall in stress after the peak is in contrast to the smoother fall observed at the macroscopic level.

Figure 6-4 presents microscale constrained shear data for loading in the cross direction. The curve is very similar in shape to the machine direction stress-strain curve. An initial linear region is followed by brief non-linearity; this transition happens at 32% strain. The peak stress is 0.76 MPa and occurs at 37% strain. Following this, the stress drops precipitously to a value of 0.14 MPa, after which decline is slow but steady.

At the microscale level, there is a much larger variation in failure strain between the machine and cross direction than at the macroscale. This is due to the same issues with fixture slackness and motor stuttering discussed in Chapter 4. In addition, the

glue used to attach the paperboard to the fixtures could sustain significant amounts of strain if it was applied too thickly. Errors in microscale stress data are discussed in Appendix A.

Figures 6-5 through 6-10 are images of constrained shear loading in the MD direction. The first image, Figure 6-5, shows the specimen at no load. In Figure 6-6, the specimen has been loaded into the non-linear region of the stress-strain curve with no observable change. Failure occurred shortly after this image was captured. The next image shows the specimen immediately after failure; this image corresponds with the bottom of the precipitous drop in the stress-strain curve. The material has delaminated at a mechanical-layer/mechanical-layer interface near the center of the specimen. This delamination happens suddenly through the cross section of the specimen, causing this very fast drop in load. It is likely that in a larger specimen delamination begins locally and spreads along the interface, rather than happening throughout the specimen simultaneously. This explains why stress drops more gently after the peak at the macroscopic level than at the microscopic level.

Figures 6-8 and 6-9 were taken in the region of slowly decreasing stress. Although delamination has occurred, there is friction between the two surfaces and fibers still engaged across the gap. The upper portion of the specimen is stationary, and the bottom portion is moving to the left. Although it is difficult to see in these images due to charging of the uncoated material exposed by failure, bridging fibers are pulled along by the moving portion of the specimen. Some bridging fibers initially had their right end in the stationary material and their left end in the moving material. These fibers simply slide out of one part of the specimen as the test progresses. Some of the fibers, however, were oriented the opposite way. That is, their right end was embedded in the portion of the specimen moving to the left. As the right end of a fiber was pulled closer to the left end, the fiber was rotated and compressed along its length due to the constrained nature of the test. However, during unconstrained shear, these rotating fibers push open the gap between the delaminated surfaces rather than being compressed, as shall be shown later in the chapter.

A full view of the specimen is shown in Figure 6-10. The dark material near the

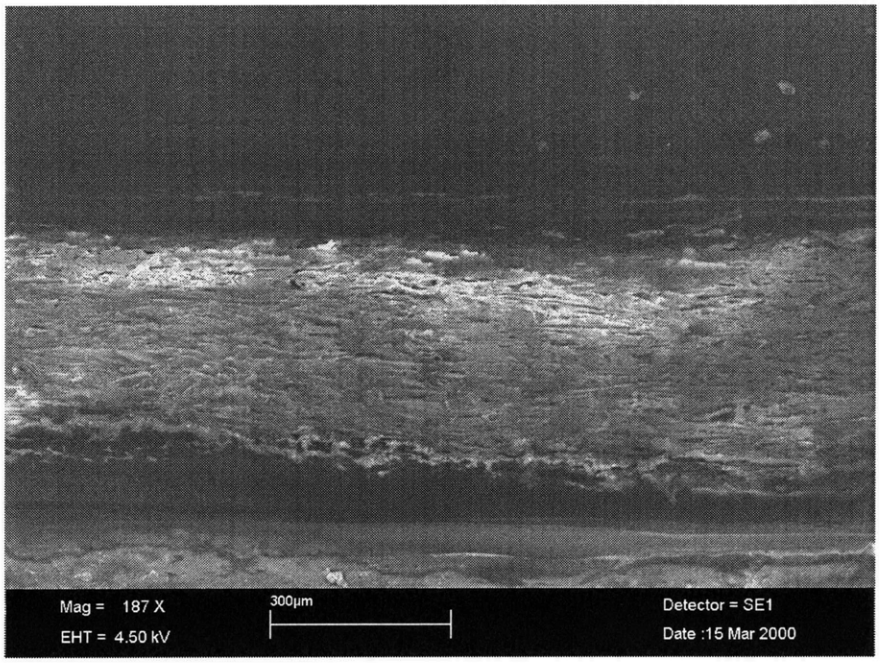

Figure 6-5: Triplex MD shear test at no load (Step 1)

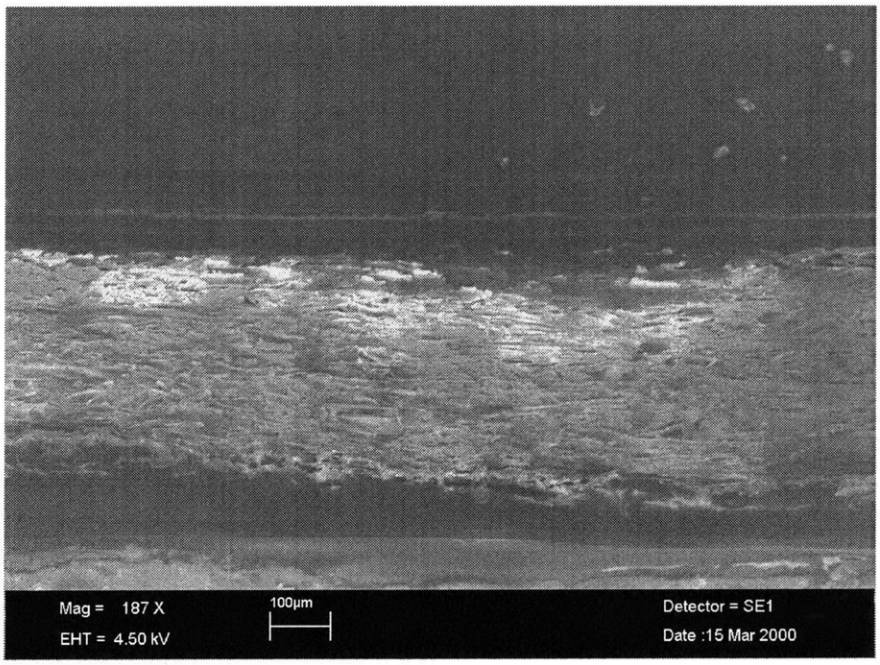

Figure 6-6: Triplex MD shear test (Step 2)

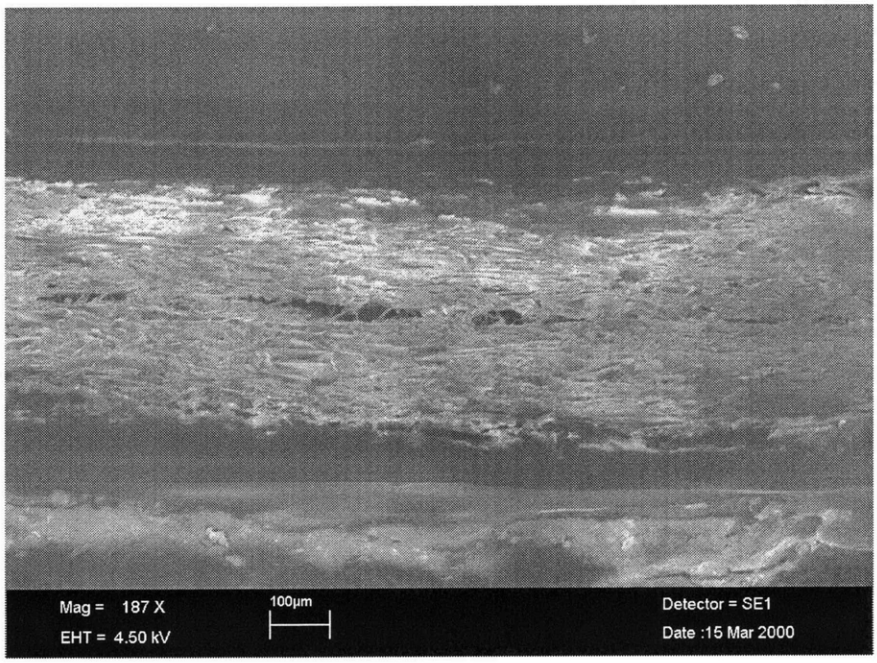

Figure 6-7: Triplex MD shear test (Step 3)

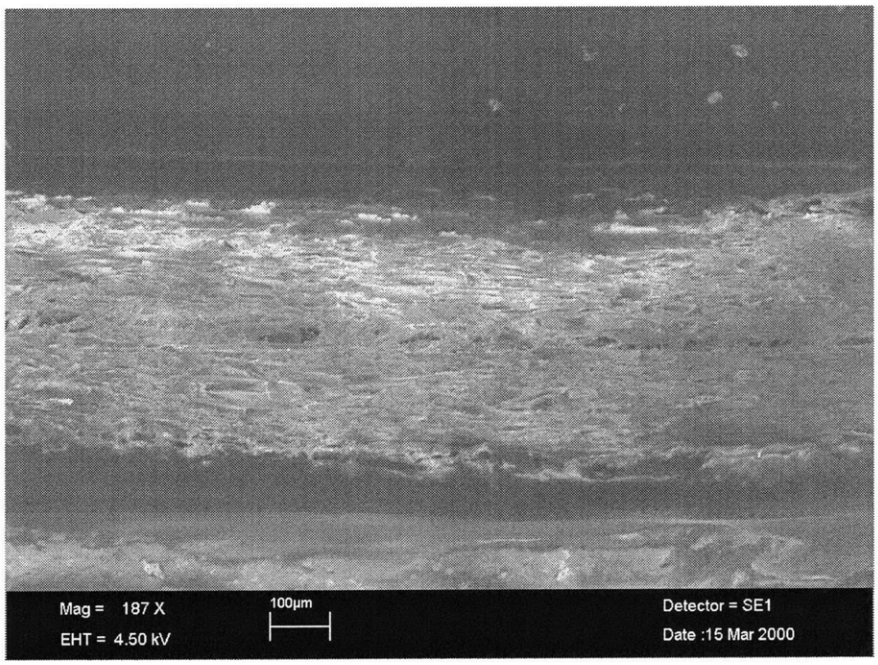

Figure 6-8: Triplex MD shear test (Step 4)

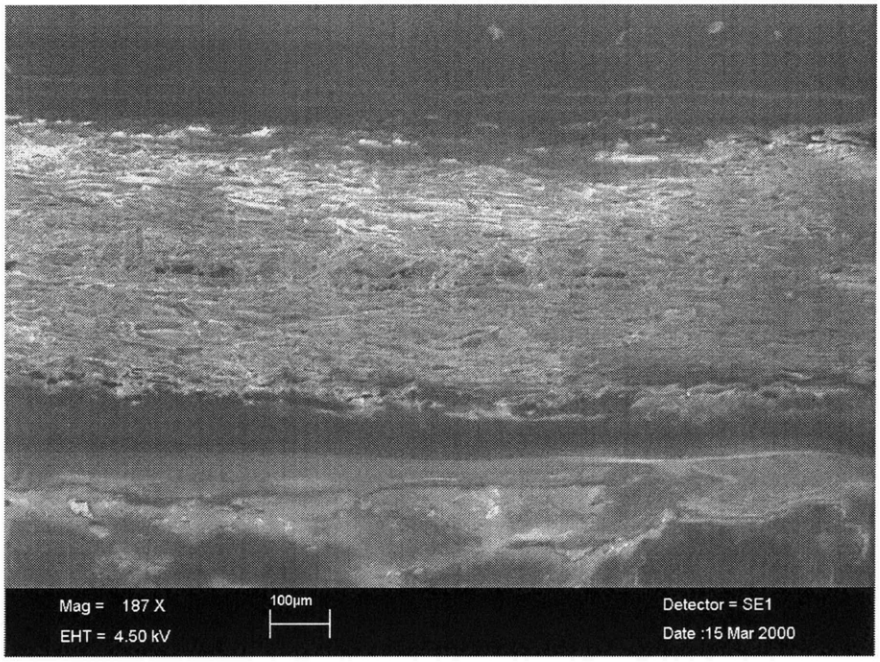

Figure 6-9: Triplex MD shear test (Step 5)

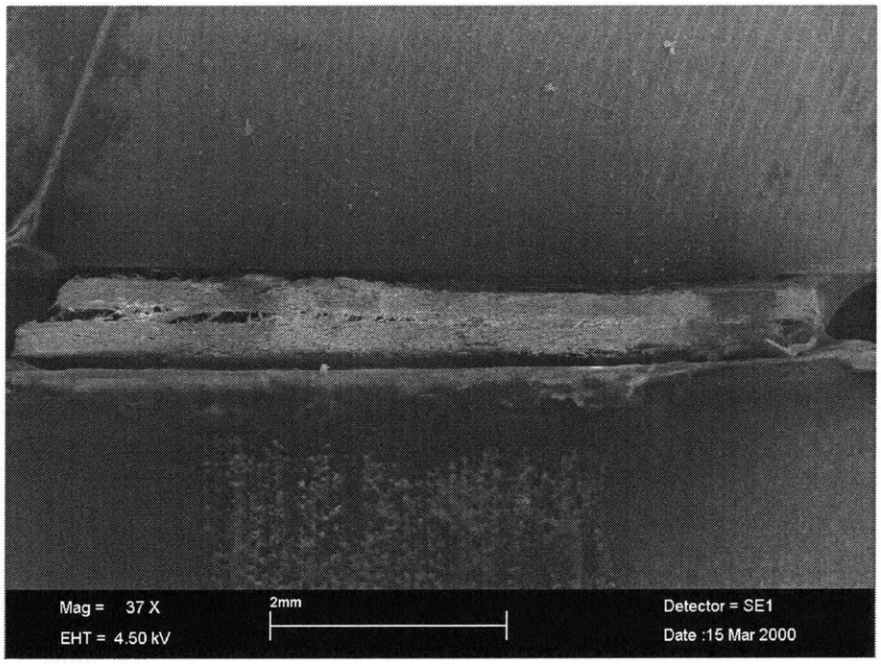

Figure 6-10: Full view of Triplex MD shear test (Step 5)

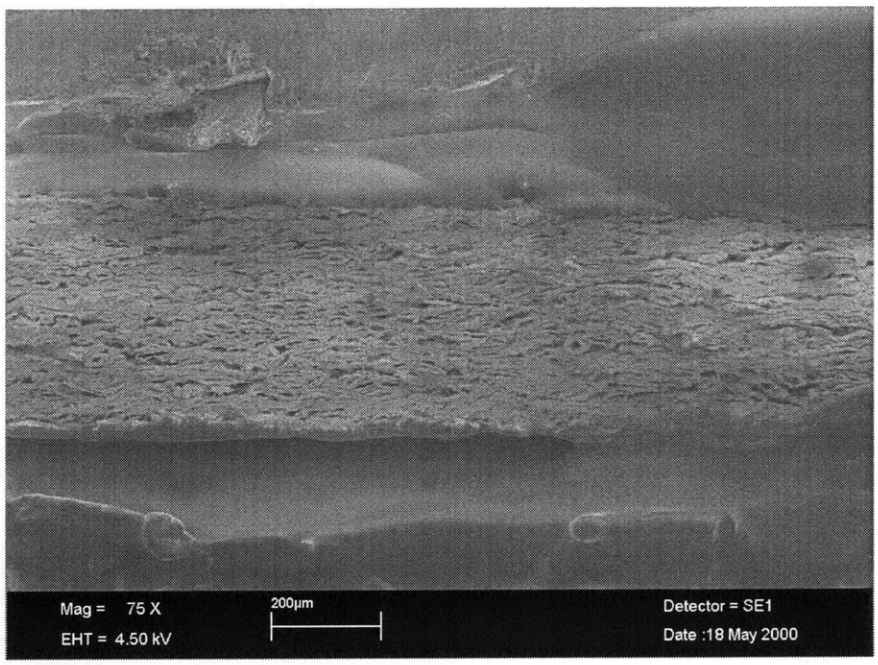

Figure 6-11: Triplex CD shear test at no load (Step 1)

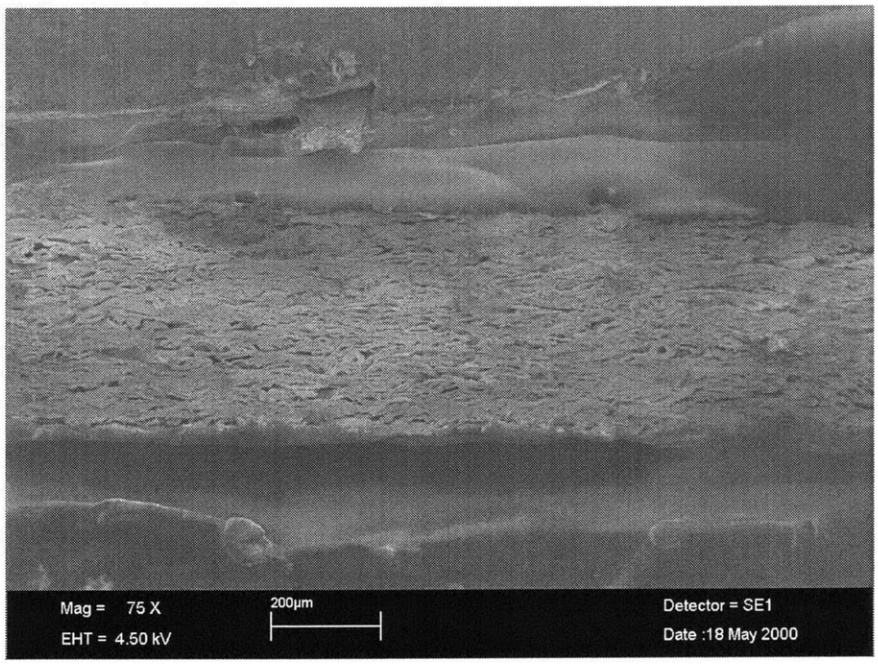

Figure 6-12: Triplex CD shear test (Step 2)

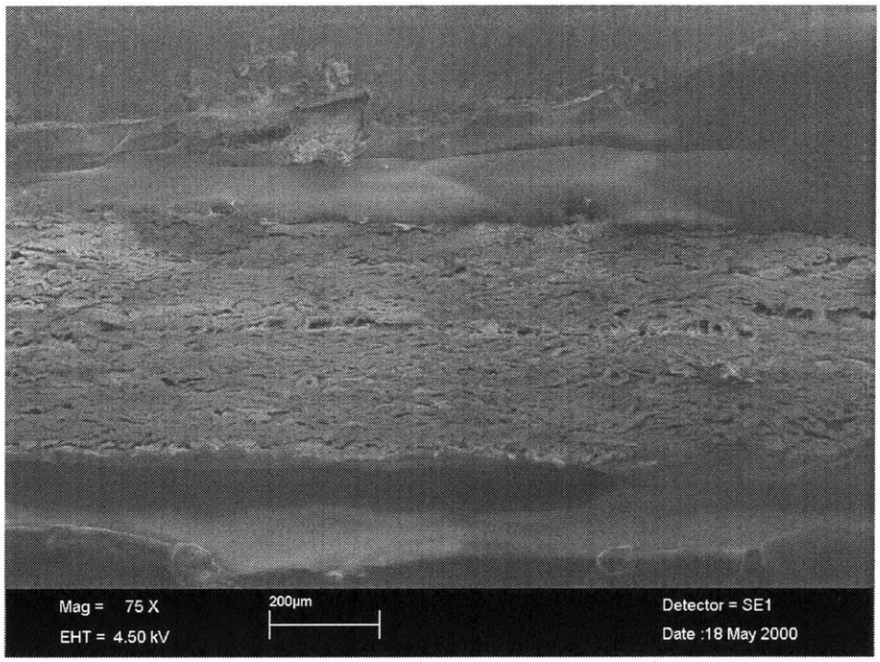

Figure 6-13: Triplex CD shear test (Step 3)

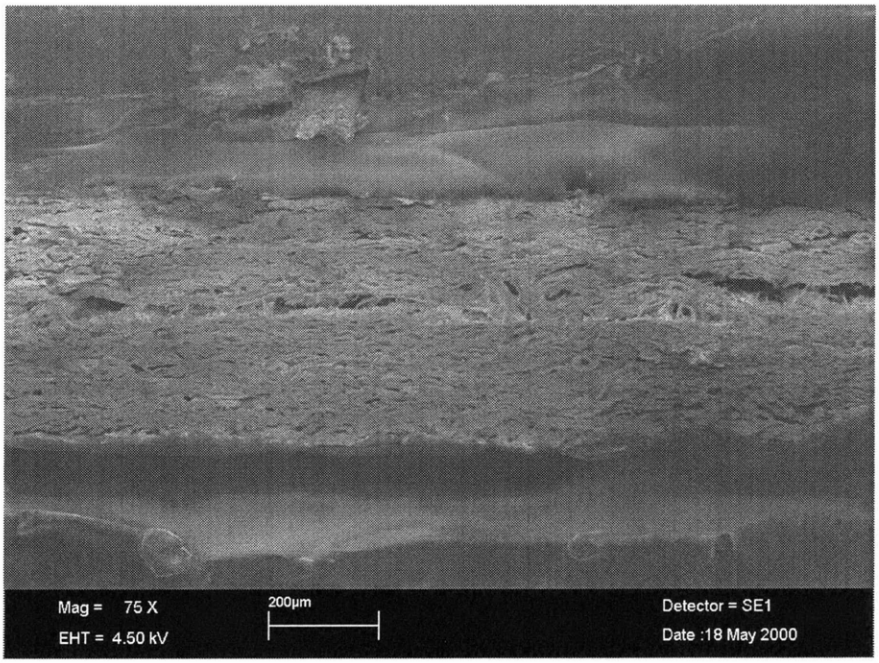

Figure 6-14: Triplex CD shear test (Step 4)

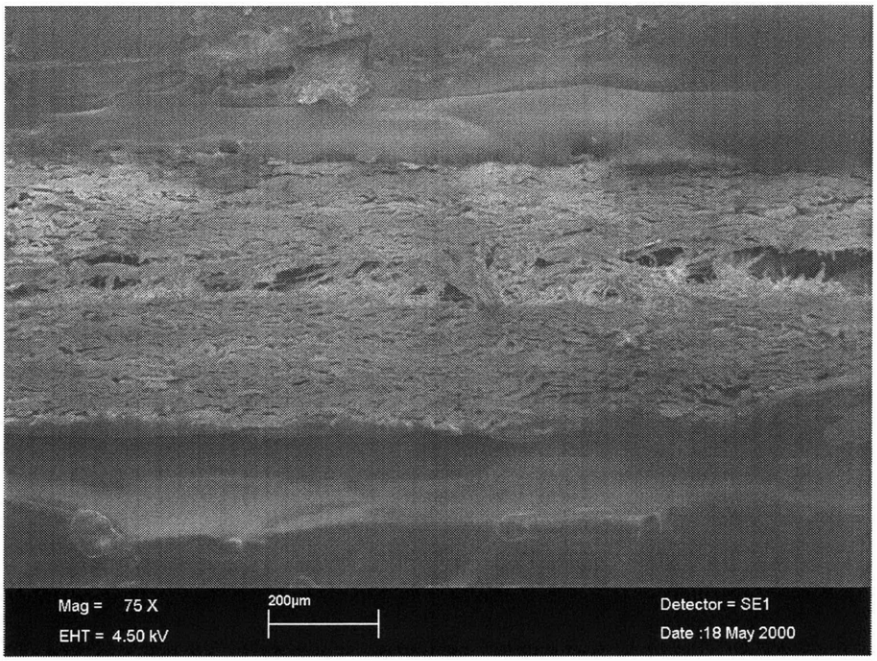

Figure 6-15: Triplex CD shear test (Step 5)

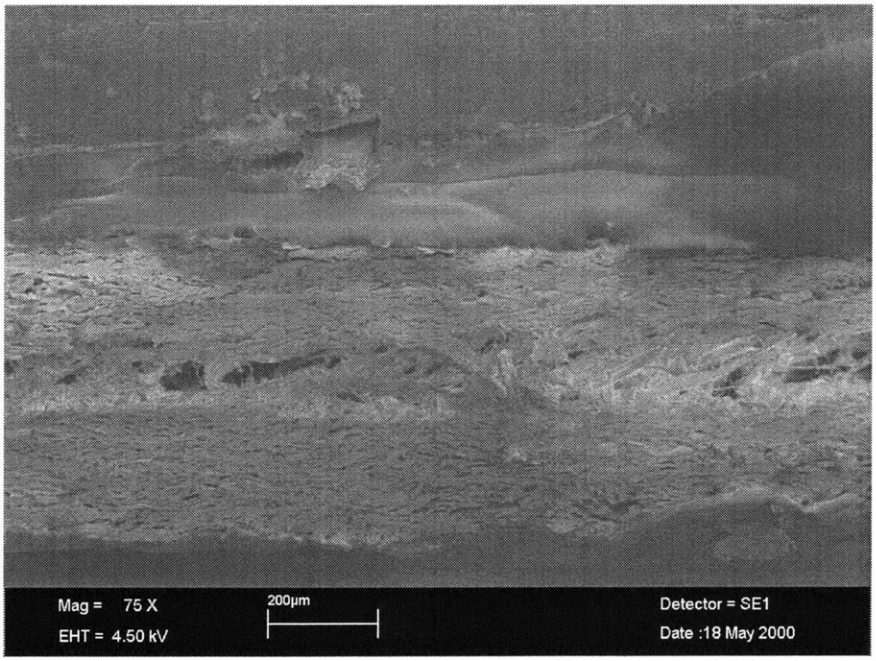

Figure 6-16: Triplex CD shear test (Step 6)

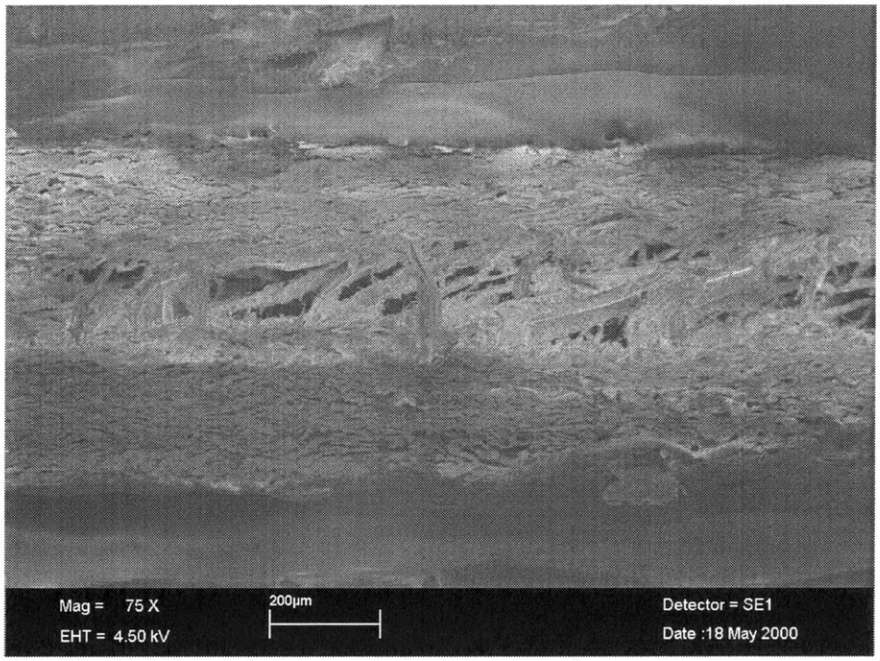

Figure 6-17: Triplex CD shear test (Step 7)

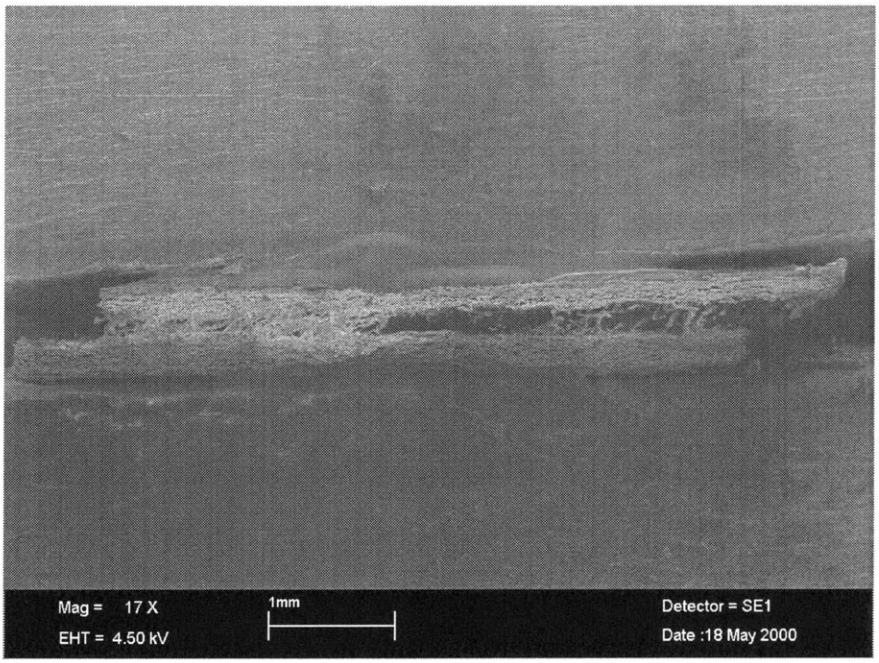

Figure 6-18: Full view of Triplex CD shear test (Step 7)

right end of the specimen is a small amount of excess glue. The brighter region just to the left is the region shown in the higher magnification images. Near the left end, the gap can be clearly seen, as little charging has occurred. In this region, bridging fibers are visible. Most are slanting down and to the left, but a few are oriented down and slightly to the right. These fibers were rotated and compressed during the test, as described.

Shear loading in the cross direction is shown in Figures 6-11 through 6-12. In the first image, the specimen has not been loaded. Figure 6-12 shows the specimen under load, but there is no discernible deformation. Figure 6-13 was captured immediately after failure. The specimen has delaminated throughout the observable length. The next four images, Figures 6-14 through 6-17, were taken in the region of slowly decreasing stress. These images clearly show some fibers being pulled out of the material matrix on one side of the gap while other fibers are rotated and compressed. A particularly notable rotated, compressed fiber is near the center of the frame in Figure 6-17. Figure 6-18 is a full view of the test specimen.

6.2 Unconstrained Expansion Results

Microscale stress-strain curves for free-expansion shear are presented in Figures 6-19 and 6-20. These curves are generally similar to those presented for constrained shear. However, there are some important differences. The effects of fixture slack in the region of increasing stress are more pronounced than in the constrained shear data. This is due to the expansion slots in the fixture. The slots made small misalignment of the fixture during mounting very easy. When the fixture caught on the guideposts during testing, it would slide along the posts until alignment was corrected.

Failure stress values between constrained and free expansion shear are comparable. In the data presented here, the specimen loaded in the machine direction failed at 0.72 MPa, and the cross-direction-loaded specimen failed at 0.5 MPa. Beyond the peak, both constrained and free expansion shear feature a sudden drop in stress, followed by a region of more moderately decreasing stress. However, in the free-expansion

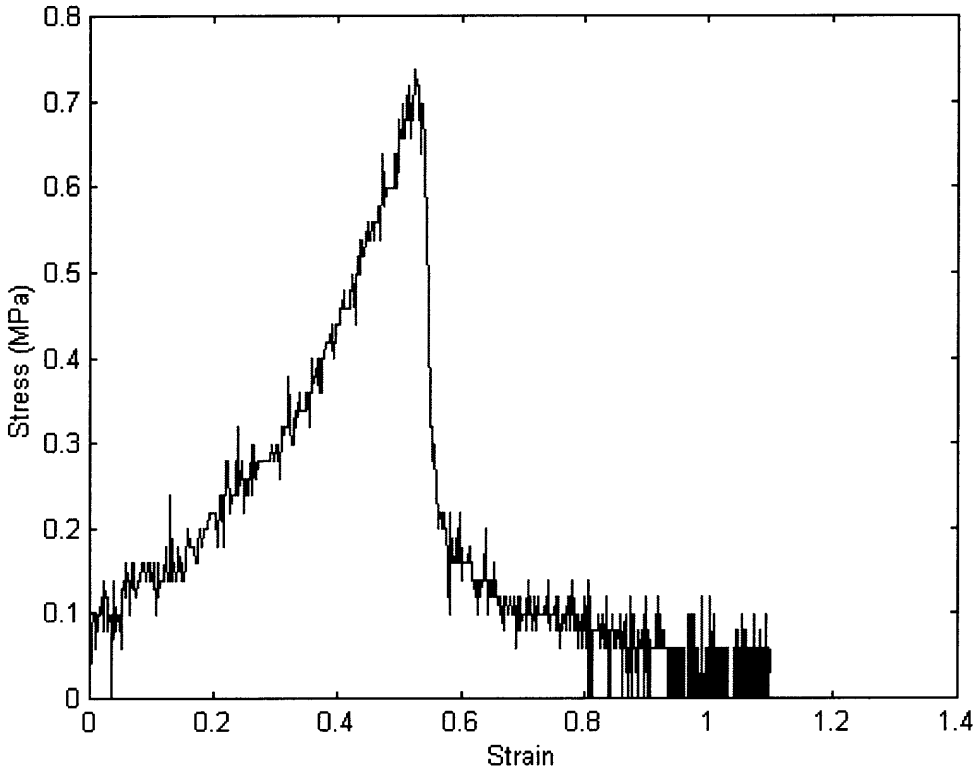

Figure 6-19: Triplex MD free-expansion shear stress-strain curve

case the stress in this last region of the curve decreases more quickly than in the constrained case. Because the delaminated surfaces are swiftly separated in the Z direction, there is no appreciable friction between them. Additionally, the Z gap means that less travel in the shearing direction is required before a given fiber will pull out of the matrix on one side of the gap. (The Z gap plus the shear displacement add up to a greater distance than shear displacement alone.)

Unconstrained shear in the machine direction is shown in Figures 6-21 through 6-26. The first of these images shows the specimen at no load. In the second image, Figure 6-22, the specimen has been loaded into the nonlinear region, with no appreciable deformation. The third image was taken immediately after the peak in stress. As with constrained shear, failure happened simultaneously throughout the cross section. In this image, the macrocrack is clearly visible across the entire frame.

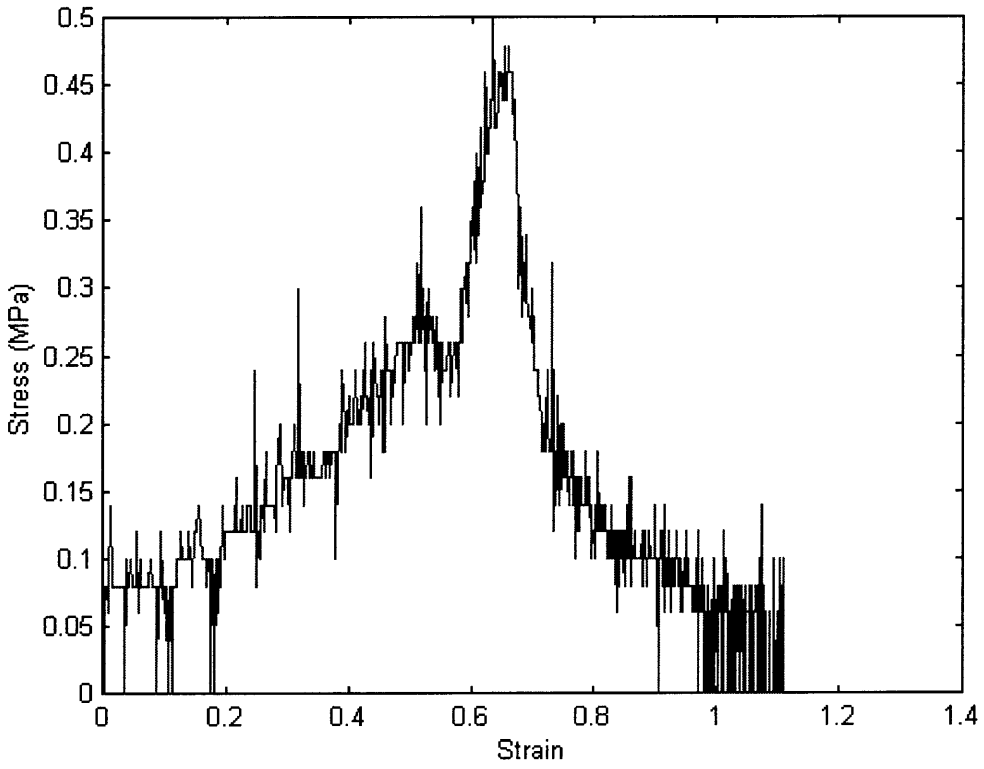

Figure 6-20: Triplex CD free-expansion shear stress-strain curve

In subsequent images, Figures 6-24 and 6-25, the crack is opening in the Z direction.

The final image is a full view of the failed specimen. The upper block of the fixture appears to have rotated slightly, causing the delamination gap to be wider near the left end of specimen than at the right. Although it is possible that the fiber rotations causing Z direction expansion also cause this kind of rotation, it is unlikely that this is the case here. The appearance of a wider gap at one end is due to charging at the other end of the specimen and to image distortion produced by the microscope at low magnifications. (The distortion causes curving of the image near the left and right edges of the frame, with the majority of the distortion occurring at the right edge.) Variation in glue thickness can also contribute to this effect. If the glue is thicker at the right end of the specimen than at the left, the specimen itself will be open slightly wider at the left end when the fixturing blocks are aligned.

Figures 6-27 through 6-32 show unconstrained shear in the cross direction. These

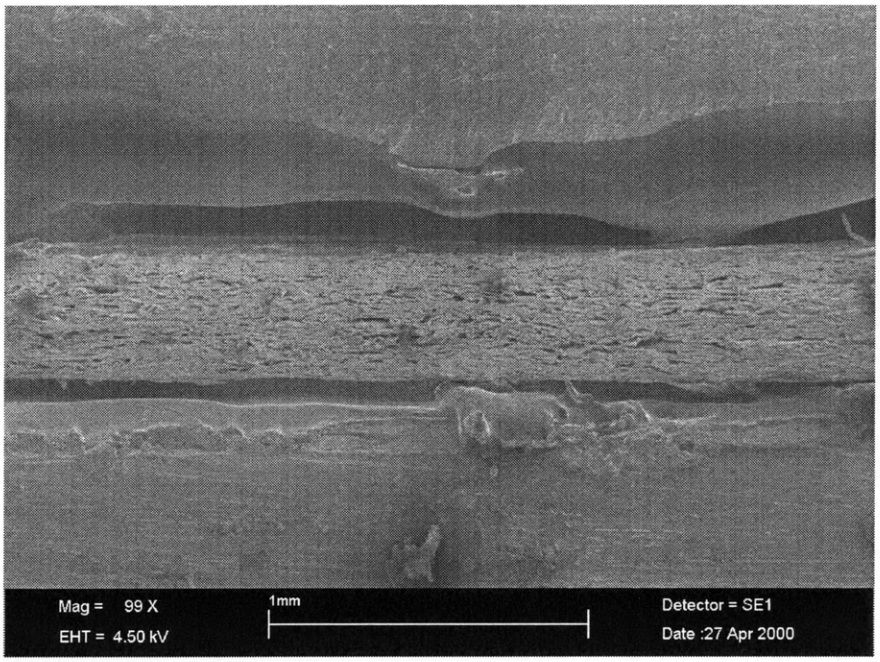

Figure 6-21: Triplex MD free expansion shear test at no load (Step 1)

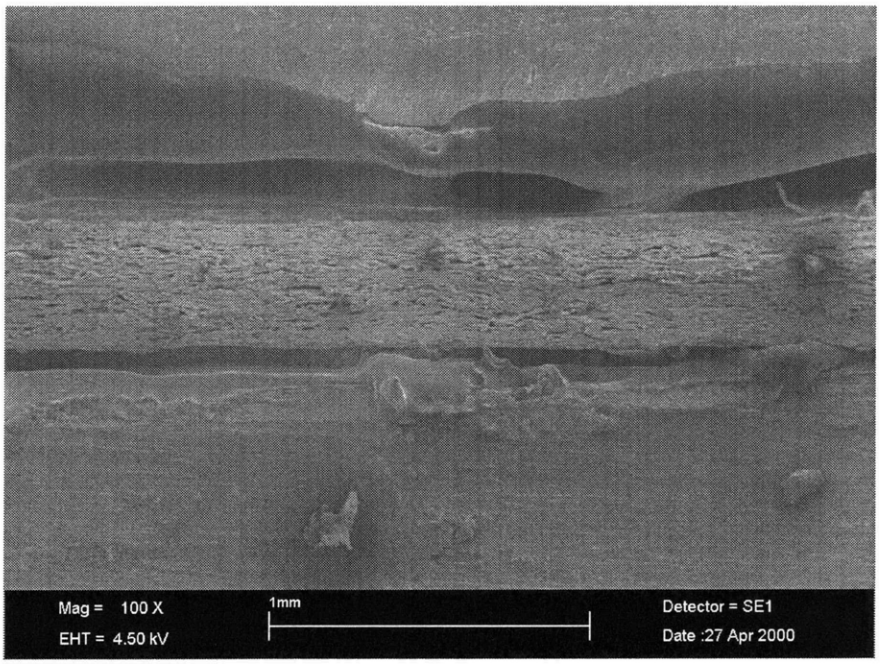

Figure 6-22: Triplex MD free expansion shear test (Step 2)

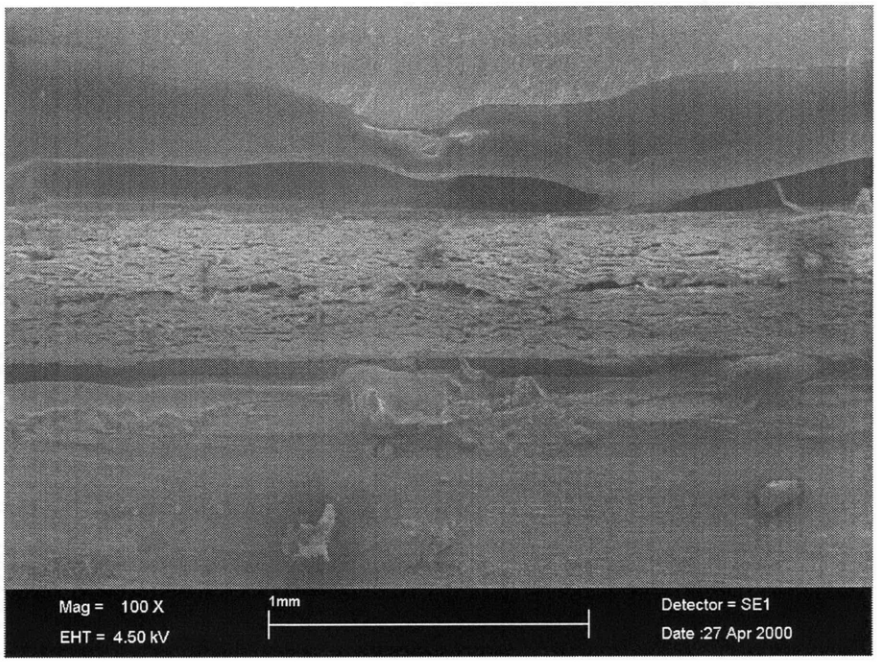

Figure 6-23: Triplex MD free expansion shear test (Step 3)

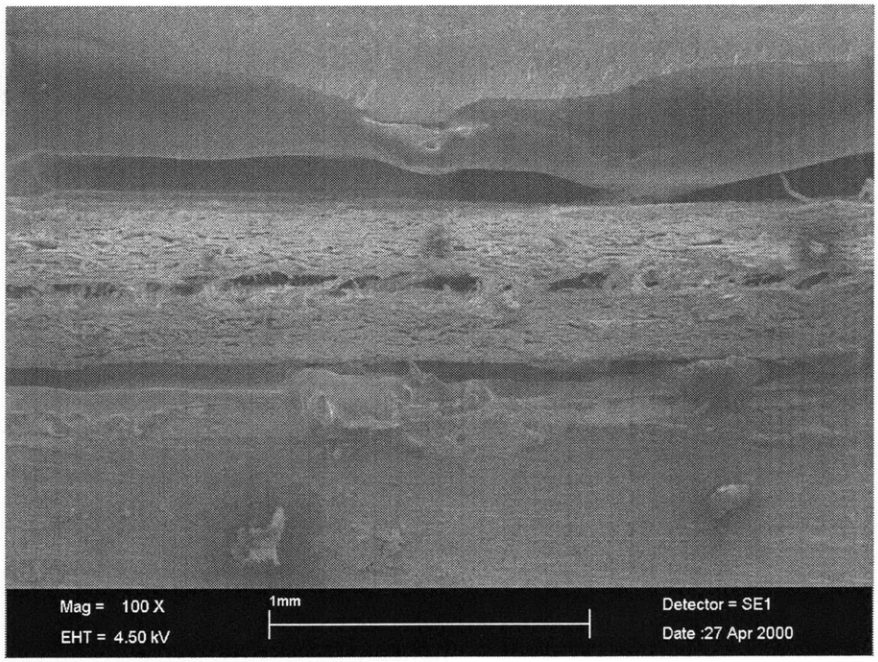

Figure 6-24: Triplex MD free expansion shear test (Step 4)

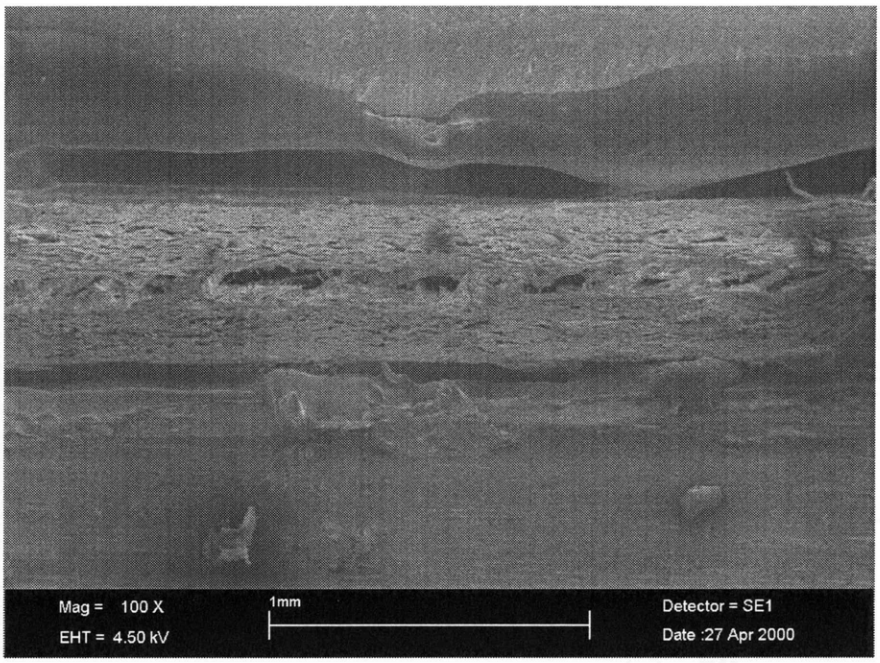

Figure 6-25: Triplex MD free expansion shear test (Step 5)

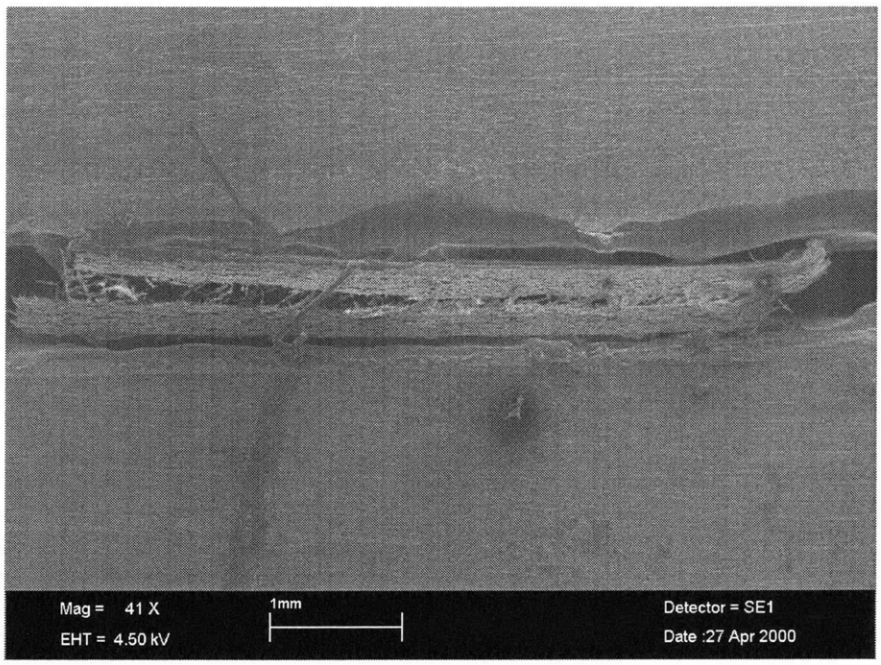

Figure 6-26: Full view of Triplex MD free expansion shear test (Step 5)

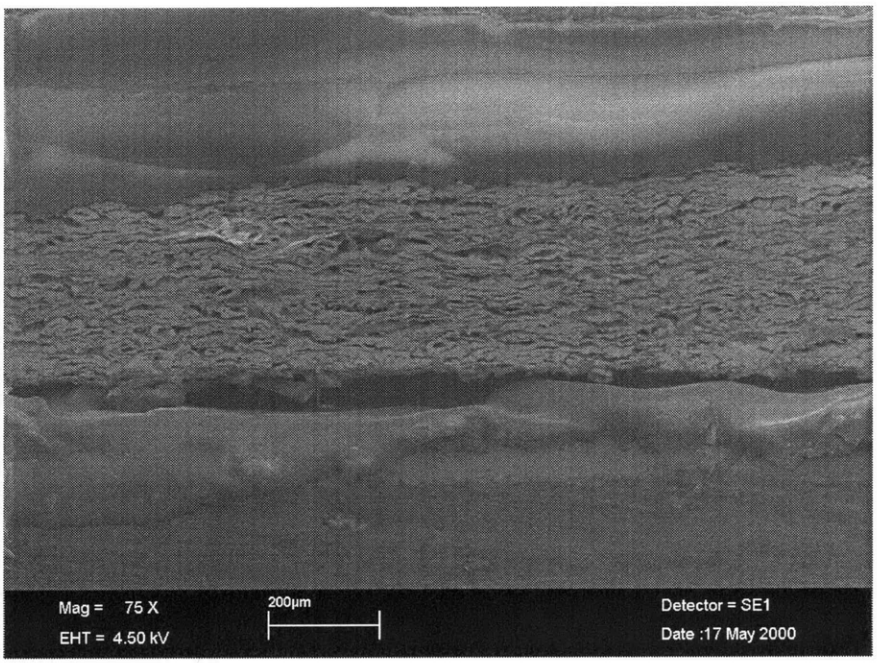

Figure 6-27: Triplex CD free expansion shear test at no load (Step 1)

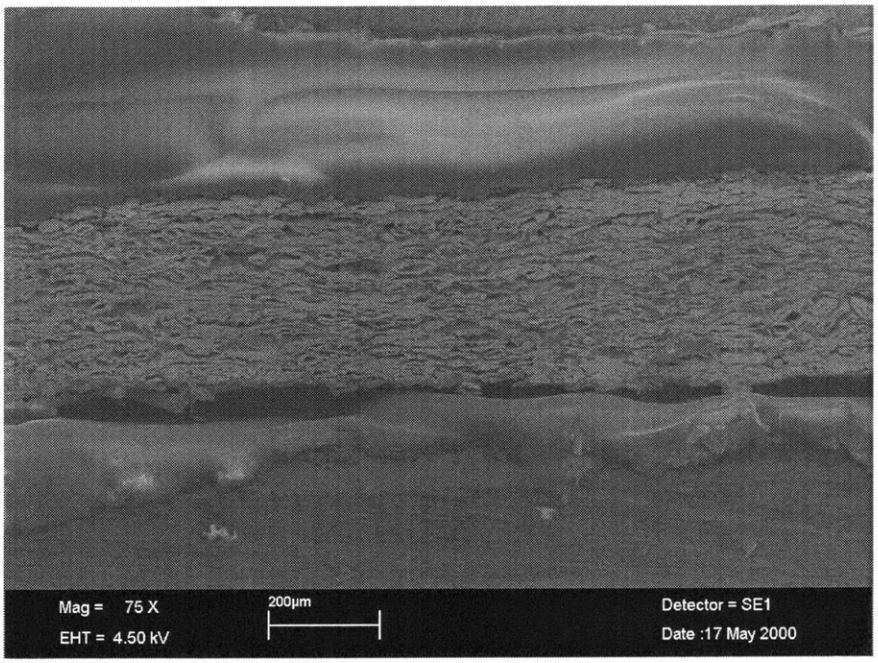

Figure 6-28: Triplex CD free expansion shear test (Step 2)

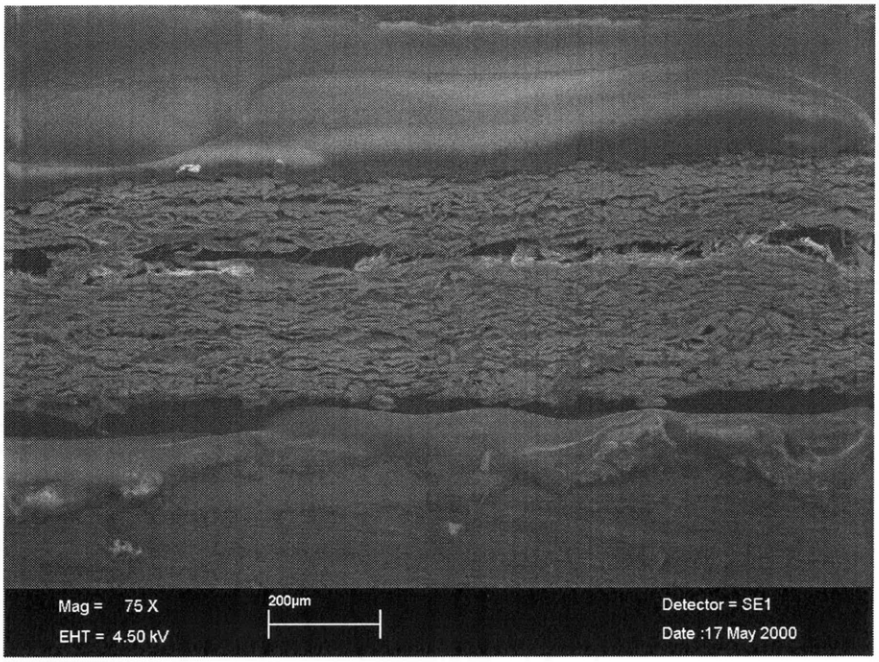

Figure 6-29: Triplex CD free expansion shear test (Step 3)

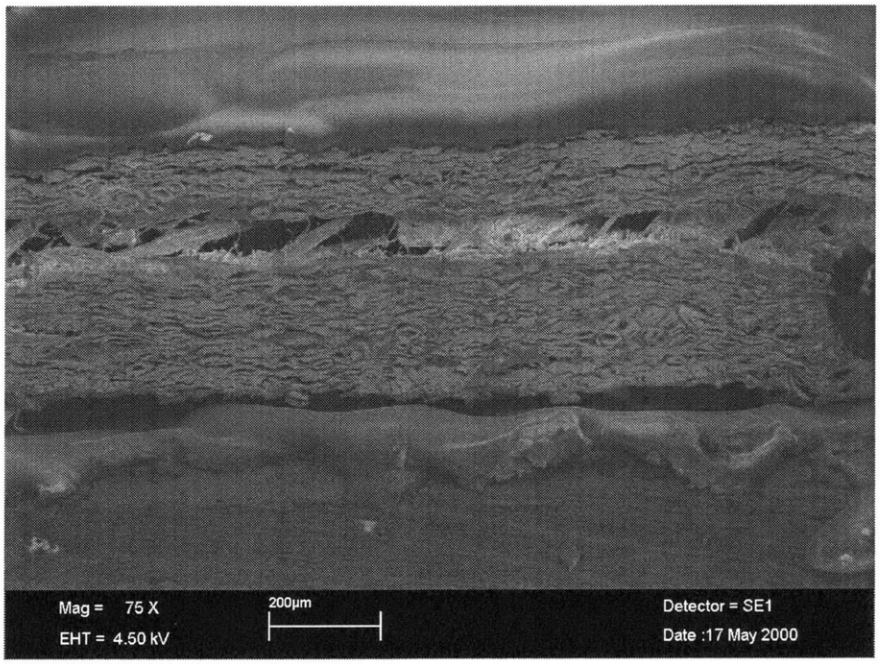

Figure 6-30: Triplex CD free expansion shear test (Step 4)

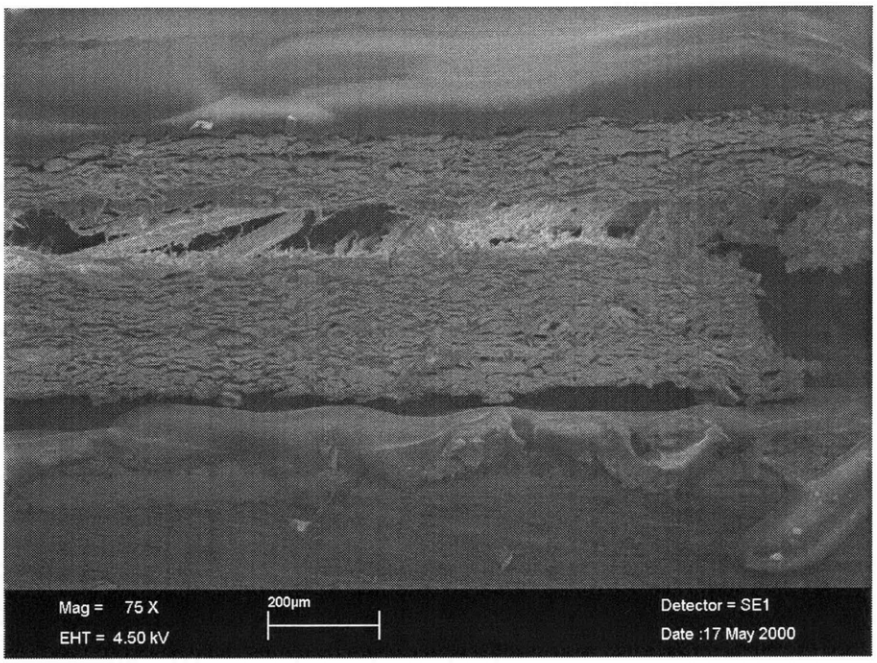

Figure 6-31: Triplex CD free expansion shear test (Step 5)

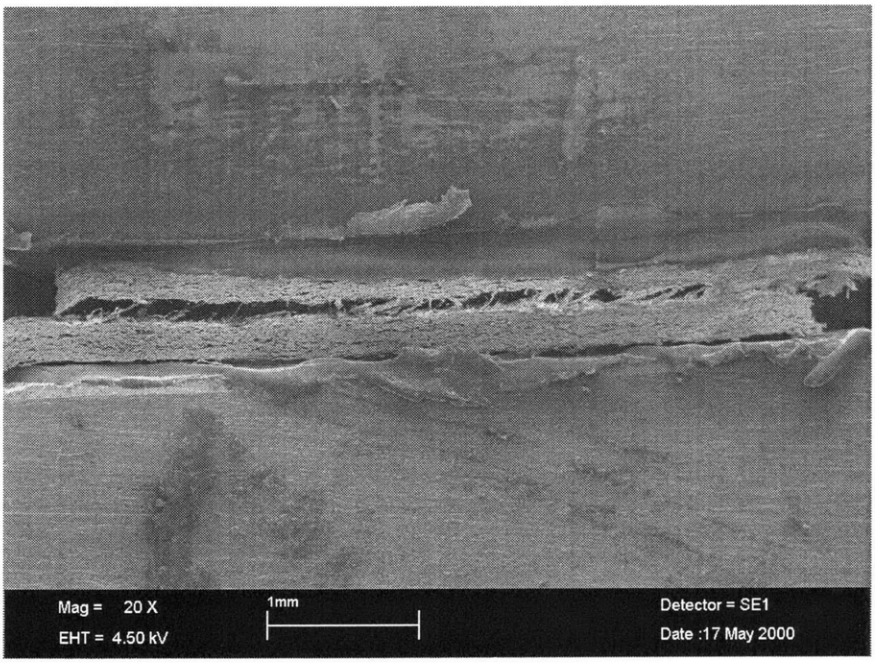

Figure 6-32: Full view of Triplex CD free expansion shear test (Step 5)

images show the same deformation patterns observed in the other image sets presented here. Figure 6-27 depicts the specimen at no load. In Figure 6-28, the specimen has been loaded into the nonlinear region. Although the specimen has shifted slightly with respect to the frame due to fixture slackness, there is no appreciable deformation of the material. Failure occurred shortly after this image was captured. The material failed suddenly and throughout the entire cross section, as is shown in Figure 6-29. The remaining images show the paperboard opening in the Z direction as bridging fibers rotate. A full view of the specimen, Figure 6-32, shows the large gap between failure surfaces.

Paperboard loaded in out-of-plane shear deforms without sustaining damage until sudden failure by delamination. At small length scales, this delamination happens throughout the entire specimen simultaneously, although at larger length scales is may occur locally and propagate through the material. There is some residual load carrying capacity after delamination, due to friction between the failure surfaces and fibers that are interwoven on both sides of the gap. The interwoven fibers may rotate to align with the loading direction. During rotation, the fibers may be compressed along their length. The force of the compressed fibers pushing back on the matrix material causes the material to expand in the Z direction if unconstrained.

Chapter 7

Combined-Loading Experimental Results

This chapter presents the results of experiments combining out-of-plane tension and shear loading. Stress-strain behavior at both the macroscale and microscale shows a transition between tension-dominated behavior to shear-dominated behavior as the ratio of shear to tension increases. The stress-strain data was used to construct a failure surface for Triplex under out-of-plane loading.

Images taken at the microscopic level also show a transition between the mechanisms dominant in through-thickness tension and those dominant in interlaminar shear. Under primarily tensile combined load, the material experienced extensive microcracking before macrocrack formation. Under loads with a larger shear component, the material showed little or no microcracking before macrocrack formation.

7.1 Stress-Strain Behavior

Stress-strain behavior for combined-loading at the macroscopic level is presented in Figures 7-1 and 7-2. This data represents loadings where the shear component is in the machine direction. Stress-strain behavior with shear loading in the cross direction was not available at the macroscopic level. The legend in each figure indicates the type of combined-loading for each curve. Recall from Chapter 2 that through-thickness

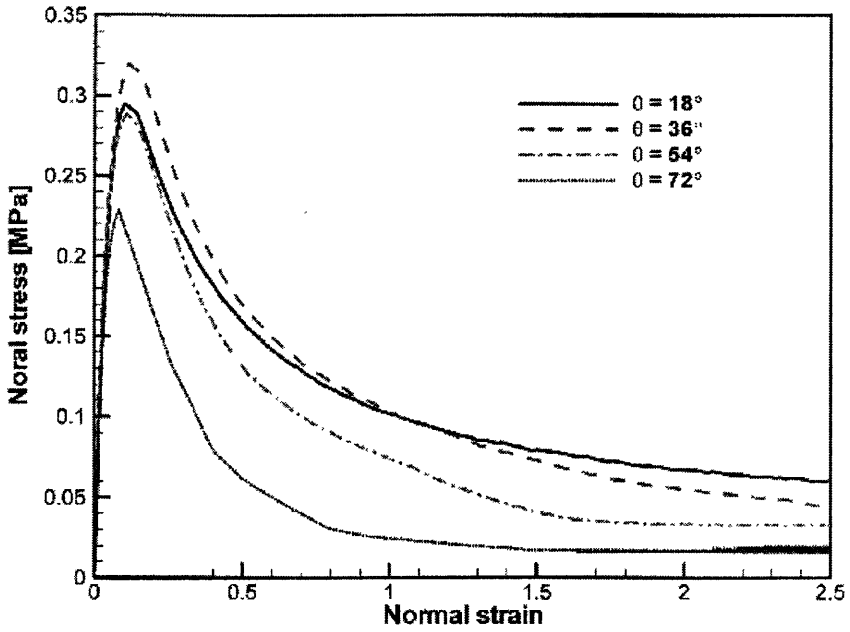

Figure 7-1: Normal components of Triplex MD macroscale combined loading stress-strain data. (Courtesy of N. Stenberg.)

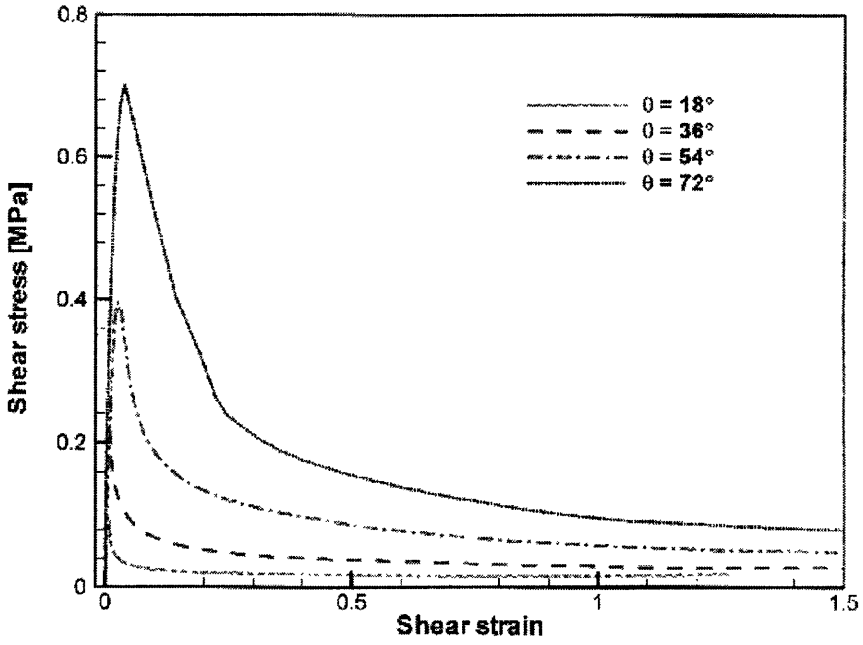

Figure 7-2: Shear components of Triplex MD macroscale combined loading stress-strain data. (Courtesy of N. Stenberg.)

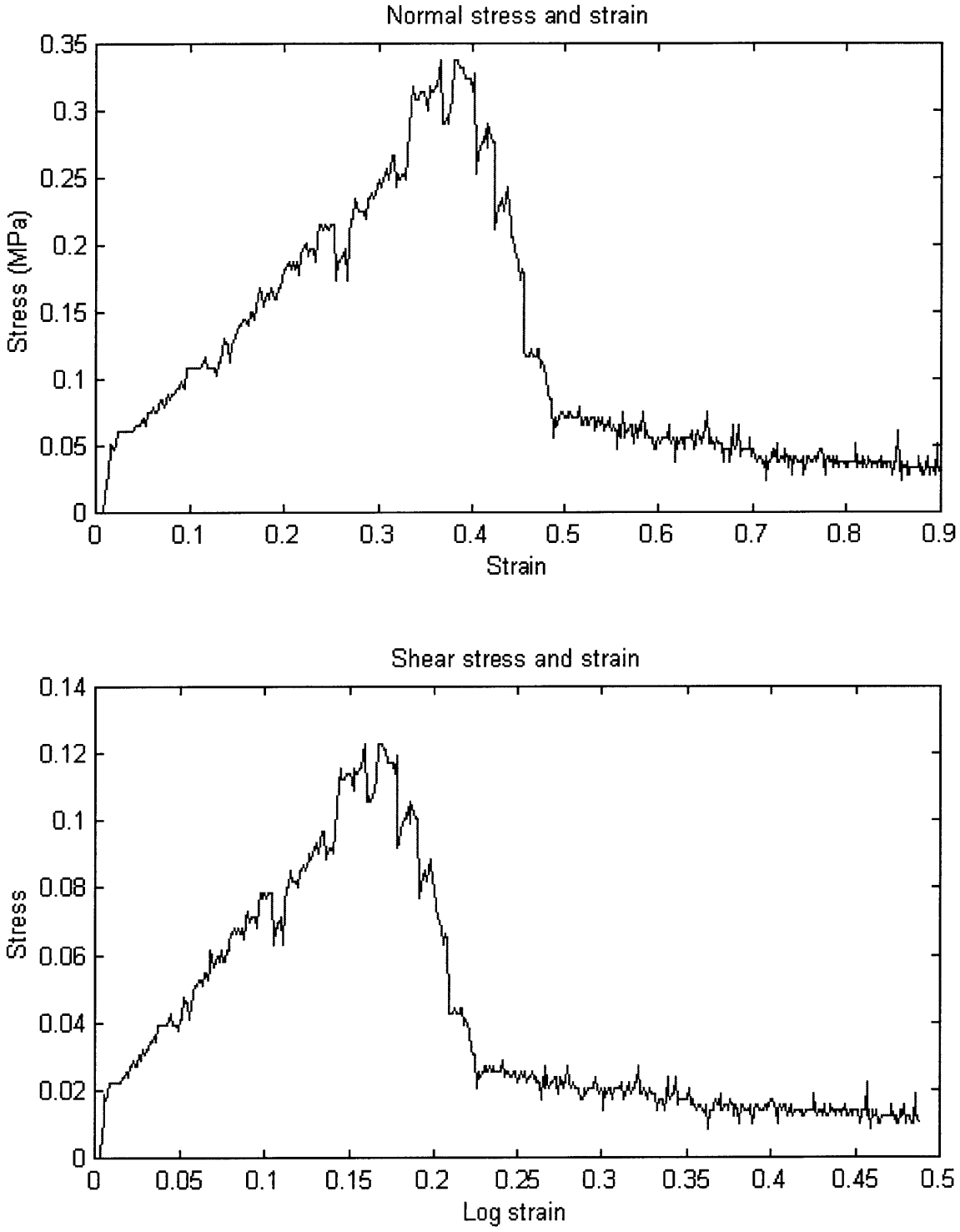

Figure 7-3: Microscale Triplex MD 20-degree combined loading stress-strain data.

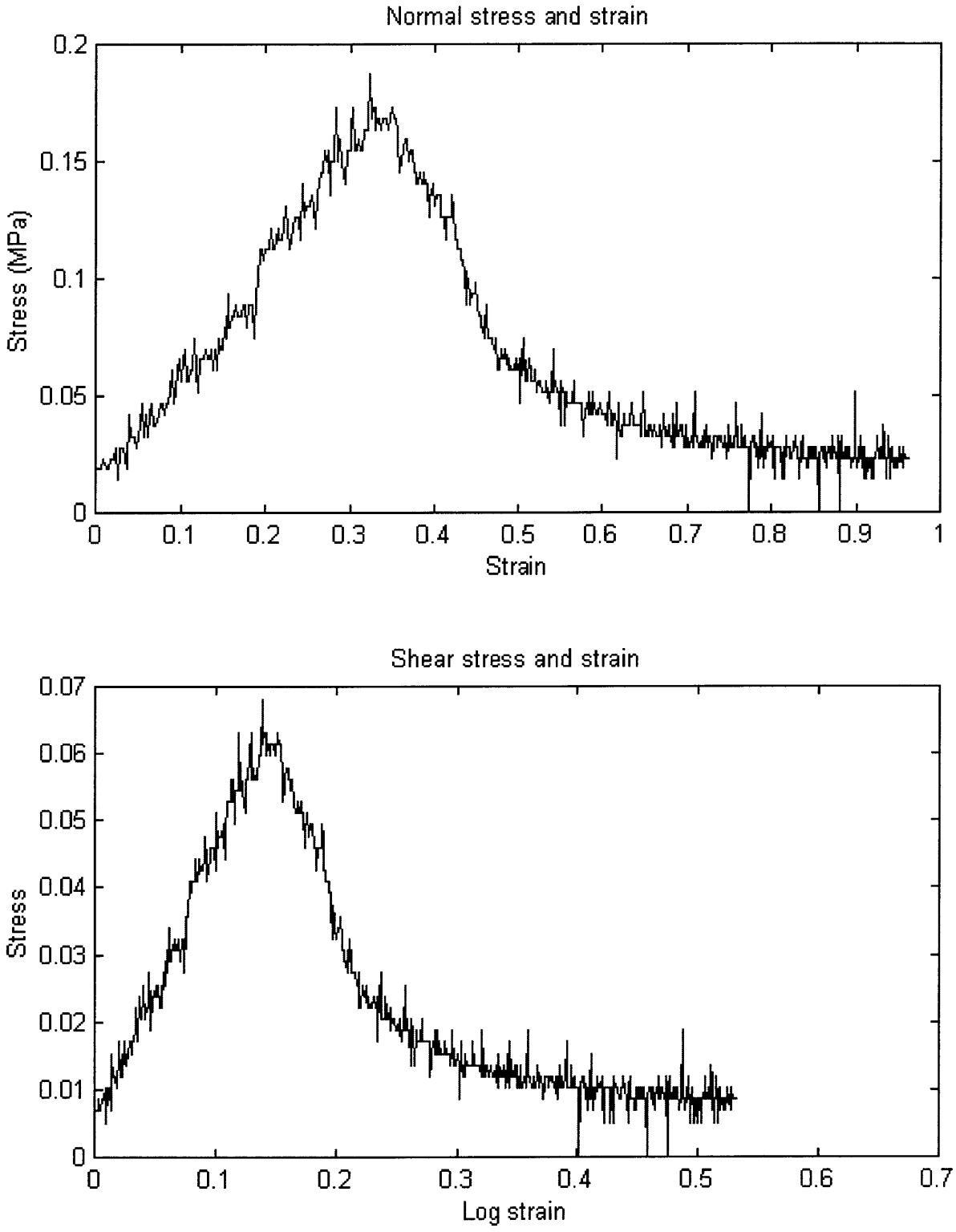

Figure 7-4: Microscale Triplex CD 20-degree combined loading stress-strain data.

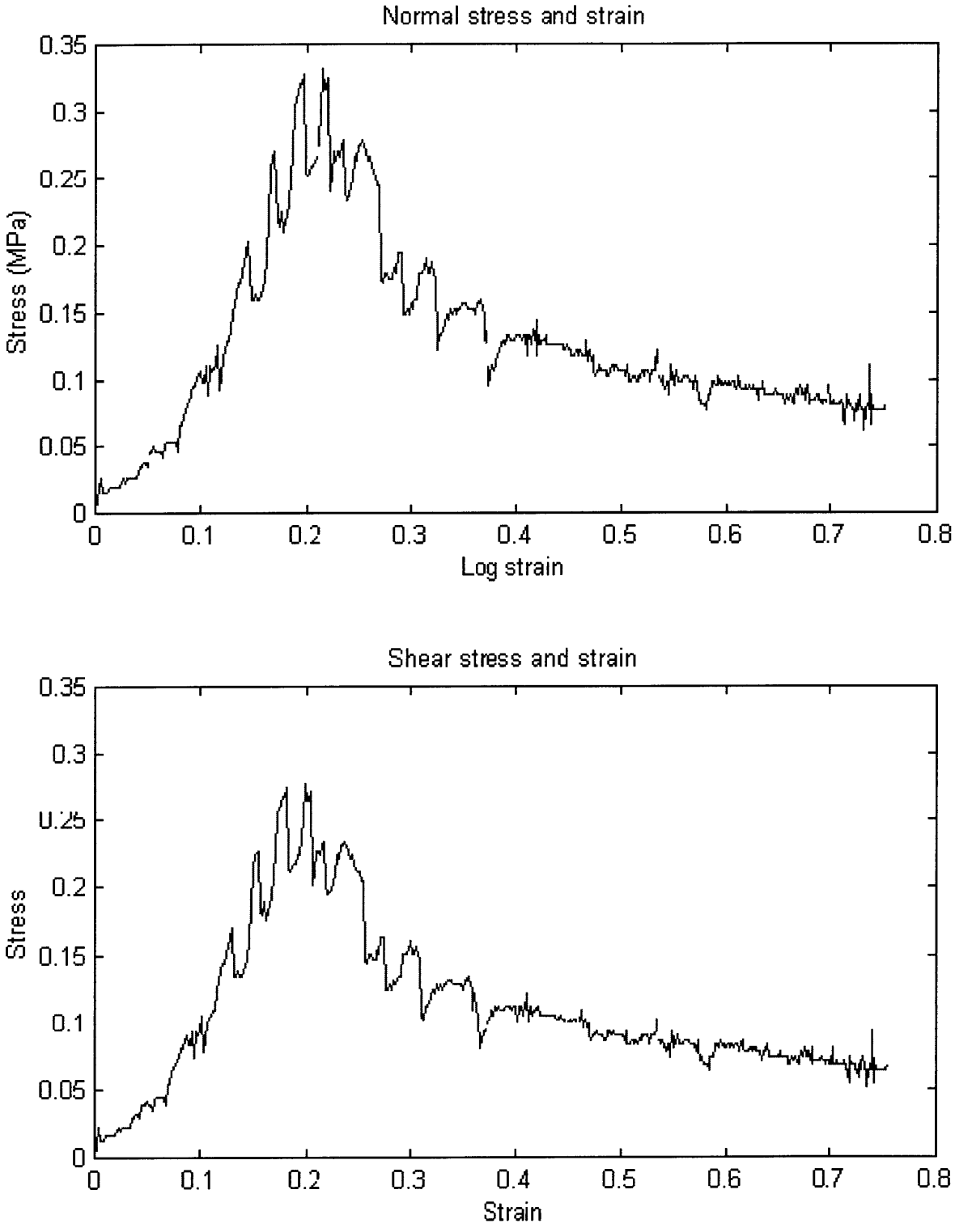

Figure 7-5: Microscale Triplex MD 40-degree combined loading stress-strain data.

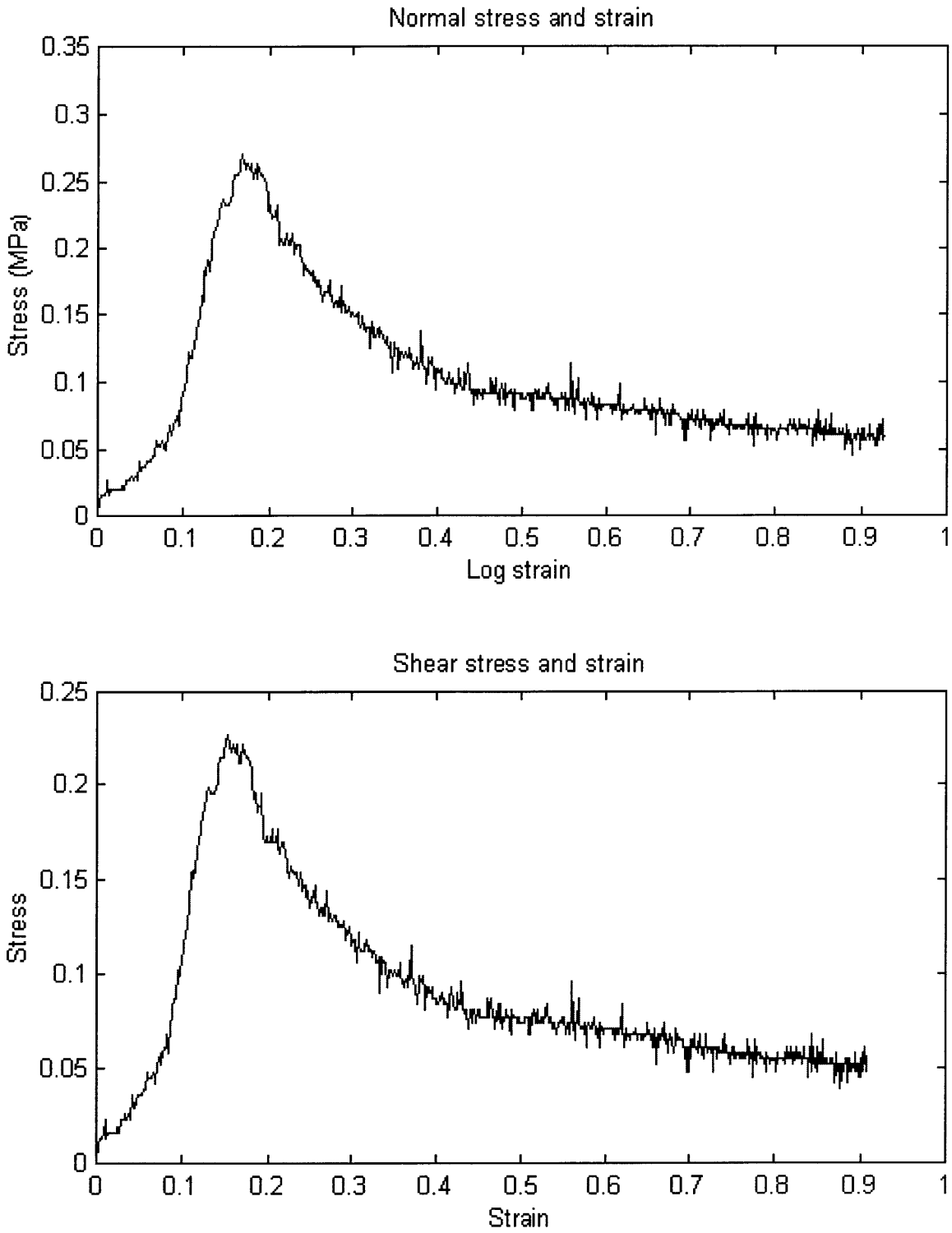

Figure 7-6: Microscale Triplex CD 40-degree combined loading stress-strain data.

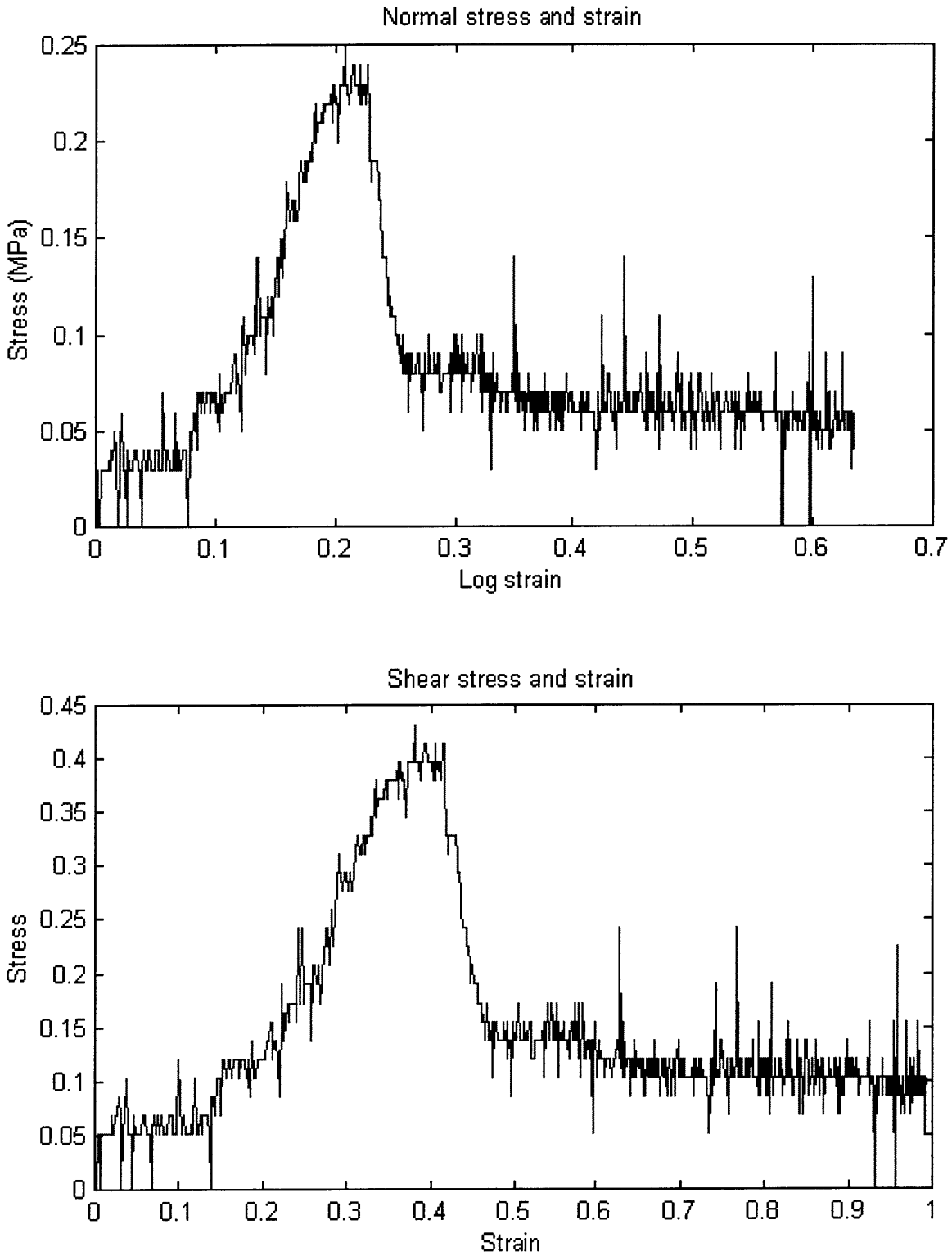

Figure 7-7: Microscale Triplex MD 60-degree combined loading stress-strain data.

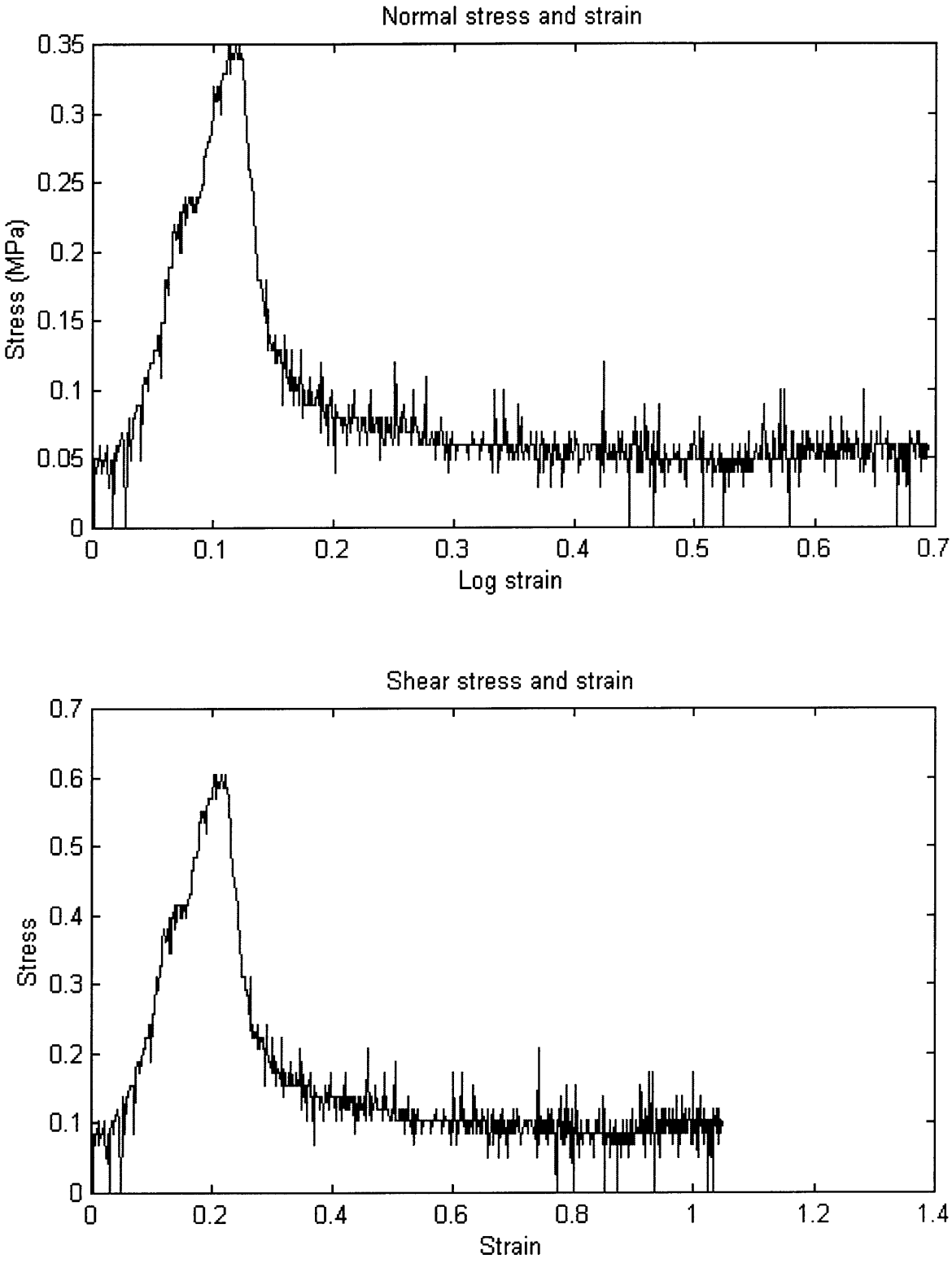

Figure 7-8: Microscale Triplex CD 60-degree combined loading stress-strain data.

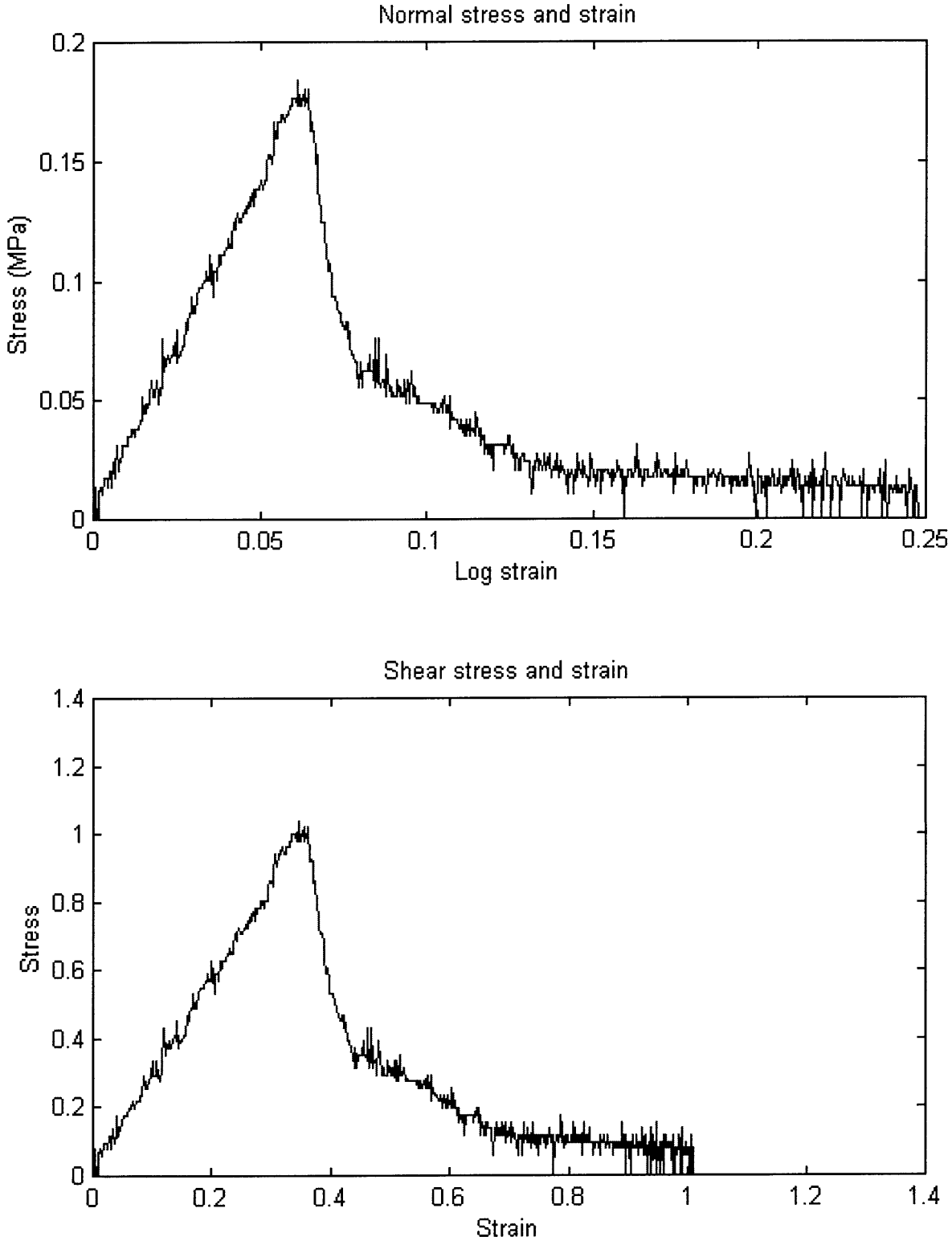

Figure 7-9: Microscale Triplex MD 80-degree combined loading stress-strain data.

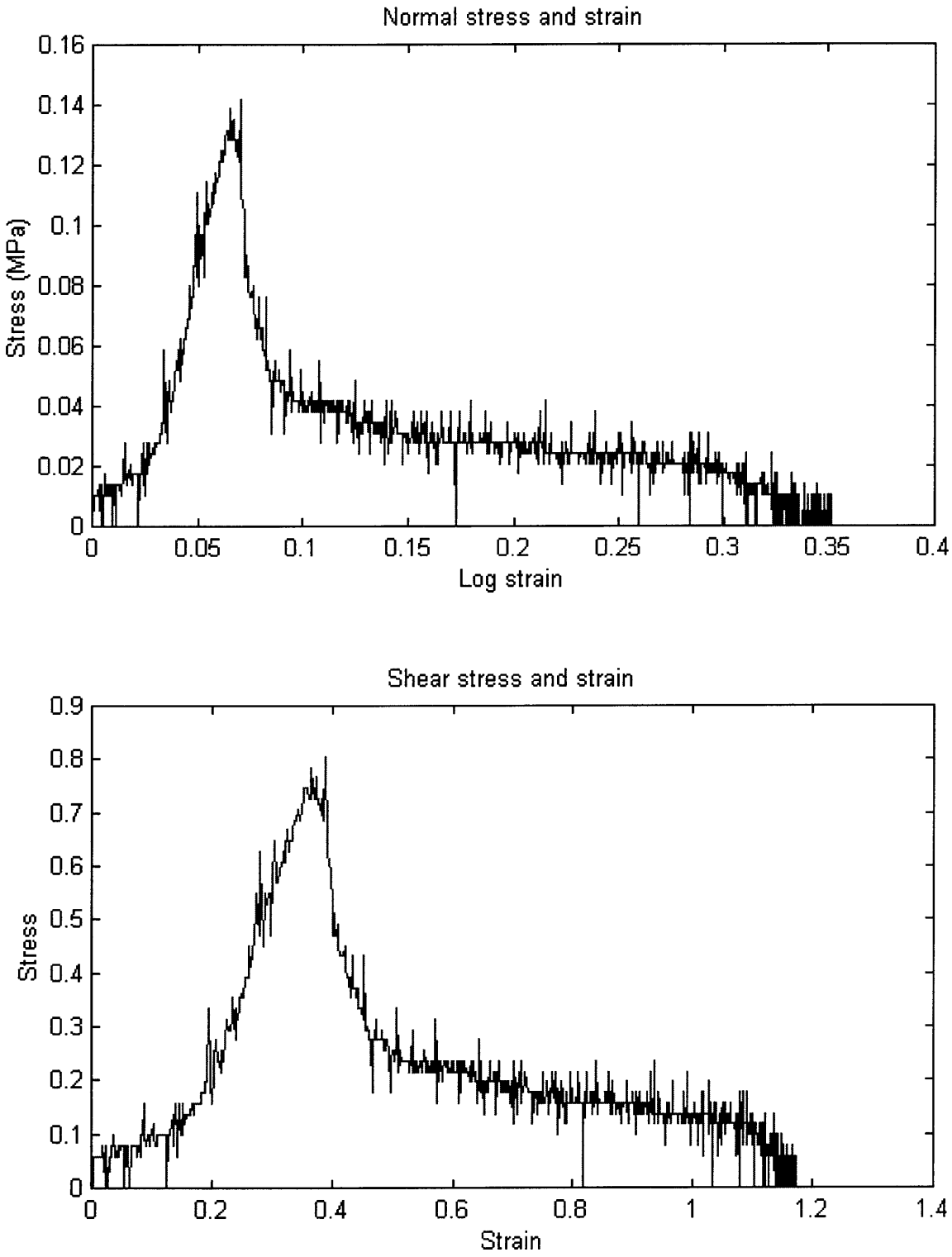

Figure 7-10: Microscale Triplex CD 80-degree combined loading stress-strain data.

tension is defined as $\theta = 0^o$, and interlaminar shear is defined as $\theta = 90^o$. Thus, small-angle loads are primarily tensile. Larger-angle loads are primarily shear in nature. Stress and strain in these and all curves presented in this chapter were calculated using the definitions given in Chapters 4 (tensile components) and 6 (shear components).

The general shape of the curves does not change with increasing angle, but the amount of stress and strain exhibited does change. The change in the normal stress component, viewed as a function of normal strain between 18^o and 72^o, loading is relatively small. The peak stress decreases from 0.30 MPa only to 0.23 MPa, a change of 0.07 MPa. The peak stress actually increases slightly between the first two combined-loading levels, 18^o and 36^o. This is likely due to variation between specimens and highlights the relative insensitivity of tensile peak stress to loading angle. In contrast, the peak stress component in shear changes drastically, falling from just over 0.7 MPa at 72^o to about 0.1 MPa at 18^o, a change of 0.6 MPa.

The change in strain at peak shows similar variability. The tensile strain at peak fell from 10% at 18^o loading to about 6% at 72^o loading. This is less than a factor of two difference. Shear strain at peak increased from approximately 0.5% at 18^o loading to 3.5% at 72^o loading. Although the absolute change of 3% was less than that in tensile strain, relative change was much larger, a factor of 7.

Figures 7-3 through 7-10 present microscopic stress-strain behavior under various combined-loadings. This data should be compared to the macroscopic data with caution, as the experimental techniques were different for each. The macroscopic experiments were performed on the modified Arcan device described in Chapter 2. The Arcan device has a one-point pin connection to the test head on each side, so no moment can be transferred. Knowing the load being applied by the test head, one can calculate the normal and shear components with confidence.

The microscopic experiments were performed on a series of fixtures, also described in Chapter 2, that were rigidly connected to the deformation stage. A rigid constraint does transmit the desired load in the direction of travel, but it also transmit load perpendicular to this direction and a moment load. The normal and shear displacement can be calculated with surety, but the actual loads on the specimen cannot be de-

termined from the load along the travel direction alone. The microscopic data does still offer useful insights, but the difference between the microscopic and macroscopic data must be kept in mind.

In the machine direction, peak tensile stress decreased from 0.33 MPa to 0.18 MPa with a change in loading from 20^o to 80^o. Peak shear stress changed much more dramatically, increasing from 0.12 MPa at 20^o to 1.0 MPa at 80^o. Values for shear loading in the cross direction show the same trends. A comparison of strain at the peak is not as useful at the microscopic level as at the macroscopic level due to the the fixture slackness and motor stutter discussed in Chapter 4.

Unlike the macroscopic data, the microscopic data does show a change in shape with combined-loading level. In general, data collected at 20^o and 40^o, loadings dominated by through-thickness tension, displays a more gentle post-peak drop than data collected at the shear-dominated 60^o and 80^o loading levels. Recall from earlier chapters that a more gentle post-peak drop is commonly observed in through-thickness tension data than in shear data at the microscopic level. Stress typically drops off very dramatically after the peak in shear loading. However, this trend is not commonly noticed at the macroscopic level in pure tensile and shear loadings, as is the case with the macroscopic combined-loading data presented here.

Figure 7-11 is the peak stress surface for Triplex with shear loading in the machine direction. The macroscopic data shown was compiled by taking an average of failure stress values collected at each loading level. The difference in range on the axes makes the surface appear to be a circular arc. However, curve fitting this data produced a parabolic model for the failure surface, where S represents failure strength.

$$S_{shear,md} = S_{o,md} - 1.53S_{normal,md} - 3.13\frac{S^2_{normal,md}}{S^*} \tag{7.1}$$

In this expression, the constant $S_{o,md}$ is 1.06 MPa, and S^* is 1.0 MPa. The microscopic data follows the same general trend as the macroscopic data, but shows large variation at each load level. This is due to the error sources discussed in Appendix A.

Similar trends are seen in Figure 7-12, a peak stress surface for Triplex with shear

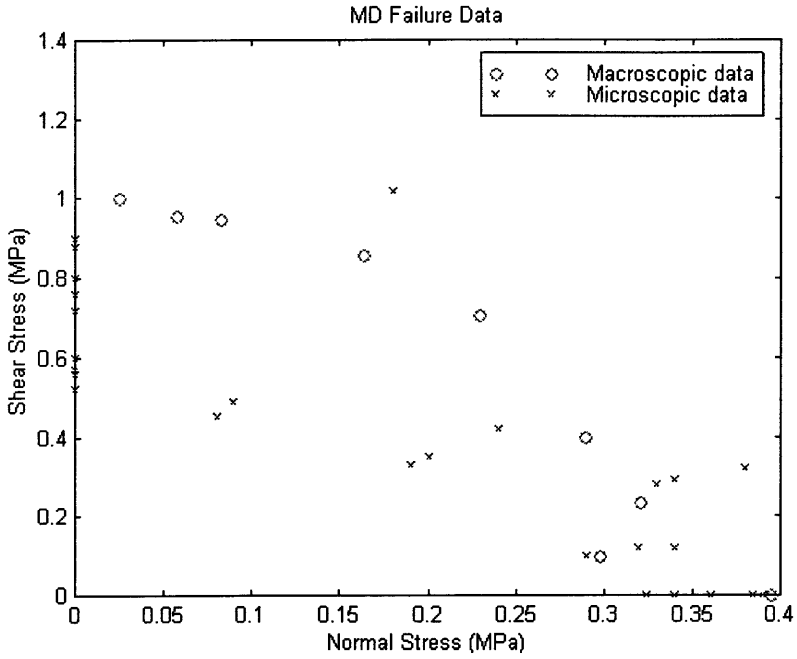

Figure 7-11: Peak stress surface for Triplex with shear loading in the machine direction. (Macroscopic data courtesy of N. Stenberg.)

loading in the cross direction. The macroscopic data in this figure was also curve fit to a parabolic model.

$$S_{shear,cd} = S_{o,cd} - 1.36S_{normal,cd} - 2.44\frac{S_{normal,cd}^2}{S^*} \tag{7.2}$$

Here, $S_{o,cd}$ is 0.94 MPa. S^* is again 1.0 MPa.

7.2 Microscopic Level Deformation Images

Images of combined-loading tests were collected at the microscopic level for shear loads in both the machine and cross directions. The images showed a transition between the extensive microcracking of tension-dominated loading to the sudden failure by macrocrack of shear-dominated loading. Figures 7-13 through 7-20 show a 20^o combined-loading experiment, with shear load in the machine direction. In a 20^o test, the tensile component of the load is dominant, and the mechanisms observed

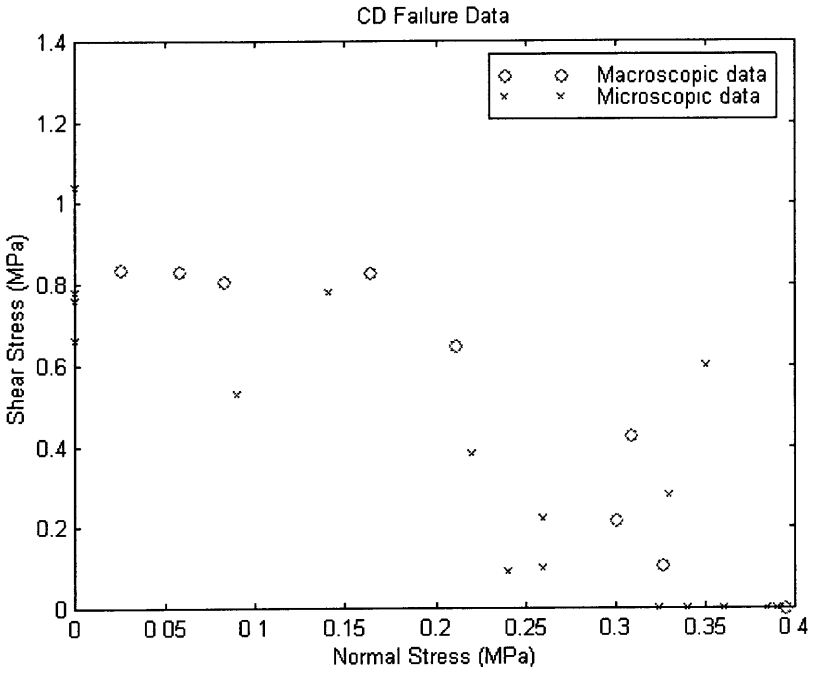

Figure 7-12: Peak stress surface for Triplex with shear loading in the cross direction. (Macroscopic data courtesy of N. Stenberg.)

are similar to those seen in through-thickness tension experiments.

Figure 7-13 depicts the specimen at no load. The specimen is under significant load in the next image, but shows no discernable deformation. The third image, Figure 7-15, was taken almost exactly at the peak in stress. Microcracking is beginning, although the damage is barely visible in this image. The next image, taken shortly after the peak, shows the growing microcracks clearly. In the image of step 5, microcracks near the left edge of the specimen are begining to coalesce into a macrocrack. This image was taken at the beginning of a plateau in the data, similar to those seen in through-thickness tension data. Figures 7-18 and 7-19 show the macrocrack growing and other microcracks closing up. The fibers bridging the macrocrack rotate to align with the direction of loading as the test progresses. The final image shows the entire specimen. The amount of shear deformation, along the length of the specimen, is very small compared to the normal deformation, through the thickness of the specimen. In summary, this specimen exhibited deformation mechanisms similar

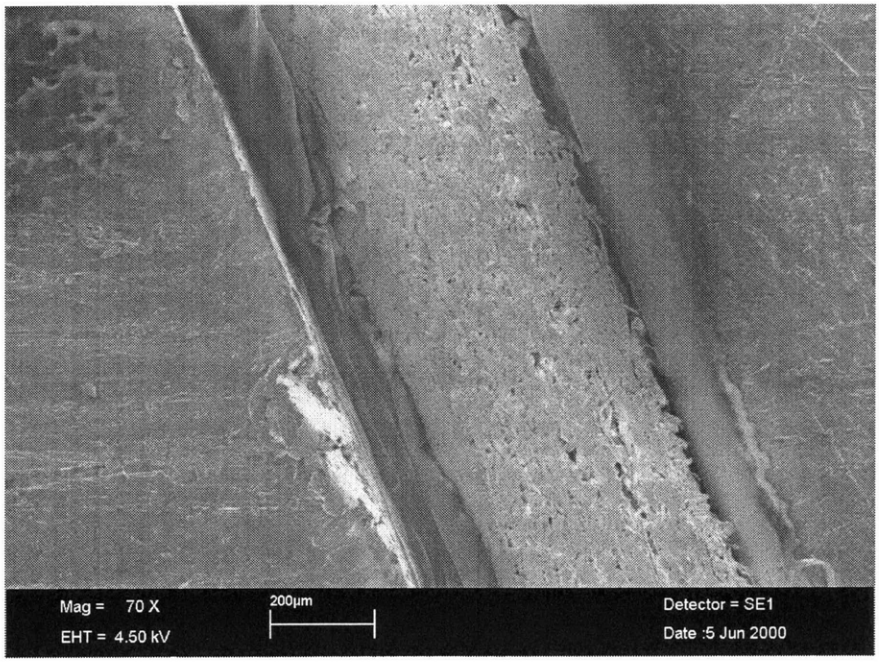

Figure 7-13: Triplex MD 20-degree combined-loading test at no load (Step 1).

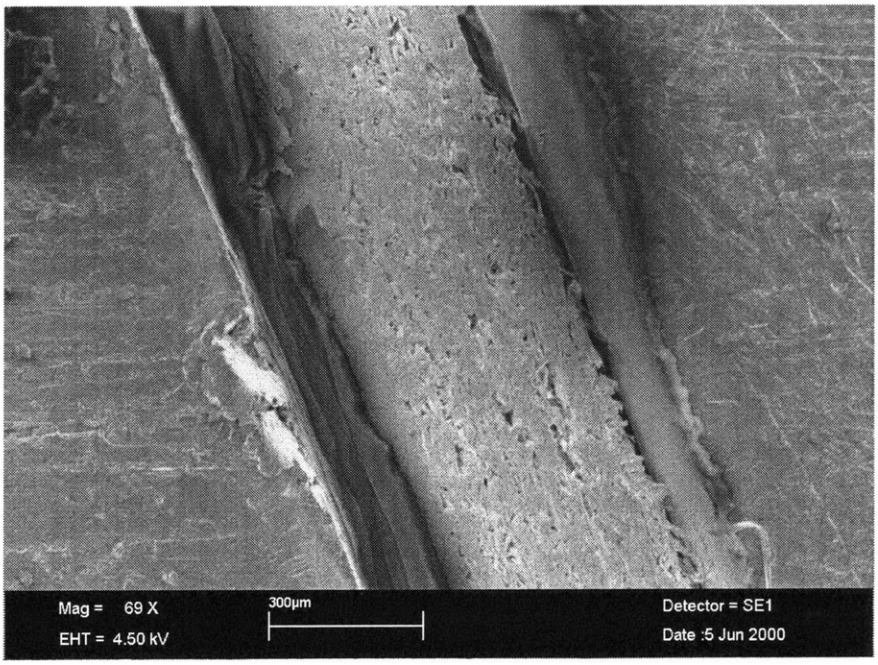

Figure 7-14: Triplex MD 20-degree combined-loading test (Step 2).

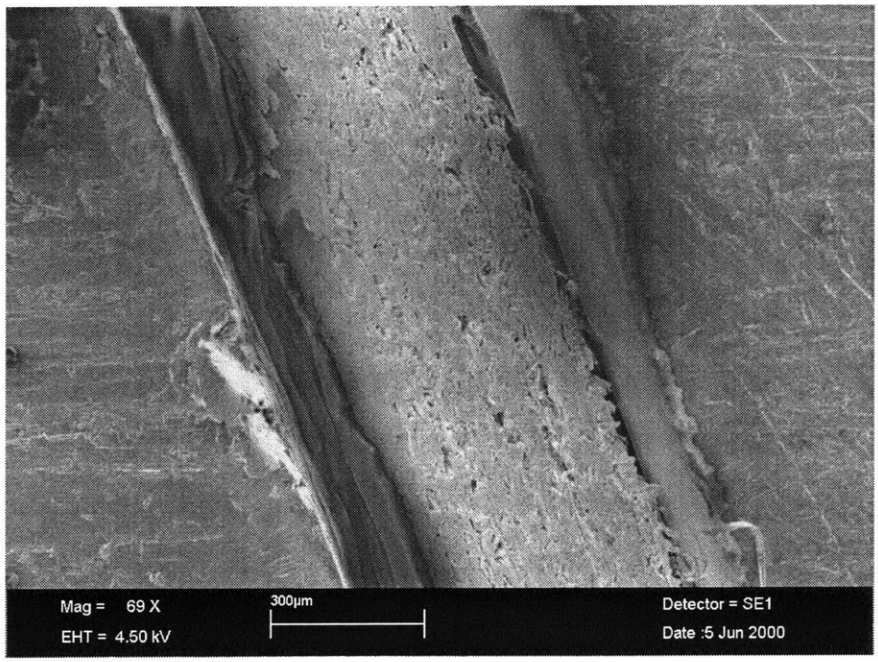

Figure 7-15: Triplex MD 20-degree combined-loading test (Step 3).

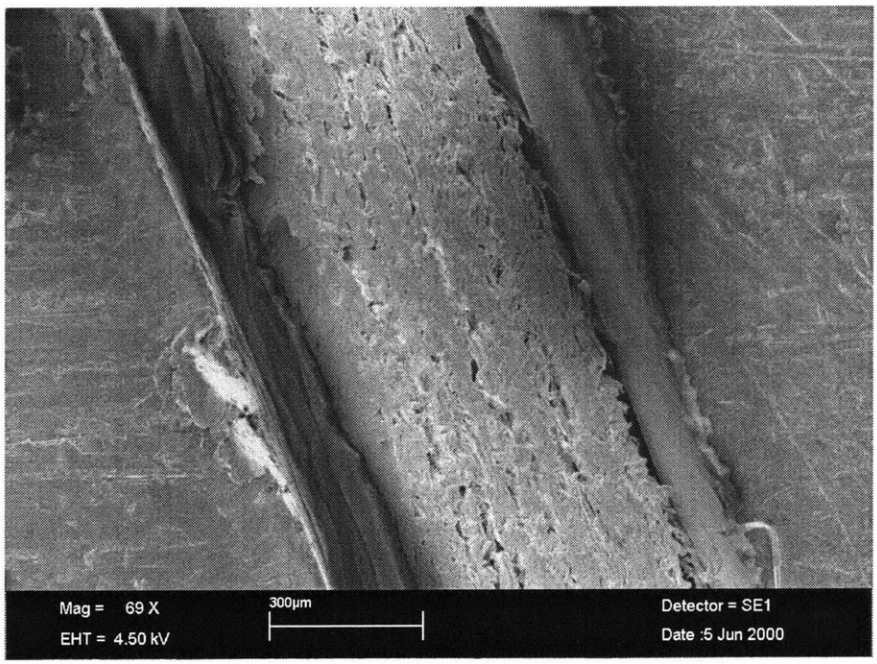

Figure 7-16: Triplex MD 20-degree combined-loading test (Step 4).

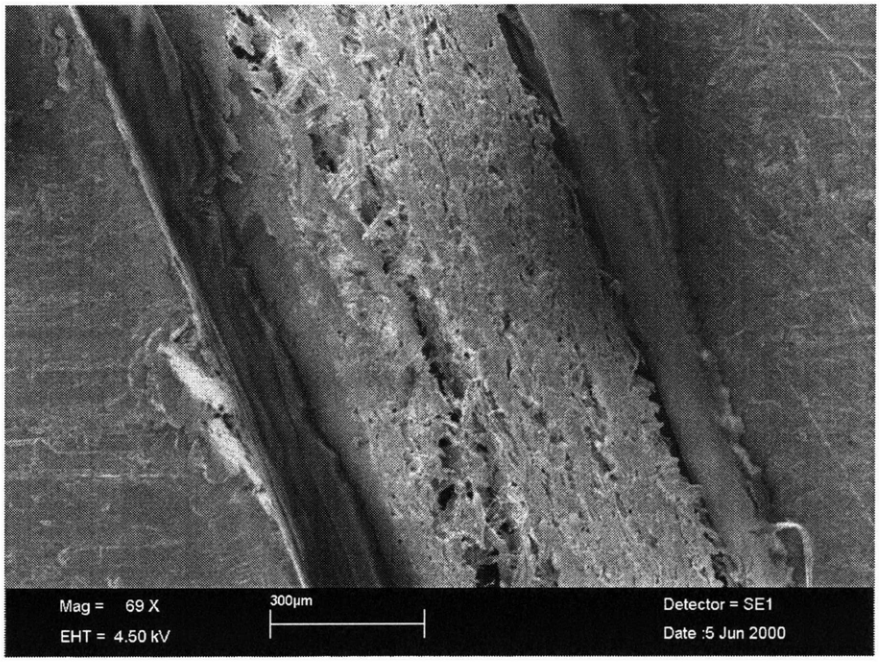

Figure 7-17: Triplex MD 20-degree combined-loading test (Step 5).

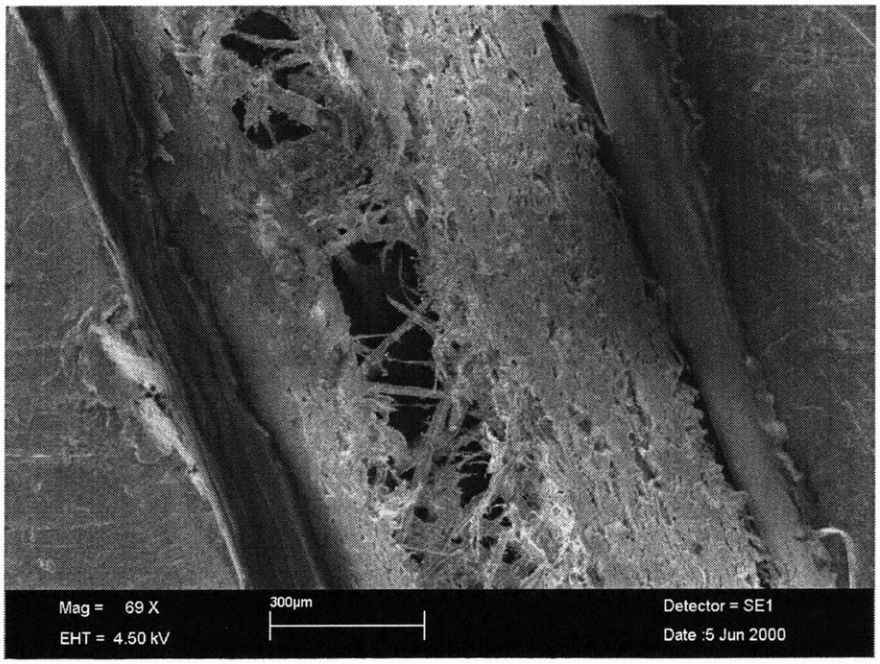

Figure 7-18: Triplex MD 20-degree combined-loading test (Step 6).

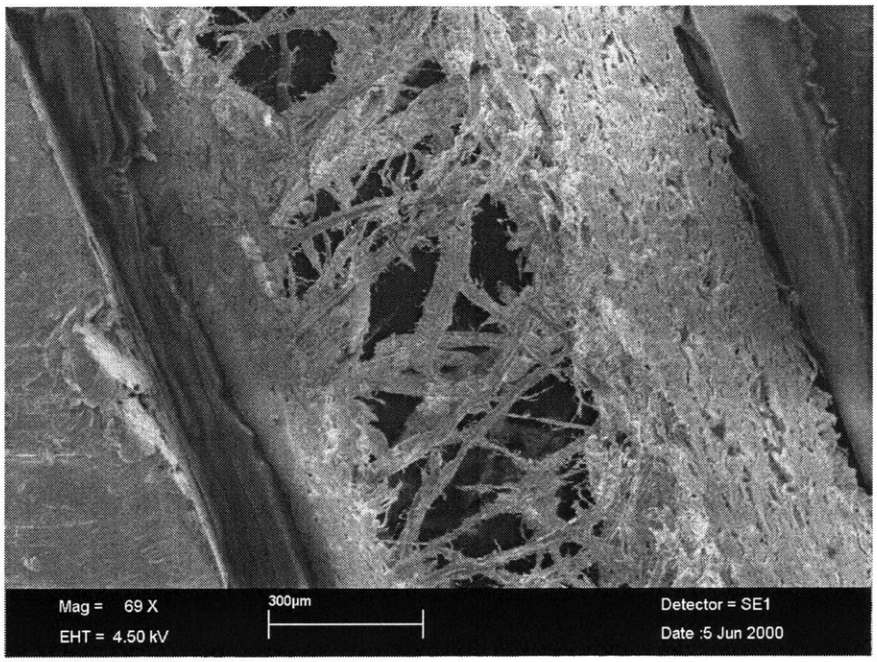

Figure 7-19: Triplex MD 20-degree combined-loading test (Step 7).

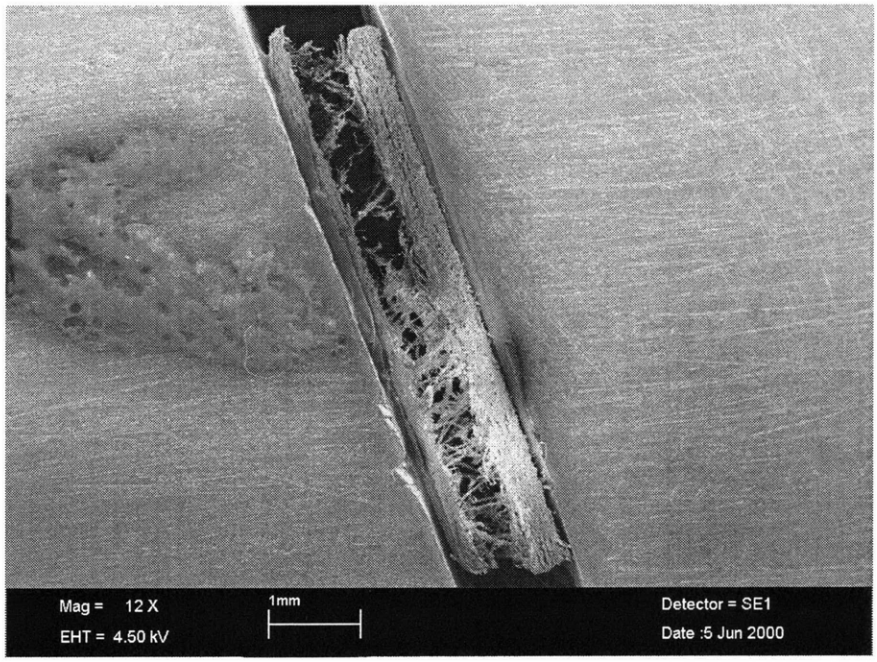

Figure 7-20: Full view of Triplex MD 20-degree combined-loading test (Step 7).

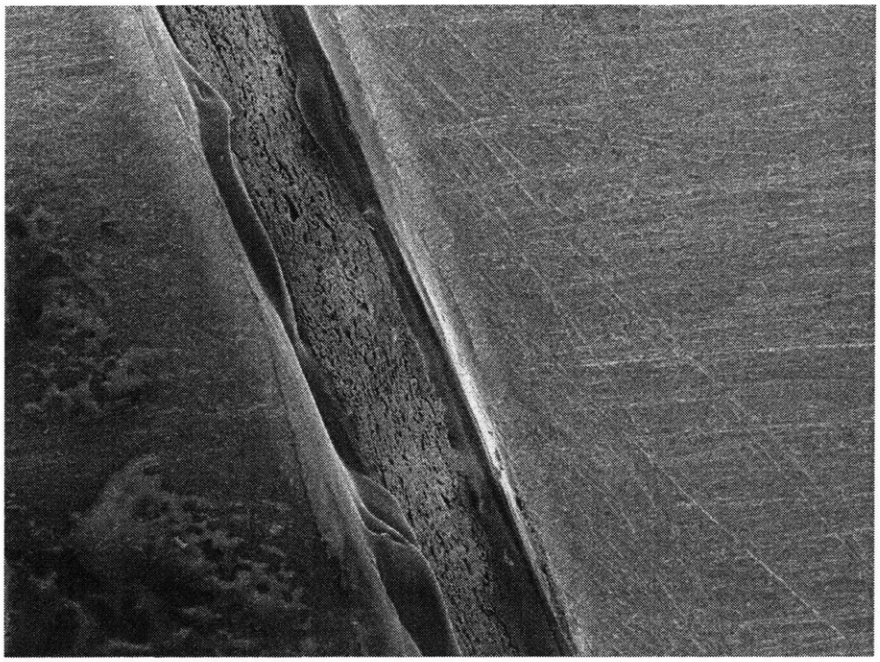

Figure 7-21: Triplex CD 20-degree combined-loading test at no load (Step 1).

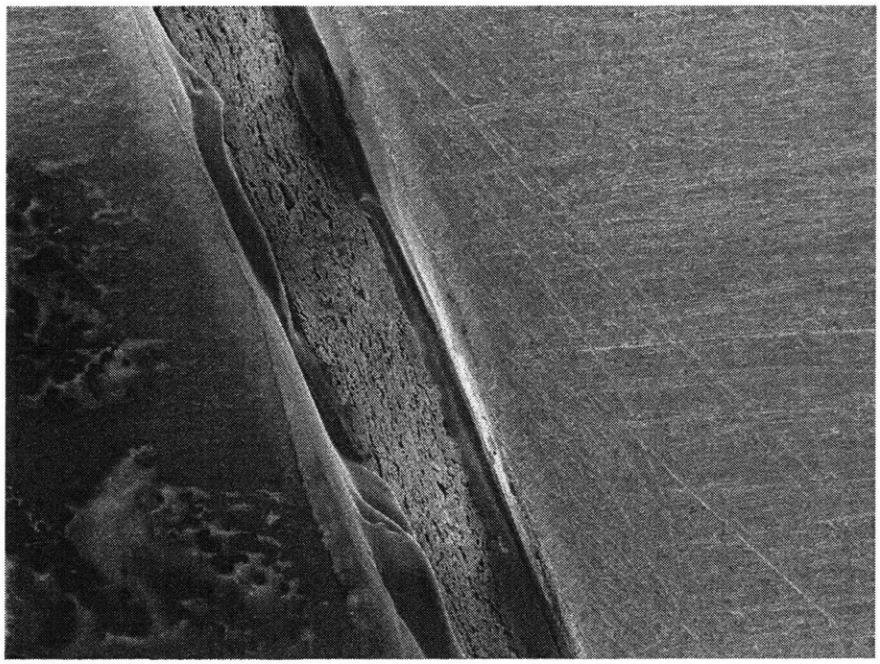

Figure 7-22: Triplex CD 20-degree combined-loading test (Step 2).

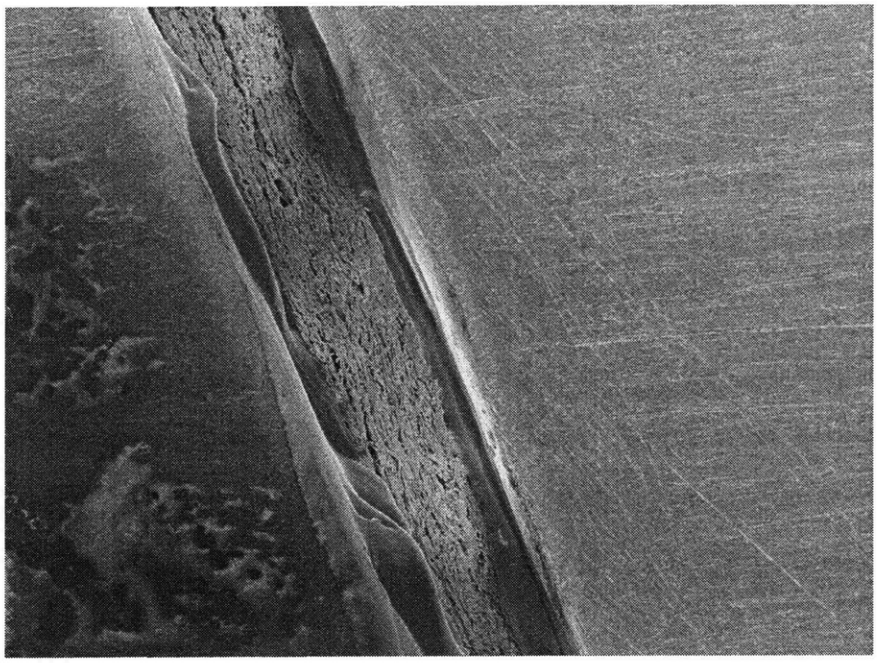

Figure 7-23: Triplex CD 20-degree combined-loading test (Step 3).

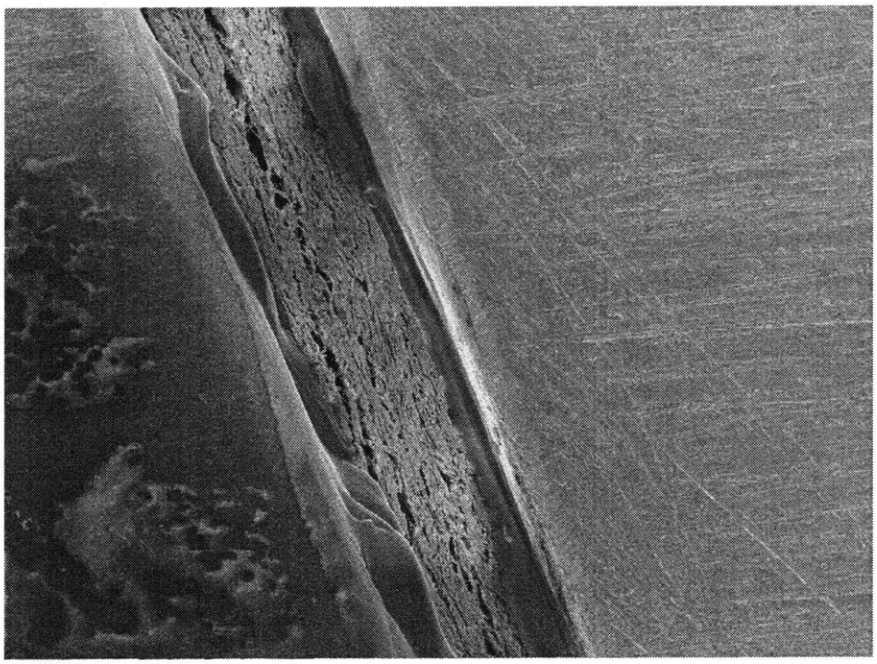

Figure 7-24: Triplex CD 20-degree combined-loading test (Step 4).

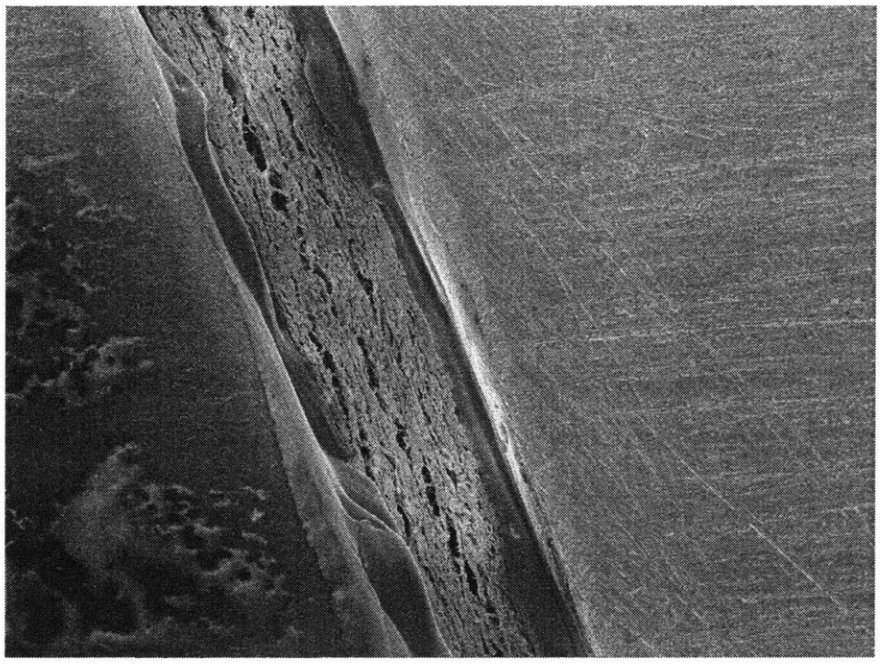

Figure 7-25: Triplex CD 20-degree combined-loading test (Step 5).

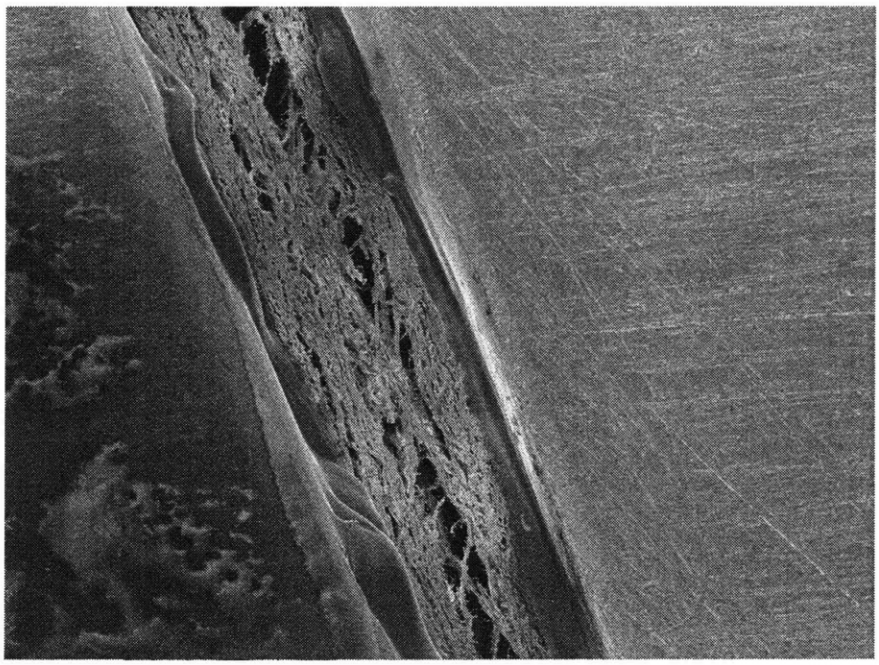

Figure 7-26: Triplex CD 20-degree combined-loading test (Step 6).

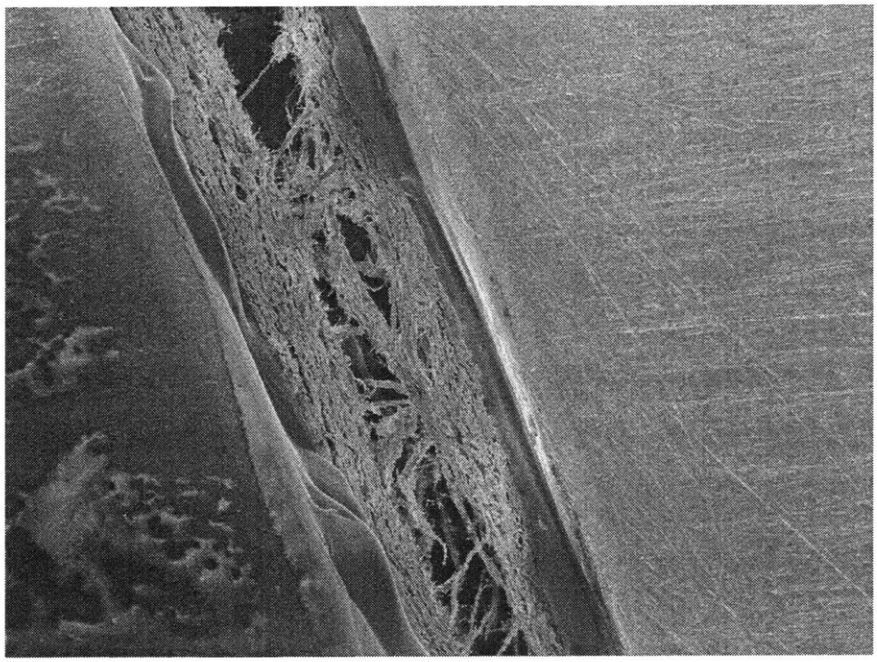

Figure 7-27: Triplex CD 20-degree combined-loading test (Step 7).

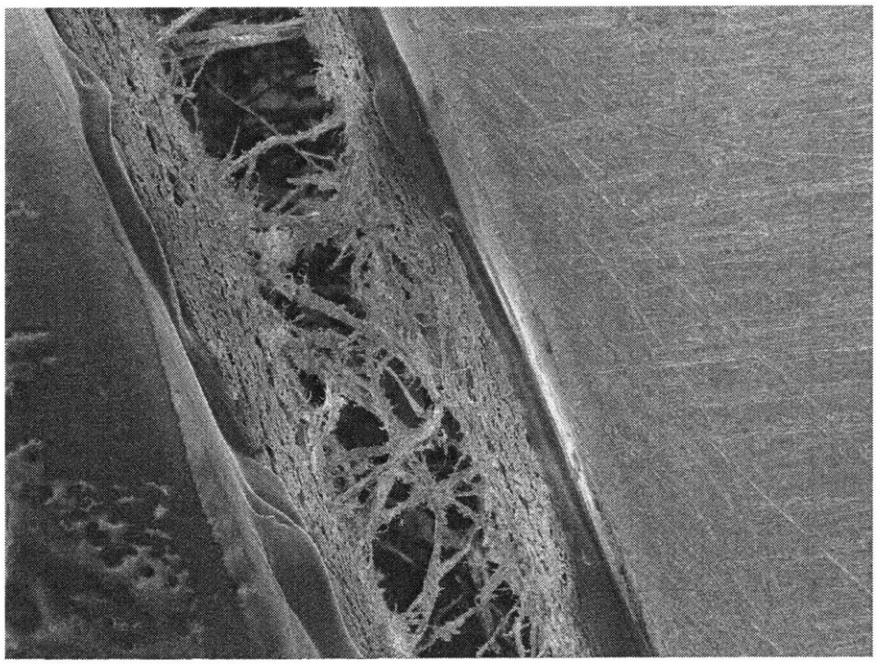

Figure 7-28: Triplex CD 20-degree combined-loading test (Step 8).

to those of material loaded in through-thickness tension. No notable deformation occurred before the peak in stress. At the peak, microcracks began to form in the material. Stress decreased quickly as the cracks grew and began to level off as one crack became dominant.

A similar pattern of deformation is observed in Figures 7-21 through 7-28, a 20^o combined-loading experiment with cross-direction shear. The specimen is depicted under no load in the first image. Microcracking begins in the third step. The microcracks begin to coalesce into a macrocrack in Figure 7-26, step 6. This macrocrack continues to grow through the remaining images as the surrounding microcracks relax and close up. Although load was not recorded when each image in this text was taken, correlation of images with events on the stress-strain curve can be extrapolated from past observations. Step 3, in which microcracking began, would correspond to a point at or shortly after the peak in the stress-strain curve, and step 6, the onset of macrocracking, would correspond to leveling out of the curve.

Images taken at 40^o combined-loading are also dominated by through-thickness tension mechanisms. A 40^o combined-loading experiment with machine-direction shear loading is shown in Figures 7-29 through 7-36. In step 1, the material is not loaded. The next image, step 2, was taken at the peak in the stress-strain curve. Microcracks are beginning to form. The microcracks grow in steps 3 and 4 and begin to coalesce in step 5, Figure 7-33. The macrocrack grows as the microcracks relax in the subsequent images. Figure 7-36 shows the full failed specimen.

A 40^o combined-loading experiment with cross-direction shear is presented as Figures 7-37 through 7-44 and follows the same deformation pattern seen thus far. In step 1, taken at no load, some pre-existing material flaws are visible. In step 3, taken at the peak in the stress-strain curve, microcracks begin to form, nucleating at the pre-existing flaws. The growing microcracks along one interface begin to merge into a microcrack in Figure 7-41. Further deformation is accommodated at the macrocrack as the microcracks close up.

At 60^o, the shear component of the combined-loading has become dominant. The deformation mechanisms begin to resemble those observed in shear experiments.

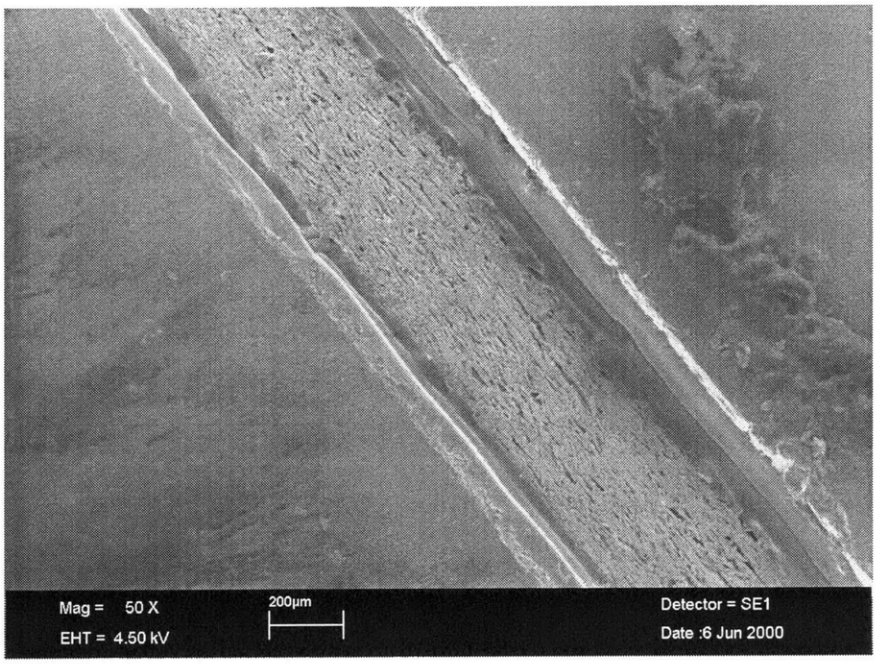

Figure 7-29: Triplex MD 40-degree combined-loading test at no load (Step 1).

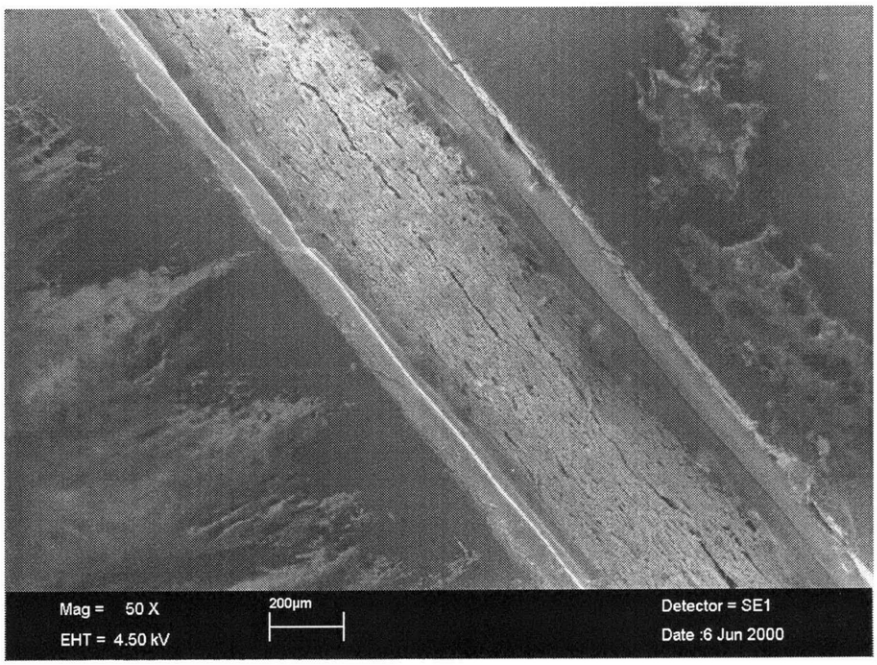

Figure 7-30: Triplex MD 40-degree combined-loading test (Step 2).

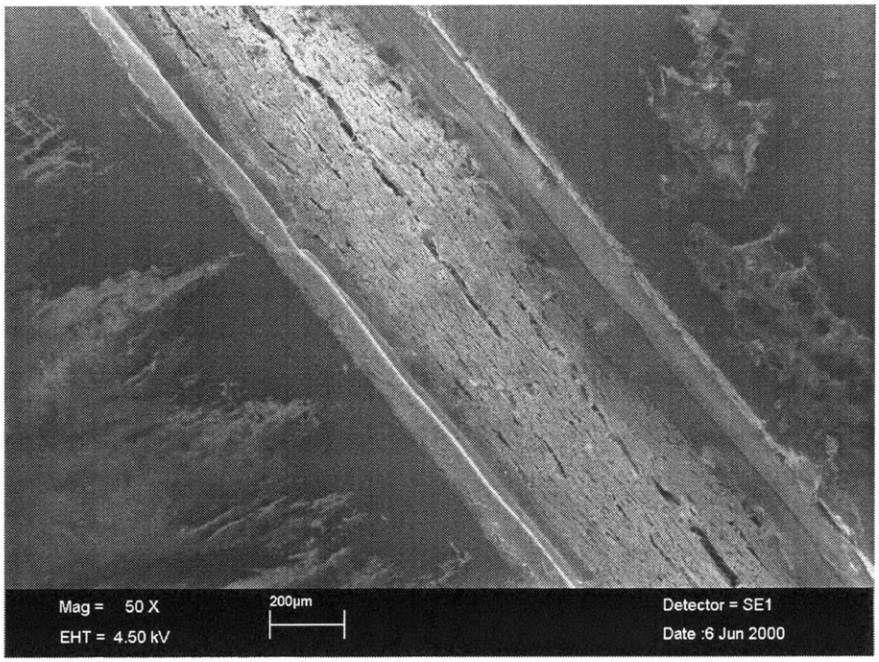

Figure 7-31: Triplex MD 40-degree combined-loading test (Step 3).

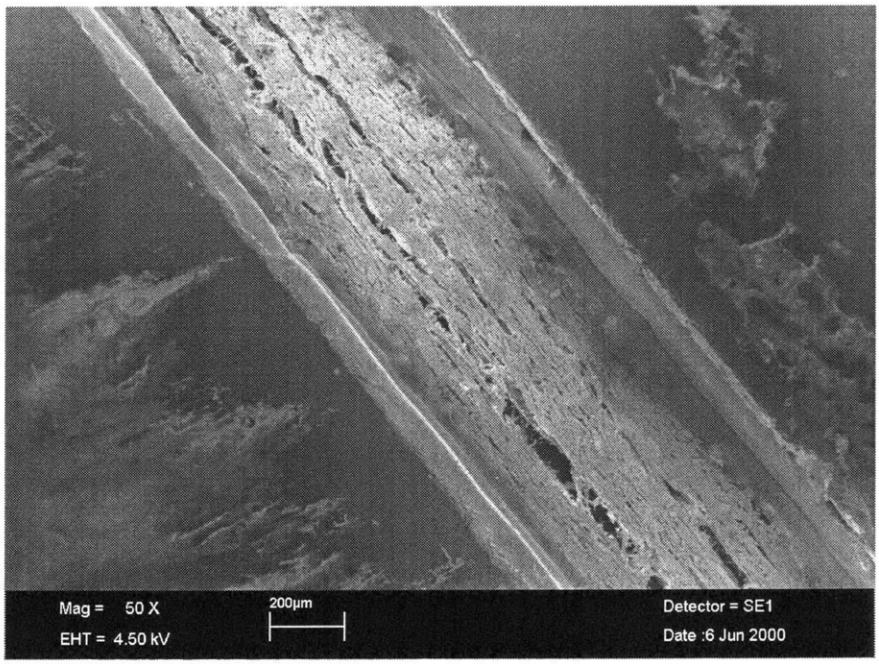

Figure 7-32: Triplex MD 40-degree combined-loading test (Step 4).

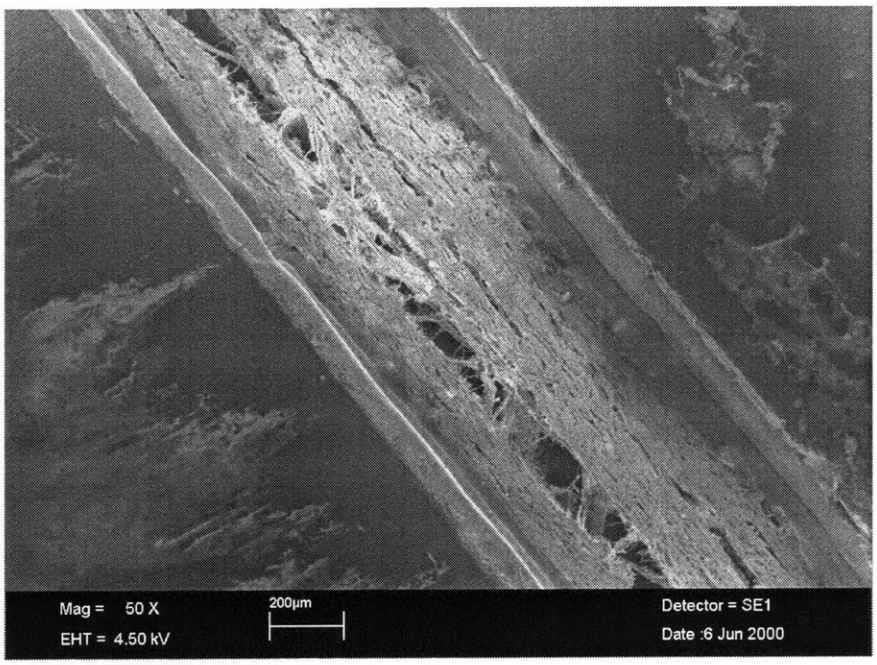

Figure 7-33: Triplex MD 40-degree combined-loading test (Step 5).

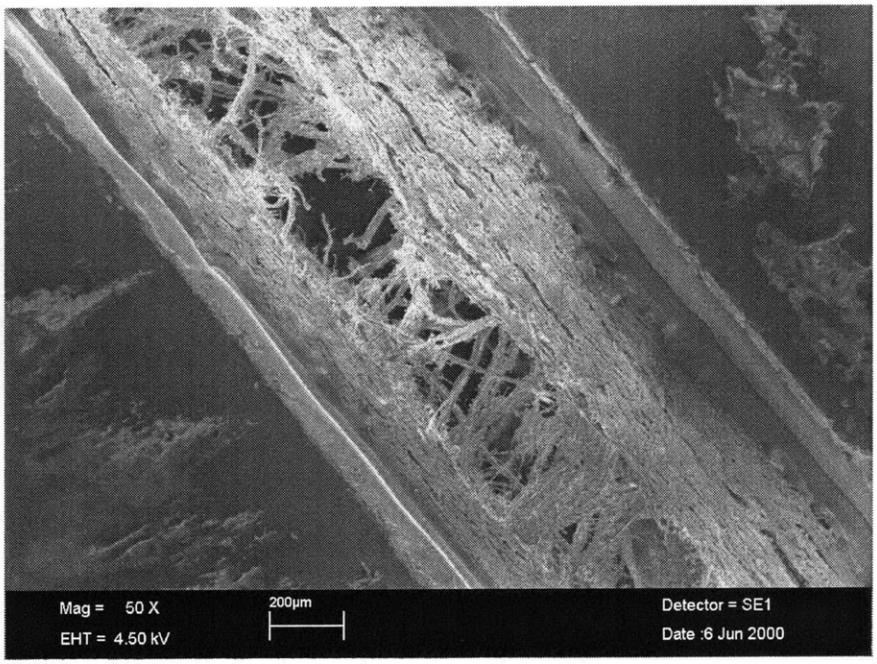

Figure 7-34: Triplex MD 40-degree combined-loading test (Step 6).

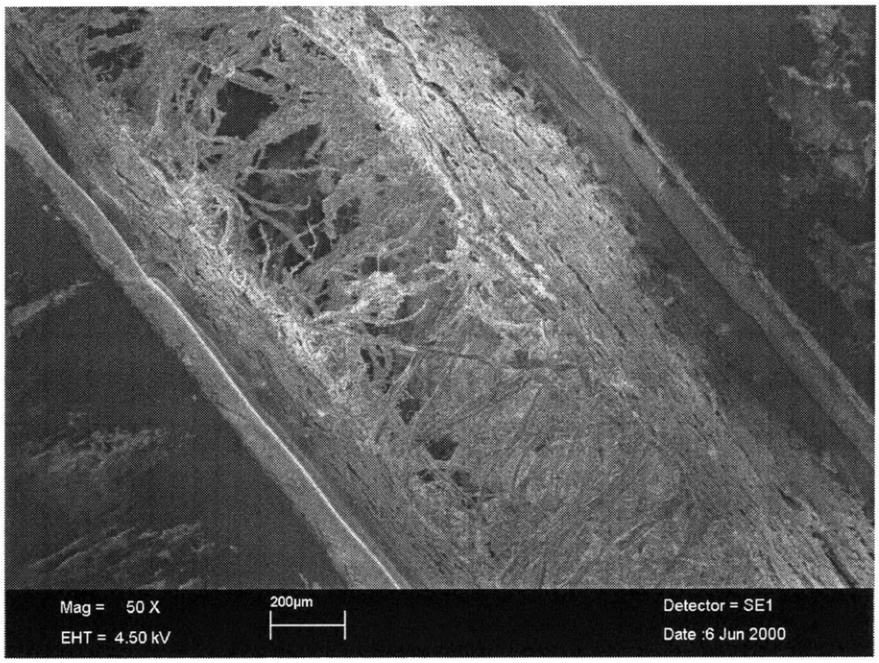

Figure 7-35: Triplex MD 40-degree combined-loading test (Step 7).

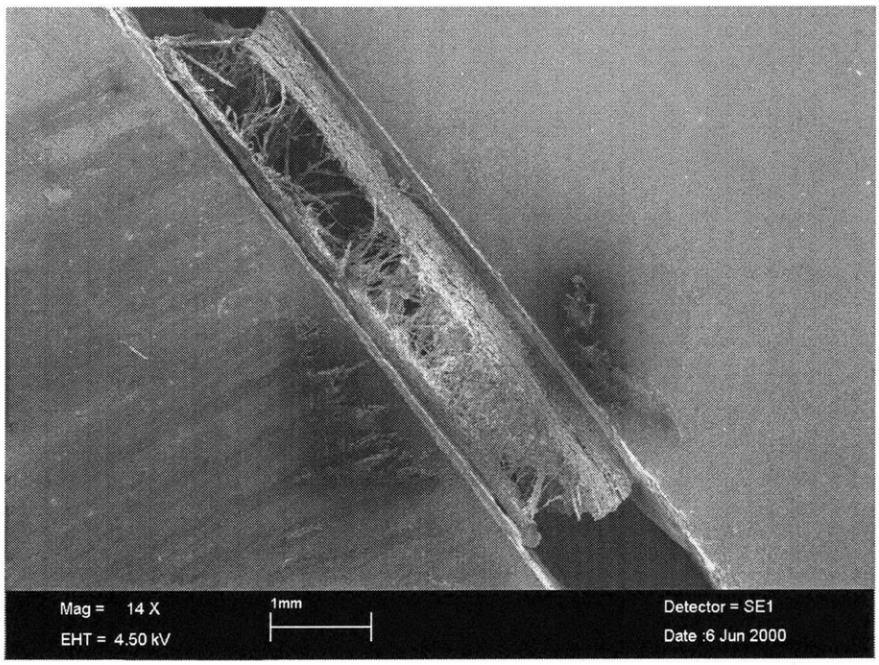

Figure 7-36: Full view of Triplex MD 40-degree combined-loading test (Step 7).

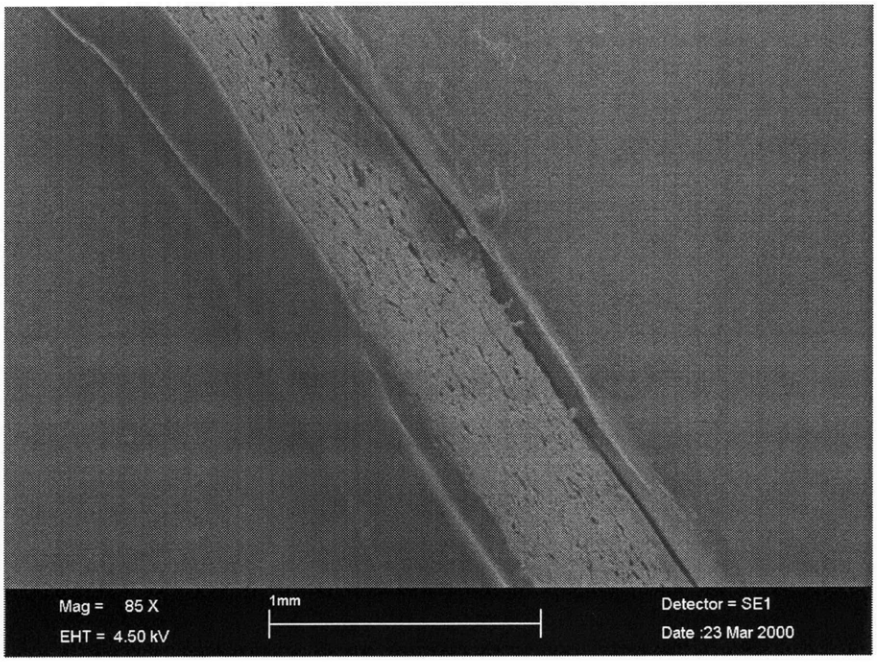

Figure 7-37: Triplex CD 40-degree combined-loading test at no load (Step 1).

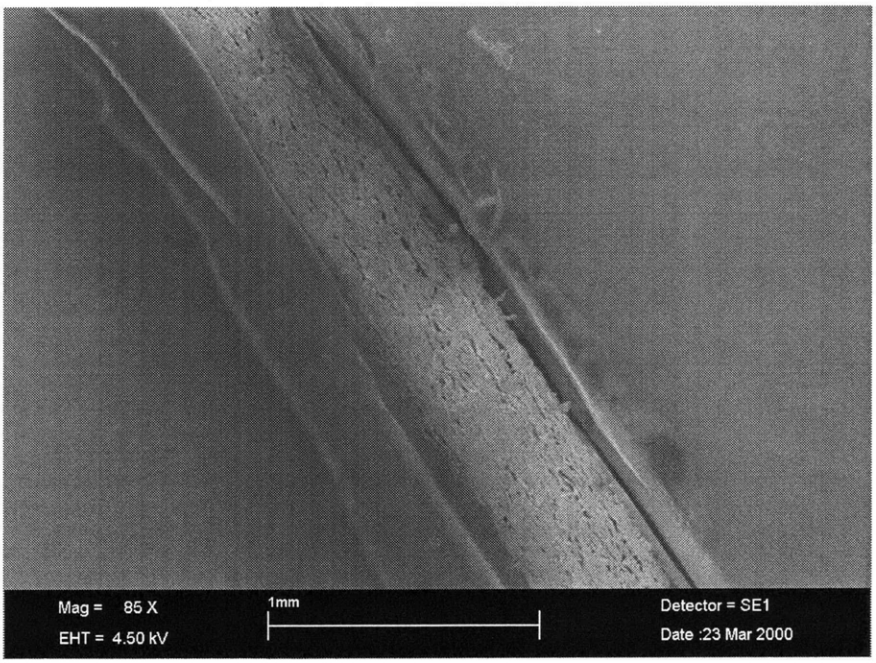

Figure 7-38: Triplex CD 40-degree combined-loading test (Step 2).

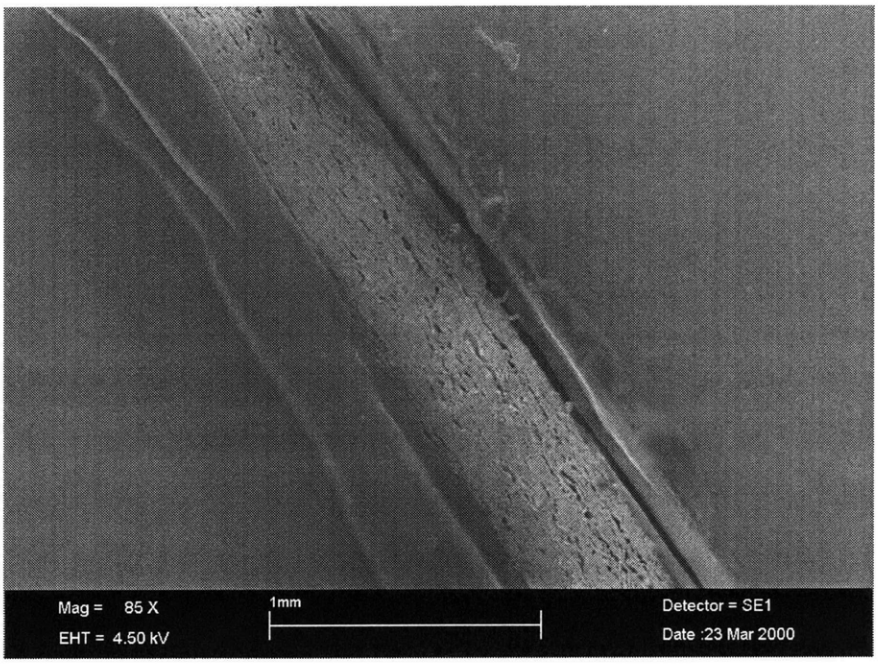

Figure 7-39: Triplex CD 40-degree combined-loading test (Step 3).

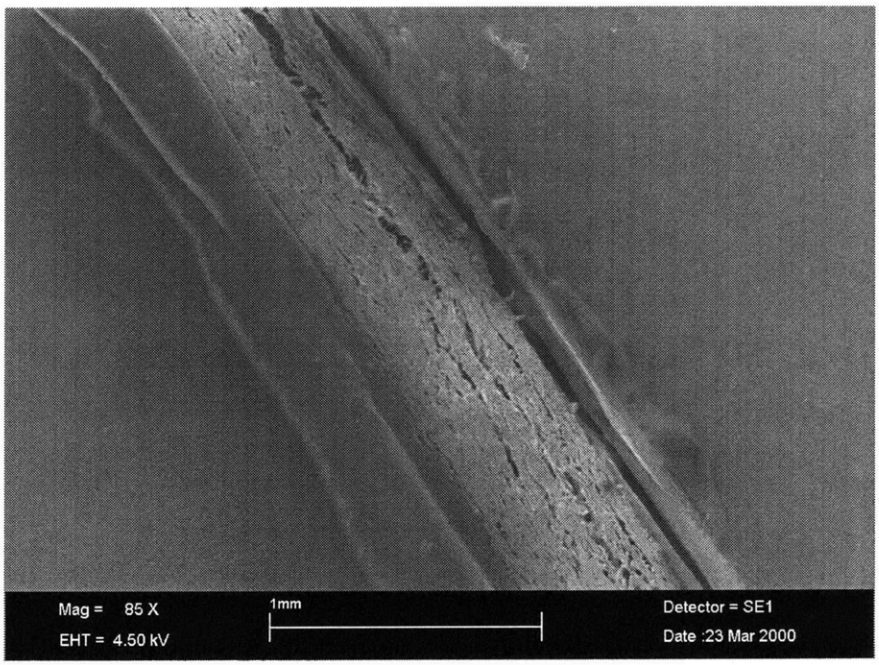

Figure 7-40: Triplex CD 40-degree combined-loading test (Step 4).

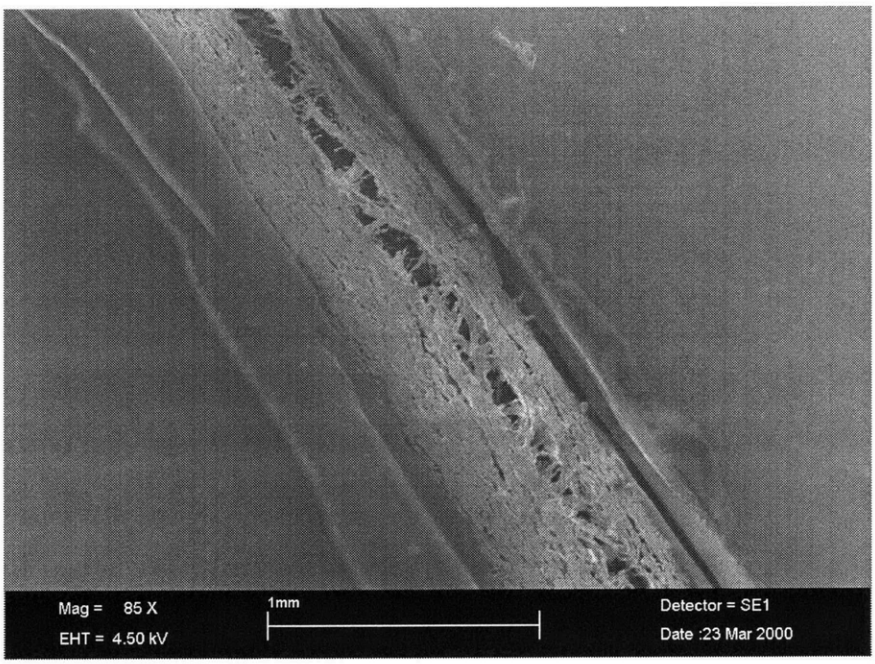

Figure 7-41: Triplex CD 40-degree combined-loading test (Step 5).

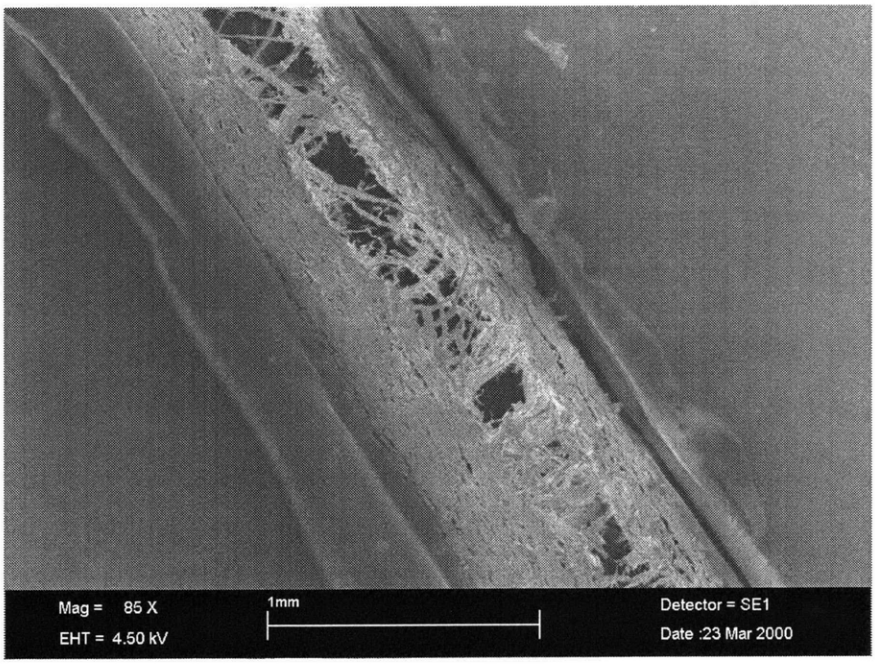

Figure 7-42: Triplex CD 40-degree combined-loading test (Step 6).

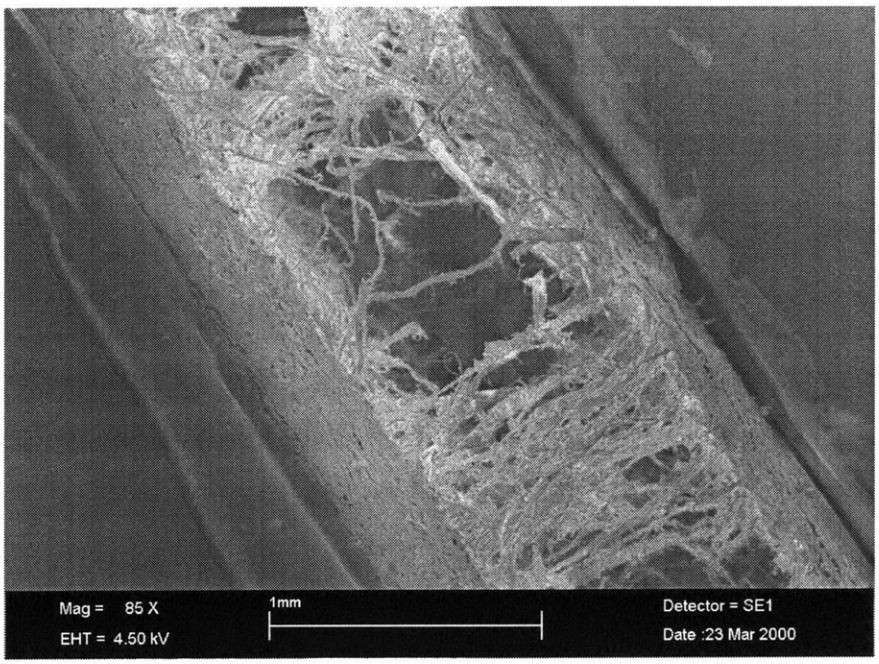

Figure 7-43: Triplex CD 40-degree combined-loading test (Step 7).

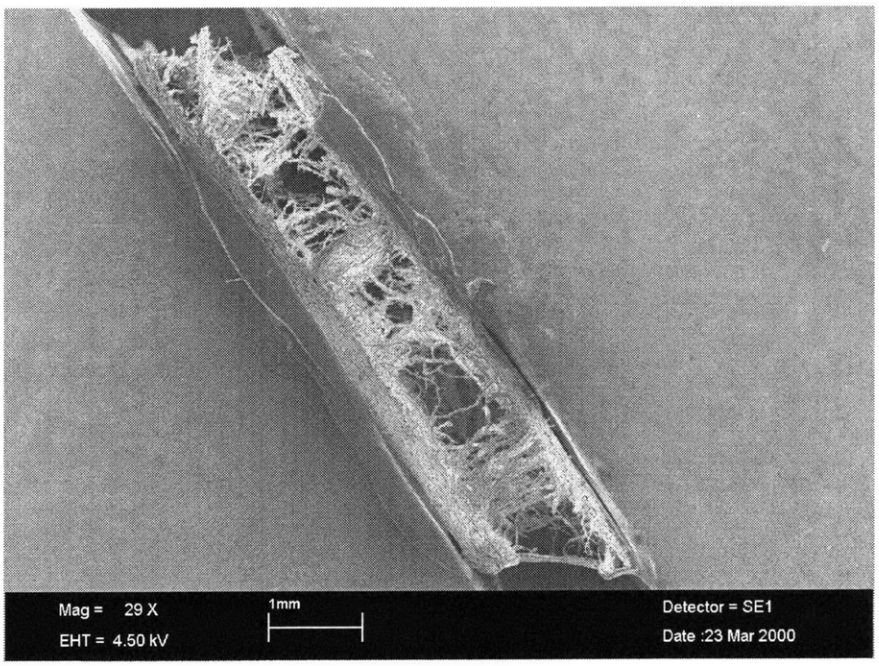

Figure 7-44: Full view of Triplex CD 40-degree combined-loading test (Step 7).

Although there is some microcracking, the microcracks are generally few and grow only a little before one becomes dominant. This is a transition state between the extensive microcracking of through-thickness tension to the sudden failure by macrocracking of interlaminar shear. The images of 60^o loading experiments presented here, as well as 80^o images, are not correlated with load. The specimens used were chosen for image quality and were too large for loads to be measured on the available load cell.

A 60^o combined load test with machine direction shear is shown in Figures 7-45 through 7-54. The first image shows the specimen at no load. Microcracks are first visible in step 3, Figure 7-47. The cracks are larger and more visible in step 4. This image shows that cracks are forming along only two of four material interfaces. In step 6, Figure 7-50, the microcracks along one interface have united to form a macrocrack. Only one other sizable microcrack is visible at this point in the experiment, although it is difficult to distinguish in this image due to charging.

Through the remaining images, the macrocrack grows, and the bridging fibers rotate to align with the direction of loading. A full view of the deformed specimen, Figure 7-54, shows the differing amounts of shear and normal displacement.

Figures 7-55 through 7-64 are images of a 60^o combined-loading experiment with cross direction shear. In step 1, no load has been applied, although there are many pre-existing material flaws visible in the specimen. In step 4, microcracks begin to nucleate at these flaws. In Figures 7-59 and 7-60, the microcracks are growing. In these images, microcracks are seen only along two interfaces, and along each interface there is only one notable crack. By step 7, one crack has clearly become dominant. The only other competing microcrack has started to relax and close up. Macrocrack growth continues through the remaining images. Figure 7-64 is a full view of the specimen. In all full views of failed combined-loading specimens presented here, failure occurred when a microcrack propagated along one interface of the specimen. In through-thickness tension tests, two significant microcracks will sometimes form along different interfaces. That has not been observed in any of the combined-loading specimens tested in this study, likely because of the shear effect. It is possible that

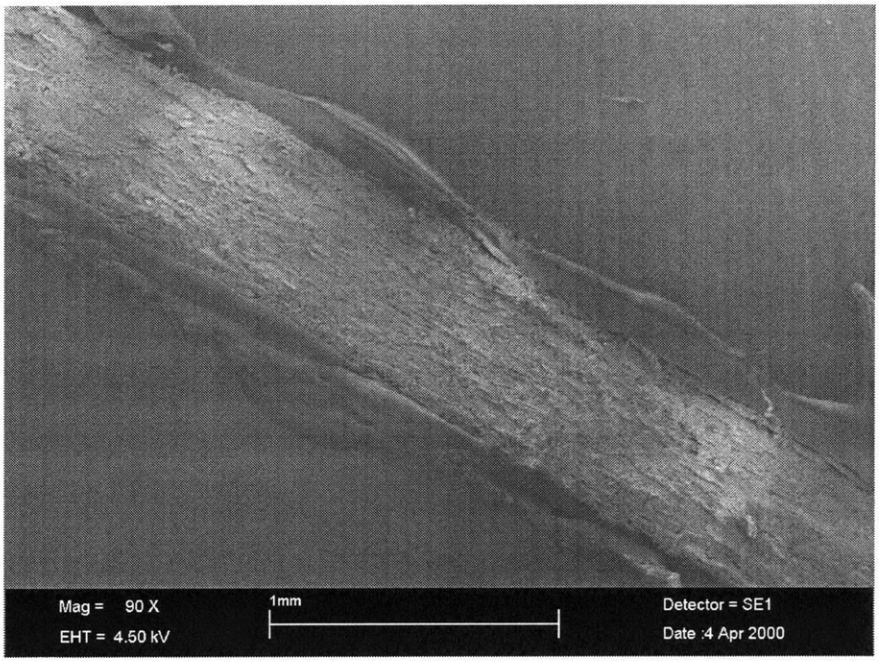

Figure 7-45: Triplex MD 60-degree combined-loading test at no load (Step 1).

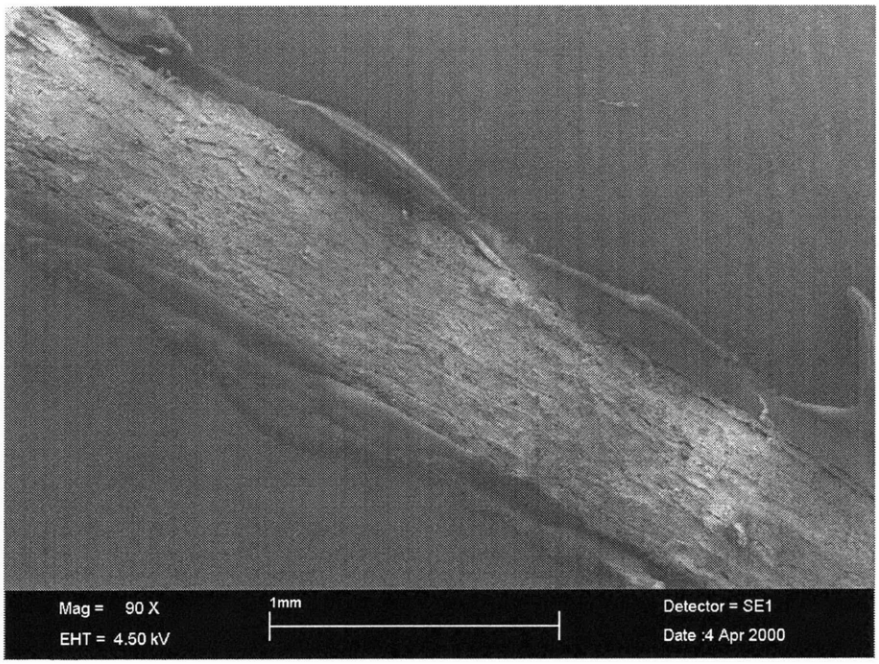

Figure 7-46: Triplex MD 60-degree combined-loading test (Step 2).

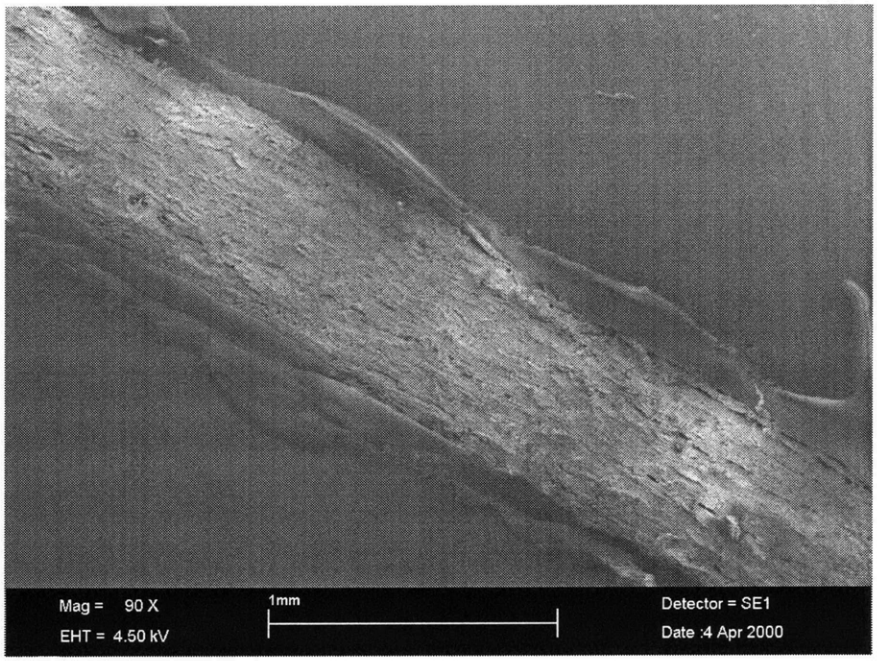

Figure 7-47: Triplex MD 60-degree combined-loading test (Step 3).

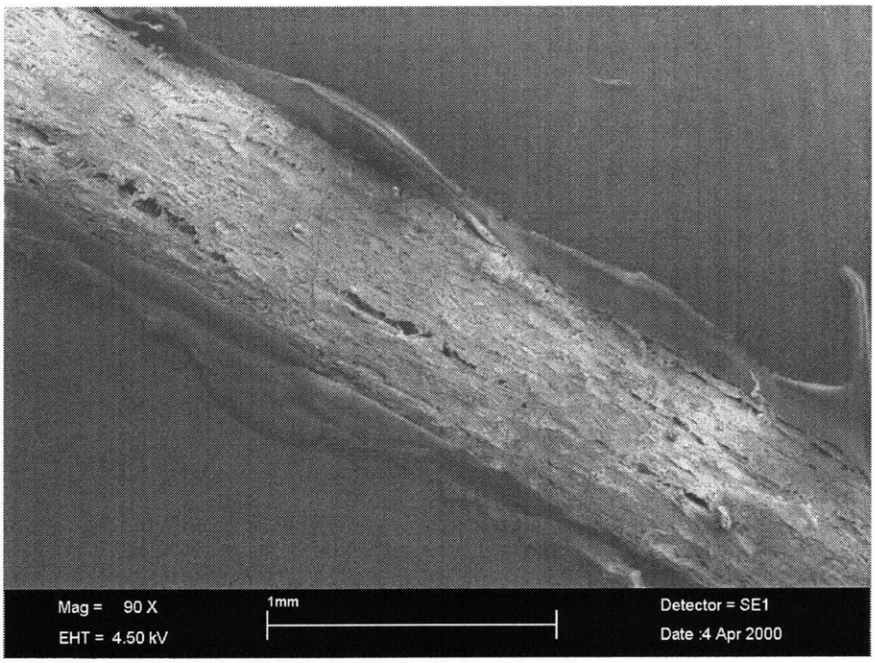

Figure 7-48: Triplex MD 60-degree combined-loading test (Step 4).

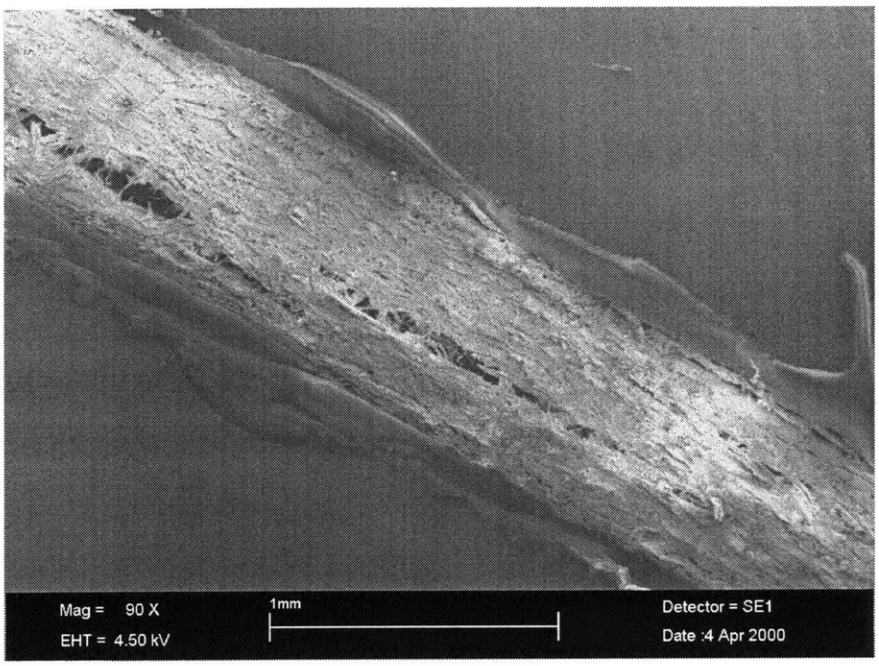

Figure 7-49: Triplex MD 60-degree combined-loading test (Step 5).

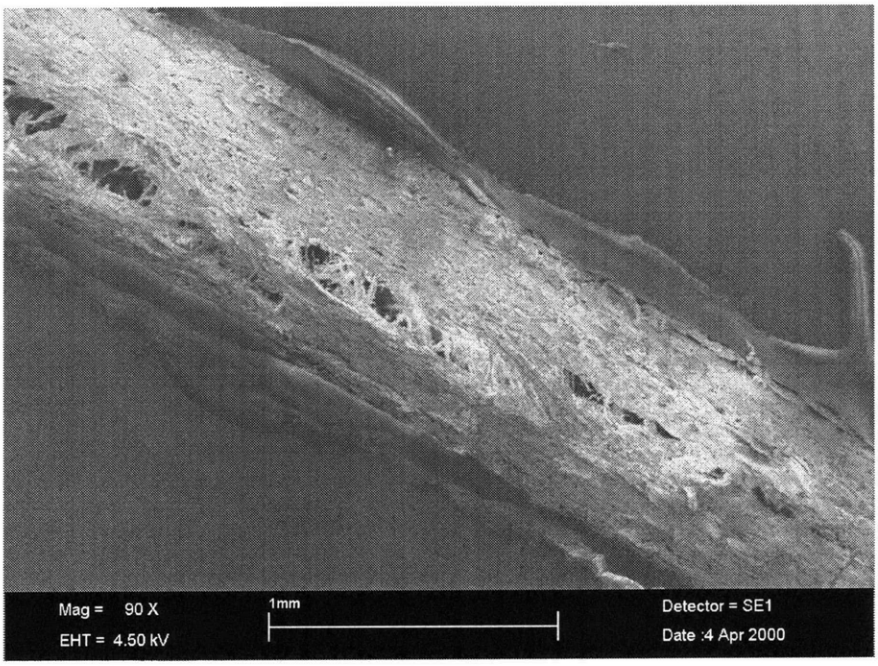

Figure 7-50: Triplex MD 60-degree combined-loading test (Step 6).

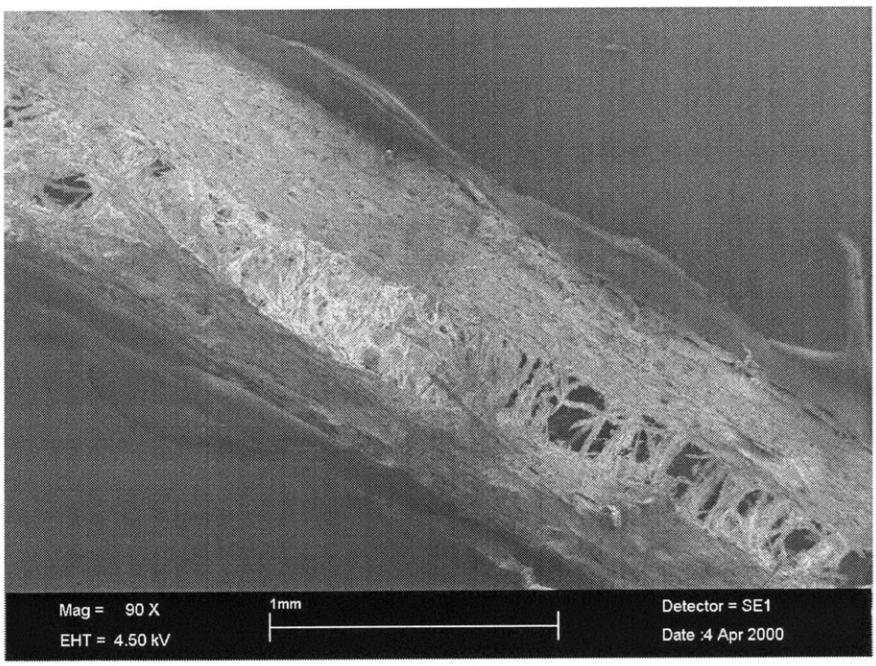

Figure 7-51: Triplex MD 60-degree combined-loading test (Step 7).

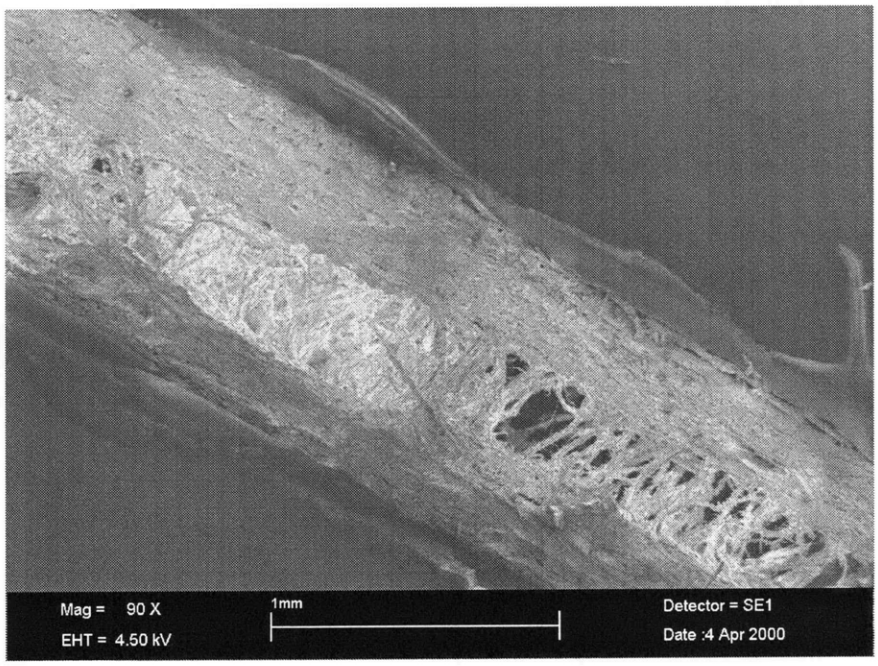

Figure 7-52: Triplex MD 60-degree arcan test (Step 8).

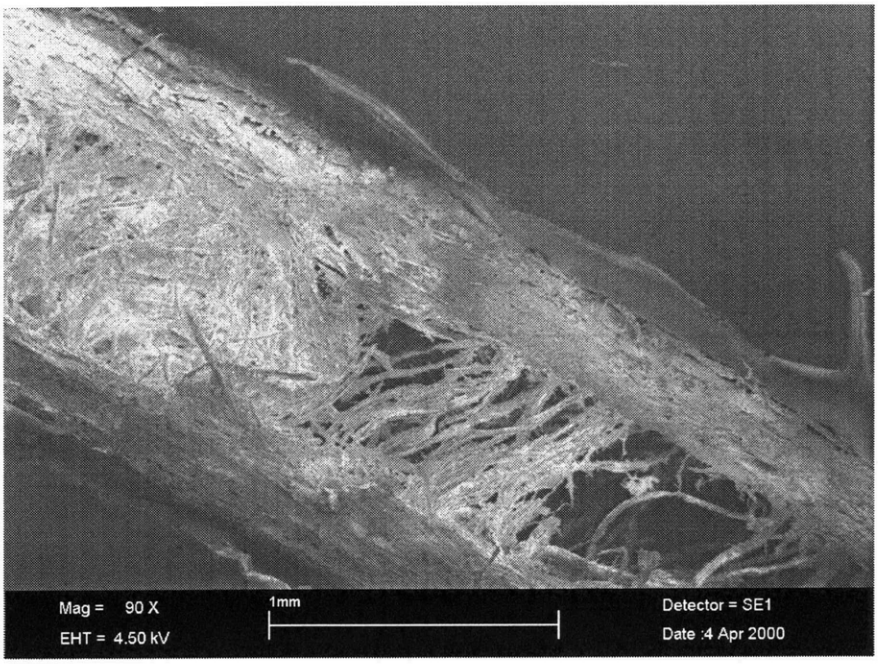

Figure 7-53: Triplex MD 60-degree combined-loading test (Step 9).

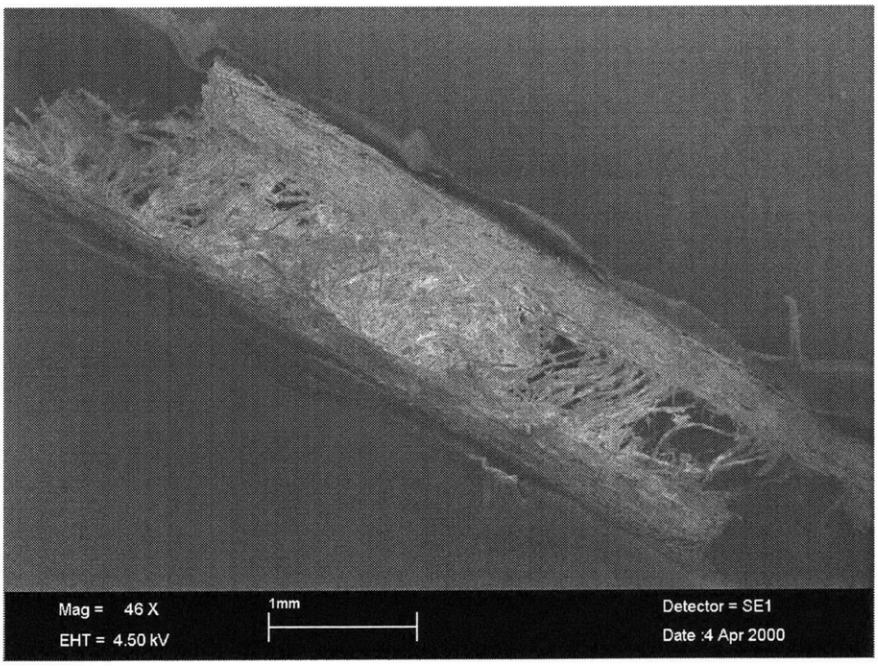

Figure 7-54: Full view of Triplex MD 60-degree combined-loading test (Step 9).

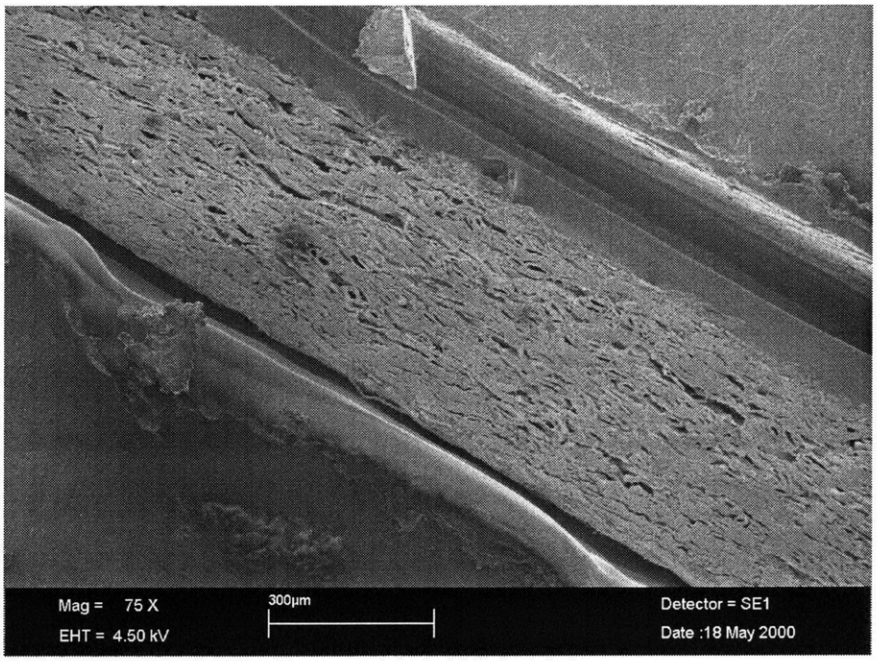

Figure 7-55: Triplex CD 60-degree combined-loading test at no load (Step 1).

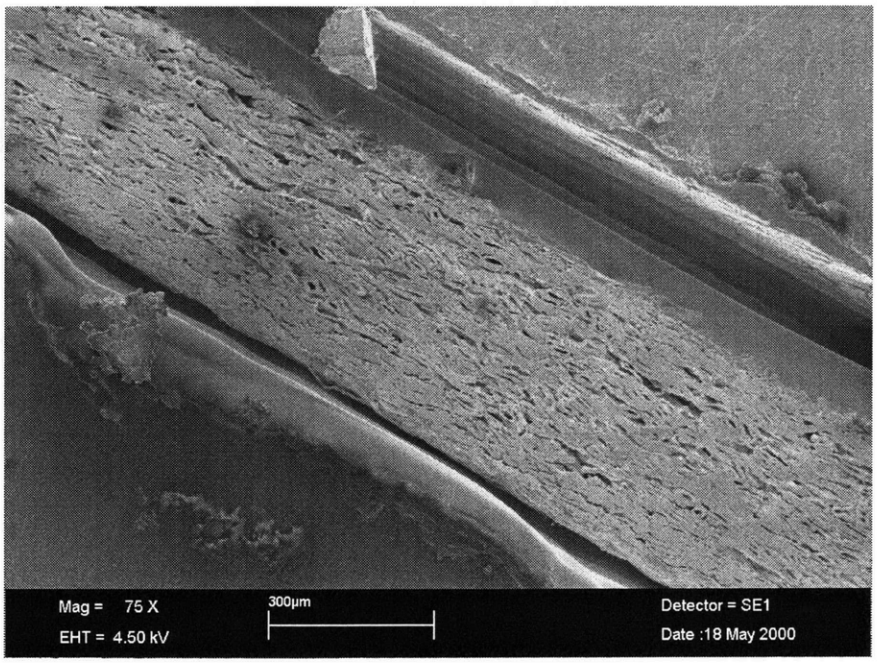

Figure 7-56: Triplex CD 60-degree combined-loading test (Step 2).

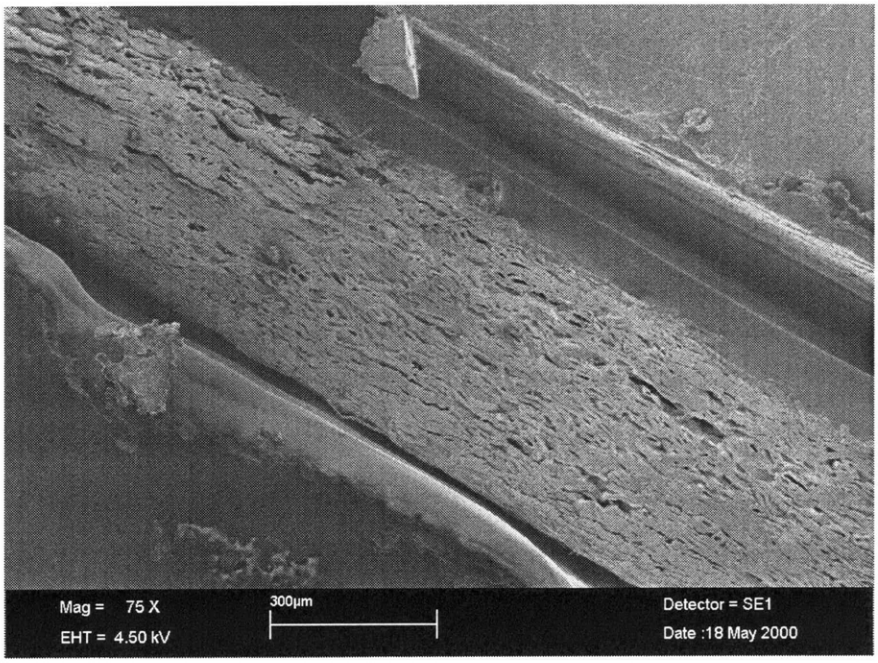

Figure 7-57: Triplex CD 60-degree combined-loading test (Step 3).

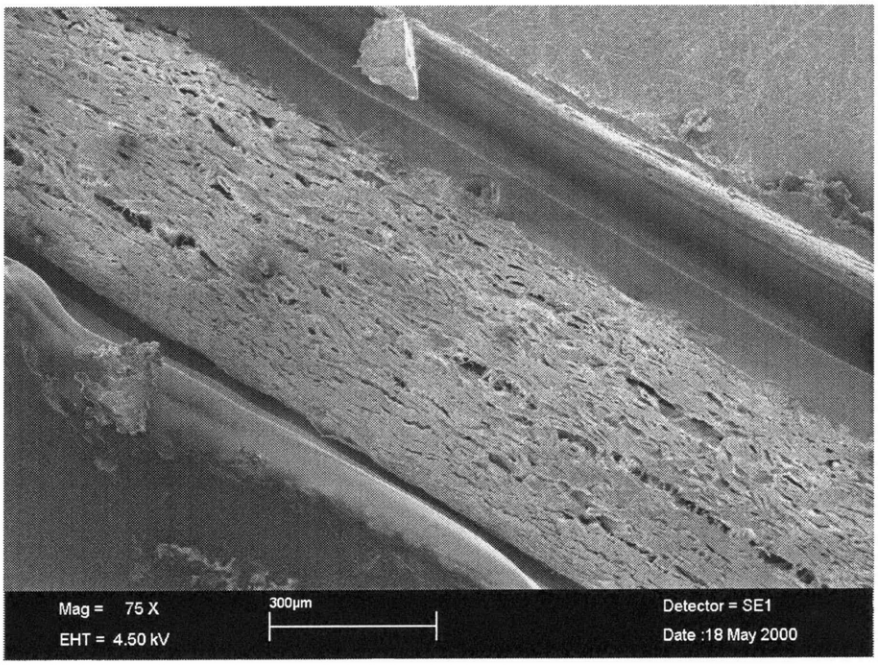

Figure 7-58: Triplex CD 60-degree combined-loading test (Step 4).

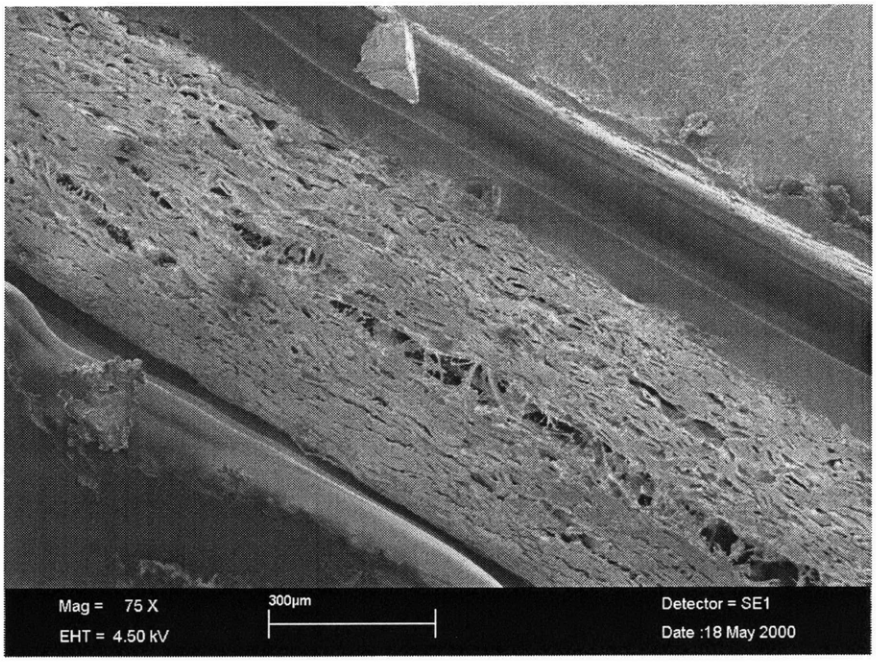

Figure 7-59: Triplex CD 60-degree combined-loading test (Step 5).

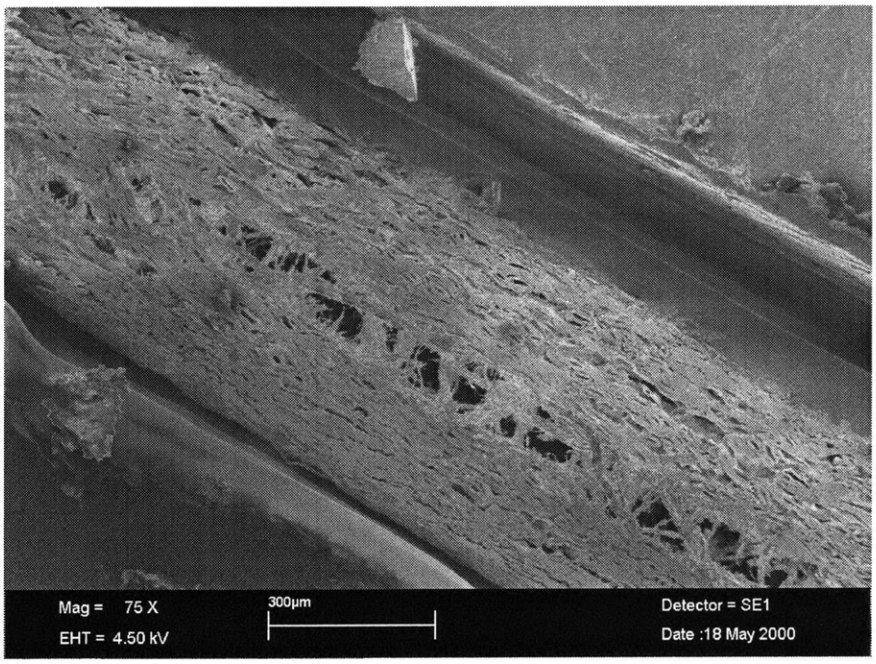

Figure 7-60: Triplex CD 60-degree combined-loading test (Step 6).

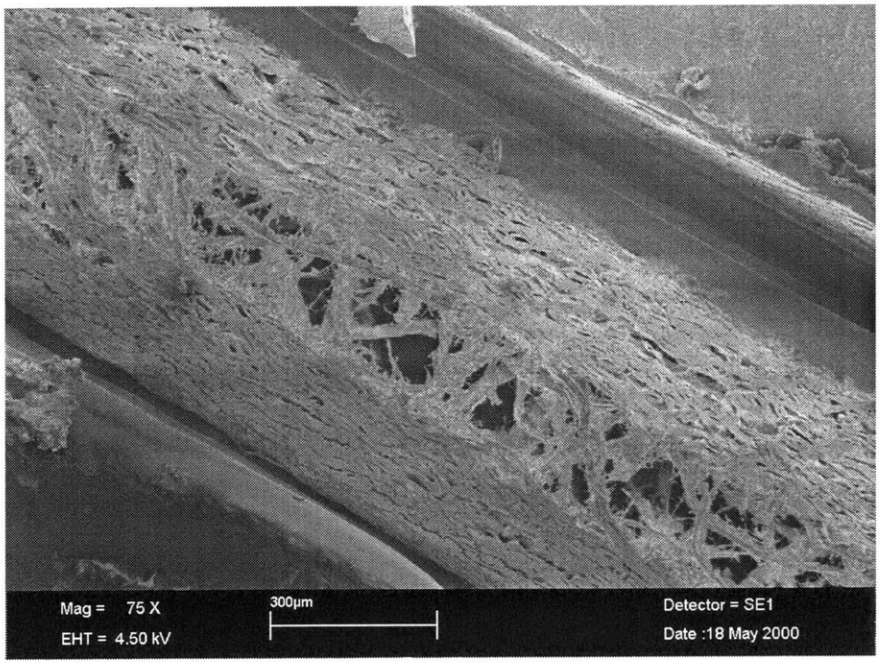

Figure 7-61: Triplex CD 60-degree combined-loading test (Step 7).

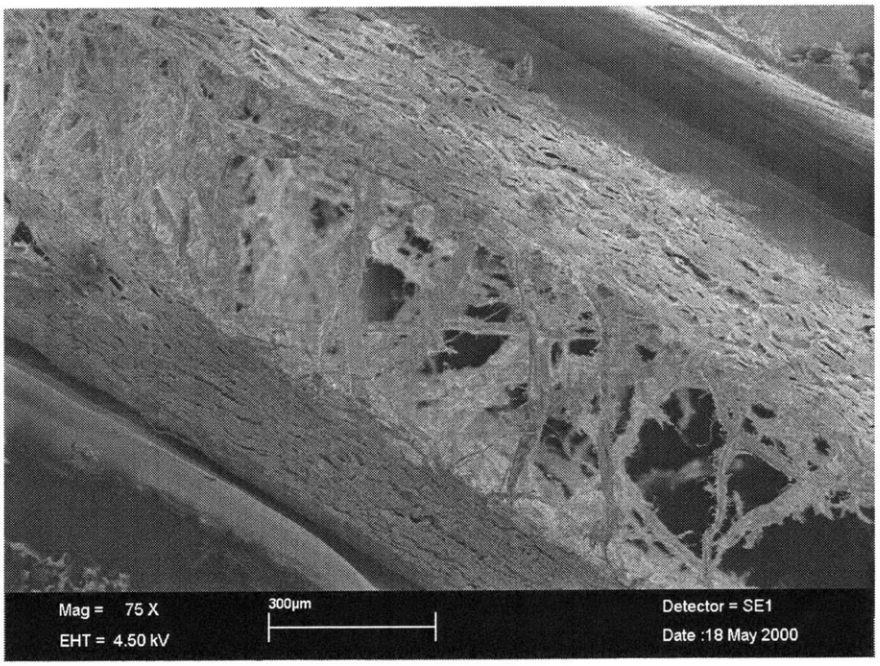

Figure 7-62: Triplex CD 60-degree combined-loading test (Step 7).

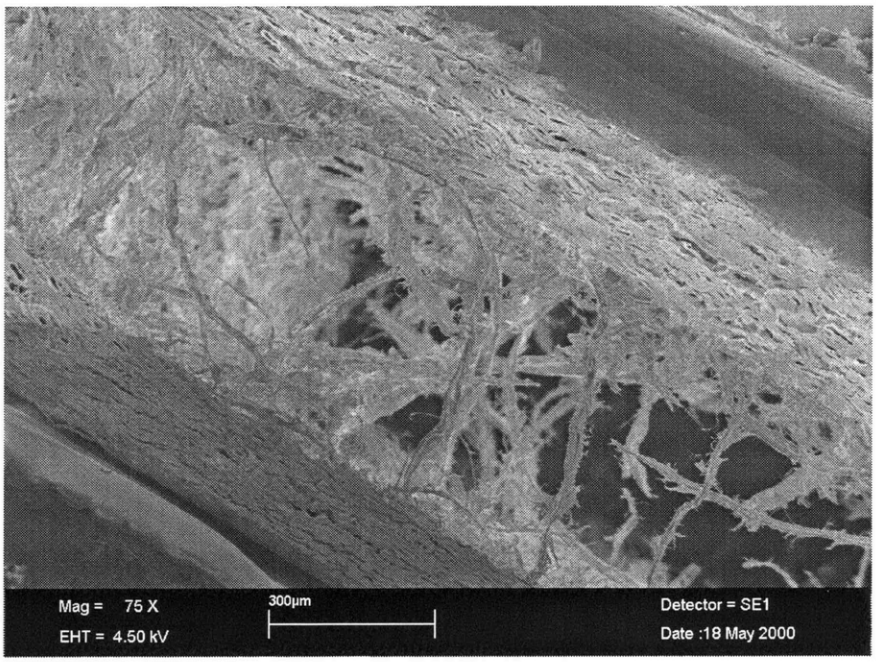

Figure 7-63: Triplex CD 60-degree combined-loading test (Step 9).

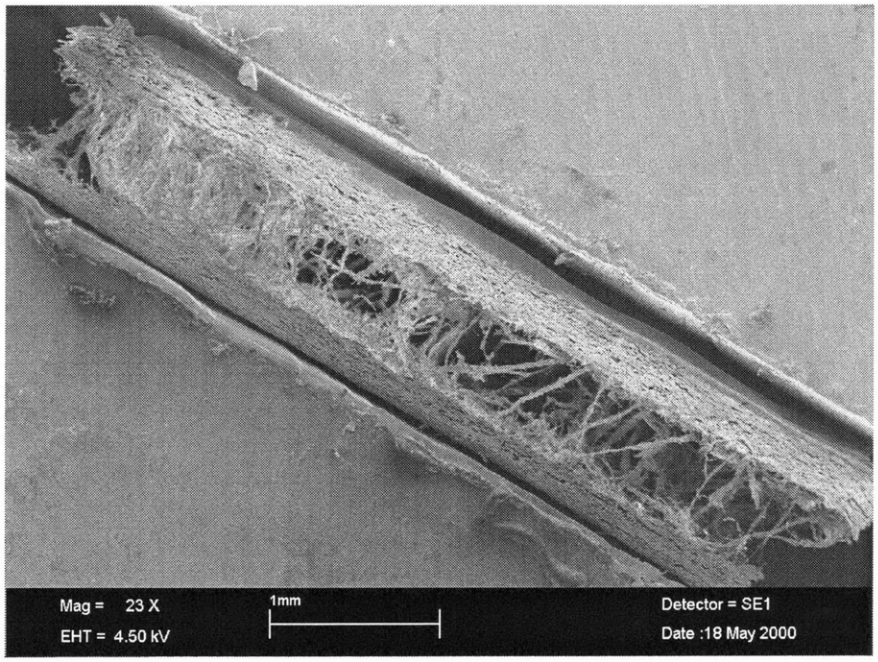

Figure 7-64: Full view of Triplex CD 60-degree combined-loading test (Step 9).

at a length scale large enough to exclude simultaneous shear failure across an entire cross-section, competing macrocracks on different interfaces might be seen under combined-loading.

At 80^o, the stress state is heavily dominated by shear stress. An 80^o experiment with machine-direction shear is pictured in Figures 7-65 through 7-72. The observed deformation mechanisms are primarily shear in nature. The first image shows the specimen at no load. In the next image, steps 2 and 3, a few very small areas of damage are observed in the material. However, most of the deformation seen in these image has occurred in the glue, as may happen if the glue layer is applied too thickly. The damaged areas develop slightly in steps 3 and 4, but the total amount of observable damage in the specimen is minimal before sudden failure by macrocracking in Figure 7-70. Through the remaining figures, the macrocrack grows and bridging fibers rotate, as was seen in other combined-loading experiments. This is the same sort of fiber rotation that contributes to Z-direction expansion in pure shear loading. Figure 7-72 shows the full deformed specimen. The ratio of shear displacement to normal displacement within the specimen is smaller than usual for an 80^o test due to the glue deformation.

The 80^o combined-loading experiment presented in Figures 7-73 through 7-82 has a more suitable amount of glue and is not affected by significant glue deformation. The specimen is a cross-direction specimen, and significant pre-existing material flaws are visible. As load is applied, cracks begin to nucleate at those flaws. Crack nucleation is first seen in step 4, Figure 7-76. Although the cracks do begin as microcracks, they form along only one interface. There are no competing microcracks, and these cracks grow quickly to coalesce in step 6. The macrocrack grows through the subsequent images. Figure 7-82 shows the full failed specimen. The relative amounts of shear and normal displacement in this image are more typical of an 80^o combined-loading test than that seen in the machine direction test.

The combined-loading experiments presented here show a transition from tensile to shear dominated behavior as the loading angle increases. At the microscopic level, this transition is seen both in the shape of the stress-strain curve and in the deformation

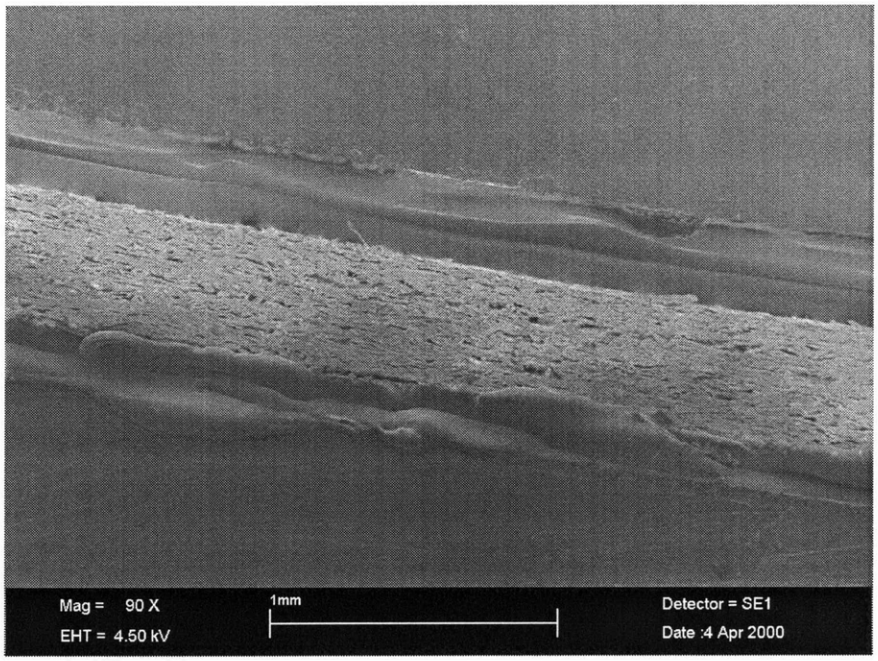

Figure 7-65: Triplex MD 80-degree combined-loading test at no load (Step 1).

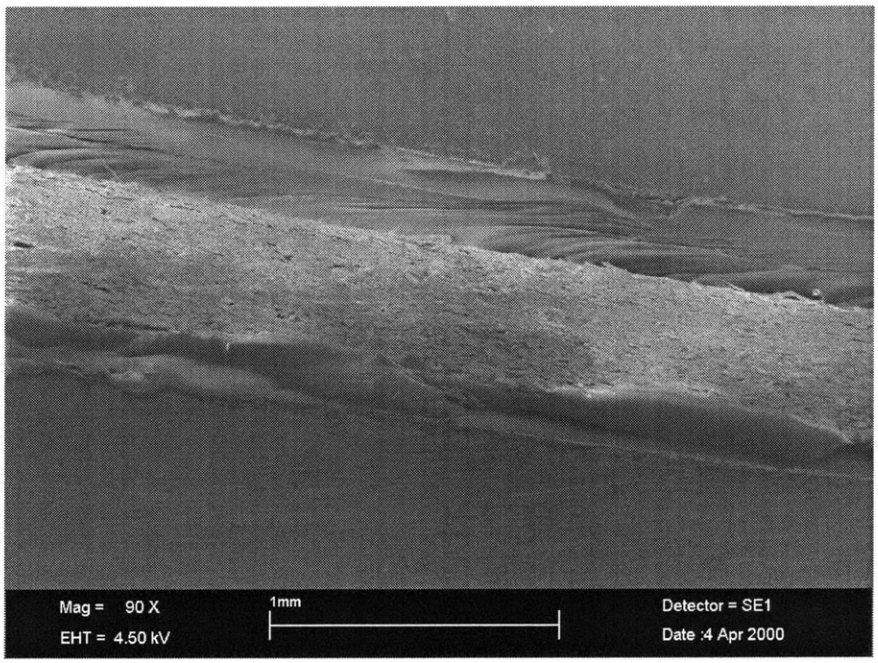

Figure 7-66: Triplex MD 80-degree combined-loading test (Step 2).

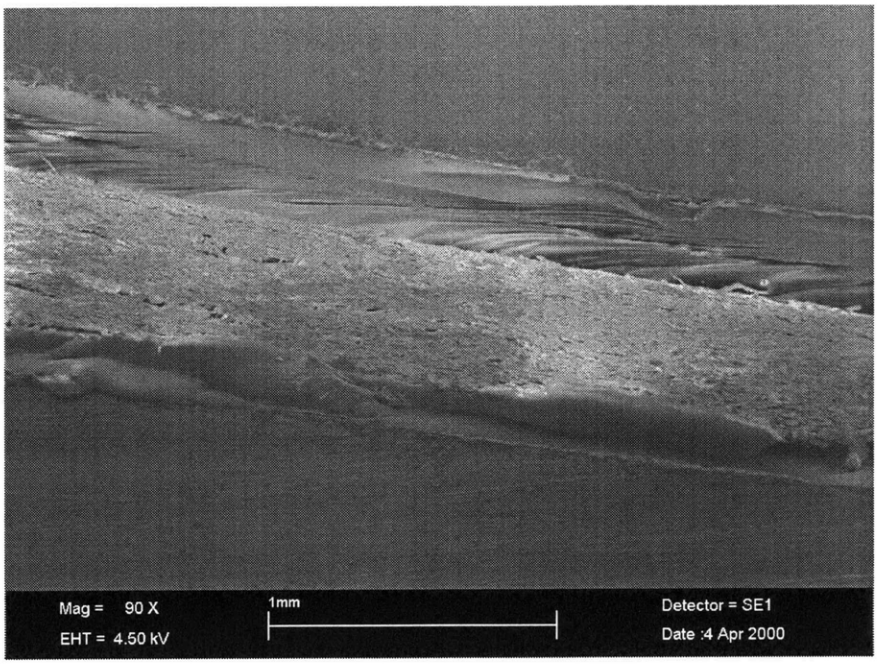

Figure 7-67: Triplex MD 80-degree combined-loading test (Step 3).

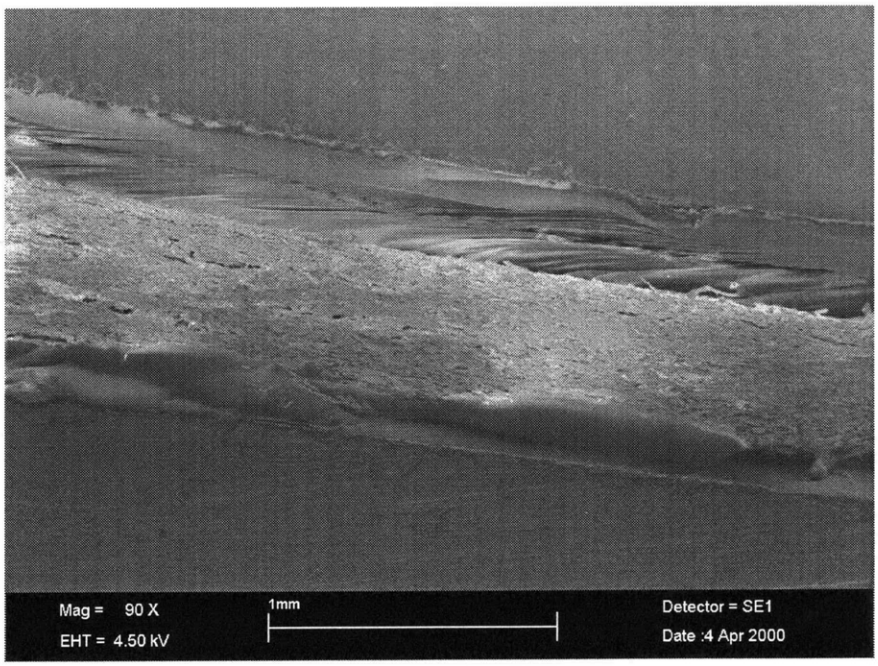

Figure 7-68: Triplex MD 80-degree combined-loading test (Step 4).

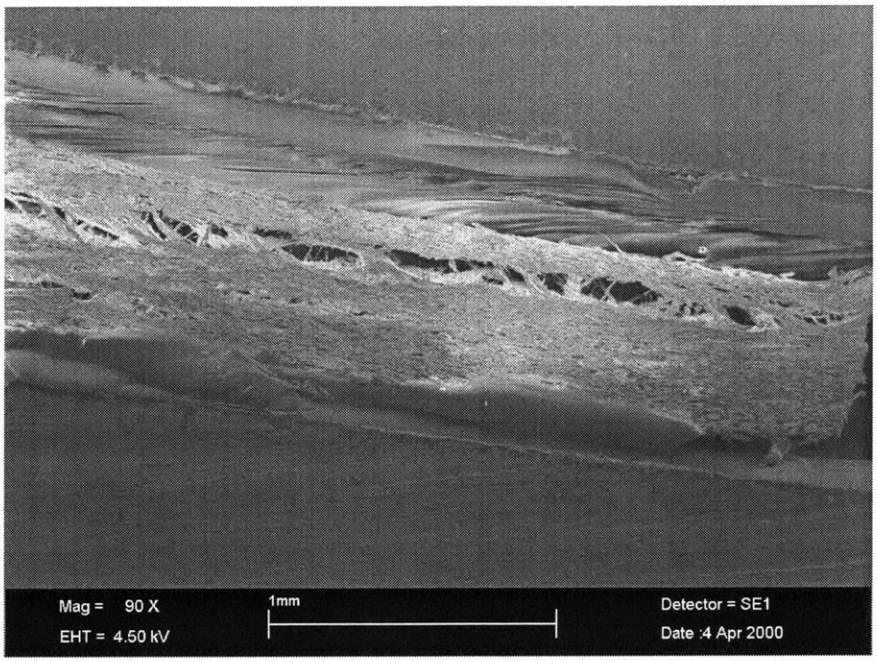

Figure 7-69: Triplex MD 80-degree combined-loading test (Step 5).

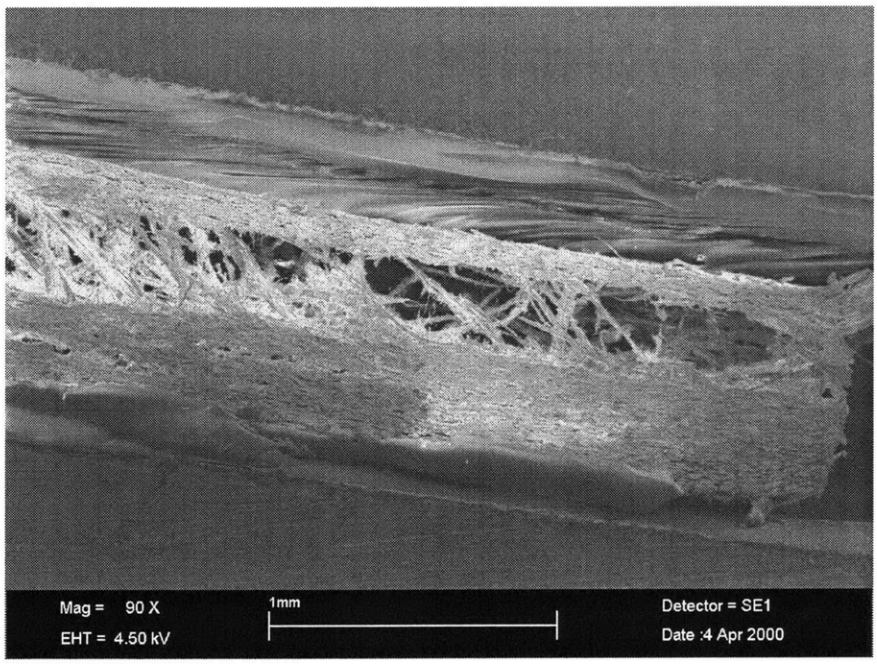

Figure 7-70: Triplex MD 80-degree combined-loading test (Step 6).

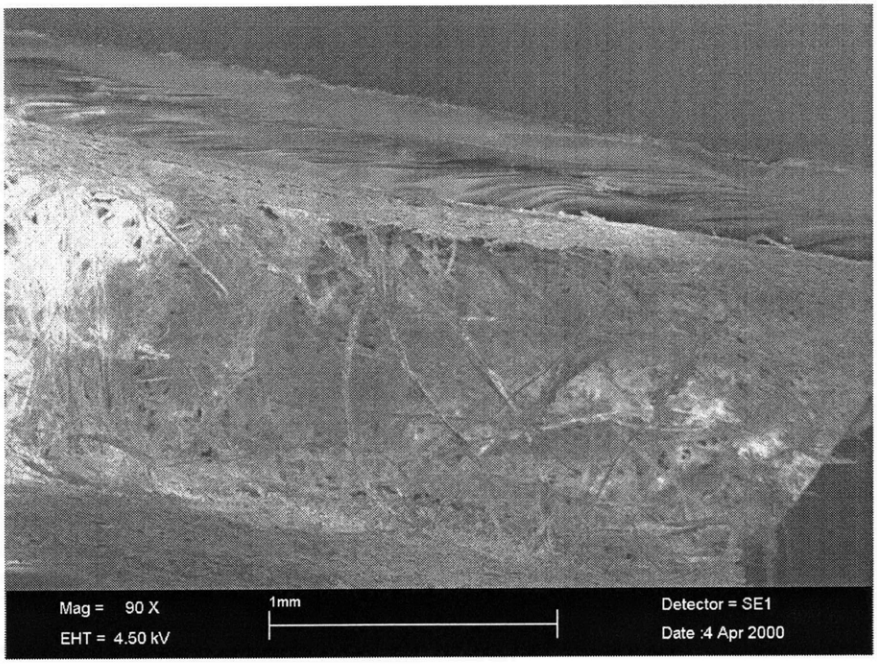

Figure 7-71: Triplex MD 80-degree combined-loading test (Step 7).

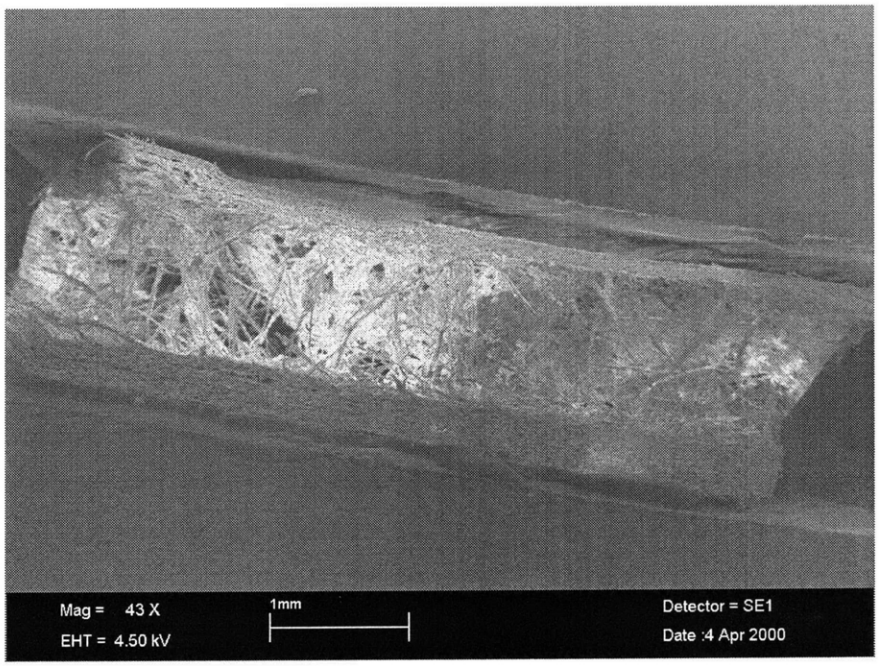

Figure 7-72: Full view of Triplex MD 80-degree combined-loading test (Step 7).

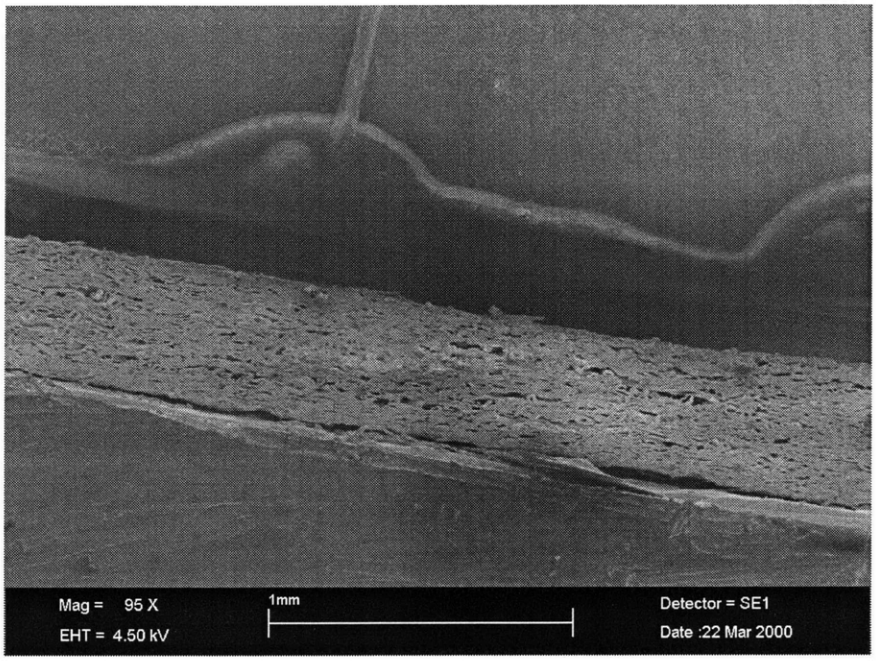

Figure 7-73: Triplex CD 80-degree combined-loading test at no load (Step 1).

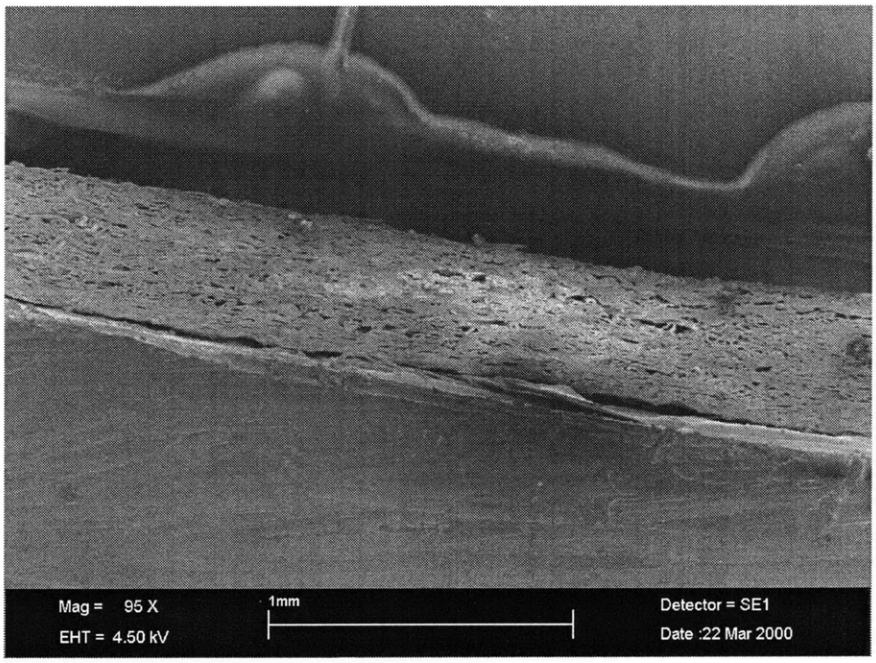

Figure 7-74: Triplex CD 80-degree combined-loading test (Step 2).

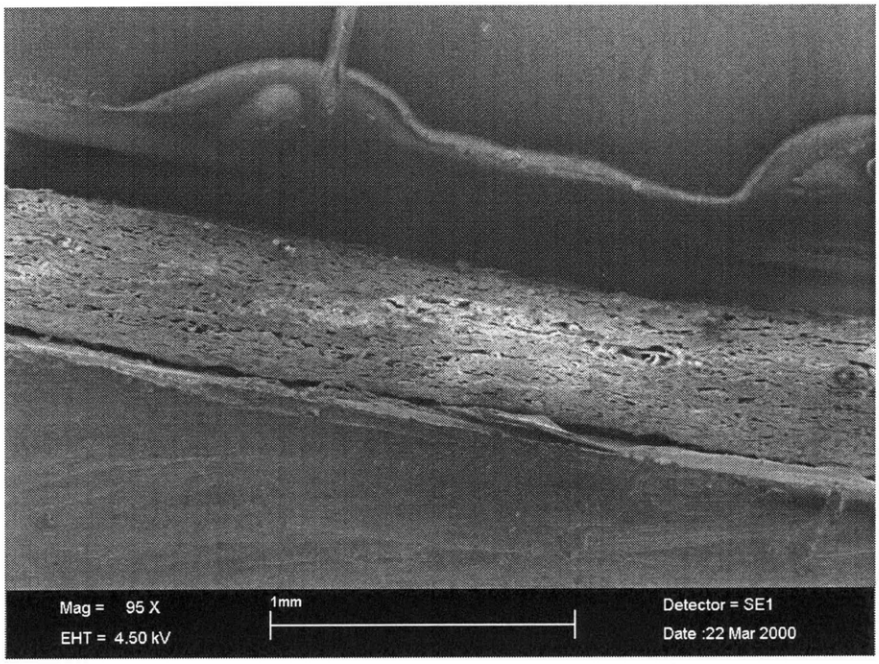

Figure 7-75: Triplex CD 80-degree combined-loading test (Step 3).

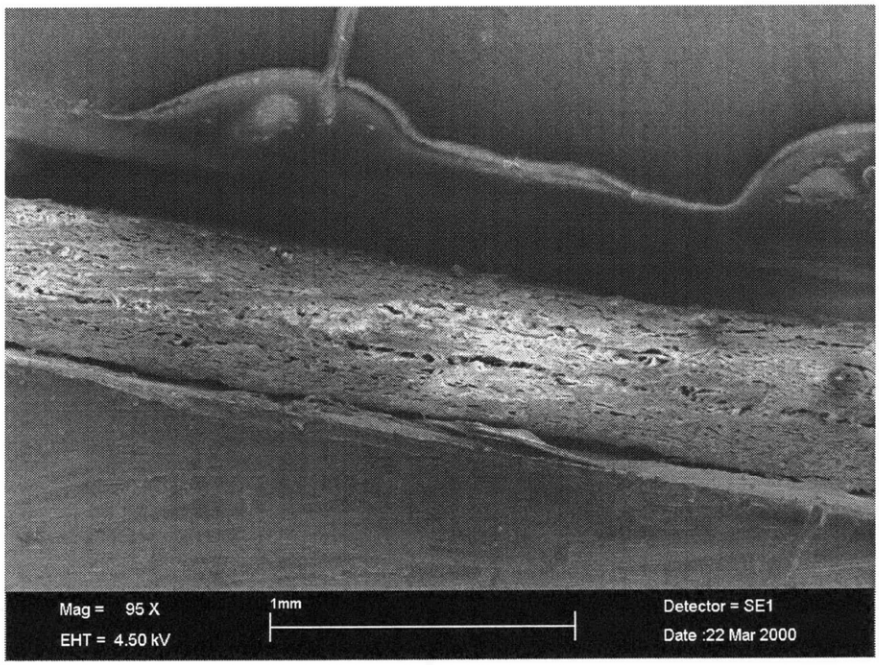

Figure 7-76: Triplex CD 80-degree combined-loading test (Step 4).

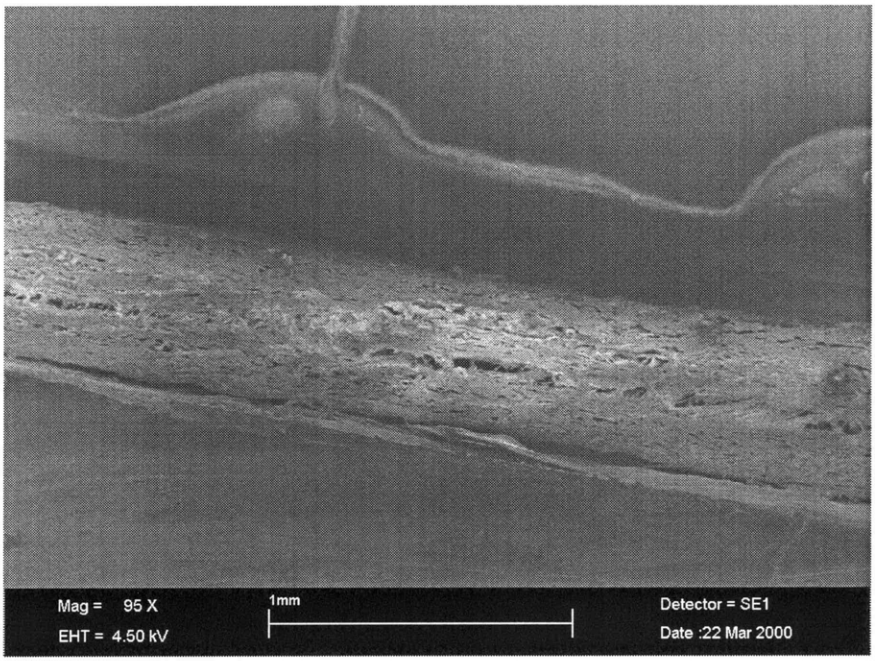

Figure 7-77: Triplex CD 80-degree combined-loading test (Step 5).

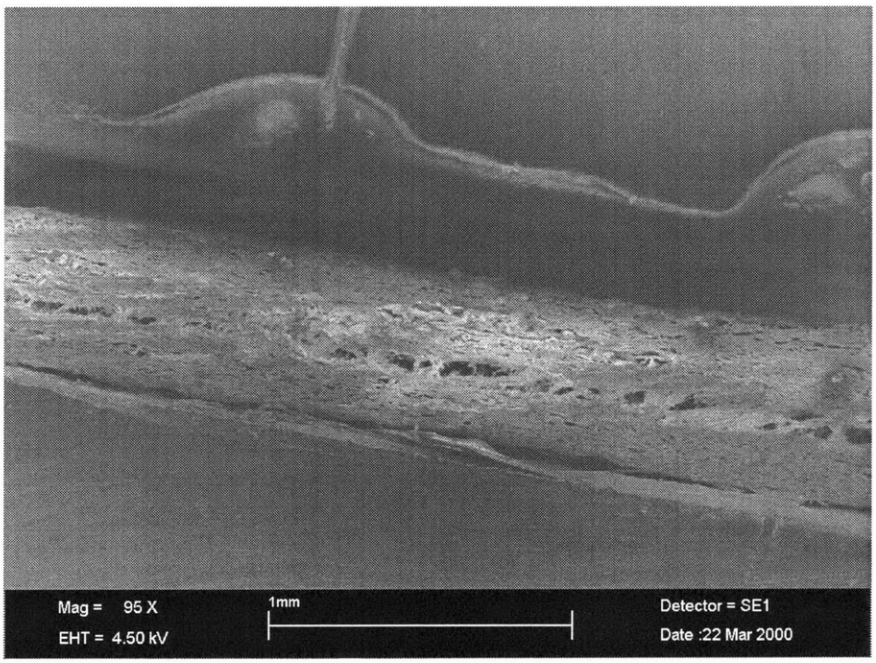

Figure 7-78: Triplex CD 80-degree combined-loading test (Step 6).

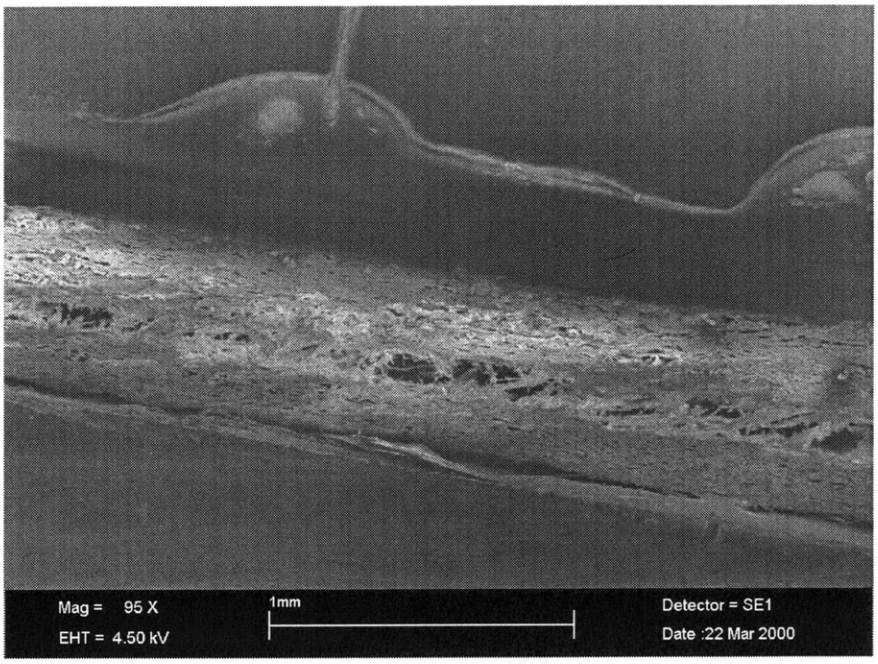

Figure 7-79: Triplex CD 80-degree combined-loading test (Step 7).

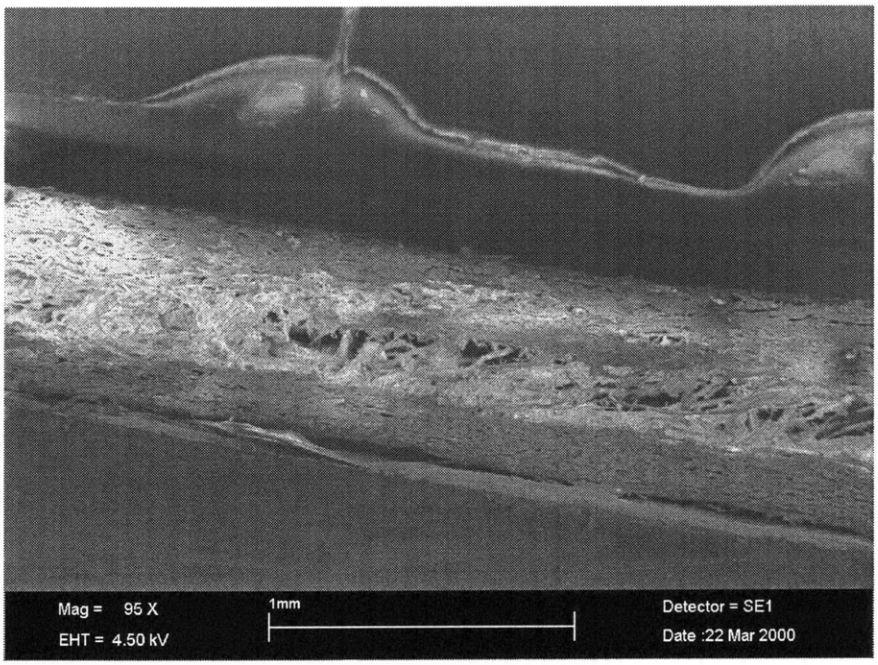

Figure 7-80: Triplex CD 80-degree combined-loading test (Step 8).

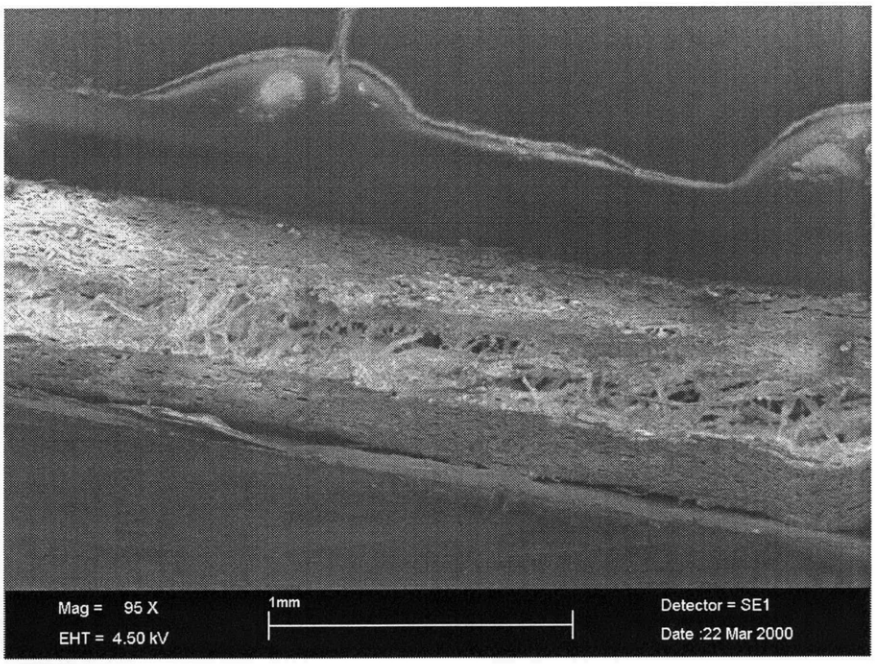

Figure 7-81: Triplex CD 80-degree combined-loading test (Step 9).

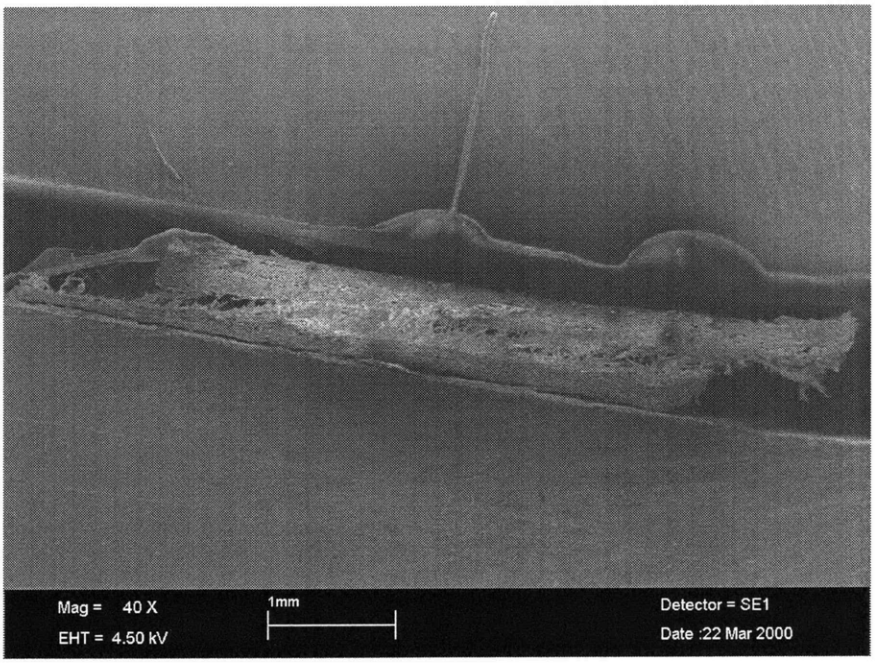

Figure 7-82: Full view of Triplex CD 80-degree combined-loading test (Step 9).

images. The macroscopic data shows that the effect of the shear varies more with the loading angle than does the tensile effect, creating a much larger variation in shear components of failure stress and strain than in the normal components. This is also demonstrated by the microscopic images. Although the tensile mechanism of microcracking has an effect at each of the loading angles studied, shear effects are only discernable at the larger angles.

Chapter 8

In-Plane Tension Experimental Results

This chapter presents the experimental results of in-plane tension experiments at both macroscopic and microscopic levels. Stress-strain data was collected at the macroscopic level. This data revealed that Triplex is both stiffer and stronger in the machine direction than in the cross direction under in-plane tension. It also showed that Triplex experiences strain hardening in the plane, with a higher strain hardening slope in the machine direction than in the cross direction. Both planar and edge-view images of the in-plane tension process were collected at the microscopic level. These images revealed the mechanisms corresponding to features of the stress-strain curve. Particular emphasis was placed on determining the hardening and failure mechanisms.

8.1 Macroscopic Work

Figure 8-1 presents stress versus strain data for Triplex loaded in uniaxial in-plane tension at the macroscopic level. The stress and strain measures used are both nominal, as defined in Appendix B. Triplex is a layered composite material, with outer layers of chemical pulp sandwiching core layers of mechanical pulp. Behavior under in-plane loading will be affected by properties of both component materials. The results for tension in the machine and cross-directions are presented together for comparison.

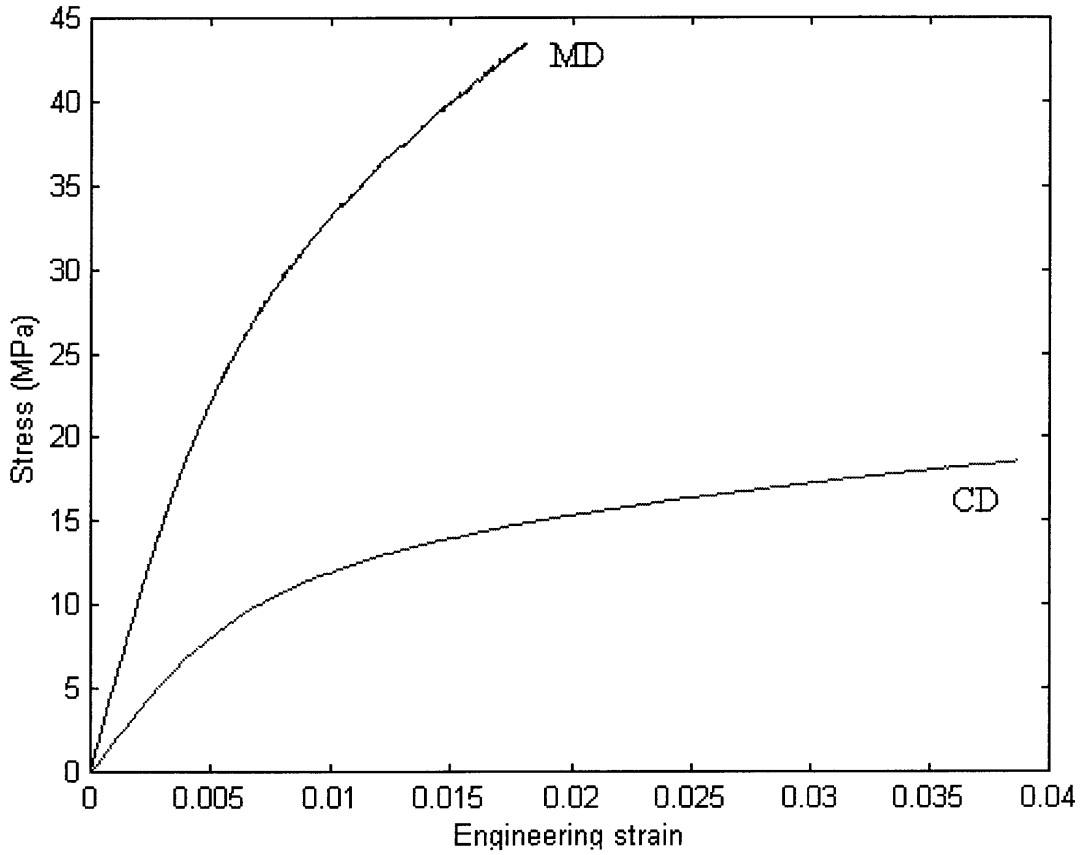

Figure 8-1: Macroscopic stress-strain data for uniaxial in-plane tension. (Courtesy of N. Stenberg.)

Both curves show an initial linear elastic region. Elastic modulus values were calculated using the data from several in-plane tests. The elastic modulus in the machine direction is 4330 MPa, about three times larger than the cross-direction modulus of 1700 MPa. Yield, defined here as departure from linearity, happens at similar strains in both directions. In the machine direction, the departure happens at 0.32% strain, while in the cross-direction it is at 0.35%. However, the stresses at yield are very different. Yield stress in the machine direction is about 14 MPa, more than twice the 6 MPa seen at yield in the cross direction.

Beyond the linear region, the material begins to strain harden. The rate of hardening with respect to total strain is much less in the cross direction. The yield stress

increases from 6 MPa to 19 MPa over a strain range of approximately 3.5%. In the machine direction, yield stress evolves from 14 MPa to 43 MPa over a strain range of only 1.5%. Yield stress increases by a factor of three in both cases, but it occurs over a much shorter strain range in the machine direction.

The curves presented here terminate at the peak stress or failure point. Although the post-peak region is not shown, other experiments have indicated that the stress falls dramatically immediately after the peak. This precipitous fall begins to slow when the stress reaches values in the 5-10 MPa range. Beyond this point the stress falls slowly with increasing strain.

8.2 Microscopic Work

Microscopic observation of in-plane tension experiments allowed correlation of mechanisms to events on the stress-strain curve. In the region of the curve featuring increasing stress, no notable change is observed at the microscopic level other than slight global stretching of the material. Failure is sudden and dramatic at the peak in the curve. The paperboard fails simultaneously at many points in one region of material. At large strains, fibers bridging the initial failure are pulled out, causing a gradual decrease in stress.

Figures 8-2 through 8-9 show planar views of paperboard subjected to in-plane tension in the machine direction. The material shown cannot properly be called Triplex, for one outer chemical layer has been removed in these images. Initial tests were conducted with the chemical layer in place, but as the chemical layer is both very dense and stiff, there was little deformation of individual fibers. Removing the chemical layer allows observation of individual fiber behavior in a more loosely packed mechanical layer.

Figure 8-2 shows the board at no load. The next image was taken at 50 N of load, equivalent to roughly 39 MPa. (It is difficult to establish stress values for an in-plane test with an outer chemical layer removed. In removing the chemical layer, some sections of the neighboring mechanical layer may also pull away, causing the

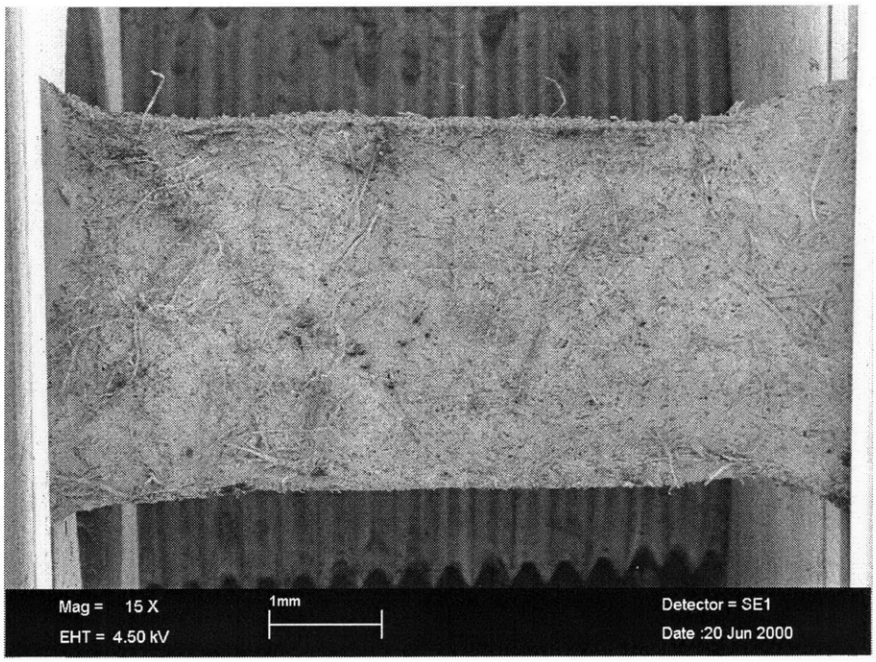

Figure 8-2: MD in-plane tension test at no load (Step 1). The material is Triplex with an outer chemical layer removed, exposing a core mechanical layer for imaging.

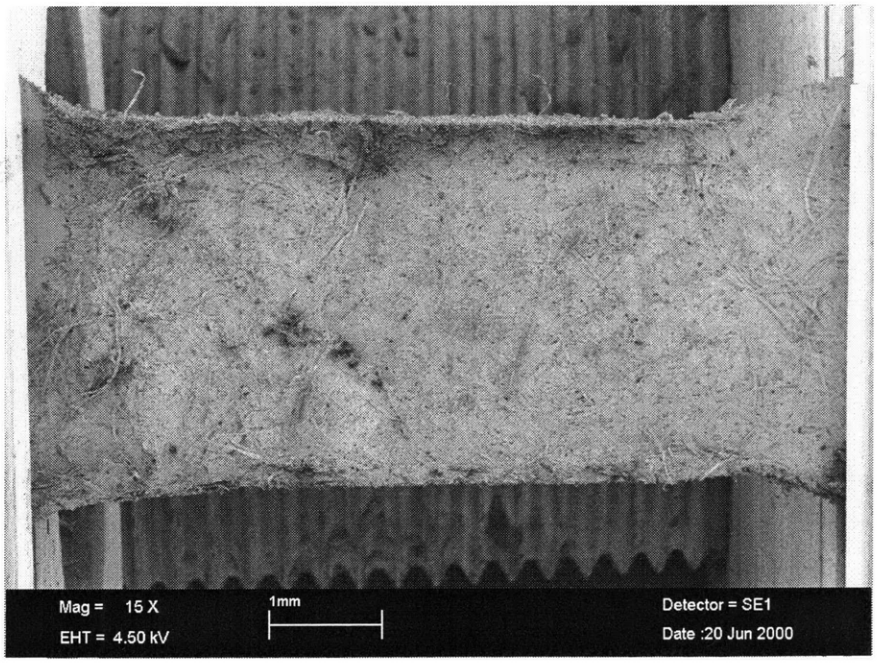

Figure 8-3: MD in-plane tension test (Step 2).

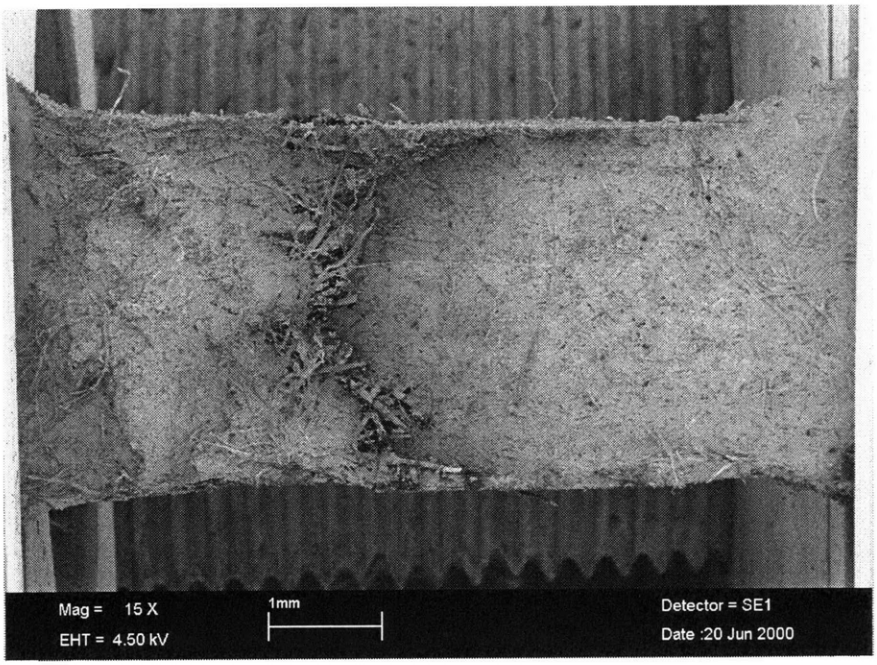

Figure 8-4: MD in-plane tension test (Step 3).

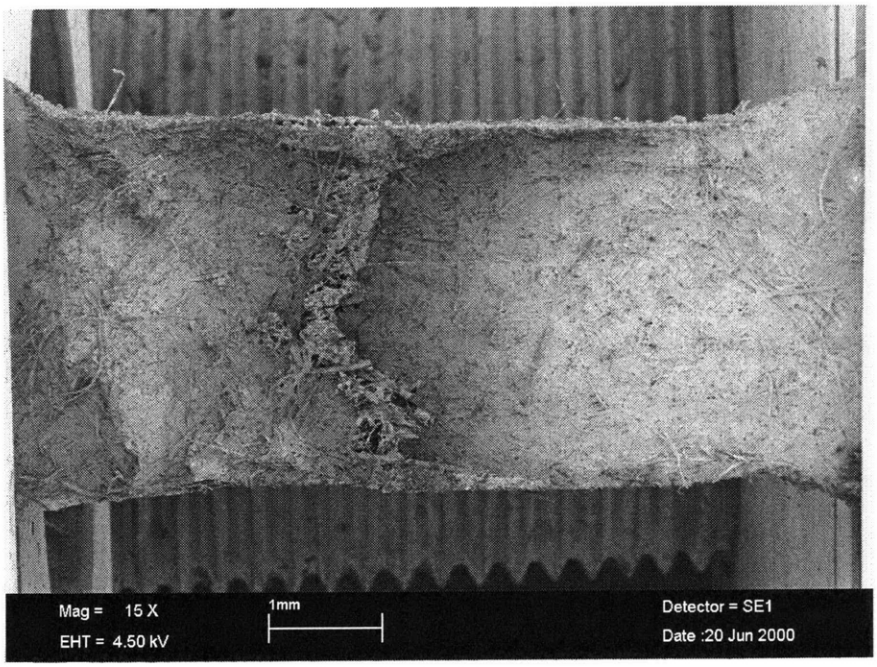

Figure 8-5: MD in-plane tension test (Step 4).

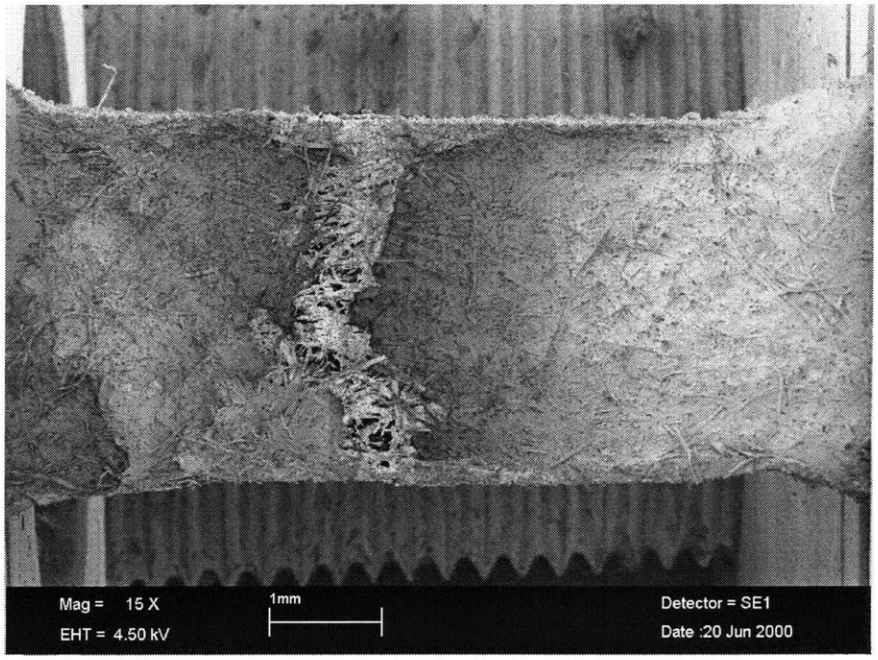

Figure 8-6: MD in-plane tension test (Step 5).

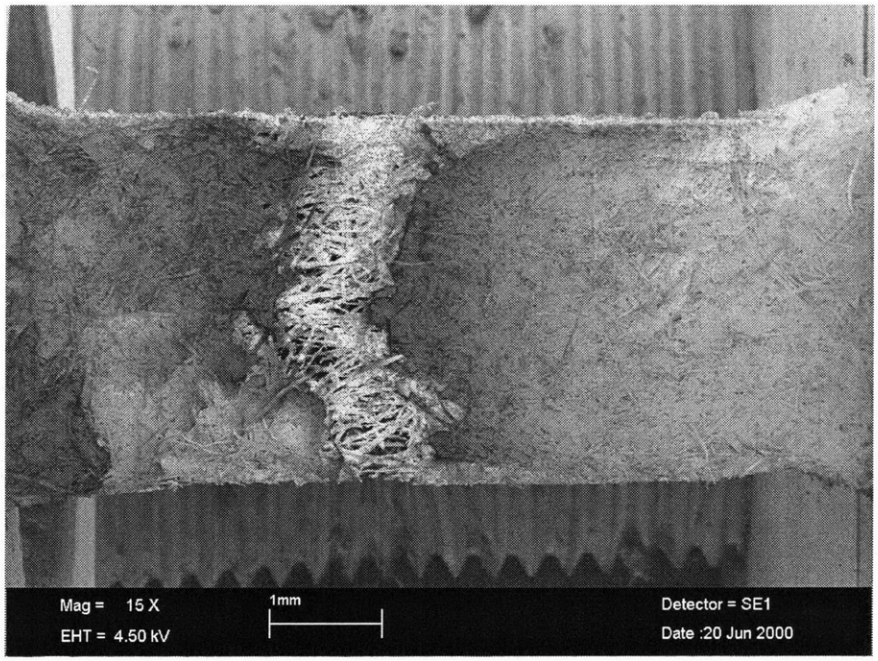

Figure 8-7: MD in-plane tension test (Step 6).

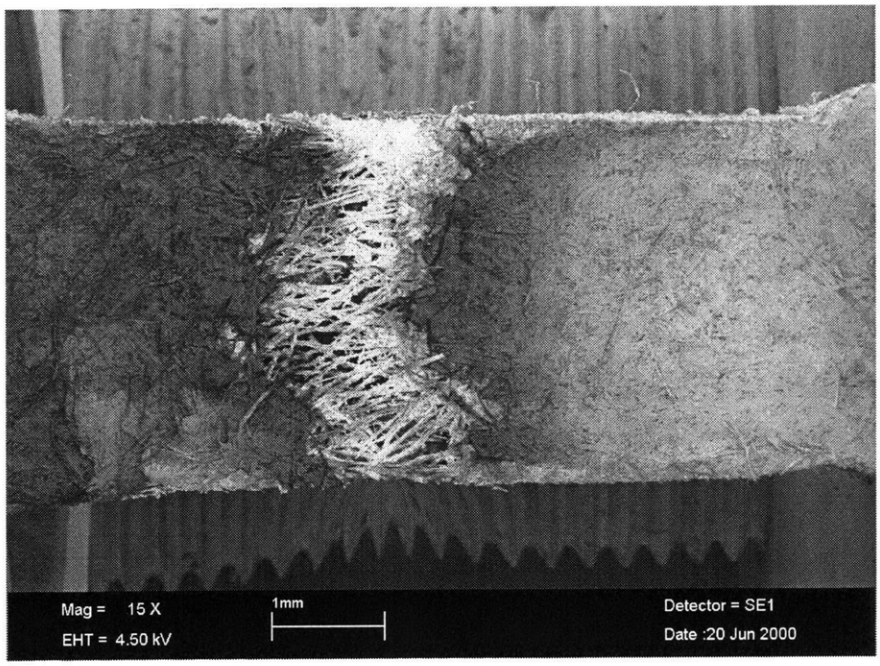

Figure 8-8: MD in-plane tension test (Step 7).

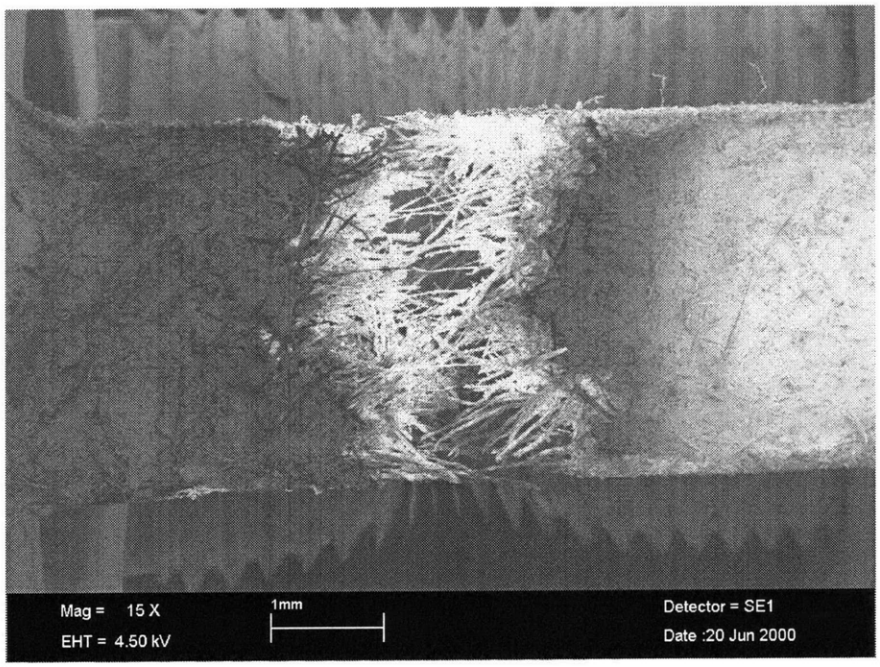

Figure 8-9: MD in-plane tension test (Step 8).

thickness of the specimen to vary considerably in the plane. Thus the cross-sectional area and the stress value cannot be stated confidently. The stress value given here is based on an estimated thickness of 0.4 mm.) This is well into the strain hardening region, but there is no notable difference in fiber positions or orientations. The load in this test peaked at 55 N and fell dramatically. Figure 8-4 was taken immediately after the peak, and load had already fallen to 5 N.

Through the remaining images, Figures 8-5 through 8-9, the load fell slowly, almost reaching zero by the last image. In these images, the material begins to separate along the failure line observed in step 3. As the material separates, fibers bridging the gap become clearly visible. These fibers were uncoated, causing them to charge under the electron beam and to appear much brighter than the surrounding material. The density of bridging fibers decreases in each subsequent image, corresponding to the decrease in load. In the last image, Figure 8-9, single fibers are visible protruding from one side of the gap, unconnected to material on the other side. In all of these images, the bridging fibers are lined up along or within a small angle of the machine direction.

In-plane tension in the cross direction is shown in Figures 8-10 through 8-17. The basic mechanisms observed are the same as those for tension in the machine direction, although the different orientation does cause some deviation.

In Figure 8-10, the specimen is loaded to 0.9 N. In Figure 8-11, the load has increased to 10 N, but there is no observable change in fiber orientations or positions. The load in this test peaked at 19 N. Figure 8-12 was taken immediately post-peak at 4.7 N. The failure line is visible near the left end of the frame. In the remaining images, the position of the specimen relative to the image frame has been adjusted to view the failure zone more fully.

The motor was not advanced between steps 3 and 4. During the pause to capture to image of step 3, the material relaxed sufficiently to reduce the load to 4.1 N in step 4, shown in Figure 8-12. In this image, the material around the failure line has started to separate, suggesting that the unloading happened in material outside the failure zone.

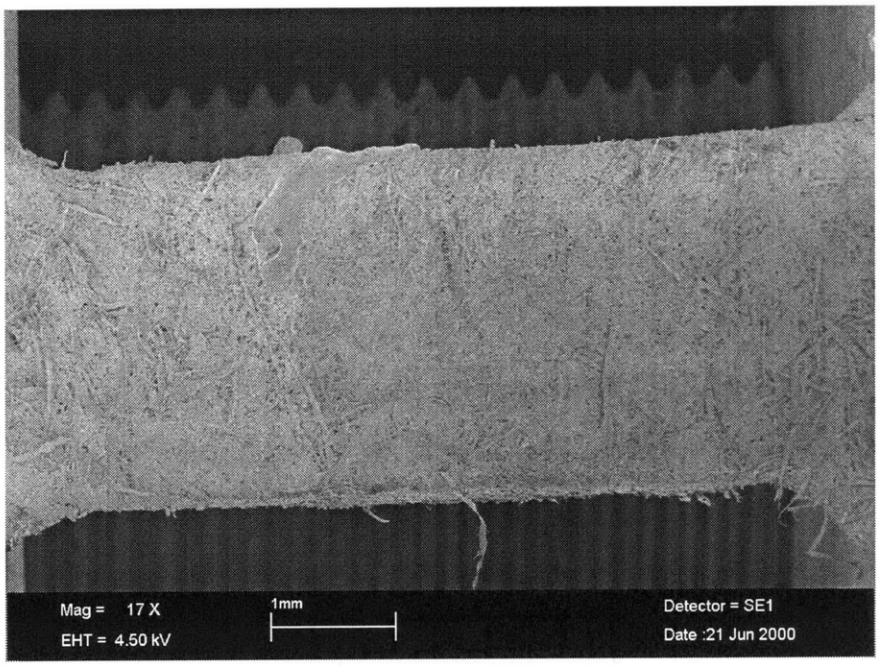

Figure 8-10: CD in-plane tension test at no load (Step 1). The material is Triplex with an outer chemical layer removed, exposing a core mechanical layer for imaging.

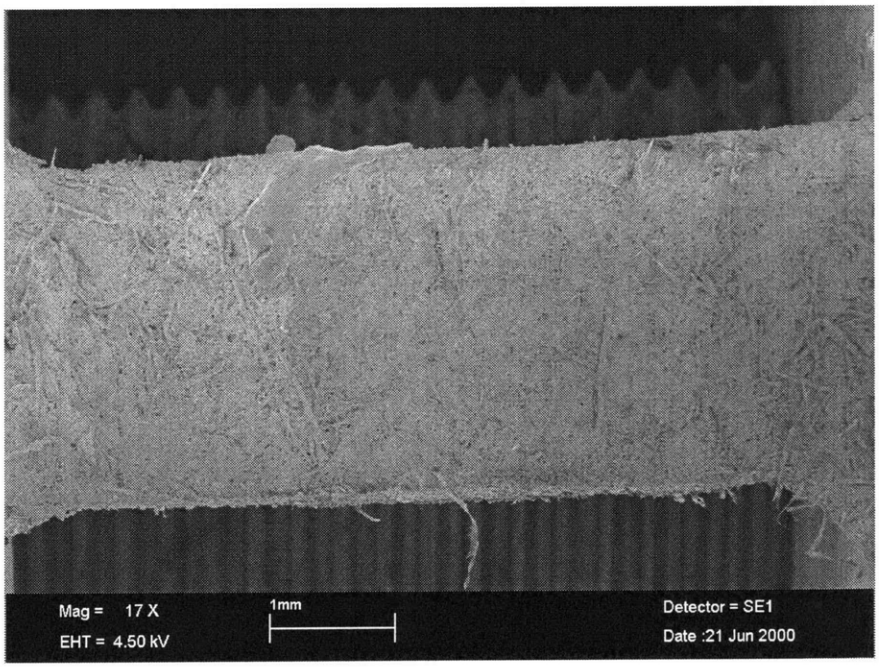

Figure 8-11: CD in-plane tension test (Step 2).

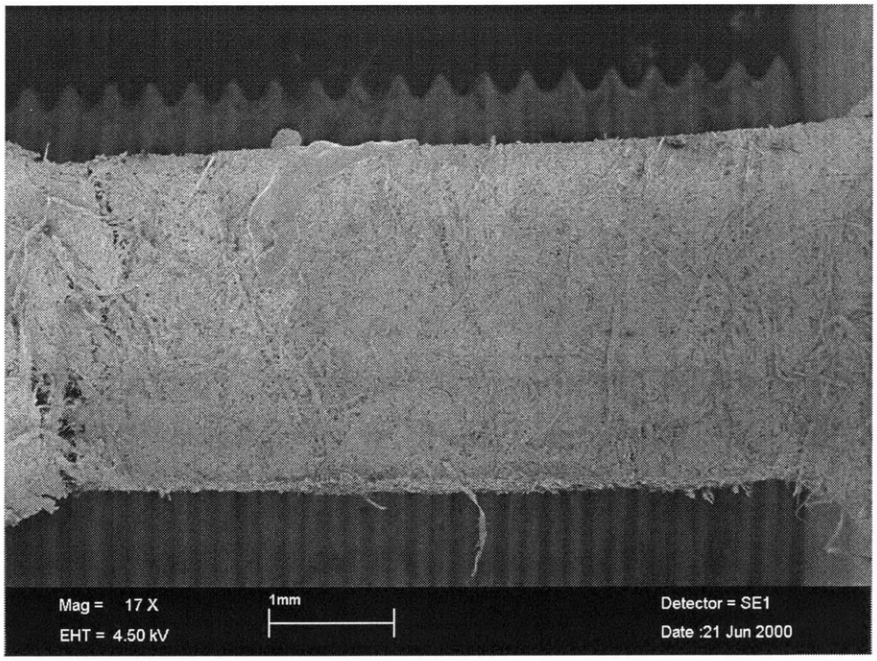

Figure 8-12: CD in-plane tension test (Step 3).

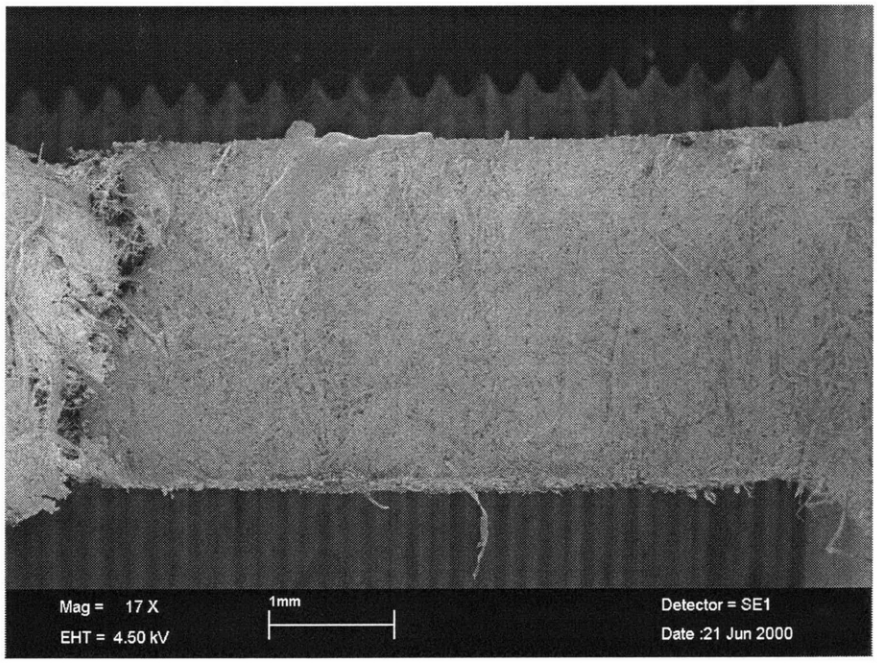

Figure 8-13: CD in-plane tension test (Step 4).

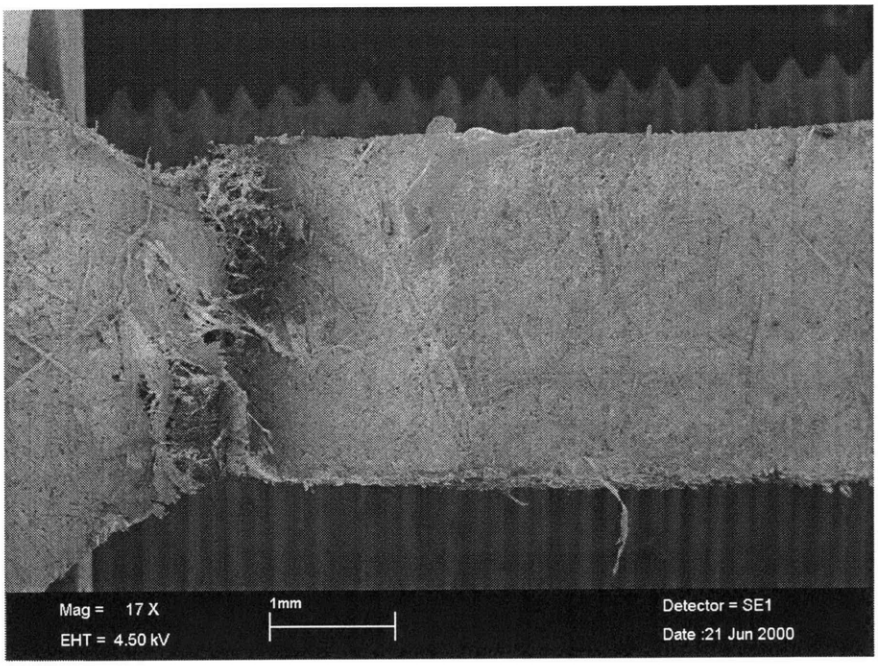

Figure 8-14: CD in-plane tension test (Step 5).

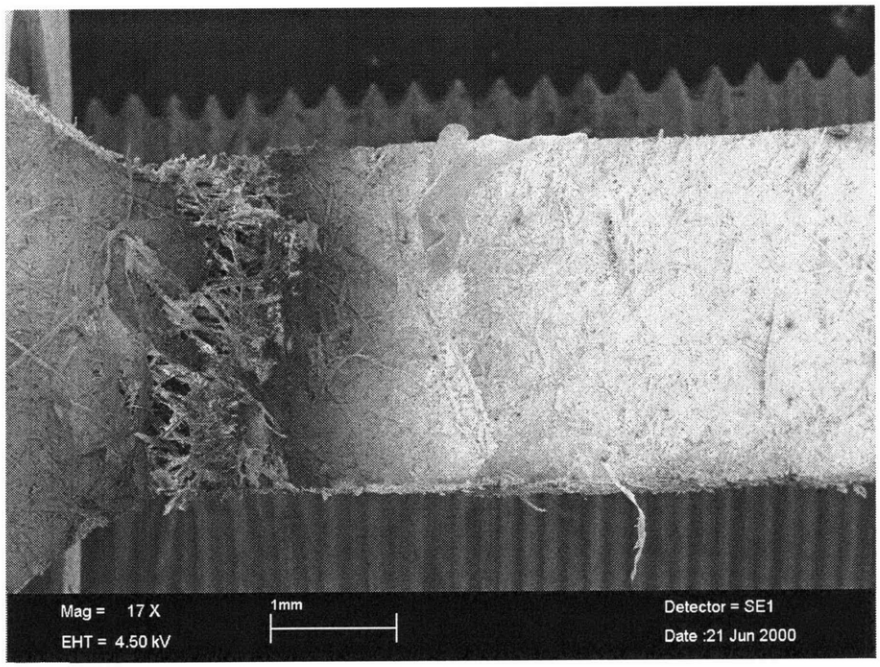

Figure 8-15: CD in-plane tension test (Step 6).

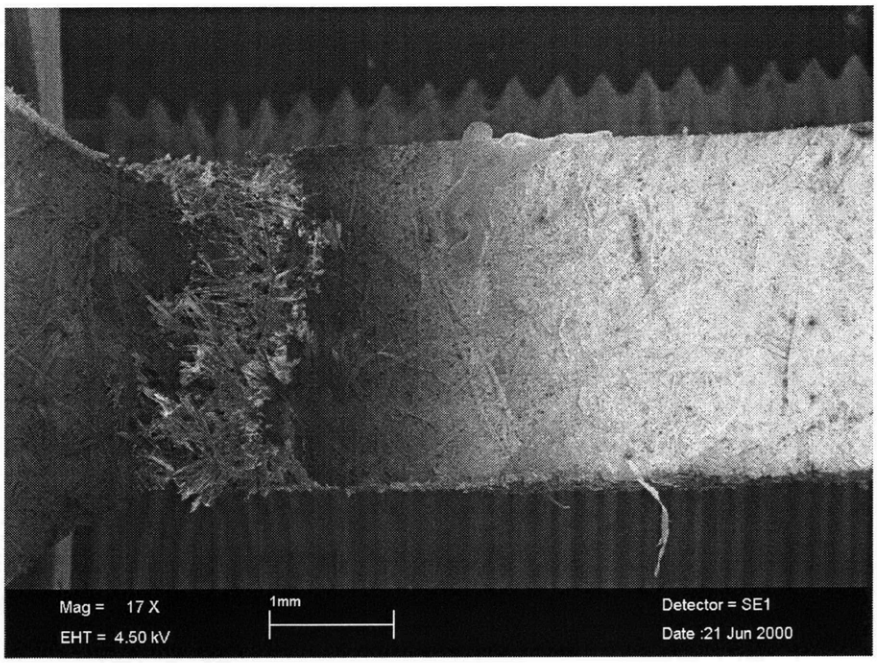

Figure 8-16: CD in-plane tension test (Step 7).

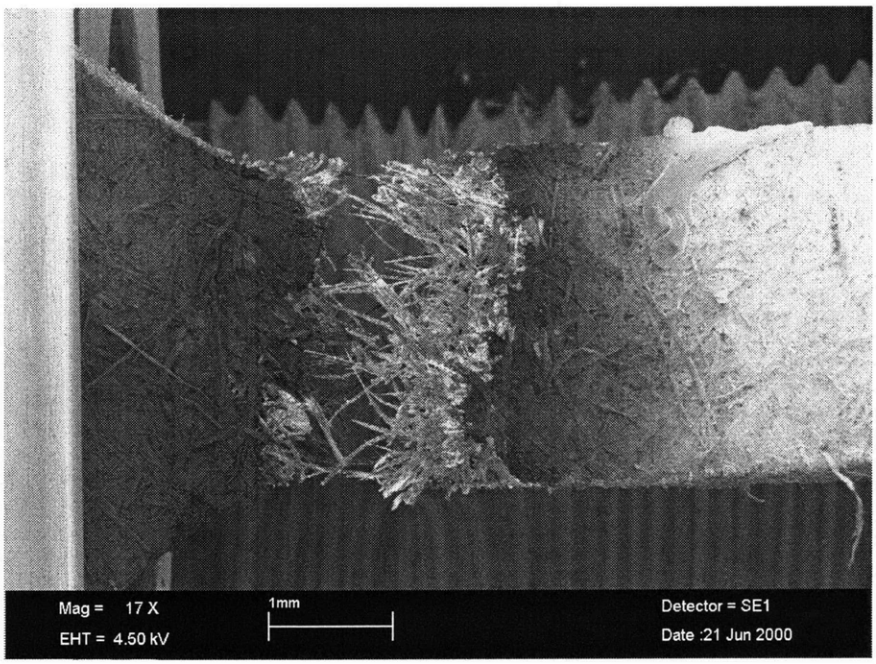

Figure 8-17: CD in-plane tension test (Step 8).

Deformation was continued through the remaining images, and load fell from 1.3 N in Figure 8-14 to almost zero in Figure 8-17. As the material separates at the failure line, bridging fibers are again in evidence. In steps 5 and 6, most of the bridging images are at a large angle to the loading direction, as they are lined up primarily along or near the machine direction. There is some re-orientation of fibers with deformation, so by step 8 there are a significant number of fibers oriented along or near the loading direction. However, the majority of fibers are still oriented closer to the machine direction. As a result, there is much less intermeshing of fibers across the gap than was the case in the machine-direction loading experiment.

Figures 8-18 through 8-25 give an edge-view of an in-plane tension test. In this test, the chemical layer has not been removed, and the paperboard is loaded in the machine direction. Figure 8-18 shows the specimen at a load of 1 N. The next two steps are also in the pre-peak region. These two images seem to show some disturbance of the edge surface. It is not known what causes these disturbances, although they may be the result of a differential Poisson contraction.

The load in this test peaked at 27 N. Figure 8-21 was taken directly after the peak at a load of 4.2 N. The failure region is at the left end of the frame. Fracture is clearly observable in the outer, chemical layers. These layers have delaminated from the inner layers in the failure region and have splayed slightly outward. The delamination and splaying in the images suggest that failure begins in the chemical layers and is followed quickly by failure in the mechanical layers, an idea supported by the mechanics. The chemical and mechanical layers are subject to the same strain as in-plane load is applied. However, the chemical layers are much stiffer than the mechanical layers and therefore feel a higher stress. If the strengths of the chemical and mechanical layers are similar, the chemical layers will fail first. Failure of the chemical layers would drasticly decrease the load-bearing area of the specimen. This would raise the stress in the mechanical layers, possibly causing them to fail immediately following chemical layer failure. Although this is a plausible scenario, it is not possible to discern from the images if this is definitely what is taking place. Without more information on the relative strengths of the chemical and mechanical layers, it is only possible to

speculate.

The remaining images show the material separating around the failure zone. Delamination and outward splaying of the outer layers becomes more pronounced in each successive step. In Figure 8-24, failure through the entire thickness is observable. This figure shows that each layer fails individually at a different location within the failure zone. The failure location in each layer is likely dictated by the location of pre-existing defects in that layer. The individual layer failures are even more pronounced in Figure 8-25. This image shows that the mechanical layers fail differently than the outer chemical layers. In the failed mechanical layers, individual fibers extend from each end of the break, suggesting that failure occurs by bond breaking and fibers pulling out of the matrix. The chemical layers display much cleaner breaks. Few individual fibers protrude from the material on each side of the break, and fibers that do protrude do so only a short distance. This suggests that the chemical layers fail primarily by fiber breakage rather than fiber pull-out.

One of the primary goals of the microscopic study of in-plane tension was to determine the mechanisms of yield and strain hardening for modelling purposes. The large disparity in strain to failure between the machine and cross directions first suggested that the hardening might be due to fiber reorientation. In the hardening phase, the fibers would line up with the direction of loading. When the material is loaded in the machine direction, most fibers would already be oriented close to the machine direction, so minimal additional strain would be necessary to line up the fibers. When the material is loaded in the cross direction, most fibers would be oriented almost perpendicular to the direction of loading. Much more strain would be required to reorient the fibers completely. Observations at the microscopic level dispelled this theory, however. As seen in the images here, there is no observable change in fiber orientation before failure. Additionally, consideration of the angle rotations necessary to reorient fibers in a CD specimen shows that the small strains attained in these experiments would not be sufficient for complete reorientation.

This left the possibility that the paperboard material was actually hardening rather than changing form in a way that resembles material hardening. One pos-

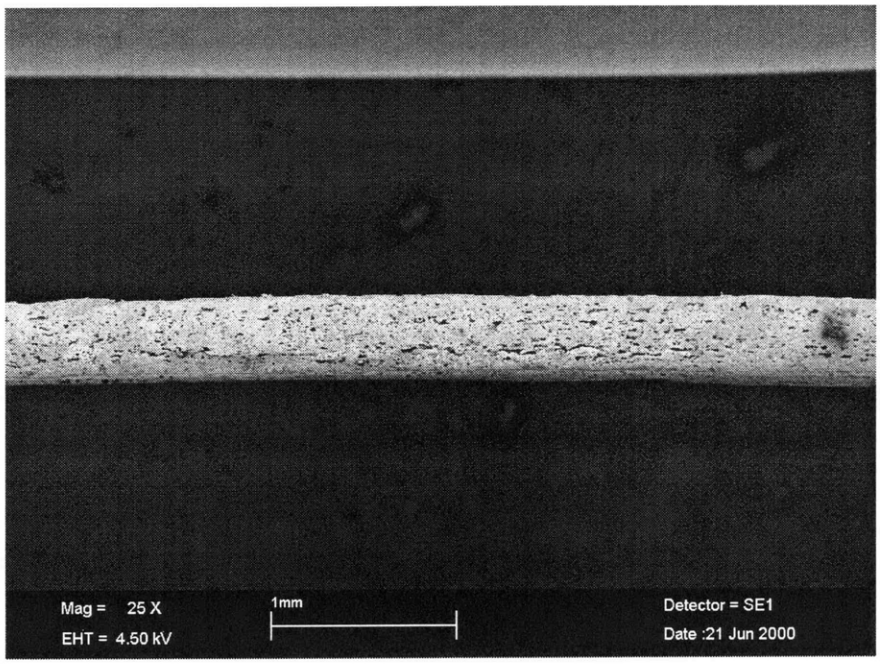

Figure 8-18: Triplex MD in-plane tension test at no load (Step 1).

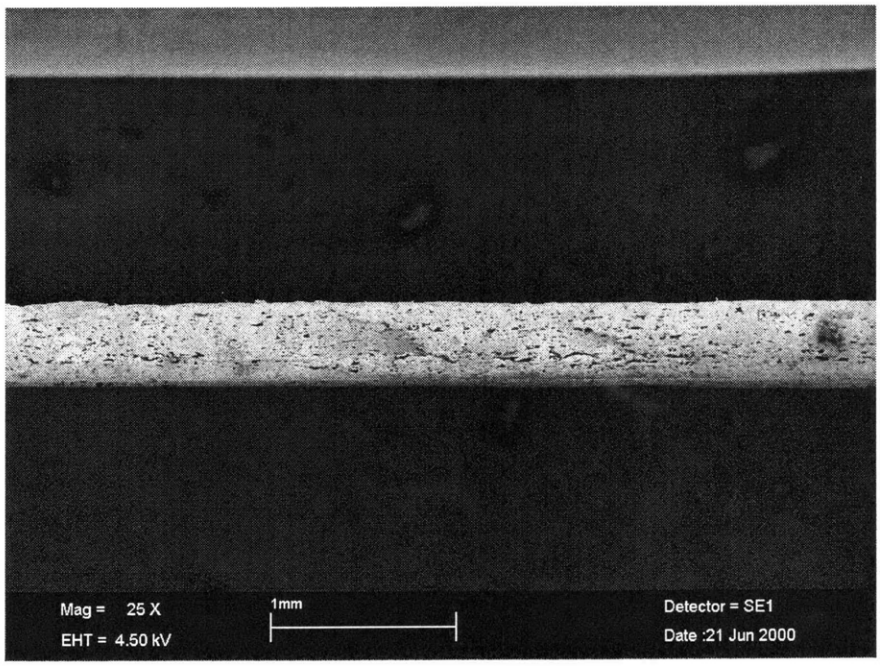

Figure 8-19: Triplex MD in-plane tension test (Step 2).

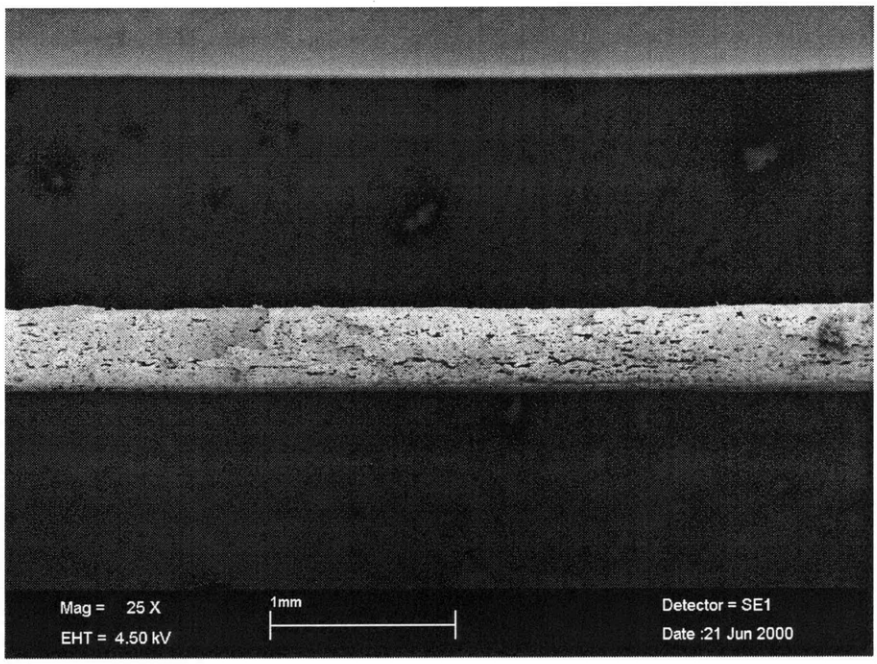

Figure 8-20: Triplex MD in-plane tension test (Step 3).

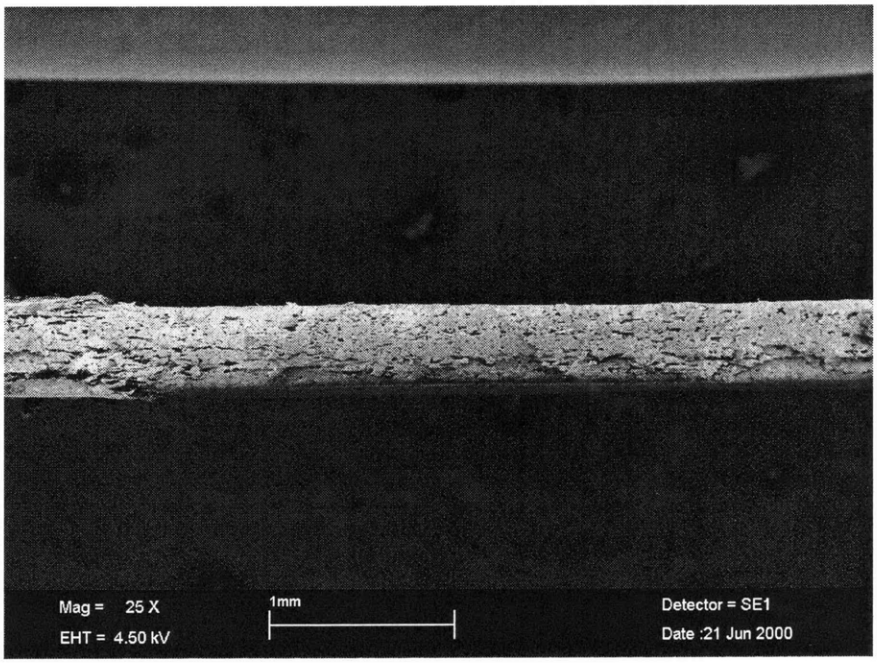

Figure 8-21: Triplex MD in-plane tension test (Step 4).

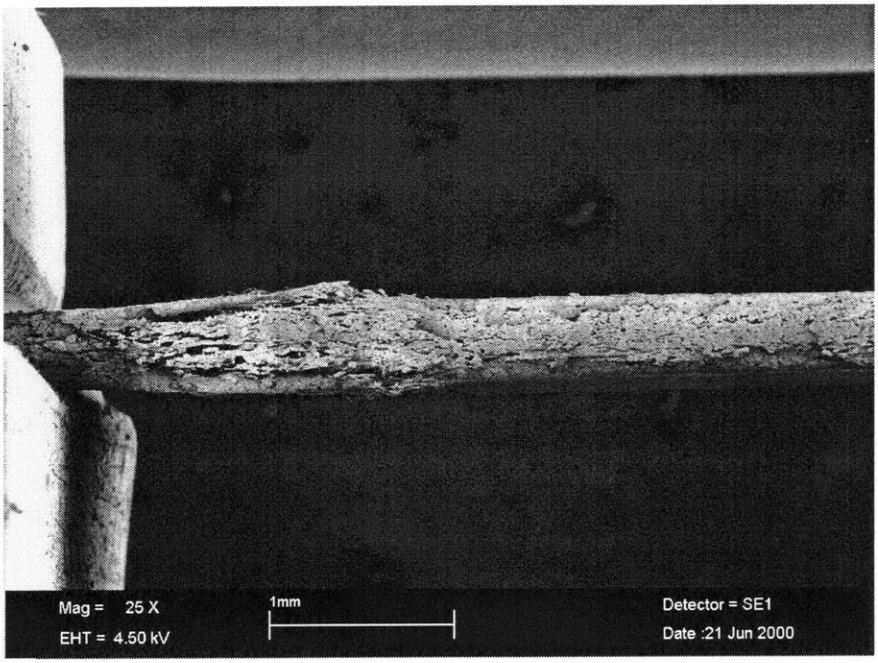

Figure 8-22: Triplex MD in-plane tension test (Step 5).

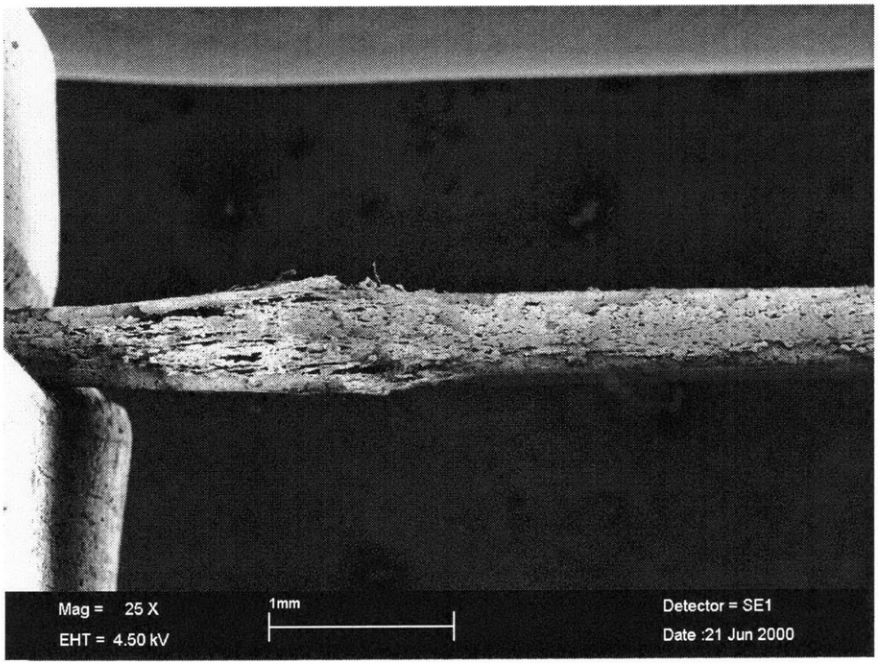

Figure 8-23: Triplex MD in-plane tension test (Step 6).

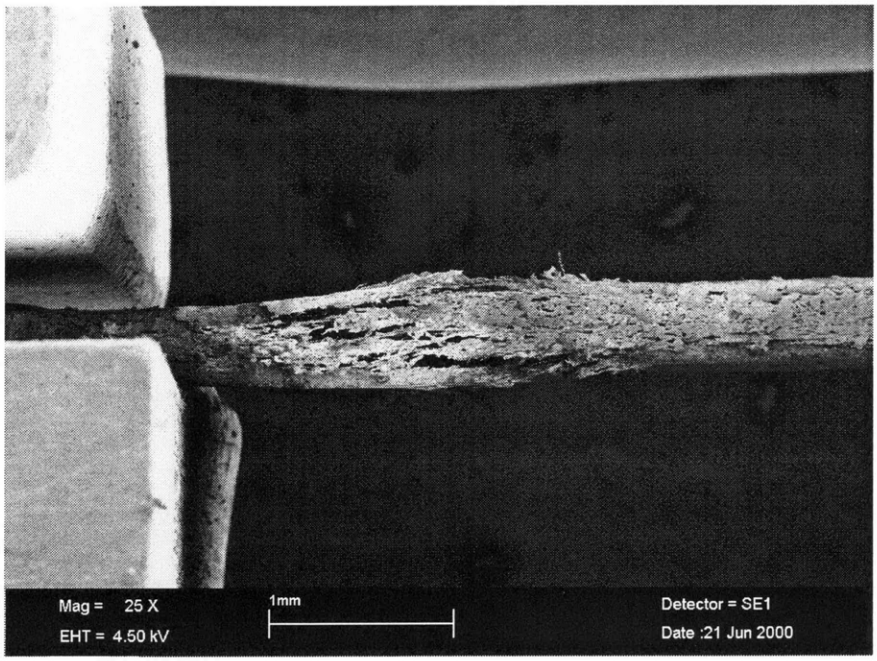

Figure 8-24: Triplex MD in-plane tension test (Step 7).

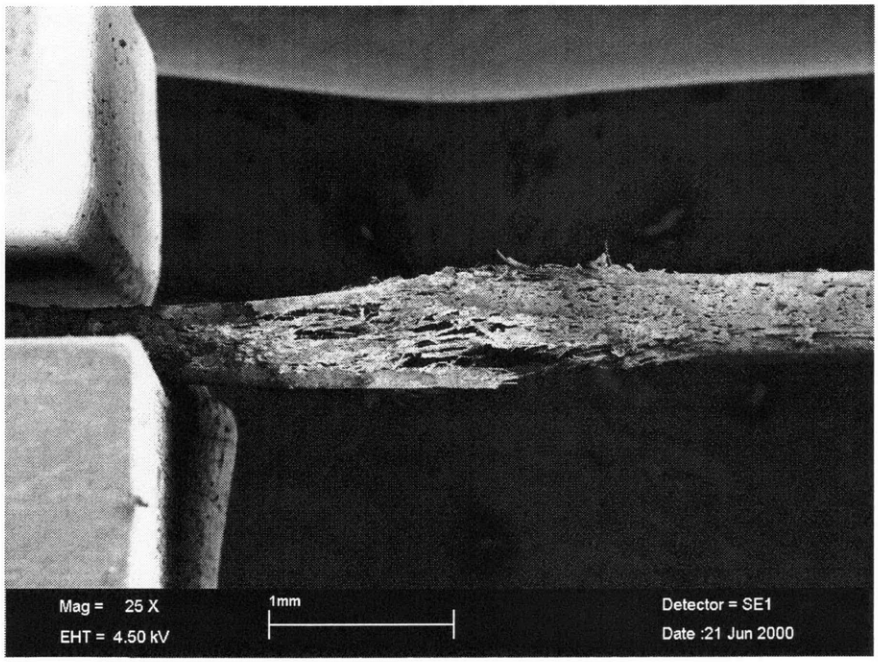

Figure 8-25: Triplex MD in-plane tension test (Step 8).

sibility for hardening within the material is hardening of the individual fibers. A second possibility is hardening due to load transfer at the bonds between fibers. To determine the dominant mechanism, attention was focused on the paperboard failure mechanism. If load is carried primarily by the fibers, failure should occur by fiber breakage. If load is carried primarily at the bonds, failure should occur by bond breakage and fiber pull-out.

The planar images of in-plane tension presented here suggest that failure occurs by fiber pull-out. To further investigate this idea, high-magnificaton images of paperboard immediately after in-plane failure were taken under variable pressure in the scanning electron microscope. Variable pressure mode maintains a small pressure in the microscope chamber, minimizing charging of non-conductive materials like paper. A mosaic of high-magnification images was constructed to show the entire failure region. In the mosaic, regions that were coated in gold are lighter in color than uncoated regions. Examining individual fibers in the mosaic, some were found that were light in color along the entire observable length except for small stripes of darker material. These stripes were former bond locations; the uncoated material was exposed when the bond was broken. This shows that the material was failing by interfiber bond breakage.

The mosaic images may not have accurately represented failure through the entire material thickness, however, as they were taken of a mechanical layer. The chemical layer of the specimen had been removed. Edge-view images of in-plane tension which were taken later showed that chemical layers and mechanical layers do not fail in the same manner. As discussed above, the mechanical layers fail primarily by bond breakage, but in the denser chemical layer, failure is due to fiber breakage.

This fits with our knowledge of the structure of the mechanical and chemical layers. In the mechanical layers, fibers are loosely packed with relatively few bonds along their lengths. Fibers in the chemical layers are packed more densely and have many more bonds along their length. Both fibers and bonds have a peak load that they can carry. If a fiber has many bonds along its length, the total load carried by each bond will be small. In this case, the fiber should reach its peak load before any

of the bonds will, causing the fiber to fail. A fiber with few bonds along its length will experience a lower load relative to the load at each bond. If there are few enough bonds, the critical load at a bond will be reached before the critical load of the fiber, causing a bond to fail. This explains why a densely-bonded chemical layer would experience fiber failure, while a sparsely-bonded mechanical layer would fail by fiber pull-out. Although it is not possible to isolate the causes of strain hardening from these observations, they do reveal much about the mechanisms of in-plane tension in paperboard.

Chapter 9

Discussion and Conclusions

Creasing experiments performed in this study demonstrate several important facts about the process. Bending paperboard to create a corner creates in-plane tensile stresses on the outside of the bend and in-plane compression at the interior. To create a good crease and prevent tearing of the outer material, the inner material must buckle in association with through-thickness delamination. This delamination occurs at the interfaces between layers of the paperboard. Thus, a material with numerous interfaces, like Triplex, is desirable to allow sufficient delamination. In addition, the delamination in a good crease occurs exactly at the center of the corner, rather than off to one side. Delamination central to the bend increases the strength of the corner under axial compression and improves the appearance of the crease by making it sharp and straight. The location of delamination relative to the corner is determined by factors such as punching die sizes (male and female), punch depth, magnitude of web tension, and bending moment arm length.

The creasing experiments also show the loading modes prominent in the creasing process, as shown in Chapter 3. During the punching step, paperboard under the punch is loaded in through-thickness compression. Along the sides of the punch, the material sustains interlaminar damage due to out-of-plane shear loading. The material in this region also shows bulging, the effects of shear dilation. In addition, the material in the punch region is subjected to in-plane tension. During the bending stage, the primary mechanism is delamination in the manner of through-thickness

tension. Based on these observations, experiments were performed to investigate out-of-plane tension, compression, and shear, as well as in-plane tension.

Macroscopic stress-strain curves for through-thickness tension show an intial linear elastic region followed by a region of nonlinear behavior resembling yield followed by strain hardening. Beyond the peak in stress, the material softens. Microscopic images of through-thickness tension indicate that this softening corresponds to the formation of microcracks at the interfaces between layers in the material. The microcracks typically nucleate at pre-existing flaws or weak locations on the interfaces. As deformation continues, microcracks along one interface coalesce into a macrocrack. This corresponds to a decrease in the rate of softening. All further deformation is accommodated at the macrocrack, and remaining microcracks relax.

In through-thickness compression, Triplex again displays initial linear elastic behavior with stiffness similar to that observed in tension. Beyond the elastic region, the material hardens exponentially. Deformation occurs in two stages. In the first stage, voids and gaps in the material are compressed. Although it was difficult to correlate mechanisms with stress-strain curve features in this study, it is likely that this deformation phase corresponds to the linear region of the curve. After voids have been largely eliminated, the entire thickness of the material begins to compress. This phase is probably correlated with the nonlinear region of the stress-strain curve.

Macroscopic experiments on interlaminar shear show initial linear behavior followed by a nonlinear region resembling strain hardening, as was the case with tension. The material is both stiffer and stronger in the machine direction, and consequently fails at smaller displacements. Beyond the peak in load, the material softens rapidly. This softening is much more dramatic in the microscopic level data collected than in the macroscopic data, suggesting a length scale effect. Microscopic images of shear deformation show that the dramatic softening corresponds to sudden failure by delamination. At the microscopic level, this delamination appears to happen throughout the entire cross section simultaneously. However, it is possible that at the macroscopic level, delamination happens locally and propagates through the material, explaining the less severe softening observed. Delamination in shear occurs at only one interface,

in contrast to through-thickness tension where delaminaton in the form of microcracks occurs along multiple interfaces.

Paperboard loaded in out-of-plane shear shows another curious deformation mechanism. After delamination failure, some fibers remain embedded in material on both sides of the gap. Some of the fibers are rotated as additional shear displacement is applied. The rotating fibers push the delamination gap further open, creating shear dilation of the material. This is the same phenomenon that causes bulging of paper around the male die in the punching step of creasing.

Combined tension-shear loading experiments were conducted to determine a failure surface for Triplex in out-of-plane loading and to study the mechanisms of deformation and failure under combined loading. The experiments showed a transition between tensile effects and shear effects as the proportion of shear to tensile load increased. This transition was particularly apparent in the microscopic images of deformation. At small angles, dominated by the tensile component of loading, the material undergoes extensive microcracking before macrocrack formation. At larger angles, however, much less microcracking occurs before macrocrack formation, due to shear deformation. Failure strengths collected at both the macroscopic and microscopic levels were compiled to create failure surfaces that fit parabolic regression curves.

These experimental results suggest several features that should be included in modeling paperboard behavior under out-of-plane load. The model should incorporate two types of elements, interface and continuum. These element types allow the model to capture damage at the interfaces while accurately representing the properties of the individual layers. The varied strength distribution of an interface also should be captured by the model, as damage nucleates at weak points along the interfaces. Finally, the continuum element material models should reflect the nonlinear behavior displayed by paperboard in the region preceding peak stress in through-thickness tension and in the entire strain range of through-thickness compression.

Experiments were also performed to study in-plane tension. Macroscopic data shows that the initial stress-strain response is linear elastic. Triplex is both much

stronger and much stiffer in the machine direction than in the cross direction under in-plane tension. However, beyond the linear region the material displays nonlinear behavior similar to hardening. Triplex can sustain much more strain in the cross direction in this nonlinear region, leading to much higher strains to failure than in the machine direction. This difference in strain capacity suggested that the nonlinear behavior might be the result of fiber reorientation to align with the loading direction. Microscopic images showed that this was not the case. This left two other possible causes of nonlinear behavior, load transfer at the bonds and actual strain hardening of individual fibers.

Analysis of images taken of in-plane tensile failure showed that nonlinearity is caused by a combination of these effects. The outer chemical layers fail by fiber fracture, while the core mechanical layers fail at the bonds between fibers. In both the chemical and mechanical layers, there is load transfer through the bonds. The amount of load transferred to a fiber at each bond depends on the number of bonds along the fiber length. In the dense chemical layers with high bond density, the load transfer at each bond was small while the total load transfered to the fiber was large, causing failure of the fiber. In the mechanical layers, bond density is lower. Load at each bond is larger compared with the total load carried by the fiber, so the bonds fail before the fibers. These observations do not reveal the causes of material nonlinearity, but they do give good insight to the mechanisms of in-plane tension in paperboard.

A model of in-plane behavior should include both the linear and nonlinear behavior. The model should also represent the different material properties exhibited by the different types of layers, in this case chemical and mechanical.

Additional testing would further improve understanding of material load-deformation response and deformation mechanisms at the layer and fiber level. One loading mode not extenstively investigated in this study was in-plane compression. Preliminary work indicated that in-plane compression is very different at different length scales. At a relatively long length scales of several millimeters, the paperboard fails by global buckling. At the small sub-millimeter scale, the board fails by individual layer buckling. These mechanisms should be studied, as in-plane compression plays a role in

the folding step of creasing.

Out-of-plane shear and in-plane tension experiments in this study were limited to loading in the machine and the cross directions. A complete model of paperboard should also accurately represent loading between these two directions, requiring additional experimentation. A complete parametric study of creasing, with male die size, female die size, and depth of punch as parameters, could also be beneficial. In addition to increasing understanding of creasing, it would supply a wealth of experimental results to compare with predictions made by the numerical model.

Appendix A

Error Analysis

Recall the discussion of data scatter at the microscopic level in Chapter 2. Scatter in stress values at the microscopic level may be due to specimen size, glue amounts, or load cell calibration. Specimen size for microscopic tension tests is nominally 6 mm by 6 mm. However, the specimens are measured and cut by hand, using a ruler, pencil, and razor blade. This can create significant variation in specimen size which is not accounted for in stress calculations. An upper and lower bound of actual specimen size can be estimated and compared to the value used in stress calculations. Actual specimen size is given by the following expression, where x and y refer to the deviation in specimen dimension in each direction from the nominal 6 mm.

$$(6 \pm x)\ mm \times (6 \pm y)\ mm = [36 + 6(x + y) + xy]\ mm^2 \tag{A.1}$$

An estimate for maximum x and y values is 0.5 mm. This yields an upper bound on actual area of 42.25 mm^2 and a lower bound of 30.25 mm^2. Stress values calculated using an area of 36 mm^2 may overestimate stress by up to 17% or underestimate by up to 16%. An actual stress value of 0.4 MPa, a typical peak stress for through-thickness tension of Triplex, could be reported anywhere between 0.34 MPa and 0.47 MPa, depending on actual specimen size.

This analysis can be repeated for the specimens used in shear testing, which are 3 mm by 3 mm in size. Equation A.1 becomes the following for these smaller

specimens.

$$(3 \pm x)\ mm \times (3 \pm y)\ mm = [9 + 3(x + y) + xy]\ mm^2 \tag{A.2}$$

Again using 0.5 mm as a maximum value for x and y, the upper bound on actual area is 12.25 mm^2. The lower bound is only 6.25 mm^2. Stress values calculated using an area of 9 mm^2 may results in overestimates of up to 36% or underestimates up to 31%. A typical peak stress for interlaminar shear of Triplex in the machine direction is 1 MPa. Variation in specimen size could cause an actual stress of 1 MPa to be reported anywhere between 0.69 MPa and 1.36 MPa.

A second source of scatter is glue coverage. The amount of glue spread over such a small area may also vary from one specimen to another, further changing the effective cross-sectional area. The effects of glue coverage cannot be evaluated precisely, because the unglued area will still carry some load. If it is near the center of the specimen, there will be load transfer from material on all sides. If the unglued area is closer to the edge, load transfer effects may be small at first, but will become significant at larger strains, particularly after delaminaton begins. Despite this, the effects can be estimated. The calculation presented here assumes that the unglued area contributes no load-carrying capacity, so it overestimaes the total error.

Suppose insufficient glue is applied to a tension fixture and only 90% of one side of the specimen suface is covered, the effective cross sectional area is reduced. Suppose the actual specimen size is 30.25 mm^2, the lower bound found above. Glue coverage of only 90% further reduces effective cross sectional area to 27.23 mm^2. Caculated stress values for such a specimen would be almost 25% lower than actual values. An actual peak stress of 0.4 MPa would be reported as only 0.30 MPa. For an undersized shear specimen 6.25 mm^2 in area, this would result in an effective area of 5.63 mm^2, less than 2/3 the area used in calculations. An actual stress of 1 MPa would be reported as only 62.5 MPa. It is also possible for excess glue to cause attachment between the opposing blocks of a fixture. The effect of excess glue is harder to quantify than the effect of insufficient glue, but as careful specimen preparation can generally eliminate excess glue, the effects are not of concern.

The load cells used for microscopic testing experience small amounts of drift between calibrations. This is corrected by resetting the strain gauge indicator parameter "reading offset" between each test. However, drift that occurs during a test will affect reported stress values. A typical amount of drift during one test would be 0.1 N. For a specimen with area 36 mm^2, this causes stress to be misreported by only 0.003 MPa. A specimen with area 9 mm^2 would see stress misreporting by only 0.01 MPa. This effect is very small, but when combined with variations in glue and specimen size, the total effect can be considerable.

Strain values vary widely between tests due to fixture slackness and motor speed fluctuations, as discussed previously.

Appendix B

Stress and Strain Definintions

All through-thickness tension and compression stress-strain curves use nominal stress and true strain measures. Nominal stress, as defined in Equation B.1, is the applied load divided by the initial area. It does not reflect changes in the stress state due to change in specimen area.

$$\sigma = P/A_o \tag{B.1}$$

True strain is defined in Equation B.2, where t is the deformed thickness of the specimen, and t_o is the initial thickness.

$$\epsilon = ln(\frac{t}{t_o}) \tag{B.2}$$

The interlaminar shear data presented here also uses nominal stress.

$$\tau = P/A_o \tag{B.3}$$

The microscale shear curves use the rigorous strain defintion of Equation B.4.

$$\gamma = arctan(d/t) \tag{B.4}$$

In this expression, d represents the displacement in the shear direction, and t is the specimen thickness. As stated in Chapter 6, this expression can be simplified at small

displacements to Equation B.5.

$$\gamma = d/t \tag{B.5}$$

The material behavior curves presented for in-plane tension used nominal stress, as defined above in Equation B.1, and nominal strain. Nominal strain is defined in Equation B.6.

$$\epsilon = \frac{L}{L_o} \tag{B.6}$$

In this expression, L is the deformed length of the specimen, and L_o is the initial length.

Bibliography

[1] Carlsson, L. Fellers C., and De Ruvo A. The mechanism of failure in bending of paperboard. *Journal of Materials Science*, 15:2636-2642, 1980.

[2] Donner, B. C., and Backer, S. The role of continuum instabilities in compression and bending failure of paper and board. *1987 International Paper Physics Conference*, 231-236, 1987.

[3] Carlsson L., De Ruvo A., and Fellers C. Bending properties of creased zones of paperboard related to interlaminar defects. *Journal of Materials Science*, 18:1365-1373, 1983.

[4] Koubaa, A., and Koran, Z. Measure of the internal bond strength of paper/board. *TAPPI Journal*, 78(3): 103-111, March 1995.

[5] Persson, K. Material model for paper. Diploma report, Lund Institute of Technology, Lund, Sweden, 1991.

[6] Johnston, R. E., Ting, T. H. P., and Chiu, W. K. Characterizing network changes in paper under compression in the Z-direction. *1995 International Paper Physics Conference*, 115-119, 1995.

[7] Ratto, P., and Rigdahl, M. The deformation behavior in the thickness direction of paper subjected to a short pressure pulse. *Nordic Pulp and Paper Research Journal*, 13(3): 180-185, 1998.

[8] Schaffrath, H. J., and Goettsching, L. Compression behavior of paper in the Z-direction. *Das Papier*, 46(10A): V74-V81, October 1992.

[9] Byrd, V. L., Setterholm, V. C., and Wichmann, J. F. Method for measuring the interlaminar shear properties of paper. *TAPPI Journal*, 58(10): 132-135, 1975.

[10] Fellers, C. Procedure for measuring interlaminar shear properties of paper. *Svensk Papperstidning*, 80(3), 1977.

[11] Waterhouse, J. E. Out-of-plane deformation of paper and board. *1983 International Paper Physics Conference*, 111-119, 1983.

[12] El Maachi, A., Sapieha, S., and Yelon, A. Angle dependent delamination of paper: Determination of deformation and detachment work in paper peeling. *Journal of Pulp and Paper Science*, 21(12): J401-J407, December 1995.

[13] Tryding, J. In-plane fracture of paper. Lund Institute of Technology, Lund, Sweden, 1996.

[14] Arcan M., Hashin Z., and Voloshin A. A method to produce uniform plane-stress state with applications to fiber-reinforced materials. *Experimental Mechanics*, 18(4):141-146, 1978.

[15] Nystroem, T. Development report no. 3082. Technical report, TetraPack, Sweden, 1986.

[16] Smith, C. A. *Micromechanisms of the Through-Thickness Deformation of Paperboard.* Master of Science thesis, Massachusetts Institute of Technology, Cambridge, MA, 1999.